



**APPLICATION OF SPLINE VARIATIONAL
ANALYSIS METHOD IN THE MODELING OF
COMPOSITE REPAIRS**

THESIS

Brian M. Fredrickson, Second Lieutenant, USAF
AFIT/GAE/ENY/06-M09

**DEPARTMENT OF THE AIR FORCE
AIR UNIVERSITY**

AIR FORCE INSTITUTE OF TECHNOLOGY

Wright-Patterson Air Force Base, Ohio

APPROVED FOR PUBLIC RELEASE; DISTRIBUTION UNLIMITED

The views expressed in this thesis are those of the author and do not reflect the official policy or position of the United States Air Force, Department of Defense, or the United States Government.

AFIT/GAE/ENY/06-M09

APPLICATION OF SPLINE VARIATIONAL ANALYSIS METHOD IN THE
MODELING OF COMPOSITE REPAIRS

THESIS

Presented to the Faculty

Department of Aeronautics and Astronautics

Graduate School of Engineering and Management

Air Force Institute of Technology

Air University

Air Education and Training Command

In Partial Fulfillment of the Requirements for the
Degree of Master of Science in Aeronautical Engineering

Brian M. Fredrickson, BS

Second Lieutenant, USAF

March 2006

APPROVED FOR PUBLIC RELEASE; DISTRIBUTION UNLIMITED.

AFIT/GAE/ENY/06-M09

APPLICATION OF SPLINE VARIATIONAL ANALYSIS METHOD IN THE
MODELING OF COMPOSITE REPAIRS

Brian M. Fredrickson, BS
Second Lieutenant, USAF

Approved:

Anthony Palazotto (Chairman)

date

Ted Nicholas (Member)

date

Greg Schoeppner (Member)

date

Abstract

The purpose of this thesis is to apply a non-commercialized spline-based (B-Spline Analysis Method or BSAM) computer program to model and predict strain fields in two composite repairs, a scarf joint and a stepped-lap joint, subjected to static tensile loading. Test specimens with scarf and stepped-lap joints are fabricated using quasi-isotropic sixteen ply panels made from IM6/3501-6 prepreg with a $[+45_2/0_2/-45_2/90_2]_s$ lay-up. The panels were bonded together with FM-300M (0.05psf), a 176°C cure film adhesive, under positive pressure. A total of five coupons of each joint type are made. Two of the stepped-lap and scarf coupons are instrumented with acoustic emission sensors and loaded in tension to failure to determine appropriate loading for experimentation. Moire interferometry, a high resolution full-field optical technique used to measure displacements on a surface, is used to acquire experimental strain data. Diffraction grating is applied to the polished edge of two stepped-lap and two scarf coupons, while one coupon of each was selected for experimentation under a static tensile load of 450lb_f.

Using measurements from the actual coupon specimens, idealized models of the stepped-lap and scarf joints are developed for the BSAM computer program. For the scarf joint, a linear bond-line and uniform adhesive layer are modeled. In reality, the bond-line was not exactly straight and the adhesive layer varied in thickness across the length of the repair. For the stepped-lap joint, steps with perfectly square corners are modeled; in reality, the bottom of each step was rounded.

Full-field strains along the free-edge are predicted and compared to experimental strain data. Line plots are generated from predicted and experimental data extracted at several points across the width of the repair to provide a more quantitative assessment. Overall, both the full-field strain images and line plots show a good agreement between the BSAM analysis and the experiment.

Acknowledgements

The completion of this thesis would not have been possible without the help from several individuals at AFIT and AFRL/ML. First of all, I would like to thank my academic advisor, Dr. Anthony Palazotto, and my AFRL/ML advisor, Dr. Greg Schoeppner. Dr. Palazotto provided invaluable guidance, advice, and support throughout the course of my thesis effort. His positive attitude and outlook on solid mechanics (and life in general) was a great source of motivation. Dr. Greg Schoeppner took an immense amount of time to teach me the ropes of BSAM and guide me through my entire thesis effort as well. In the process, he has given me confidence as I make the transition from academics in the classroom to research in the laboratory.

When I first came to AFRL/MLBC to start my thesis, I had little knowledge of how to actually lay-up, cure, or machine composites. Experts in the field, Ron Trejo, Ron Esterline, and John Camping, went out of their way to make sure I didn't mess anything up too much. Ron Trejo showed me how to lay-up and cure panels from the original pre-impregnated carbon-epoxy sheets, while John Camping provided the technical skills necessary to machine the steps for the stepped-lap specimens. Without Ron Esterline, I would not have been able to run the tensile tests needed to determine appropriate loading in the moiré apparatus. I would like to thank these individuals for their help at pivotal points in my thesis effort.

I would especially like to thank Paul Childers of AFRL/MLSA. During the first few months of my time at ML, I was able to make progress by tapping into Mr. Childer's technical knowledge and expertise on a daily basis. Not only did Paul walk me through and oversee the machining of the scarf repairs and bonding and curing of all specimens, but the design and creation of the scarf angle fixture can be attributed entirely to his ingenuity and craftsmanship. When I needed to get something done or wanted advice at any point in the manufacturing process, I went to him, as he proved to be friendly, knowledgeable, and action oriented. Dan McCray of AFRL/MLSA also gave me key advice and references throughout the my thesis effort.

The individual who provided crucial help in the testing portion of my thesis effort was Dr. David Mollenhauer of AFRL/MLBC. Without his extensive knowledge of moiré fringe pattern data collection and analysis, it would have been impossible for me to gather the experimental data for this thesis. In addition to demonstrating a great deal of technical expertise in his field, Dr. Mollenhauer provided me with theoretical insight throughout the data collection process. On the BSAM program side of the thesis effort, Dr. Endel Iarve of AFRL/MLBC also provided some key technical support.

Brian M. Fredrickson

Table of Contents

	Page
Abstract.....	iv
Acknowledgements.....	vi
Table of Contents.....	vii
List of Figures.....	ix
List of Tables.....	xv
I. Introduction.....	1
Motivation.....	1
Background.....	2
Composite Repair Techniques.....	2
The Scarf Joint.....	6
The Stepped-Lap Joint.....	8
Experimental Studies on Scarf Joints.....	9
Experimental Studies on Stepped-Lap Joints.....	10
Modeling of Scarf and Stepped-Lap Joints.....	12
Development of Spline Approximation Applications.....	14
Problem Statement.....	15
Overview of Thesis.....	16
II. B-Spline Analysis Method.....	18
Theory.....	18
BSAM Computer Code.....	23
III. Methodology: Specimen Fabrication.....	27
Panel Manufacture.....	27
Scarf Specimen Manufacture.....	31
Stepped Lap Joint Specimen Manufacture.....	45
IV. Experimentation: Moiré Interferometry.....	56
Moiré Diffraction Grating Replication.....	56
Experimentation.....	70
Generation of Plots.....	75
V. Results and Analysis.....	81
Full-field Strain Images.....	81
Stepped-Lap Joint.....	81
Scarf Joint.....	85
Analysis of Results.....	86
Line Plots: Stepped-Lap Joint.....	87
Line Plots: Scarf Joint.....	104
VI. Conclusions and Recommendations.....	125

	Page
1. Stepped-Lap Joint.....	125
2. Scarf Joint.....	126
Manufacture of straight scarf joint	128
Theory versus reality of stepped-lap joints.....	128
Continue to refine the BSAM computer program's graphical user interface (GUI)	129
 Appendix B: Computational Modeling of Specimens.....	 150
Problem Summary	152
Failure Input Block (Evolution Rules)	153
Material Input Block	154
Constitutive Model Input Block	158
Geometry Input Block	160
Discretization Input Block.....	169
Spline Input Block.....	173
Approximation Input Block.....	175
Model Input Block.....	180
Cluster Input Block.....	182
Set Input Block	185
Structure Input Block.....	186
Verifying accuracy of model	190
Boundary Conditions Block	192
Output Block	194
Process Input Block.....	204
 Appendix C: Determination of appropriate loading	 206
Background on acoustic emissions.....	207
Test Procedure	208
Tests 1-3: Virgin (unrepaired) Specimens.....	209
Tests 4-5: Stepped-lap Specimens.....	215
Tests 6-7: Scarf Specimens	220
Summary	224
 Appendix D: Initial line plots comparing predicted strain data and experimental results.....	 226
 Appendix E: Refined line plots comparing predicted and experimental data.....	 247
 Appendix F: Idealization of scarf specimens.....	 274
 Bibliography	 279
 Vita.....	 283

List of Figures

	Page
Figure 1. Adhesively Bonded Joint Types (Tong and Soutis).....	4
Figure 2. Failure modes for different bonded joint types (Tong).....	5
Figure 3. Idealized adhesive shear stress distributions of various joint configurations.....	6
Figure 4. Strength of Materials Analysis of Scarf Joint (Baker).....	7
Figure 5. Schematic of stepped-lap joint (Baker).....	8
Figure 6. Bagging Schematic (Cycom).....	28
Figure 7. Autoclave Curing Cycle for IM6/3501-6.....	29
Figure 8. C-scan of Panel #524.....	30
Figure 9. C-scan of Panel #525.....	30
Figure 10. Quartered Test Panel #525.....	31
Figure 11. Apparatus used to Create Scarf.....	32
Figure 12. Interaction between Radial Sander and Apparatus.....	32
Figure 13. Adhesive used to fix panel to apparatus.....	33
Figure 14. Panel fixed to Apparatus used to create scarf.....	33
Figure 15. Desired Slope Angle of Scarf Joint.....	33
Figure 16. Actual scarf angle achieved during manufacture.....	34
Figure 17. Direction of Sander Rotation.....	35
Figure 18. Scarf Surface created without use of Guide.....	36
Figure 19. Guide made to decrease user degrees of freedom.....	36
Figure 20. Dotco Hand Grinder.....	37
Figure 21. Scarf Surfaces created using $[0/45/-45/90]_{2s}$ Practice Panels.....	37
Figure 22. Final scarf surfaces from above.....	39
Figure 23. Jig used during adhesive curing.....	40
Figure 24. Panel during bagging process.....	41
Figure 25. Autoclave used during cure adhesive.....	41
Figure 26. Autoclave curing cycle for FM300M adhesive.....	42
Figure 27. C-scan of test panel with cured adhesive.....	43
Figure 28. C-scan of test panel with cured adhesive after removal of excess adhesive.....	44
Figure 29. Final scarf repaired specimens.....	44
Figure 30. Set-up for Stepped-Lap Joint Machining.....	45
Figure 31. Digital Coordinate Input for Milling Machine.....	45
Figure 32. View of test specimen being machined in water bath.....	46
Figure 33. Plan for manufacturing of stepped-lap specimen.....	46
Figure 34. Eight, two-ply steps at 10° machined in dummy panel.....	47
Figure 35. Rough sketch of rounding in steps.....	48
Figure 36. Machined surfaces from available bits.....	48
Figure 37. Repair angle of stepped-lap joint.....	49
Figure 38. Bonded practice specimen with stepped-lap repair.....	49
Figure 39. C-scan of practice stepped lap joint specimen.....	50
Figure 40. Method of machining on mill to minimize twisting and warping.....	50
Figure 41. Overhead view of machined stepped-lap surfaces for test panels.....	51
Figure 42. Machined stepped-lap surface for test panel.....	51
Figure 43. Profile of machined stepped-lap surface for test panel.....	52
Figure 44. Vacuum oven used to dry machined panels.....	53
Figure 45. Machined panels were sand blasted for final surface preparation.....	53
Figure 46. C-scan of adhered stepped-lap region.....	54
Figure 47. Final stepped-lap repaired specimens.....	54
Figure 48. Diffraction grating under high magnification (Post).....	56
Figure 49. Dust particles on the diffraction grating (Post).....	57
Figure 50. Moiré interferometry set-up (Mollenhauer).....	58
Figure 51. Steps involved in replication of diffraction grating (Mollenhauer).....	59

	Page
Figure 52. Clamped specimens for polishing.	60
Figure 53. Desired surface of specimens for diffraction grating application.....	60
Figure 54. Radial disk polisher.....	61
Figure 55. Wet sander tray.	61
Figure 56. Exaggerated top view sketch of specimens after initial polishing.....	62
Figure 57. Exaggerated top view sketch of specimens placed together out of order.....	63
Figure 58. Clamped specimens in configuration used for replication of diffraction grating.	63
Figure 59. Gathering coordinates for final polished edges.	64
Figure 60. Photomechanics diffraction grating.....	65
Figure 61. Determining position of reflected laser light.....	66
Figure 62. Using laser light reflection to square diffraction grating.....	67
Figure 63. Diffraction grating placed against specimens.....	68
Figure 64. Diffraction grating replicated on test specimens.	69
Figure 65. Flawed specimen.....	69
Figure 66. Labeled diagram of moiré interferometry experimental test-set up.....	70
Figure 67. Clamping specimen prior to placing in load fixture.	71
Figure 68. Load fixture mount for moiré interferometry.....	71
Figure 69. Fixture used to apply tensile load.....	72
Figure 70. Tabs used to obtain desired fringe patterns.	73
Figure 71. Stitching together of fringe patterns.....	74
Figure 72. Example of fiducial mark on diffraction grating.....	75
Figure 73. Screen capture of moiré data set in Transform.....	76
Figure 74. Screen capture of image being generated in Transform.....	77
Figure 75. Shifted BSAM data set.....	79
Figure 76. Coordinate system defined for full-field strain images.	81
Figure 77. BSAM (top) and moiré (bottom) full field strain (ϵ_x) images of stepped-lap joint.....	82
Figure 78. Overlap of stepped-lap bond-line contour onto BSAM strain (ϵ_x) field.....	82
Figure 79. BSAM (top) and moiré (bottom) full field strain (ϵ_z) images of stepped-lap joint.....	83
Figure 80. Overlap of stepped-lap bond-line contour onto BSAM strain (ϵ_z) field.	83
Figure 81. BSAM (top) and moiré (bottom) full field shear strain (γ_{xz}) images of stepped-lap joint.....	84
Figure 82. Overlap of stepped-lap bond-line contour onto BSAM shear strain (γ_{xz}) image.....	84
Figure 83. BSAM (top) and moiré (bottom) full field strain (ϵ_x) images of scarf joint ($0 < \epsilon_x < 0.0014$) ...	85
Figure 84. BSAM (top) and moiré (bottom) full field strain (ϵ_z) images of scarf joint.....	86
Figure 85. BSAM (top) and moiré (bottom) full field shear strain (γ_{xz}) images of scarf joint.....	86
Figure 86. x-location of extracted stepped-lap strain data for line plots.....	87
Figure 87. Stepped-Lap Joint: strain distribution (ϵ_x) through specimen thickness (z) at x = 0mm (data not smoothed).....	88
Figure 88. Stepped-Lap Joint: strain distribution (ϵ_y) through specimen thickness (z) at x = 0mm (data not smoothed).....	88
Figure 89. Stepped-Lap Joint: shear strain distribution (γ_{xy}) through specimen thickness (z) at.....	89
Figure 90. Refined discretization of BSAM stepped-lap model.....	90
Figure 91. Effect of smoothing on data.	91
Figure 92. Stepped-lap Joint: strain (ϵ_x) through thickness (z) at x = 0mm.....	92
Figure 93. Stepped-lap Joint: strain (ϵ_z) through thickness (z) at x = 0mm.....	92
Figure 94. Stepped-lap Joint: shear strain (γ_{xz}) through thickness (z) at x = 0mm.....	93
Figure 95. Stepped-lap Joint: strain (ϵ_x) through specimen thickness (z) at x = 5mm.....	93
Figure 96. Stepped-lap Joint: strain (ϵ_z) through specimen thickness (z) at x = 5mm.....	94
Figure 97. Stepped-lap Joint: strain (γ_{xz}) through specimen thickness (z) at x = 5mm.....	94
Figure 98. Stepped-lap Joint: strain (ϵ_x) through specimen thickness (z) at x = -9.6mm.....	96
Figure 99. Stepped-lap Joint: strain (ϵ_z) through specimen thickness (z) at x = -9.6mm.....	96
Figure 100. Stepped-lap Joint: shear strain (γ_{xz}) through specimen thickness (z) at x = -9.6mm (data smoothed 250 times).....	97
Figure 101. Two-dimensional stress (σ_x) through the adhesive at x = 9.6mm.....	99
Figure 102. Two-dimensional stress (σ_z) through the adhesive at x = 10mm.....	100
Figure 103. Portion of stepped-lap adhesive bondline.....	101

	Page
Figure 104. Screen capture of edge view of segment of BSAM stepped-lap model in Mat Lab.....	102
Figure 105. Comparison of BSAM stepped-lap model to experimental test specimen.	103
Figure 106. Location of strain peak disparity for stepped-lap joint.....	103
Figure 107. x-location of extracted scarf strain data for line plots.	104
Figure 108. Scarf Joint: strain distribution (ϵ_x) through specimen thickness (z) at x = 0mm.....	105
Figure 109. Scarf Joint: strain distribution (ϵ_y) through specimen thickness (z) at x = 0mm.....	105
Figure 110. Scarf Joint: shear strain distribution (γ_{xy}) through specimen thickness (z) at x = 0mm.....	106
Figure 111. Scarf Joint: strain (ϵ_x) through thickness (z) at x = 0mm.....	107
Figure 112. Scarf Joint: strain (ϵ_z) through thickness (z) at x = 0mm.....	107
Figure 113. Scarf Joint: shear strain (γ_{xz}) through thickness (z) at x = 0mm.....	108
Figure 114. Scarf Joint: strain (ϵ_x) through thickness (z) at x = 5mm.....	108
Figure 115. Scarf Joint: strain (ϵ_z) through thickness (z) at x = 5mm.....	109
Figure 116. Scarf Joint: shear strain (γ_{xz}) through thickness (z) at x = 5mm.....	109
Figure 117. Scarf Joint: strain (ϵ_x) through specimen thickness (z) at x = -10.3mm.....	110
Figure 118. Scarf joint: strain (ϵ_z) through specimen thickness (z) at x = -10.3mm.....	111
Figure 119. Scarf joint: shear strain (γ_{xz}) through specimen thickness (z) at x = -10.3mm.....	111
Figure 120. Scarf Joint: strain (ϵ_x) through thickness (z) at x = 10.3mm.....	112
Figure 121. Scarf Joint: strain (ϵ_z) through thickness (z) at x = 10.3mm.....	113
Figure 122. Example of shift in z-location of peak strain for scarf joint.....	114
Figure 123. Second example of shift in z-location for scarf joint.....	114
Figure 124. Deviations between actual scarf bond line and idealized model.	116
Figure 125. Comparison of experimental and modeled scarf joint.....	117
Figure 126. Comparison of modeled and experimental bond line (not to scale).	118
Figure 127. x-locations from BSAM and moiré corresponding to same z-location.....	119
Figure 128. Scarf Joint: Comparison of peak strain magnitudes at corrected x-locations.....	120
Figure 129. Comparison of scaled BSAM strain data with unaltered moiré strain data.....	122
Figure 130. Flow chart of BSAM input file.....	151
Figure 131. Evolution Rules on flowchart.....	153
Figure 132. Failure block of BSAM input file.....	153
Figure 133. Material input block on flowchart.....	154
Figure 134. Material block of BSAM input file.	157
Figure 135. Constitutive model input block on flowchart.	158
Figure 136. Constitutive input block for BSAM program.....	159
Figure 137. Geometry input block on flow chart.....	160
Figure 138. Anatomy of stepped-lap joint.....	161
Figure 139. Cross sectional view of stepped-lap joint.....	161
Figure 140. Acceptable cluster/grid configuration.	162
Figure 141. Grid of geometries required for stepped-lap model.....	162
Figure 142. Closer view of portion of stepped-lap repair.....	163
Figure 143. Patterns emerging in stepped-lap geometries.	163
Figure 144. Unique geometries in stepped-lap model.	164
Figure 145. Geometry type used for stepped-lap and scarf models.....	165
Figure 146. Geometry input block for stepped-lap model.....	166
Figure 147. Clusters for scarf model.	166
Figure 148. Geometries for scarf model.	167
Figure 149. Geometry input block for scarf model.....	167
Figure 150. Modeling the adhesive bond-line for scarf specimen #1.....	168
Figure 151. Discretization, splines, approximation, and model blocks from flowchart.....	169
Figure 152. Discretization input block.	170
Figure 153. Splines highlighted in discretization input block.....	170
Figure 154. Type I: uniformly discretized.....	171
Figure 155. Type II: 1-way biasing of discretization.....	171
Figure 156. Type III: 2-way biasing of discretization.....	172
Figure 157. Bias ratio < 1.....	172
Figure 158. Bias ratio > 1.....	172

	Page
Figure 159. Spline input block for scarf model	173
Figure 160. Spline input block for stepped-lap model.....	174
Figure 161. Approximation input block for scarf joint.....	176
Figure 162. Cluster faces and edges defined	177
Figure 163. Splines input block for stepped-lap model.....	178
Figure 164. Model input block for scarf model.....	181
Figure 165. Completion of BSAM flow chart foundation.....	182
Figure 166. Cluster number assignment convention for scarf model	183
Figure 167. Development of clusters input block for scarf model.....	184
Figure 168. Clusters required to build stepped-lap model.....	184
Figure 169. Sides and edges of cluster defined.	187
Figure 170. Connection type 2 and 5.....	187
Figure 171. Screen capture of top view of BSAM scarf model in Mat Lab.	190
Figure 172. Screen capture of top view of segment of BSAM scarf model in Mat Lab.....	190
Figure 173. Screen capture of edge view of segment of BSAM scarf model in Mat Lab.	191
Figure 174. Screen capture of BSAM stepped-lap model in Mat Lab.....	191
Figure 175. Screen capture of top view of segment of BSAM stepped-lap model in Mat Lab.	191
Figure 176. Screen capture of edge view of segment of BSAM stepped-lap model in Mat Lab.....	192
Figure 177. Mat Lab Output Option.....	194
Figure 178. Average Traction Output Option	194
Figure 179. Region defined for BSAM output for stepped-lap model (not to scale).....	195
Figure 180. Region defined for BSAM output for scarf model (not to scale).	196
Figure 181. Geometries of stepped-lap model (not to scale).	197
Figure 182. Moire output block from input file for geometry 7 clusters	198
Figure 183. Cluster numbering system for stepped-lap model.....	199
Figure 184. More complex shape of scarf model geometries.....	199
Figure 185. Determining local coordinates for scarf model.	200
Figure 186. Clusters in scarf model.....	201
Figure 187. Output block for cluster 3 in stepped-lap model.	203
Figure 188. Location of process input block on BSAM input file flowchart.	204
Figure 189. Process input block for scarf model.	205
Figure 190. Acoustic sensor attached to specimen.	207
Figure 191. Test set-up.....	209
Figure 192. Load versus displacement of virgin specimens.....	210
Figure 193. Fractured virgin specimen 1 in MTS machine.	211
Figure 194. Fractured surface of virgin specimen #1.	211
Figure 195. Fracture surface of virgin specimen #2.	212
Figure 196. Counts versus load (lb_f) chart for virgin specimen #1.....	212
Figure 197. Count rate versus load (lb_f) chart for virgin specimen #1.	213
Figure 198. Counts versus load (lb_f) of virgin specimen #2.....	214
Figure 199. Count rate versus load (lb_f) of virgin specimen #2.....	214
Figure 200. Load versus displacement of stepped-lap specimens.	215
Figure 201. Fracture surface of stepped-lap specimen #1.	217
Figure 202. Fracture surface of stepped-lap specimen #5.	217
Figure 203. Profile of fracture surface of stepped-lap specimen #5.	217
Figure 204. Counts versus load (lb_f) for stepped-lap specimen #1.....	218
Figure 205. Count rate versus load (lb_f) for stepped-lap specimen #1.....	218
Figure 206. Counts versus load (lb_f) for stepped-lap specimen #5.....	219
Figure 207. Count rate versus load (lb_f) for stepped-lap specimen #5.....	219
Figure 208. Load versus displacement for scarf specimens.	220
Figure 209. Fracture surface of scarf specimen 2.....	221
Figure 210. Fracture surface of scarf specimen 3.....	221
Figure 211. Counts versus load (lb_f) for scarf specimen #2.	222
Figure 212. Count rate versus load (lb_f) for scarf specimen #2.	222
Figure 213. Counts versus load (lb_f) for scarf specimen #3.	223

	Page
Figure 262. Stepped-lap Joint: strain (ϵ_x) through thickness (z) at x = 5mm.....	249
Figure 263. Stepped-lap Joint: strain (ϵ_x) through thickness (z) at x = 9.6mm.....	250
Figure 264. Stepped-lap Joint: strain (ϵ_x) through thickness (z) at x = 10mm.....	250
Figure 265. Stepped-lap Joint: strain (ϵ_x) through thickness (z) at x = 15mm.....	251
Figure 266. Stepped-lap Joint: strain (ϵ_z) through thickness (z) at x = -15mm	251
Figure 267. Stepped-lap Joint: strain (ϵ_z) through thickness (z) at x = -10mm	252
Figure 268. Stepped-lap Joint: strain (ϵ_z) through thickness (z) at x = -9.6mm	252
Figure 269. Stepped-lap Joint: strain (ϵ_z) through specimen thickness (z) at x = -5mm	253
Figure 270. Stepped-lap Joint: strain (ϵ_z) through thickness (z) at x = 0mm.....	253
Figure 271. Stepped-lap Joint: strain (ϵ_z) through specimen thickness (z) at x = 5mm.....	254
Figure 272. Stepped-lap Joint: strain (ϵ_z) through thickness (z) at x = 9.6mm.....	254
Figure 273. Stepped-lap Joint: strain (ϵ_z) through thickness (z) at x = 10mm.....	255
Figure 274. Stepped-lap Joint: strain (ϵ_z) through thickness (z) at x = 15mm.....	255
Figure 275. Stepped-lap Joint: shear strain (γ_{xz}) through thickness (z) at x = -15mm.....	256
Figure 276. Stepped-lap Joint: shear strain (γ_{xz}) through thickness (z) at x = -10mm.....	256
Figure 277. Stepped-lap Joint: shear strain (γ_{xz}) through thickness (z) at x = -9.6mm.....	257
Figure 278. Stepped-lap Joint: shear strain (γ_{xz}) through thickness (z) at x = -5mm.....	257
Figure 279. Stepped-lap Joint: shear strain (γ_{xz}) through thickness (z) at x = 0mm.....	258
Figure 280. Stepped-lap Joint: shear strain (γ_{xz}) through thickness (z) at x = 5mm.....	258
Figure 281. Stepped-lap Joint: shear strain (γ_{xz}) through thickness (z) at x = 9.6mm	259
Figure 282. Stepped-lap Joint: shear strain (γ_{xz}) through thickness (z) at x = 10mm	259
Figure 283. Stepped-lap Joint: shear strain (γ_{xz}) through thickness (z) at x = 15mm	260
Figure 284. Scarf Joint: strain (ϵ_x) through thickness (z) at x = -15mm.....	260
Figure 285. Scarf Joint: strain (ϵ_x) through thickness (z) at x = -10.3mm.....	261
Figure 286. Scarf Joint: strain (ϵ_x) through thickness (z) at x = -10mm.....	261
Figure 287. Scarf Joint: strain (ϵ_x) through thickness (z) at x = -5mm.....	262
Figure 288. Scarf Joint: strain (ϵ_x) through thickness (z) at x = 0mm	262
Figure 289. Scarf Joint: strain (ϵ_x) through thickness (z) at x = 5mm	263
Figure 290. Scarf Joint: strain (ϵ_x) through thickness (z) at x = 10mm	263
Figure 291. Scarf Joint: strain (ϵ_x) through thickness (z) at x = 10.3mm	264
Figure 292. Scarf Joint: strain (ϵ_x) through thickness (z) at x = 15mm	264
Figure 293. Scarf Joint: strain (ϵ_z) through thickness (z) at x = -15mm.....	265
Figure 294. Scarf Joint: strain (ϵ_z) through thickness (z) at x = -10.3mm	265
Figure 295. Scarf Joint: strain (ϵ_z) through thickness (z) at x = -10mm	266
Figure 296. Scarf Joint: strain (ϵ_z) through thickness (z) at x = -5mm	266
Figure 297. Scarf Joint: strain (ϵ_z) through thickness (z) at x = 0mm	267
Figure 298. Scarf Joint: strain (ϵ_z) through thickness (z) at x = 5mm	267
Figure 299. Scarf Joint: strain (ϵ_z) through thickness (z) at x = 10mm	268
Figure 300. Scarf Joint: strain (ϵ_z) through thickness (z) at x = 10.3mm	268
Figure 301. Scarf Joint: strain (ϵ_z) through thickness (z) at x = 15mm	269
Figure 302. Scarf Joint: shear strain (γ_{xz}) through thickness (z) at x = -15mm	269
Figure 303. Scarf Joint: shear strain (γ_{xz}) through thickness (z) at x = -10.3mm	270
Figure 304. Scarf Joint: shear strain (γ_{xz}) through thickness (z) at x = -10mm	270
Figure 305. Scarf Joint: shear strain (γ_{xz}) through thickness (z) at x = -5mm	271
Figure 306. Scarf Joint: shear strain (γ_{xz}) through thickness (z) at x = 0mm.....	271
Figure 307. Scarf Joint: shear strain (γ_{xz}) through thickness (z) at x = 5mm.....	272
Figure 308. Scarf Joint: shear strain (γ_{xz}) through thickness (z) at x = 10mm.....	272
Figure 309. Scarf Joint: shear strain (γ_{xz}) through thickness (z) at x = 10.3mm.....	273
Figure 310. Scarf Joint: shear strain (γ_{xz}) through thickness (z) at x = 15mm.....	273

List of Tables

	Page
Table 1. Summary of results from 2D stress analysis through adhesive in stepped-lap model.	99
Table 2. Text files generated for scarf model moiré output.....	201
Table 3. Summary of tensile test results.	224
Table 4. Strength retained by repaired specimens.	224
Table 5. Summary of initial acoustic emissions in specimens.....	225

APPLICATION OF SPLINE VARIATIONAL ANALYSIS METHOD IN THE MODELING OF COMPOSITE REPAIRS

I. Introduction

Motivation

While finite element analysis has become the predominant modeling tool for stress analysis, heat transfer, and magnetic fields, other numerical analysis methods have started to be considered in recent years. Over the past few years, a small research team at the Air Force Research Laboratories (AFRL) in Dayton, OH has developed a computer program based on a spline variational analysis method, which uses B-spline approximation basis functions to build a variable continuity approximation for laminated composite structures (Iarve, 1996). This program, called “BSAM” (for B-Spline Analysis Method), is a relatively new program; in fact, only a couple of studies have been conducted to validate its accuracy since it has been developed (Schoeppner, 2004). While initial results have been promising, more studies assessing various geometries, repairs, and materials are needed to confirm BSAM’s capabilities before it can be considered an established and proven tool.

The primary motivation behind this thesis was to provide BSAM with a scenario that would test its analytical capabilities and also have some aspect of real world application or interest. With the propagation of load bearing composite components in the aerospace industry, numerical methods used to model composites and composite repairs have become an area of increased focus and importance. Over the last couple of decades, the scarf joint and stepped-lap joint have emerged as two methods of restoring strength in damaged composite components. Therefore, it would make sense that the

modeling and analysis of these two repairs would be an ideal problem for BSAM as it continues its progression towards becoming a refined and proven analytical tool.

Background

While the application of the spline variational analysis method is the focus of this thesis, developing a framework of the repairs modeled and tested in this study is also of great importance. Because of this, a general summary of composite repair techniques is presented first in this background, followed by information regarding stepped-lap and scarf joints. From there, this background summarizes important results from previous experimental studies conducted on scarf and stepped-lap joints. Other numerical methods that have been used to model scarf and stepped-lap repairs are then considered and outlined, as the B-spline analysis method is not the only method available to model composite repairs. Finally, the development of spline approximation applications and the BSAM computer program is covered.

Composite Repair Techniques

The maintenance and repair of composite aircraft structures has always been of great concern in both the private and public sectors. Damaged composite components on aircraft are often a result of maintenance mishaps, accidental impact, bird strike, hailstones, or lightning strike. Structural integrity of composites can also be compromised through the absorption of moisture or hydraulic fluid. Additionally, in comparison to their commercial counterparts, operation out of austere airfields and the chance of battle damage have placed military aircraft in an even higher risk category for damage. Overall, the risk of damage to composite aircraft structures has resulted in the

development of standard maintenance procedures and various methods of repair for composites.

Once the strength of the damaged component falls below approved allowable limits, three options are available to restore the component to operational standards: (1) temporary repair, (2) permanent repair, or (3) replacement. A temporary repair, or field repair, is used only when time, environment, and facility limitations require its use. The purpose of a temporary repair is to restore the mechanical strength needed to facilitate aircraft operation until a permanent repair can be completed or the component can be replaced. A temporary repair usually consists of a mechanically fastened external metal or composite patch. In this technique, damaged material is removed by cutting a hole, filler and adhesive materials are applied to the parent panel, and finally the patch is attached. Because replacement is the most expensive of the three options, patch type methods of repair are preferable when applicable (Tong).

While external patches can also be used for permanent repair in lightly loaded and relatively thin structures, their use is not viable for critical, highly loaded structures. This is because external patches create high bondline peel and shear stresses in highly loaded structures. Bolted and riveted repairs are also not a viable option in strength critical structures as load transfer paths through mechanical fasteners are not efficient and can cause local overloads and damaged in brittle composites. Instead, flush bonded repairs are used for the permanent repair of composite components that support primary loads. Adhesively bonded joints are also advantageous when compared to bolted and riveted repairs because of their high corrosion and fatigue resistance, crack retardance and growth, and good damping characteristics (Tsai).

Various adhesively bonded joint configurations can be seen in Figure 1. Single-lap or double-strap bonded joint types are usually used for thinner materials that handle lower load intensities. As load intensity increases, joints usually become more refined and complex, such as the stepped-lap or scarf joint. Figure 2 shows common failure modes of various joint types.

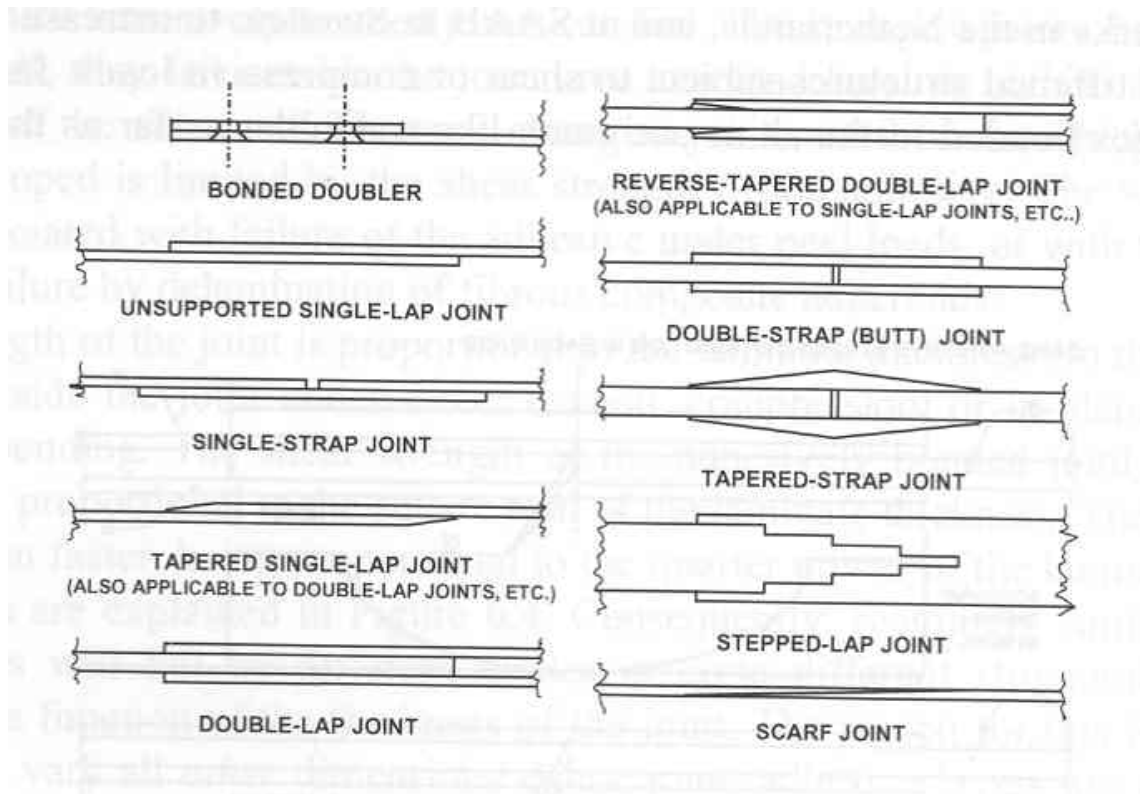


Figure 1. Adhesively Bonded Joint Types (Tong and Soutis).

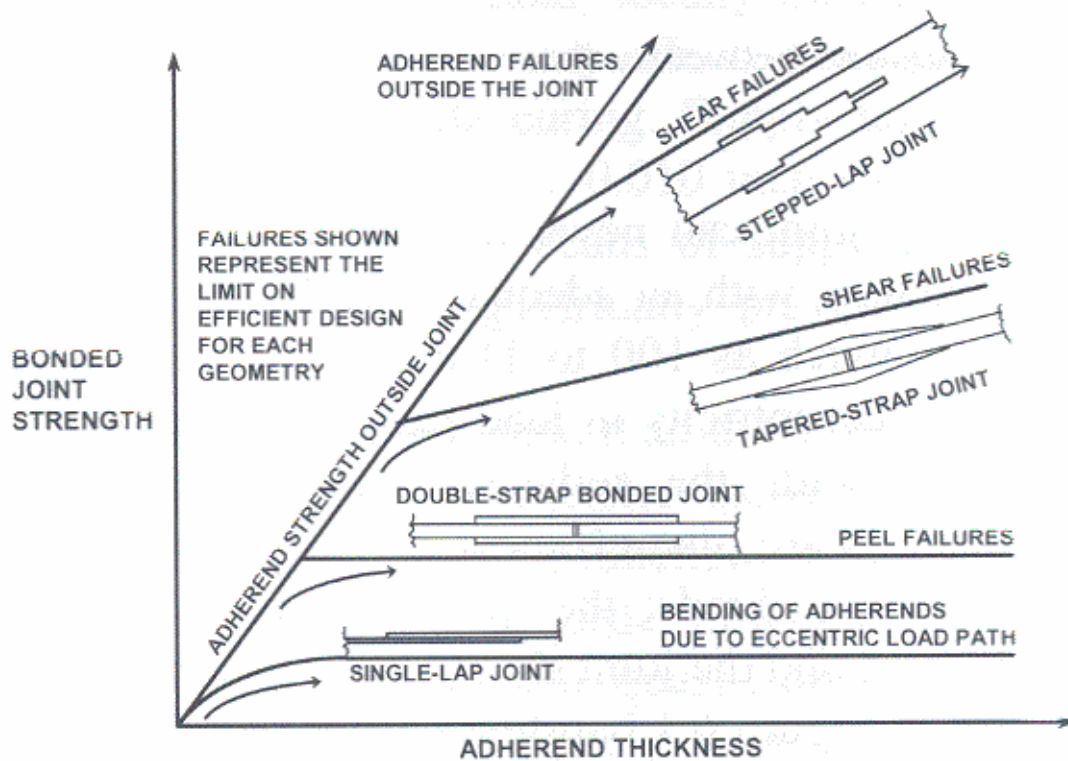


Figure 2. Failure modes for different bonded joint types (Tong).

As Figure 2 indicates, bonded joint strength increases as the thickness of the adherends and complexity of repair increases. The single-lap joint (shown at the bottom of the figure) usually fails due to bending of the adherends, while more complex joints, such as the stepped-lap joint (shown at the top of the figure) usually fails due to shear failures outside the bonded region.

While flush patch repairs, such as scarf and stepped-lap joints, are more highly refined and structurally efficient than external patches, they are also more expensive and time intensive. Flush type repairs have been more important in recent years, as usage of composite materials has spread from non-critical structures to strength-critical structures

and outer moldline requirements dictate flush repairs (Soutis and Hu). These flush repairs, specifically stepped-lap and scarf joints, are at the focus of this thesis.

The Scarf Joint

A scarf joint is a flush patch repair, where the bond line is at a set angle between the two laminates. The scarf repair patch is adhesively bonded to the parent material and can be used to gain back much of the original parent laminates stiffness or strength, while maintaining the parent materials original contour. The advantages of the scarf joint include a more uniform shear stress distribution in the adhesive and a low peel stress. The uniform shear stress distribution created by both scarf and double scarf joints can be seen below in Figure 3, as opposed to the non-uniform shear stress distribution created by the step-lap and single overlap joints. All shear stress distributions in Figure 3 are theoretical and based on 2D analysis.

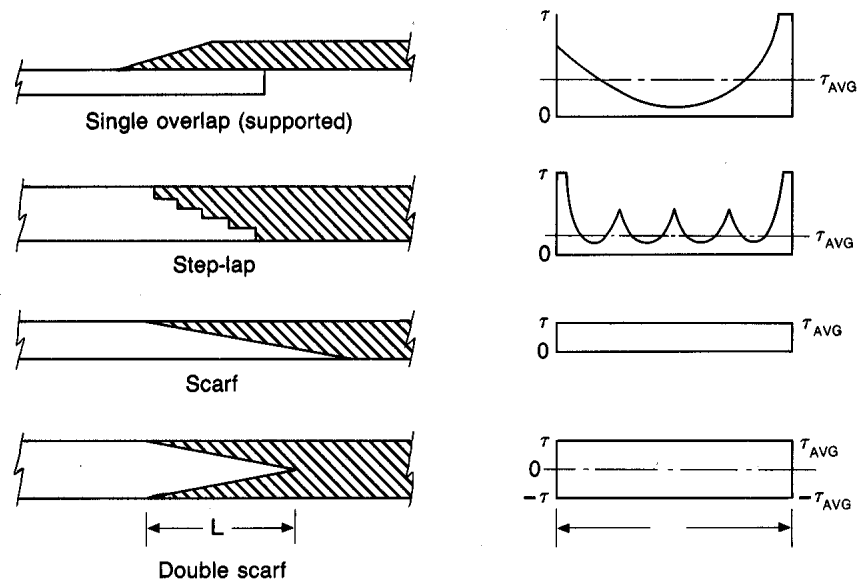


Figure 3. Idealized adhesive shear stress distributions of various joint configurations

(Baker).

One disadvantage of a scarf joint repair is that they are difficult and time consuming to apply and require the removal of a large amount of undamaged material to form the required taper angle. While a slope ratio of around 20:1 is optimal, machining the repair to a knife edge is necessary in recovering theoretical strength (Baker).

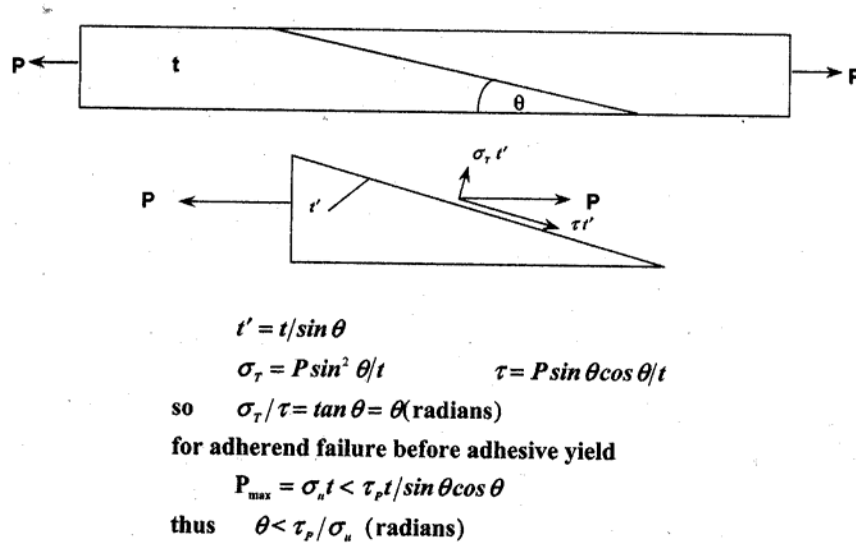


Figure 4. Strength of Materials Analysis of Scarf Joint (Baker)

Figure 4 demonstrates a strength of materials analysis calculation of shear stresses in scarf joints, where t is the thickness of the laminate, θ is the scarf angle, σ_T is the uniform normal stress, P is the applied load, τ is the uniform shear stress, τ_p is the peak shear stress, σ_u is the ultimate normal stress, and P_{\max} is the ultimate applied load.

According to Baker and others, this analysis “assumes” that the shear stress distribution is uniform and the stiffness and coefficient of expansion of the adherends are similar.

While the properties of the adherends are often similar, the condition of uniform shear stress in the adhesive holds only if the scarf is taken to a knife edge. Any imperfections in the scarf repair could result in significant stress concentrations, leading to premature failure in the joint.

The Stepped-Lap Joint

A stepped-lap joint is also a flush bond between two separate laminates, where the joint is a series of overlap steps. Since the load-carrying capacity of each step does not increase indefinitely with length, it is necessary to increase the number of steps in a stepped-lap joint to maximize its load-carrying ability. If correctly designed, a stepped-lap joint repair can have an equal load carrying capability to the scarf and may be more easily applied. The stepped-lap joint can be thought of as a hybrid between a scarf joint and a uniform lap joint. Like the scarf joint, stepped-lap repairs are also more difficult and time-consuming to apply than external patch repairs. However, because the stepped-lap configuration is readily produced by the laminating process, it is particularly well-suited to join laminated composite components (Baker).

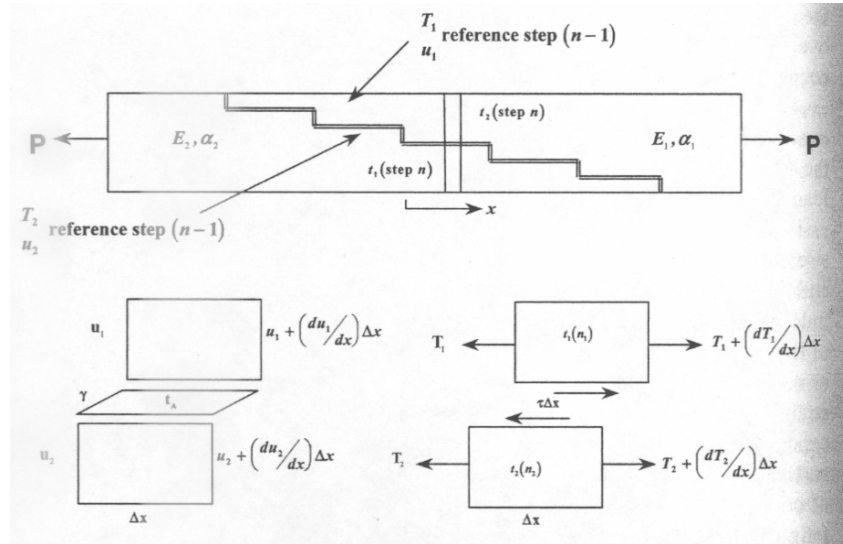


Figure 5. Schematic of stepped-lap joint (Baker).

Because the field of experimentation and modeling of bonded joints has become too large to thoroughly cover in a limited number of pages, this review will focus mainly on studies involving scarf and stepped-lap repairs. To provide a framework in which

these studies will be reviewed, they have been divided into several categories: (1) experimental studies of scarf joints, (2) experimental studies of stepped-lap joints, (3) modeling of scarf and stepped-lap joints, and (4) the development of spline approximation applications for bonded repairs.

Many of the experimental studies conducted concerning scarf repairs and stepped-lap joints have compared the original strength of virgin test specimens to the repaired strength of bonded specimens under various loading conditions, including static, impact, and fatigue loading.

Experimental Studies on Scarf Joints

In 1995, Friend and Found performed static tests on carbon fiber reinforced panels (CFRP) with circular scarf repair patches for three repair systems: two wet lay-ups and one prepreg system. The wet lay-up was made using a dry carbon cloth with the same woven cloth characteristics as the prepreg material, but the cloth was wetted with a two-part epoxy system and cured at a higher temperature. From experimental tensile loading data, it was concluded that while the most consistent results were obtained with one of the wet lay-up repairs, the prepreg system offered the greatest increase in load to failure. Both scarf joint types exhibited higher strength than unrepaired panels, with failure loads ranging from 24% to 63% above unrepaired values. Their study also showed that photoelastic and strain gauge techniques could be used to accurately determine buckling in test panels.

In 1998, Soutis and Hu conducted a failure analysis of scarf patch repaired carbon-fiber reinforced epoxy (CFRP) plates. In the study, it was concluded that scarf joints designed at an optimum angle could recover as much as 80% of its undamaged

strength. The study concluded that while a 2D simple scarf joint stress analysis predicted an optimum scarf angle of 4° , the 3D linear elastic finite element analysis predicted an optimum angle of 7° . This result was important, as the 4° scarf joint yielded by the 2D model would involve the removal of more undamaged parent material.

In that same year Charalambides and others (1998) were able to accurately predict the mechanical behavior of bonded repairs using finite element analysis results. In the experimental portion of his study, Charalambides tested the performance of scarf repairs to carbon fiber/epoxy panels under various loading conditions and environments. He concluded from experimental results that there was no major effect of the conditioning, mainly prolonged immersion in 50°C water, on the static strengths of the repaired joints. This conclusion was reached using Hexcel Composites T300/914 carbon fiber/epoxy composites and Redux 319 epoxy film adhesive. Charalambides used finite element analysis to model the repaired joints; these models yielded good agreement with experimental observations. Knox et al (2000) provided a similar example with their study of bonded repairs in glass reinforced epoxy (GRE) pipes.

In 2001, Chotard and others proposed the use of external scarf patch repairs for pultruded, impact-damaged structures as an economical way to recover more than 85% of the strength of an undamaged structure. Chotard reached this conclusion after using a four-point bending fixture for both static and fatigue testing on repaired and unrepaired specimens.

Experimental Studies on Stepped-Lap Joints

Kim and others (1995) tested stepped-lap repaired panels under static and fatigue tensile loads. From test results, Kim determined that as the length of the stepped lap of

the joint increased, the average static tensile strength of the joint increased, while the average static shear strength decreased in proportion to the length of the step. The shear and tensile strengths were determined by taking the averages of several test runs. In the study, Kim manufactured two different types of stepped-lap joints: the first joint was manufactured by stacking and curing different length carbon fiber epoxy prepregs, while the second joint was manufactured by curing prepregs stacked on a carbon fiber plate with machined steps. It was determined that the joints manufactured with machining had 70-80% of the static strength of joints manufactured without machining. No explanation was available in the paper for why machining the stepped-lap joint decreased its static strength.

Recently, Kim, Park, and Han (2004) conducted further experimental research on fatigue characteristics of composite stepped lap joints. Under static and fatigue tensile loading, it was concluded that the cracks initiated at the end of overlaps, and that tensile strength of the repair did not increase when the ratio value of joint length against the number of steps was less than 6. It was also determined that the fatigue endurance limit of a stepped lap joint was found to be 30% of static tensile loading.

Ashcroft and others also looked into the effect of environment on the fatigue of bonded composite joints in 2000. The joint at the focus of Ashcroft's analysis was the strap-lap joint, which is essentially a long overlap joint. Like Charalambides, Ashcroft experimentally determined that the fatigue resistance of the repairs did not drop significantly with changes in temperature until the glass transition temperature was reached. However, Ashcroft was able to conclude that excessive moisture exposure resulted in a reduction to the glass temperature of the adhesive. Ashcroft also observed

failure location shift from the parent material to the adhesive at elevated temperatures. In the subsequent portion of their report, Ashcroft used finite element analysis, applying principles of fracture mechanics and concepts of stress analysis in the framework of the model, to find the theoretical fatigue strength of the joints; these results matched closely with experimental findings.

Modeling of Scarf and Stepped-Lap Joints

While experimental findings have provided a great deal of insight into the mechanical behavior of scarf and stepped-lap repairs, there have also been several efforts to refine existing theoretical models concerning composite repairs. Hart-Smith (1973) conducted some of the first efforts to model scarf and stepped-lap joints, advocating the use of continuum mechanics supported by numerical solutions. He believed that every effort should be made to ensure that the adhesive was not the weakest link in the joint.

In 1998, Tsai, Oplinger, and Morton improved on classical theories of Volkersen/de Bruyne's solution for double-lap joints and Volkersen's, Goland, and Reissner's solutions for single-lap joints by accounting for adherend shear deformation. This was done by assuming linear shear stress distributions through the thickness of the adherends. It was shown that the improved theoretical solution provided a better prediction for the adhesive shear distributions and maximum values, especially in the case of fiber composite adherends.

Mortensen and Thomsen (2002) were able to develop two separate, but unified methods of analysis for various adhesive bonded joints. For the first approximation, adhesive layers were assumed to behave as linear elastic material, while the second approximation yielded a non-linear solution by combining the linear solution with a

modified von Mises criterion and a secant modulus approach. In both models, adhesive layers were modeled as continuously distributed linear tension/compression and shear springs. Their approach was validated through finite element results and was a continuation of a 1997 study which addressed only stepped lap and scarf joints. Three-dimensional analysis methods have also been developed to more accurately model the strains and stresses in composites.

In 2003, Abdel Wahab et al developed a method to predict fatigue crack propagation in bonded structures using the Paris equation. Their finite element method was based on numerical integration of the fatigue crack growth law from an initial to a final crack size. The crack growth law used was determined experimentally using double cantilever beam (DCB) samples. This law was then applied to single lap and double lap joints, yielding good agreement between predicted and experimental results in the number of cycles to failure.

In another approach, Zou, Shahin, and Taheri (2004) were able to apply classical laminate plate theory and adhesive interface constitutive model to find analytical solutions for adhesively bonded balanced composite and metallic joints. Comparing their numerical model to FEM simulations, Zou and company were able to accurately predict adhesive peel and shear stresses for single-lap and single-strap joints under tensile, moment, and transverse shear loading.

Odi and Friend (2004) were able to develop an improved 2D model for bonded composite joints. They did this by using a 2D plane stress approach that allowed ply-by-ply modeling of composite adherents in a joint. Layer stresses were calculated using Classical Laminate Theory, and the Tsai-Wu failure index was obtained from these

stresses. Their linear analysis yielded good agreement between predicted failure loads and experimental results for 3.0° , 6.2° , and 9.2° scarf joints under tensile loading. Their study also reiterated how small scarf joint angles ensured that the adhesive was never the weakest link.

Development of Spline Approximation Applications

Iarve investigated the application of spline approximations for stress analysis in laminates in 1996. Iarve reasoned that spline approximation offered continuity of displacement, strain, and stress fields while conserving the advantages of local approximation by having a simpler resultant system of equations. He also explained that spline approximations could be used to overcome the presence of field singularities and inter element compatibility problems encountered in finite element analysis. In his paper, Iarve stressed benefits of using a polynomial spline approximation approach for problems concerned with singular solution behavior, such as the stress analysis of composite plates with open holes. Using this method, Iarve was able to obtain an accurate spline approximation full field solution when compared to an asymptotic solution. Iarve later worked with Pagano to model stress fields in composite laminates, including the singularities at the ply interfaces and open hole edges (Iarve and Pagano, 2001). Iarve was able to produce a displacement approximation based on polynomial B-spline functions while Pagano proposed a hybrid approximation based on an assumed equilibrium stress field using Reissner's variational principle. These two approximations were super-positioned to evaluate the stress fields.

More recently, Schoeppner, Mollenhauer, and Iarve (2004) predicted residual strains in a composite bonded joint by using a computer program that utilized basis spline

functions to develop displacement approximations. As mentioned earlier, this analysis is referred to as the B-spline analysis method (BSAM) and provides the foundation for the BSAM computer program. This program, developed by the three researchers, is very capable and has refined analytical capabilities, but is not a commercial code.

Schoeppner, Mollenhauer, and Iarve (2004) used the same composite laminate (IM6/3501-6) and a similar film adhesive system used in this thesis. In their study, results from the BSAM method showed good agreement with strain measurements obtained using the moiré interferometry technique.

Captain Benjamin Cook (2005), an Air Force Institute of Technology (AFIT) student, used the BSAM computer program to model an adhesively bonded straight scarf repair. Following methods described by Schoeppner, Mollenhauer, and Iarve (2004), Cook compared BSAM models to strain data gathered using moiré interferometry under a tensile load of 549lb_f. While experimental results showed fair correlation with the BSAM model, Cook worked with a thin eight-ply laminate and encountered difficulty in both manufacturing the straight scarf repair and attaining accurate moiré strain data. In the process, Cook established basic procedures for machining a straight scarf repair and documented problems encountered in applying the moiré technique to thin laminates.

The methods developed and demonstrated by Schoeppner, Mollenhauer, and Iarve (2004), and experiences documented by Cook (2005), were used as a foundation for this study.

Problem Statement

The objective of this thesis is to develop BSAM models for test specimens with straight stepped-lap and scarf repairs, obtain experimental strain data through moiré

interferometry, and compare the analytical model with experimental results. Several steps were taken to accomplish this including: (1) the manufacture of composite panels with scarf and stepped-lap repairs, (2) the development and processing of two BSAM computer program models, (3) the application of moiré interferometry to acquire experimental strain data from repaired specimens under static tensile load, and (4) an analysis of analytical and experimental strain results. It is hoped that this thesis will demonstrate the capability and accuracy of the BSAM computer program, while also providing a better insight into the mechanical behavior of the stepped-lap and scarf joint.

Overview of Thesis

Chapter II outlines theory behind the B-spline analysis method. It includes a summary of the general equation progression utilized by the BSAM computer program as well as a summary of how a model is developed in BSAM. Appendix A and Appendix B can be referenced for more specific information regarding both the theory and model development.

Chapter III provides a detailed explanation of the manufacture of composite panels and fabrication of scarf and stepped-lap repairs. Test specimens with scarf and stepped-lap joints were fabricated using quasi-isotropic sixteen ply panels made from IM6/3501-6 pregreg with a $[+45_2/0_2/-45_2/90_2]_s$ lay-up. The panels were bonded together with a FM-300M (0.05psf), a 176°C cure film adhesive, under positive pressure. A total of five coupons specimens of each joint type were made measuring 25.4cm (10.0in) in length by 2.54cm (1.0in) in width. Specimens were roughly 2.29mm (0.09in) thick.

Chapter IV provides an overview of the experimental technique used in this thesis: moiré interferometry. Moiré interferometry was selected as the experimental

technique in this thesis because of its high strain resolution and full-field capabilities. In addition, this chapter includes (1) an illustrated explanation of required surface preparation and replication of diffraction grating, (2) an overview of the experimental test-set up, and (3) details regarding experimental data reduction.

Chapter V compares and analyzes predicted strain values with experimental results. Full-field strain-images of three strain components (ϵ_x , ϵ_z , and γ_{xz}) in the plane of the repair are generated in a program called Transform. For a more quantitative comparison, line plots are shown. These line plots are generated by extracted data at specific locations across the repairs. A discussion of the results, including a discussion addressing any discrepancies between predicted and experimental results is also included.

In Chapter VI, conclusions and recommendations for follow-on work are provided.

II. B-Spline Analysis Method

Theory

The B-spline analysis method is similar to the finite element analysis method in the fact that strains are derived from displacements, and stresses are calculated using stress-strain relationships. The B-spline analysis method relies on developing shape functions (defined as N_j , $X_{i,j}$, $Y_{i,j}$, or $Z_{i,j}$) for a defined set of nodes in one, two, or three dimensions. By applying boundary conditions and loads to a model, the displacements of each node (defined as A_j for 1D case) can be solved.

$$u_x = \sum A_j N_j \text{ for a one-dimensional (1D) case} \quad (1)$$

$$u(x, y) = \sum A_{ij} X_{i,j} Y_{i,j} \text{ for a two-dimensional (2D) case} \quad (2)$$

$$u(x, y, z) = \sum A_{ij} X_{i,j} Y_{i,j} Z_{i,j} \text{ for a three-dimensional (3D) case} \quad (3)$$

As a general process, functions for the overall displacement (u_x for 1D case) are defined in terms of displacements of each node (A_j for 1D case) and respective shape functions, where the displacements of each node are unknown and the shape functions are dependent on variables in the given coordinate system (x-y, x-z, etc). Displacements are differentiated to solve for strains using the following equations:

$$\varepsilon_x = \frac{\partial u}{\partial x} \text{ for a 1D case} \quad (4)$$

$$\varepsilon_x = \frac{\partial u}{\partial x}, \varepsilon_y = \frac{\partial v}{\partial y}, \text{ and } \varepsilon_{xy} = \frac{\partial u}{\partial y} + \frac{\partial v}{\partial x} \text{ for a 2D case, etc} \quad (5)$$

Stresses are then found using corresponding stress-strain relationships. For example, for a 2D case with plane stress:

$$\varepsilon_{xx} = \frac{1}{E}(\sigma_{xx} - \nu\sigma_{yy}), \sigma_{zz} = \sigma_{yz} = \sigma_{xz} = 0 \quad (6)$$

and

$$\begin{Bmatrix} \sigma_{xx} \\ \sigma_{yy} \\ \sigma_{xy} \end{Bmatrix} = \frac{E}{1-\nu^2} \begin{bmatrix} 1 & \nu & 0 \\ \nu & 1 & 0 \\ 0 & 0 & \frac{1}{2}(1-\nu) \end{bmatrix} \begin{Bmatrix} \varepsilon_{xx} \\ \varepsilon_{yy} \\ \varepsilon_{xy} \end{Bmatrix} \quad (7)$$

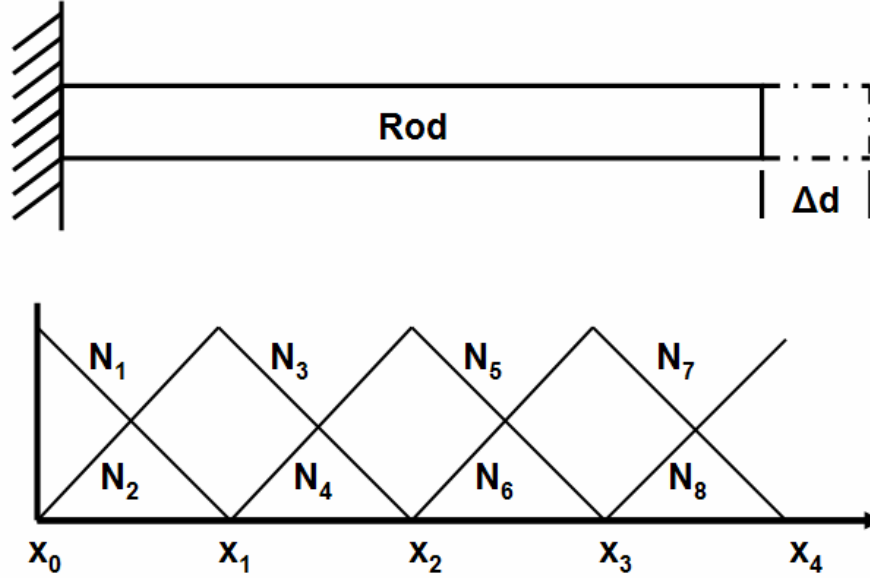
Finally, the principle of minimum potential energy is applied, with $\delta\pi = 0$. Combining like terms and simplifying will result in a system of equations, in which the displacements at each node can be solved.

This section provides an example of applying the spline analysis method to solve for displacements at defined nodes on a one-dimensional rod. More extensive examples, including two-dimensional cases, are included in Appendix A. The progression outlined is similar to how the BSAM computer program solves for strains, stresses, and displacements. The BSAM computer program is able handle three dimensional problems by propagating applicable equations in three directions.

Example: A one-dimensional rod is 10 inches long and is displaced 0.25in on the end.

The rod is subject to the following boundary conditions: $u(0) = 0.0$ in, $u(10) = 0.25$ in.

Using linear splines, find the displacements at each node (x_1 , x_2 , and x_3).



First, the shape functions must be defined for linear splines along the length of the rod.

$$N_1 = 1 - \frac{x - x_0}{x_1 - x_0} \quad \text{on the interval } x_0 \leq x \leq x_1, N_1 \text{ \& } N_2 = 0 \text{ elsewhere} \quad (8)$$

$$N_2 = \frac{x - x_0}{x_1 - x_0}$$

$$N_3 = 1 - \frac{x - x_1}{x_2 - x_1} \quad \text{on the interval } x_1 \leq x \leq x_2, N_3 \text{ \& } N_4 = 0 \text{ elsewhere} \quad (9)$$

$$N_4 = \frac{x - x_1}{x_2 - x_1}$$

$$N_5 = 1 - \frac{x - x_2}{x_3 - x_2} \quad \text{on the interval } x_2 \leq x \leq x_3, N_5 \text{ \& } N_6 = 0 \text{ elsewhere} \quad (10)$$

$$N_6 = \frac{x - x_2}{x_3 - x_2}$$

$$N_7 = 1 - \frac{x - x_3}{x_4 - x_3} \quad \text{on the interval } x_3 \leq x \leq x_4, N_7 \text{ \& } N_8 = 0 \text{ elsewhere} \quad (11)$$

$$N_8 = \frac{x - x_3}{x_4 - x_3}$$

The displacement of the entire rod can be expressed:

$$u_x = \sum_{j=1}^8 A_j N_j \text{ where } A_j = \text{values of displacement at nodes} \quad (12)$$

Applying this equation to the example,

$$u_x = A_1 N_1 + A_2 N_2 + A_3 N_3 + A_4 N_4 + A_5 N_5 + A_6 N_6 + A_7 N_7 + A_8 N_8 \quad (13)$$

For simplicity, assume that the nodes are equally spaced so that:

$$x_1 - x_0 = x_2 - x_1 = x_3 - x_2 = x_4 - x_3 = h \quad (14)$$

From boundary conditions

$$u(0) = 0 \rightarrow A_1 = 0 \quad (15)$$

$$u(10) = 1 \rightarrow A_8 = 0.25 \quad (16)$$

For displacement continuity between the four sections,

$$A_2 = A_3, A_4 = A_5, \text{ and } A_6 = A_7 \quad (17)$$

Then,

$$u_x = A_1 N_1 + A_2 N_2 + A_3 N_3 + A_4 N_4 + A_5 N_5 + A_6 N_6 + A_7 N_7 + A_8 N_8 \quad (18)$$

Becomes

$$u_x = (0)N_1 + A_2 N_2 + A_2 N_3 + A_4 N_4 + A_4 N_5 + A_6 N_6 + A_6 N_7 + (0.25)N_8 \quad (19)$$

For an axial rod, it is known that $\varepsilon_x = \frac{\partial u_x}{\partial x}$.

$$\frac{\partial N_1}{\partial x} = \frac{-1}{x_1 - x_0} \quad (20)$$

$$\frac{\partial N_2}{\partial x} = \frac{1}{x_1 - x_0}$$

$$\frac{\partial N_3}{\partial x} = \frac{-1}{x_2 - x_1}$$

$$\frac{\partial N_4}{\partial x} = \frac{1}{x_2 - x_1} \quad (21)$$

$$\frac{\partial N_5}{\partial x} = \frac{-1}{x_3 - x_2} \quad (22)$$

$$\frac{\partial N_6}{\partial x} = \frac{1}{x_3 - x_2}$$

$$\frac{\partial N_7}{\partial x} = \frac{-1}{x_4 - x_3} \quad (23)$$

$$\frac{\partial N_8}{\partial x} = \frac{1}{x_4 - x_3}$$

$$\varepsilon_x = \frac{\partial u_x}{\partial x} = (0) \frac{\partial N_1}{\partial x} + A_2 \frac{\partial N_2}{\partial x} = \frac{A_2}{x_1 - x_0} = \frac{A_2}{h} \quad \text{from } 0 \leq x \leq h$$

$$\varepsilon_x = \frac{\partial u_x}{\partial x} = A_2 \frac{\partial N_3}{\partial x} + A_4 \frac{\partial N_4}{\partial x} = -\frac{A_2}{x_2 - x_1} + \frac{A_4}{x_2 - x_1} = \frac{A_4 - A_2}{h} \quad \text{from } h \leq x \leq 2h$$

$$\varepsilon_x = \frac{\partial u_x}{\partial x} = A_4 \frac{\partial N_5}{\partial x} + A_6 \frac{\partial N_6}{\partial x} = -\frac{A_4}{x_3 - x_2} + \frac{A_6}{x_3 - x_2} = \frac{A_6 - A_4}{h} \quad \text{from } 2h \leq x \leq 3h \quad (24)$$

$$\varepsilon_x = \frac{\partial u_x}{\partial x} = A_6 \frac{\partial N_7}{\partial x} + (0.25) \frac{\partial N_8}{\partial x} = -\frac{A_6}{x_4 - x_3} + \frac{(0.25)}{x_4 - x_3} = \frac{0.25 - A_6}{h} \quad \text{from } 3h \leq x \leq 4h$$

Stresses can be found by applying Hooke's law for this one dimensional case.

$$\sigma_x = E \varepsilon_x \quad (25)$$

Then, applying the principle of minimum potential energy

$$\delta \pi = \int_0^{4h} \delta \varepsilon_x \sigma_x dx \quad (26)$$

$$\delta \pi = \int_0^h \frac{E}{h^2} A_2 \delta A_2 dx + \int_h^{2h} \frac{E}{h^2} (-A_2 + A_4) (-\delta A_2 + \delta A_4) dx +$$

$$\int_{2h}^{3h} \frac{E}{h^2} (-A_4 + A_6) (-\delta A_4 + \delta A_6) dx + \int_{3h}^{4h} \frac{E}{h^2} (A_6 - 0.25) \delta A_6 dx \quad (27)$$

Since it is defined that $h = 2.5$

$$\begin{aligned}\delta\pi = & \frac{E}{h^2} A_2 \delta A_2 (2.5) + \frac{E}{h^2} [(A_2 - A_4)(\delta A_2) + (-A_2 + A_4)(\delta A_4)](2.5) \\ & + \frac{E}{h^2} [(A_4 - A_6)(\delta A_4) + (-A_4 + A_6)(\delta A_6)](2.5) + \frac{E}{h^2} [(A_6 - 0.25)(\delta A_6)](2.5)\end{aligned}\quad (28)$$

Combining and simplifying, this becomes

$$\delta\pi = 2.5 \frac{E}{h^2} [(2A_2 - A_4)\delta A_2 + (-A_2 + 2A_4 - A_6)\delta A_4 + (-A_4 + 2A_6 - 0.25)\delta A_6] = 0 \quad (29)$$

This results in a set of 3 linear equations

$$\begin{aligned}2A_2 - A_4 &= 0 \\ -A_2 + 2A_4 - A_6 &= 0 \\ -A_4 + 2A_6 &= 0.25\end{aligned}\quad (30)$$

$$A_2 = 0.0625in$$

$$A_4 = 0.125in \quad \text{where } A_i \text{ represents the displacements at the nodes} \quad (31)$$

$$A_6 = 0.1875in$$

This same basic procedure can be used with other polynomials, such as higher order polynomial splines. As one can imagine, applying this approach to a three dimensional problem using higher order functions would be very tedious and time-consuming to do by hand.

BSAM Computer Code

While the BSAM program is very capable and has refined analytical capabilities, it is not a commercialized code. Because of this, it has an undeveloped graphical user interface (GUI) and little documentation exists on the modification or creation of input files. Depending on the complexity of the model, building an input file for BSAM can either be fairly straight forward and quick or a tedious and time-consuming undertaking. A detailed explanation of the development of the stepped-lap and scarf models developed

for this thesis and more specific information about the modification of an input file is included in Appendix B.

In general, developing a model for BSAM requires several main steps. *The first step requires defining the basics* such as properties of modeled materials, the failure criterion (if applicable), and creating orientations for composites and other materials. As an example, two different sets of material properties (for the laminate and adhesive) were defined for this thesis, while five orientations were developed to describe the different ply orientations ($+45^\circ$, 0° , -45° , 90°) and the isotropic adhesive (arbitrarily given a 0° orientation).

The second step consists of building the model. To accomplish this, “geometries” for the model are defined. These geometries describe the shape and size of the three-dimensional building blocks needed to construct the desired model. In BSAM it is possible to apply a single “geometry” to more than one “cluster.” While a “geometry” simply defines the shape and size of each building block, clusters are the actual building blocks that are put together to form the model. For instance, 374 “clusters” or building blocks were needed to build the stepped-lap model that contained only nine (9) unique or different geometries. This was because some of the clusters were the same size and shape. These clusters must then be connected together. Finally, boundary conditions and loads can be defined. After a model is built, BSAM has the ability to interface with Mat Lab to produce a three-dimensional image of the model. This can be used to verify the accuracy of the model.

The third and final step consists of specifying the details of analysis. This includes defining the order of polynomials used to discretize clusters. In discretizing a

cluster, the user can develop a mesh that allows the BSAM program to produce more accurate theoretical strain fields in a desired portion of the model. In this thesis, special care was taken to create a finer mesh in the area of repairs on the edges of the specimens. This step also includes defining the coordinates of data points where output is desired. For this thesis, 500 data points were defined through the thickness of the specimen to match the resolution of the experimental technique used. Overall, over 3.8 million data points were defined for the stepped-lap model, while over 4.4 million data points were defined for the scarf joint. These data points corresponded to the edge of the specimen where experimental strain data was acquired.

Currently, BSAM uses a notepad style input file requiring all values to be placed in an appropriate row or column. To give the reader an idea of the size of the text input files required for this thesis, the stepped-lap input file contained over 1000 lines of code while the scarf input file consisted of approximately 700 lines of code. To put this in perspective, however, it is also important to note that the stepped-lap and scarf joints are on the complicated side of models analyzed by BSAM to this point.

The BSAM computer program also outputs data in a text file. These text files can be large, as the size of the output files containing strain data for both models was about 700 megabytes. In the case of the stepped-lap joint, the output file had to be split into several smaller files before it could be handled by the computer used to run the program. Output files are then converted into files that can be opened using another computer program called Transform. Transform allows users to create color images and plots from two-dimensional data arrays. By using Transform, strain data from BSAM can be

converted into full-field strain images and data can be extracted at exact locations to produce line plots.

To reiterate, while this chapter provides a general summary of the BSAM computer program, a more thorough explanation of the development and modification of BSAM input files can be found in Appendix A. This appendix also contains detailed information concerning input files developed for both the scarf and stepped-lap models. Additionally, while the general theory behind BSAM is developed in the body of this text, more rigorous examples relating to the process and theory behind the B-spline analysis method are included in Appendix B.

III. Methodology: Specimen Fabrication

This chapter describes the methodology taken to fabricate the stepped-lap and scarf specimens. Overall, this chapter includes steps taken to (1) manufacture the panels, (2) machine the scarf and stepped-lap repairs, and (3) cut coupon specimens.

Panel Manufacture

Two composite panels were laid up using IM6/3501-6 epoxy pre-impregnated carbon fiber unidirectional tape with a $[45_2/0_2/-45_2/90_2]_s$ ply lay-up. The 16 ply panels measured 60.96cm (24 inches) by 30.48cm (12 inches) with the 0° direction oriented along the 60.96cm (24 inch) length. These panels were arbitrarily labeled as panel #524 and panel #525.

IM6/3501-6 was the graphite/epoxy system selected for this study as it is an older system with established properties. Because of this, findings from studies that include this composite material can be freely disseminated. While it is not the most recent system, examples of IM6/3501-6 applications include the wing of the Navy's EA-6B Prowler (Mehrkam) and the primary structure for the V-22 Osprey tilt rotor aircraft (Applications).

Panels were bagged using a Teflon porous peel ply and Teflon nonporous ply on both sides of the laminate. Two layers of breather cloth were placed over the Teflon covered laminate to allow the vacuum port to give a uniform vacuum over the entire panel. Both panels were bagged on a tool plate to make sure the cured panel was completely flat. Double sided sealant tape and vacuum bagging was used to seal the bagged laminate. Figure 6 shows a schematic diagram of the composite bagging process, indicating the layers used.

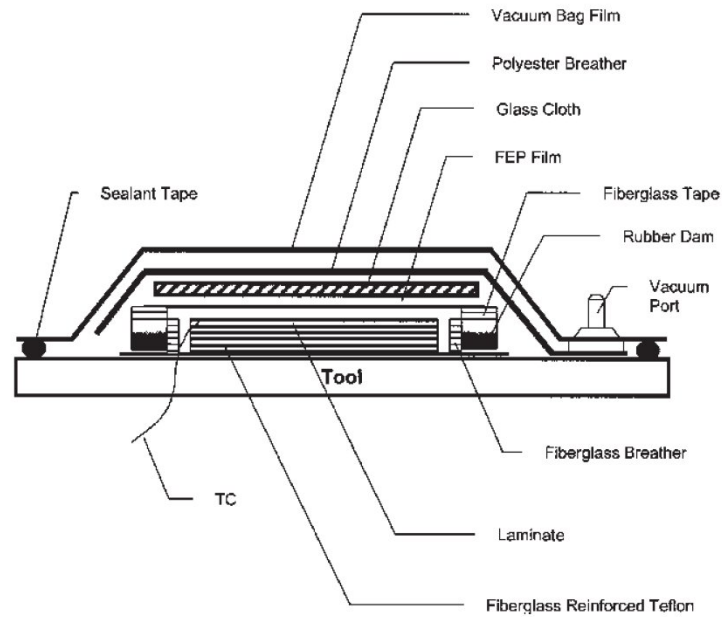


Figure 6. Bagging Schematic (Cycom)

To ensure the integrity of the 1551.4mm Hg (30psi) seal, a vacuum test was performed to make sure no more than 51.7mm Hg (1psi) of vacuum pressure was lost over a minute before the panels were cured in the autoclave.

Both lay-ups were bagged and cured together, using the manufacturer's recommended autoclave cycle. The curing cycle consisted of several segments in which the autoclave temperature was ramped to 121°C (250°F), held for an hour, and then pressurized to 5171.5mm Hg (100psi) at 176.7°C (350 °F) for two hours. Figure 7 shows the trend view from the autoclave curing cycle for both panels. A trend view is a graphical summary of an autoclave cycle, containing information such as temperature, pressure, and vacuum seal pressure.

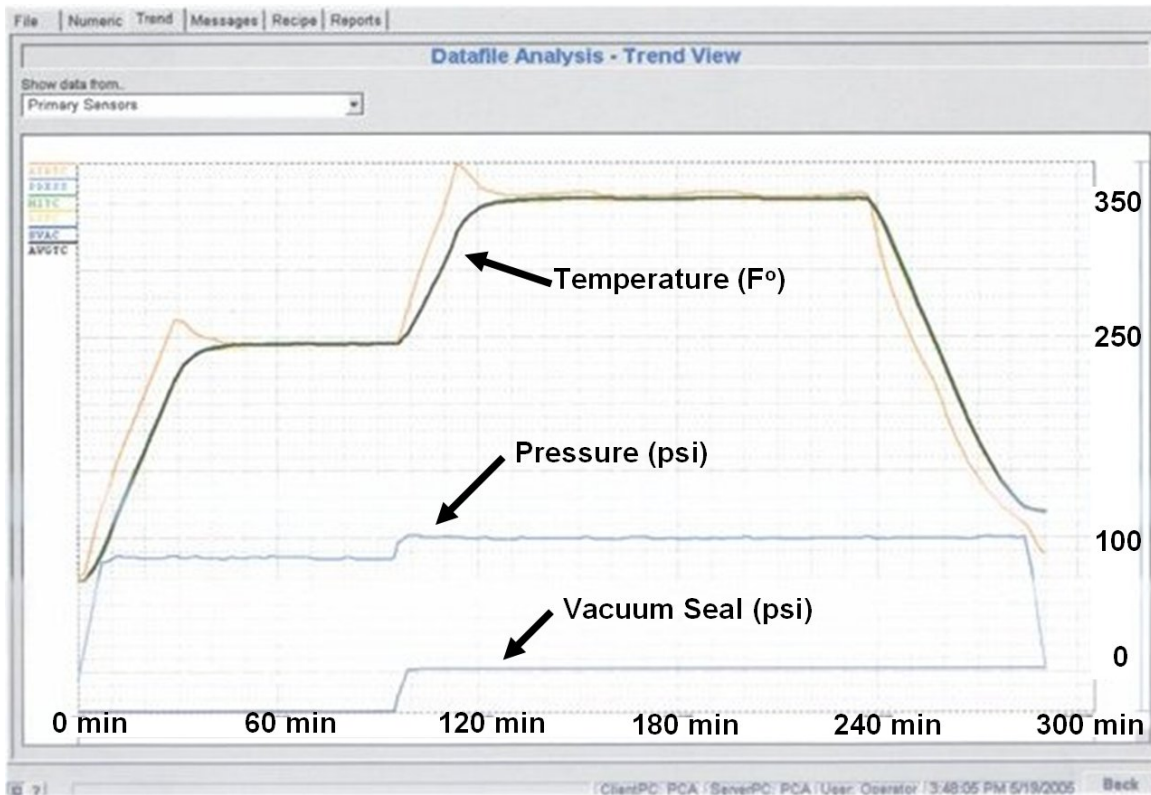


Figure 7. Autoclave Curing Cycle for IM6/3501-6

The two cured panels were then given a visual inspection to check for surface flaws, and an ultrasonic C-scan was also completed to ensure there were no significant internal flaws (see Figure 8 and Figure 9). An ultrasonic C-scan is a non-destructive technique used to examine defects inside the panel. In a high frequency ultrasonic C-scan, a high frequency signal (up to 50MHz) is transmitted to the material by a transducer. Both the material and transducer are submerged in water, which serves as a coupling medium. The signal is partially reflected back to the transducer if it encounters defects, such as porosities and strong differences in acoustic impedance in the sample. The rest of the signal is either fully reflected or continues through the sample (Ultrasonic).

The red in the C-scans indicate that 80% or more of the signal is reflected back to the transducer. For the C-scans done in this thesis, lexan was used underneath the panels as a reflective surface. Both panels were found to be defect free.

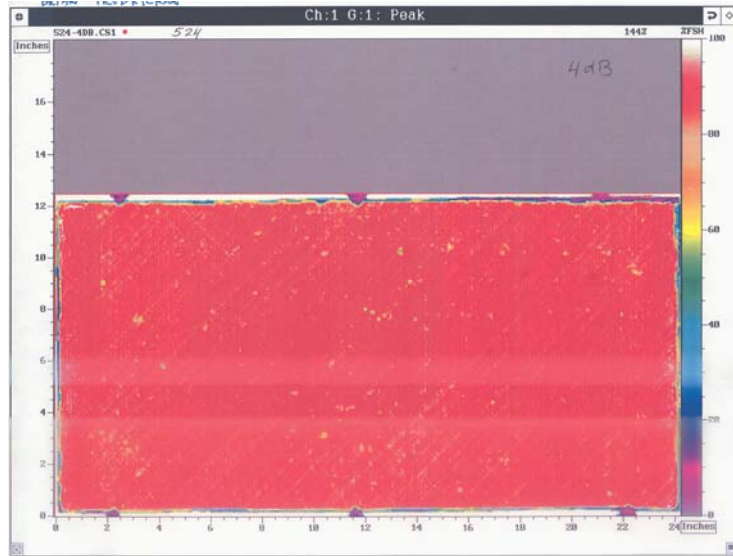


Figure 8. C-scan of Panel #524

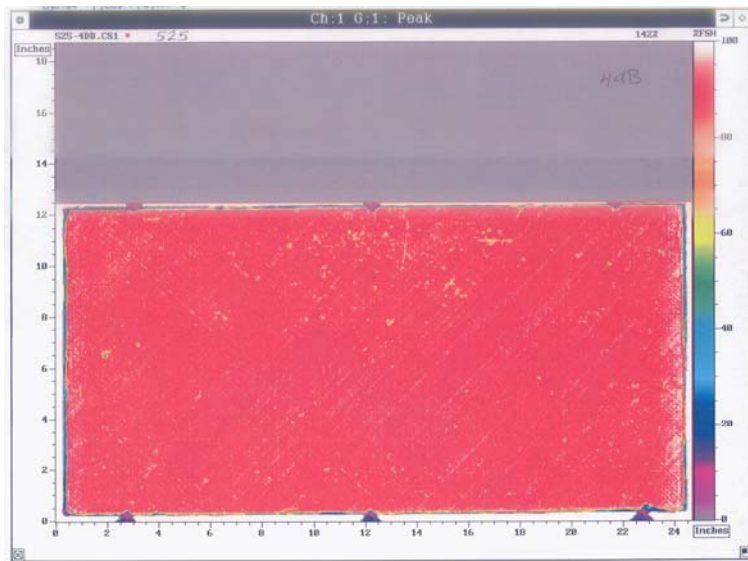


Figure 9. C-scan of Panel #525

Scarf Specimen Manufacture

Typically, a scarf joint is manufactured in the field by a skilled technician using a hand grinder, such as the Dotco grinder shown in Figure 20. The technique and precision involved in machining such a repair usually requires training and a decent amount of experience. Even when machined by a skilled technician, there usually is some margin of error and non-uniformity in the repair. To ensure the manufacture of a uniform scarf repair, a fairly unique process was developed for this study. This technique, described in the following section, was established to allow a person with limited experience and training to machine uniform scarf surfaces on a flat panel in a research/laboratory environment.

First, the edges of both panels were trimmed down by approximately a quarter inch. This eliminated epoxy saturated edges and the flashing generated from autoclave curing. Flashing is the excess epoxy that flows from the composite laminate during curing. The top 45° ply was used to align the panel to make sure edge cuts were made at 0° and 90°. The panel was then cut into four equal sections measuring approximately 14.6cm (5.75in) by 29.8cm (11.75in). Each quarter panel was labeled to indicate the top side, 0° ply direction, and panel number (shown in Figure 10). All cuts were made using a wet diamond bladed radial table saw.

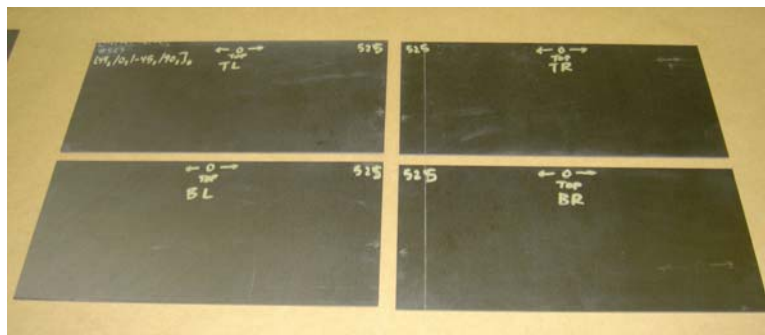


Figure 10. Quartered Test Panel #525

To create a uniform scarf angle for all the test specimens, a “scarf angle apparatus” was designed and built, as shown in Figure 11.



Figure 11. Apparatus used to Create Scarf

This apparatus was a device that could be fixed at a given angle and support a quarter panel against a radial disc sander to create an even scarf as illustrated in Figure 12. 80 grit discs were used on the radial sander. Double sided 3M tape was used fix each quarter panel to the apparatus (Figure 13 and Figure 14). The tape was used to prevent the panels from shifting or curling during machining. Quarter panels from panel #524 were used to create the scarf joint in this study.

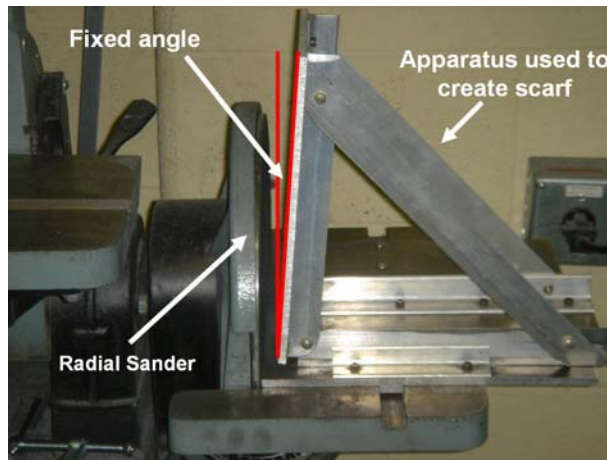


Figure 12. Interaction between Radial Sander and Apparatus

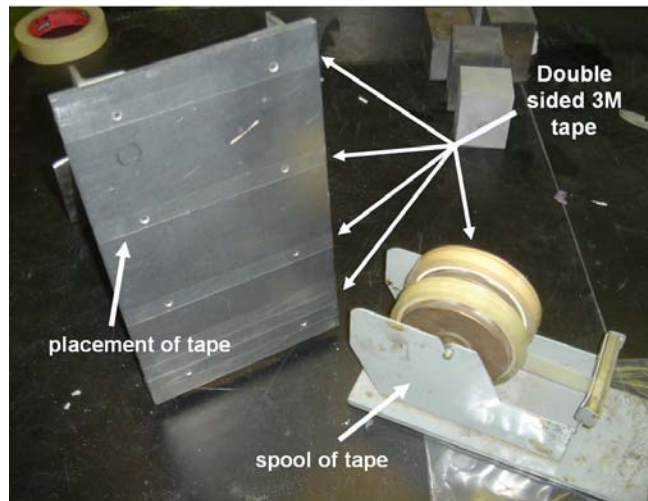


Figure 13. Adhesive used to fix panel to apparatus



Figure 14. Panel fixed to Apparatus used to create scarf

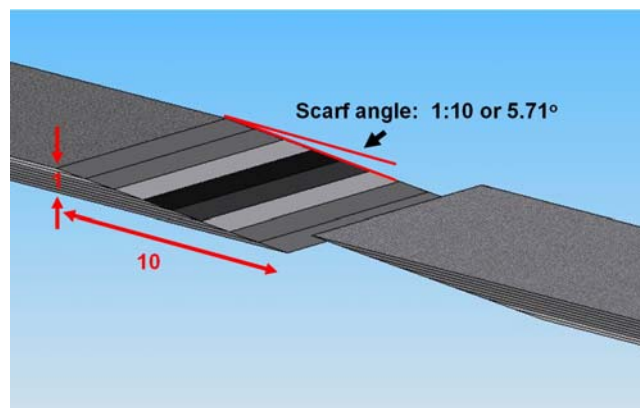


Figure 15. Desired Slope Angle of Scarf Joint

Originally, a slope angle of 1:10 was desired (shown in Figure 15), but because a precise fixed angle was difficult to obtain the actual slope angle ended up being closer to 13.15:1 or 4.35° as shown in Figure 16. A scarf angle of 1:20 is commonly used in composite repairs of aircraft; however, for a flat panel, plies removed during machining cause the laminate to become unsymmetrical in the scarf region due to warping. It was thought that a smaller scarf region (greater scarf angle) would prevent the curling and warping behavior as the laminate became unsymmetrical in the scarf area during sanding since less of each ply would be exposed. The curling and warping are due to residual curing stresses in the unsymmetric region of the scarf.

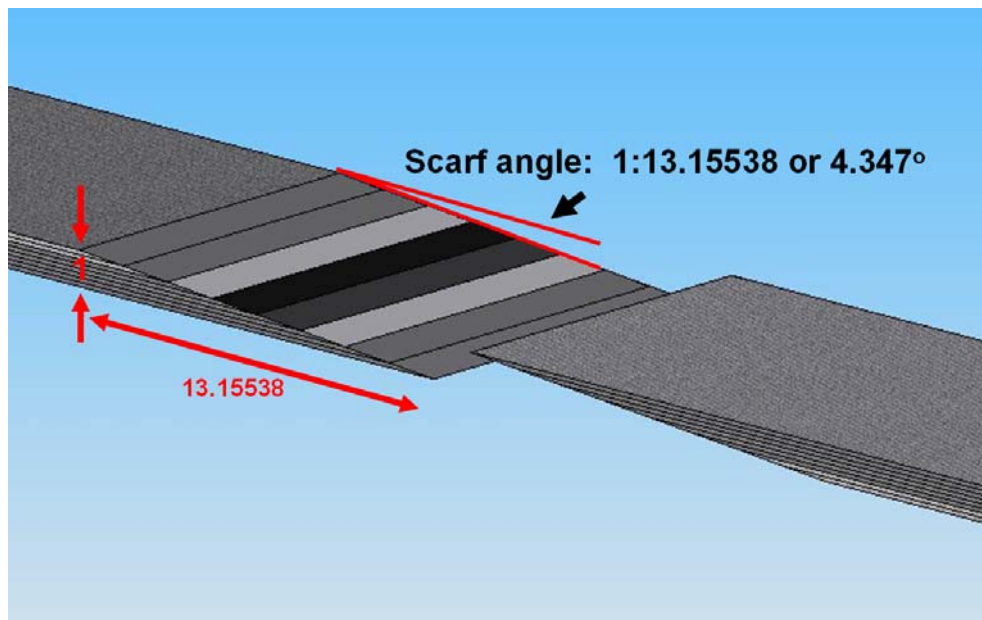


Figure 16. Actual scarf angle achieved during manufacture.

To create a joint where ply orientation lined up through the thickness of the specimen, one section was machined from the bottom while the corresponding section was machined from the top, as shown in Figure 15.

To make sure the test specimens had uniform scarf surfaces, dummy IM6/3501-6 panels with a $[0/45/-45/90]_{2s}$ ply lay-up were used for practice. Errors experienced during scarf surface preparation with the dummy panels helped in refining the machining process for the test specimens. Since the radial disk sander rotated counterclockwise (shown in Figure 17), all grinding was done on the left side of the disk where the motion of sanding was down and toward the end of the panel.



Figure 17. Direction of Sander Rotation

Initial attempts with these practice panels revealed that consistent pressure along the width of the scarf angle apparatus was necessary to form acceptable scarf surfaces. If pressure was greater on one side of the device for even a short period of time, the scarf surface would quickly become uneven. This became difficult to correct and usually more surface was taken from the outer edges of the scarf as shown in Figure 18.

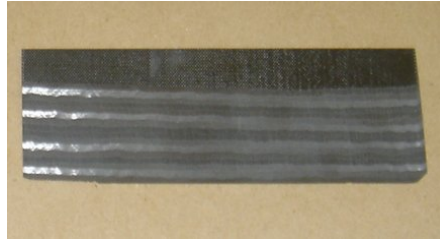


Figure 18. Scarf Surface created without use of Guide

To decrease the number of degrees of freedom for the user, a guide that could be fixed to the radial disc sander table was made. While the table attached to the radial sander prevented any tilting of the scarf fixture by the user, it did not correct for every correctable source of user error. This guide allowed the user to run the entire surface of the panel flush to the sanding surface. It is shown in Figure 19.

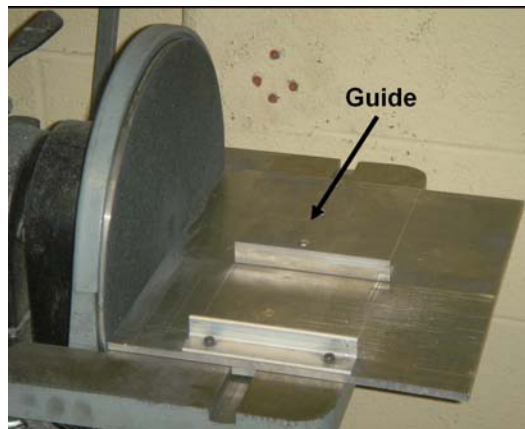


Figure 19. Guide made to decrease user degrees of freedom

While the guide helped greatly in creating a precise scarf surface, the uneven sanding nature of the radial sander still required user input to ensure an even scarf. The edges and center of the 12-inch diameter sanding disk produced machined surfaces that deviated from the rest of the sanding surface. Since the quarter panels were almost six inches wide, these center and edge effects could not be avoided. To maximize the uniformity of the scarf surface and correct these effects, a Dotco hand grinder with a 100

grit sand paper attachment was used to even out the scarf surface (as shown in Figure 20).

Overall, the quality of the final scarf ended up being a product the scarf joint apparatus and skill acquired from practice with numerous panels (Figure 21).



Figure 20. Dotco Hand Grinder

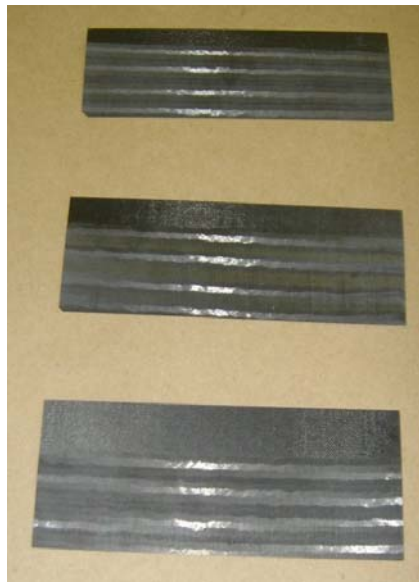


Figure 21. Scarf Surfaces created using $[0/45/-45/90]_{2s}$ Practice Panels.

After producing repeatable uniform scarf surfaces with the practice panels, the same method was applied to the test panels. However, while there was no substantial curling or warping behavior observed in the $[0/45/-45/90]_{2s}$ practice panels, there was

significant curling and warping in the $[45_2/0_2/-45_2/90_2]_s$ test panels as soon as grinding reached the plane of symmetry.

This curling and warping behavior was detrimental to the creation of an even scarf surface as one side the panel would curl up and away from scarf angle apparatus. The tendency for the test panels to curl was greater than the adhesive strength of the double sided tape, so it gradually separated from the scarf angle apparatus. Because of this, the plies in contact with the grinder became uneven over the scarf surface, resulting in an uneven scarf plane.

It was concluded that the $[0/45/-45/90]_{2s}$ dummy panels did not warp or curl significantly due to their ply lay-up. While the $[45_2/0_2/-45_2/90_2]_s$ test panels were only symmetrical about the mid-plane, the $[0/45/-45/90]_{2s}$ dummy panels were symmetrical about both the mid-plane and the quarter planes. This meant that the practice panels were essentially two symmetrical eight ply panels on top of one another. By grinding through the first eight plies of the laminate, the bottom eight plies were still symmetrical about the bottom quarter plane, so curling and warping effects were small enough for the double-sided tape remain adhered even after these bottom eight layers were machined. Also, the scarf length of each ply exposed was small enough that the curling effect of each individual 90° ply and the warping effect of each individual $\pm 45^\circ$ ply were negligible.

Significant curling and warping was observed in the $[45_2/0_2/-45_2/90_2]_s$ test panels, as the laminate was only symmetric about the mid-plane. Once the mid-plane was reached during grinding there was nothing to balance the curling and warping tendencies of plies below the plane of symmetry. This curling and warping tendency was further

exaggerated by the concurrent layer ply orientation in the lay-up. This effectively doubled the scarf length of each ply exposed.

To overcome this problem, more pressure was applied to scarf joint apparatus during machining. This alleviated some of the effects of the curling and warping as the pressure better held the scarf surface uniformly against the sander. This worked for the top of one side of the scarf, but could not be repeated for the bottom of the other side. After several unsuccessful attempts at machining the second quarter panel as a whole, the panel was cut into two smaller pieces. One piece was large enough to yield three one inch test specimens while the second piece was large enough to yield two one inch test specimens. These smaller panels yielded uniform scarf surfaces, and can be seen at the bottom of Figure 22.



Figure 22. Final scarf surfaces from above.

Each bond surface had been sanded with 80 grit sand paper, but further surface preparation was needed prior to bonding to remove any residual contaminants. After 600 grit sandpaper was used to hand sand the scarf surfaces, the surfaces were then wiped with acetone.

Next, the three machined segments were joined and cured. To keep the three machined panel sections and the adhesive from shifting during the curing process, a jig was made. This jig is shown in Figure 23. The device prevented movement in both the vertical and horizontal directions and kept a uniform bond line intact.



Figure 23. Jig used during adhesive curing.

The jig was placed on a tooling plate and bagged, similar to the process described in the Panel Manufacture section of this paper.

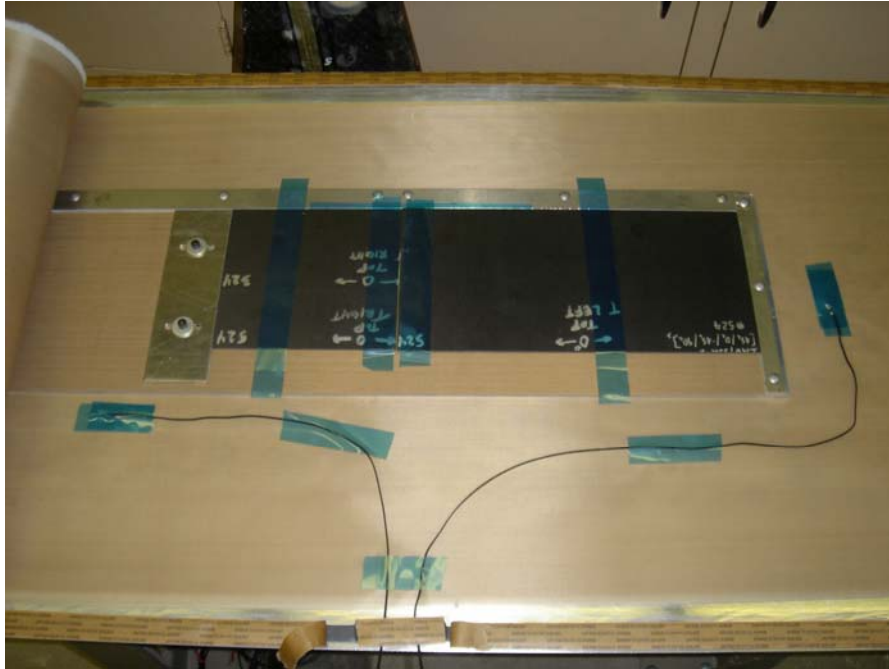


Figure 24. Panel during bagging process



Figure 25. Autoclave used during cure adhesive

A modified epoxy film adhesive produced by Cyanamid called FM300M (0.05psf) was used in this study (FM 300 Film Adhesive). Specific examples of applications for this adhesive could not be found, but it is generally regarded as a well-known and commonly used epoxy film adhesive according to a researcher in the Materials Directorate of Air Force Research Laboratories at Wright-Patterson Air Force

Base. The adhesive was cured according to the manufacturer's recommended cure cycle under 2327mm Hg (45psi) of positive pressure and the temperature was ramped to 176.7°C (350°F) and held for 60 minutes (shown in Figure 26). A silicon bladder cover was used to protect the bagged composites from metal vacuum tubing present in the autoclave. Because the cure temperature of the adhesive was not above that of the parent material, there was no effect on parent material during the adhesive cure cycle.

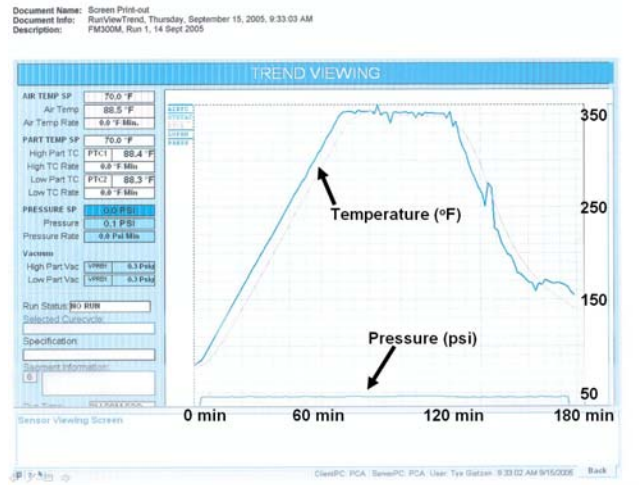


Figure 26. Autoclave curing cycle for FM300M adhesive

An ultrasonic C-scan of the adhered panel was completed to ensure the integrity of the bond line. The yellow area indicates the position of the scarf bond surface, while the green line across the panel to the right of the joint indicates where the two smaller pieces of the panel were butted against each other. The black triangles surrounding the specimen are a result of fixture blocks used to prop the panel up so that it did not contact the underlying lexan. This C-scan can be seen in Figure 27.

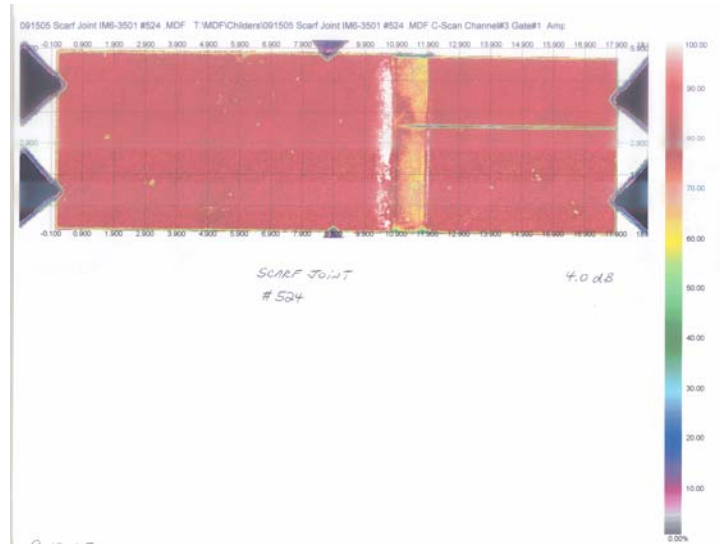


Figure 27. C-scan of test panel with cured adhesive

Since there was substantial flow of adhesive during the curing process, excess adhesive was sanded off the top and bottom of the specimen to obtain a more accurate C-scan of the scarf joint of panel #524 (as shown in Figure 28). Both C-scans indicated that a good bond line was obtained.



Figure 28. C-scan of test panel with cured adhesive after removal of excess adhesive

Following the C-scan of the section with the adhesive, the scarfed test panel was then cut into five coupons each measuring one inch by ten inches. The final specimens are shown in Figure 29. Specimen manufacture followed the specifications from ASTM 3039M-00, Standard Test Method for Tensile Properties of Polymer Matrix Composite Materials.



Figure 29. Final scarf repaired specimens

Stepped Lap Joint Specimen Manufacture

The stepped lap specimens were machined using a milling machine with digital coordinate input. To ensure that tearing and ripping of plies was minimized, special diamond coated bits were used to create the steps in the stepped-lap repair. For machining, the composite panel was also submerged in a water bath to minimize damage to the bits. The stepped-lap specimens were made from panel #525. The set-up for the machining of stepped-lap cuts is shown in Figure 30, Figure 31, and Figure 32.



Figure 30. Set-up for Stepped-Lap Joint Machining.



Figure 31. Digital Coordinate Input for Milling Machine.



Figure 32. View of test specimen being machined in water bath.

The stepped lap repair for this study consisted of eight steps, where each step had a thickness of two-ply. A sketch produced in SolidWorks (SolidWorks) of the stepped-lap test specimens is shown in Figure 33.

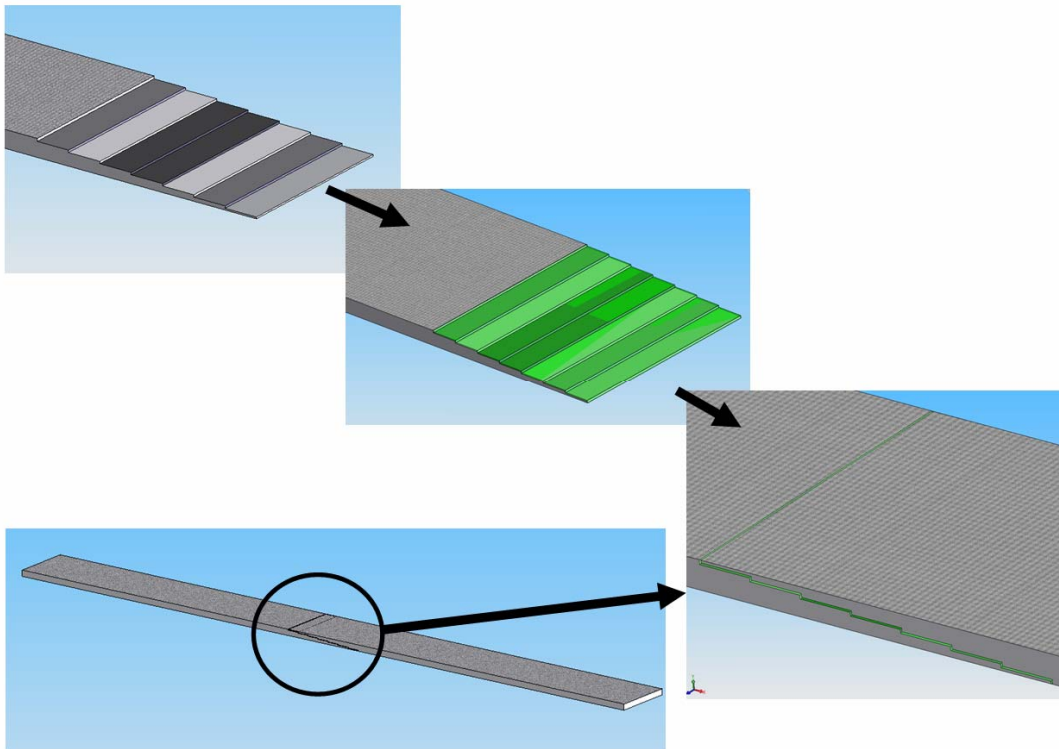


Figure 33. Plan for manufacturing of stepped-lap specimen

Because of concerns regarding the accuracy and effects of machining on the panels, $[0/45/-45/90]_{2s}$ dummy composite panels were used to test this method before actual test panels were machined. For an initial test, eight, two-ply steps at 10° were made on a dummy panel using the proposed step-up profile. This is shown in Figure 34.

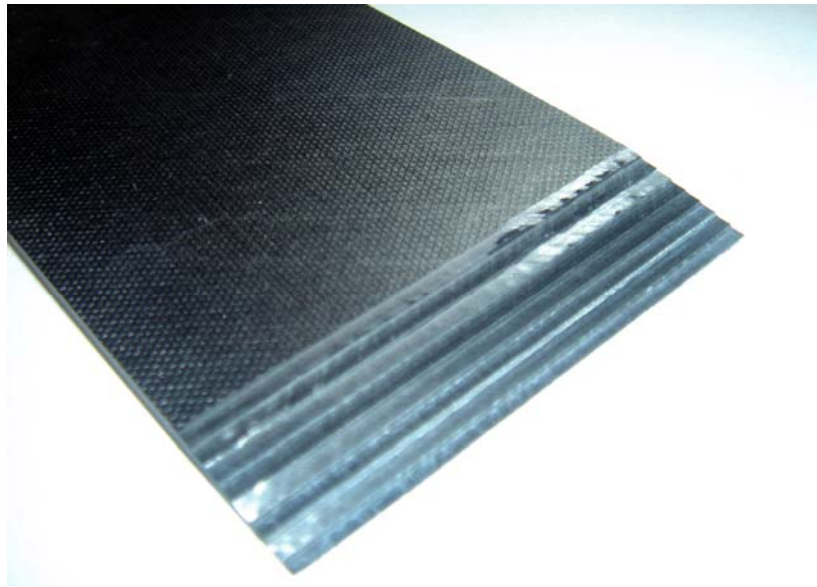


Figure 34. Eight, two-ply steps at 10° machined in dummy panel.

While results from this initial test were mostly positive, two problems were identified. First of all, magnification through a microscope revealed that the bit used for the trial run produced steps that were rounded at the bottom edges of each step (Figure 35). While the rounded corners were very small with a radius no greater than 0.127mm (0.005 inches), this produced an undesirable effect since the steps themselves were only on the magnitude of 0.381mm (0.015 inches). This rounding was significant enough that the surfaces of the stepped lap adherends did not remain flush when butted together.



Figure 35. Rough sketch of rounding in steps.

In addition, the initial test also revealed that an allowance of 0.102mm (0.004 inches) to 0.152mm (0.006 inches) for an adhesive layer would have to be factored in for a cleaner stepped lap repair. Without this allowance, there would be little room for adhesive along the flat surfaces of each step.

To minimize the rounding at the bottom of each step, all seven diamond coated bits available were tested to see which one yielded the squarest machined surfaces. The machined surfaces from these bits are shown in Figure 36.



Figure 36. Machined surfaces from available bits.

After visual inspection under a high powered microscope, the bit that produced the cleanest steps was determined and used for the remainder of the manufacturing process for the stepped-lap repaired panel.

To make sure that the machined stepped-lap surfaces would bond cleanly, another dummy panel was prepared with the stepped-lap repair using a 4.35° angle (Figure 37) to closely mirror the scarf repaired specimens.

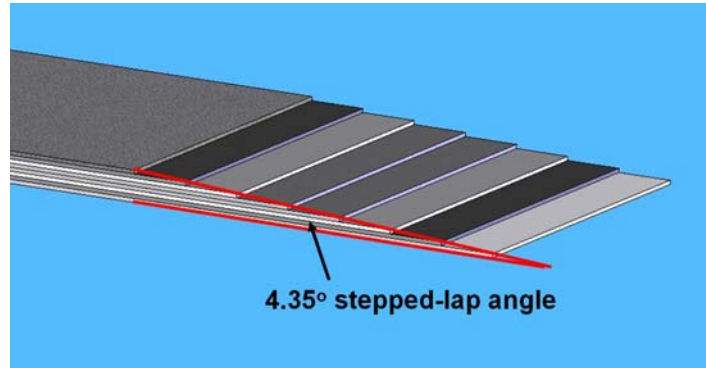


Figure 37. Repair angle of stepped-lap joint.

This time, a 0.102mm (0.004 inch) allowance for adherends was factored into the revised step profile. After the surfaces were machined, the panel was bonded and cured using FM300M epoxy film adhesive and C-scanned to evaluate structural integrity of the bond, as shown in Figure 38 and Figure 39.

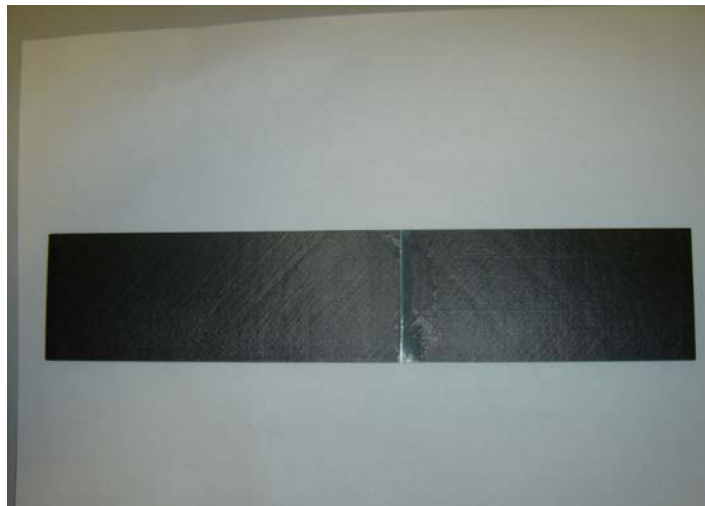


Figure 38. Bonded practice specimen with stepped-lap repair.

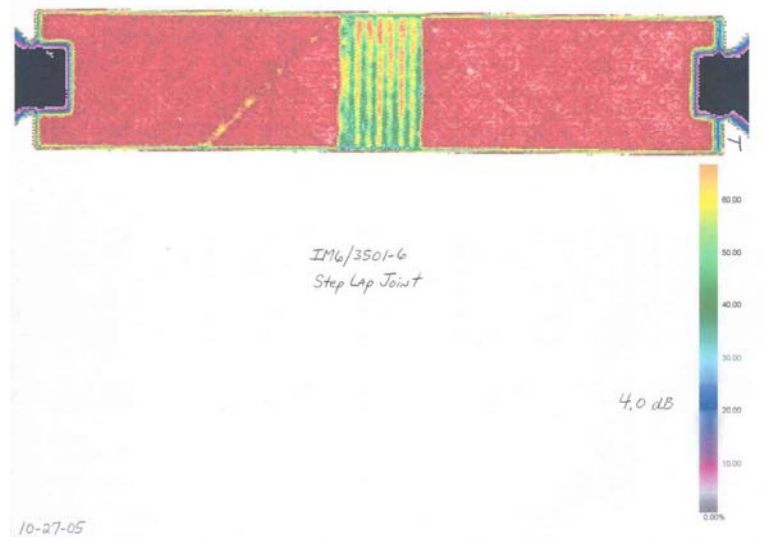


Figure 39. C-scan of practice stepped lap joint specimen.

The second trial run with the dummy panels resulted in an acceptable stepped-lap repair, so efforts were then focused toward machining the actual test panel.

Because of the nature of the test panel ply orientation, the stepped lap panel can exhibit similar twisting and warping behavior as the scarf surfaces during machining. However, because the end of the panel was pinned down throughout the machining process (Figure 40), this behavior was only present after the machined panels were removed from the milling machine.

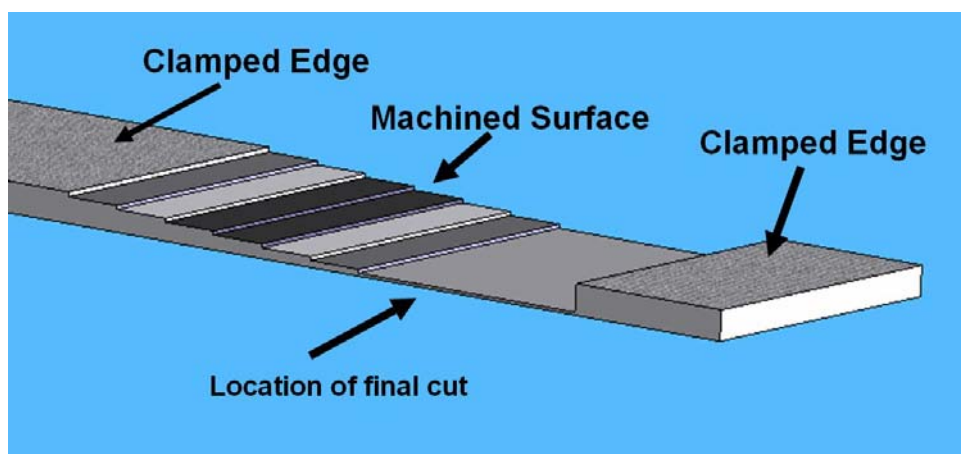


Figure 40. Method of machining on mill to minimize twisting and warping.

Since the panel was clamped flat during the actual machining process, it did not prove to be a troubling issue (as was the case for machining of the scarf surface). The final machined surfaces for the test panels are shown in Figure 41, Figure 42, and Figure 43.



Figure 41. Overhead view of machined stepped-lap surfaces for test panels.

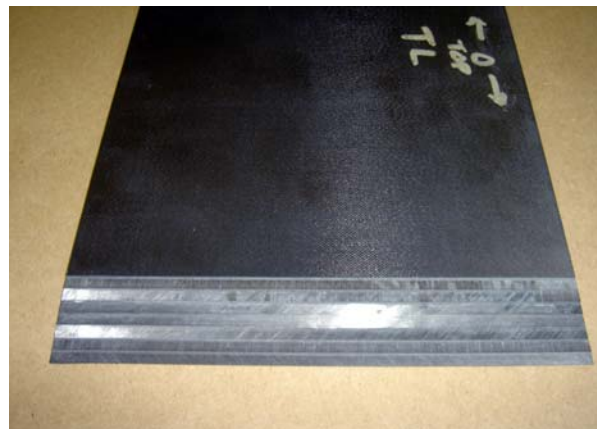


Figure 42. Machined stepped-lap surface for test panel.

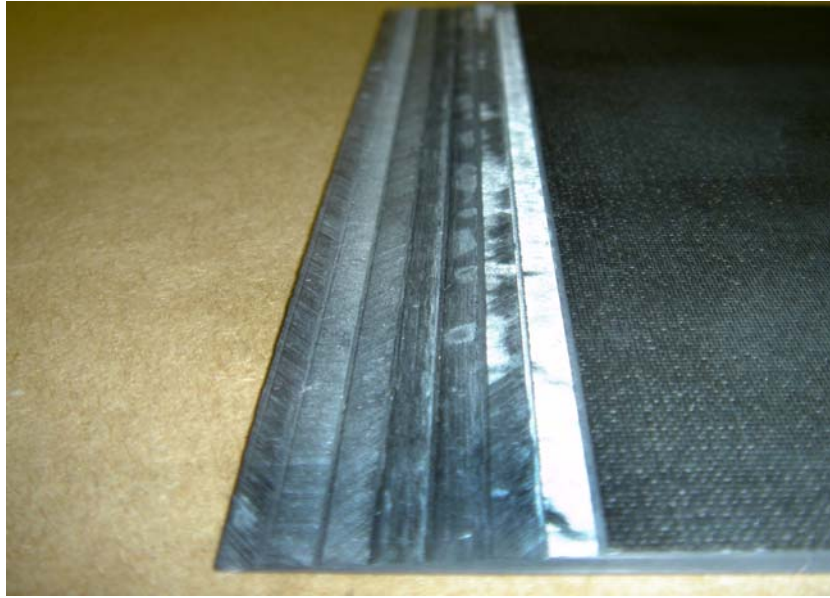


Figure 43. Profile of machined stepped-lap surface for test panel.

Since the composite panels remained submerged in the water bath during the machining process for a substantial amount of time (over 30 minutes), it was important that moisture was removed before the repair was bonded and cured. According to the General Advanced Composite Repair Processes Manual (Department of the Air Force), it is especially important to remove water or moisture prior to a heated curing process, as any water or moisture remaining in the panel will expand as temperature increases. This can cause blistering, delamination, and/or micro-crack damage in the structure. To remove any excess moisture in the stepped-lap panels, they were placed in a vacuum oven for 16 hours at 63°C (145.4°F) and -685.7mm Hg (-13.26psi), as shown in Figure 44. Technical Order 1-1-690 recommends that thoroughly drying a panel can take up to 48 hours at 82.2°C (180°F).⁵ However, experienced technicians at the Air Force Research Laboratories Materials Directorates advised that placing the panels in a vacuum oven overnight would remove enough moisture to safely cure the adhesive.



Figure 44. Vacuum oven used to dry machined panels.

To make sure any additional residual contaminants were removed from the machining process, the bond surface was wiped clean with acetone and then sand blasted (Figure 45) under light pressure.



Figure 45. Machined panels were sand blasted for final surface preparation.

Adhesive was then applied to the repair surface, and the bonded panel was cured according to the manufacturer's recommended cure cycle under positive pressure and temperature. After the adhesive was cured, the test panel was then C-scanned before it was cut into five individual coupons measuring 2.54cm (1in) wide by 25.4cm (10 in) long. The c-scan of the panel with bonded stepped-lap repair is shown in Figure 46.

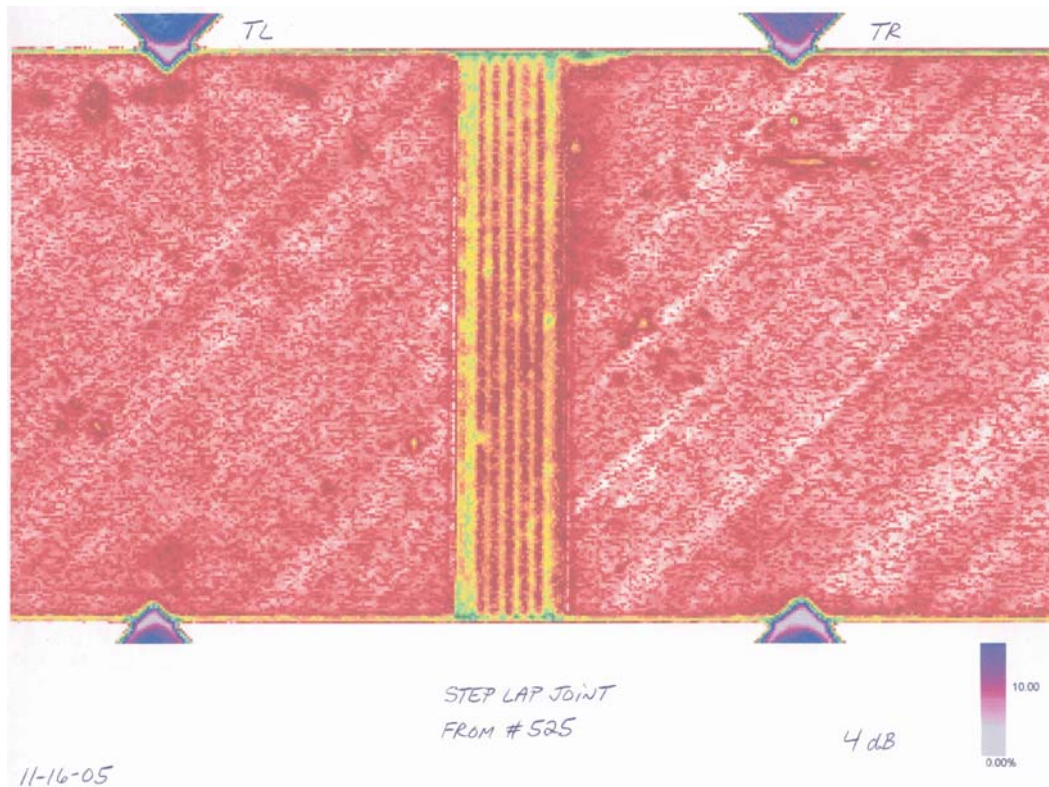


Figure 46. C-scan of adhered stepped-lap region.

The five test specimens were labeled #1 through #5 accordingly (Figure 47).

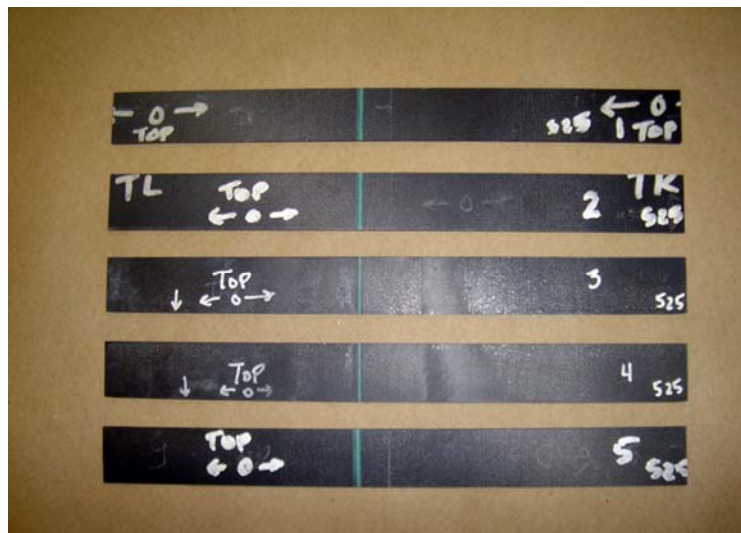


Figure 47. Final stepped-lap repaired specimens.

Specimen manufacture followed the specifications from ASTM 3039M-00 which allowed for an error margin in specimen width of $\pm 1.27\text{mm}$ ($\pm 0.05\text{in}$). Because specimen 1 measured 2.40cm (0.945in) in width, it did not meet specifications from ASTM 3039M-00, but was kept and was used to estimate the repair ultimate strength by testing to failure. Five 1" by 10" unrepaired test specimens were also machined.

IV. Experimentation: Moiré Interferometry

Experimental strain data was acquired in this thesis through an experimental technique known as moiré interferometry. Moiré inteferometry was selected as the experimental technique for this thesis because of its high strain resolution and full-field capabilities. This chapter describes how this technique was applied in this study to acquire strain data for both the scarf and stepped-lap specimen. Overall, this chapter includes (1) an overview of moiré interferometry, (2) an illustrated explanation of required surface preparation and replication of the diffraction grating, (3) a summary of the experimental test-set up, and (4) details regarding experimental data reduction.

Moiré Diffraction Grating Replication

Moiré interferometry is an optical, full-field technique that can be used to measure in-plane displacements on a surface. This is achieved by applying a contoured surface, called a diffraction grating, to a surface of interest. A photograph of diffraction grating under high magnification can be seen in Figure 48.

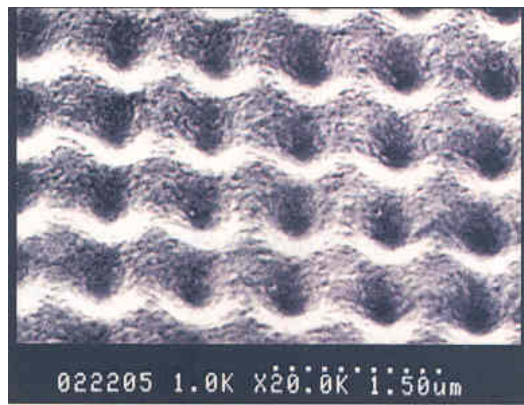


Figure 48. Diffraction grating under high magnification (Post)

Using two beams of collimated light, moiré interferometry can track precise changes in the way light refracts off of the diffraction grating. By replicating a thin diffraction grating on the surface of a specimen, laser light can be diffracted according to grating frequency, laser wavelength, and angle of incidence. When the grating deforms, the interference between the two beams creates a pattern that is a contour map of in-plane displacements. Photographs of the diffraction grating before and after the application of a load yield contour maps with slightly altered fringe patterns. Changes in the fringe pattern between the two photographs represent in-plane displacements and can be described by the equations:

$$\begin{aligned} U_x(x, z) &= \frac{1}{f} N_x(x, z) \\ U_z(x, z) &= \frac{1}{f} N_z(x, z) \end{aligned} \quad (32)$$

Figure 49, taken using a scanning electron microscope, gives an idea of the size and resolution of the fringes on the diffraction grating. The displacement sensitivity of the diffraction grating used in this study was 0.417 μm per fringe contour, or 60,960 lines/inch (Post). Moire inteferometry was selected as the experimental method in this study because of its high resolution.

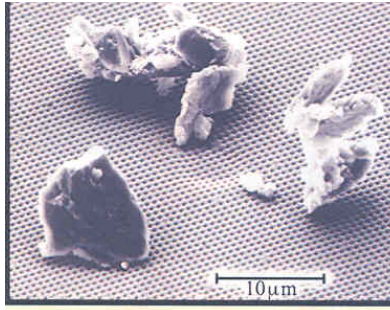


Figure 49. Dust particles on the diffraction grating (Post)

Moiré interferometry can be distinguished from other optical techniques, such as classical interferometry and holographic interferometry, which are effective in determining out-of-plane displacements (Post).

A general set-up for moiré interferometry is shown in Figure 50.

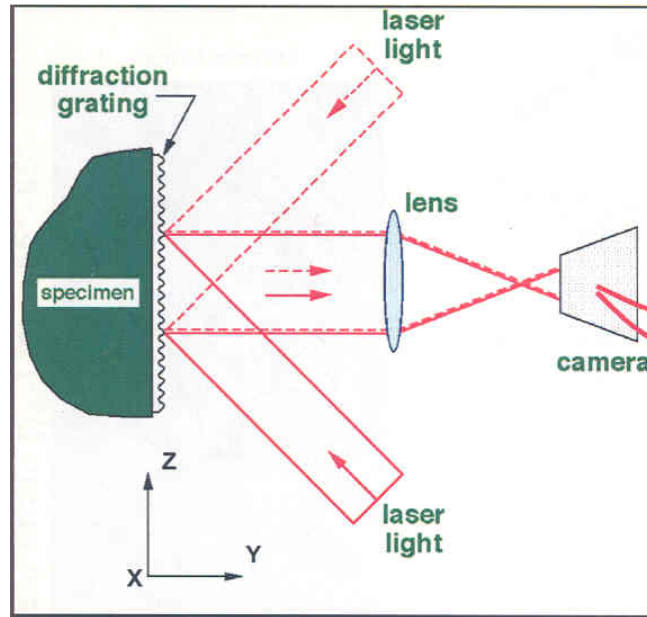


Figure 50. Moiré interferometry set-up (Mollenhauer).

From the five scarf joint specimens and five stepped-lap joint specimens produced, diffraction gratings were replicated on two specimens for each repair. Figure 51 provides an overview of the steps taken to replicate the diffraction grating on a specimen. This section outlines the steps taken during grating replication for this thesis.

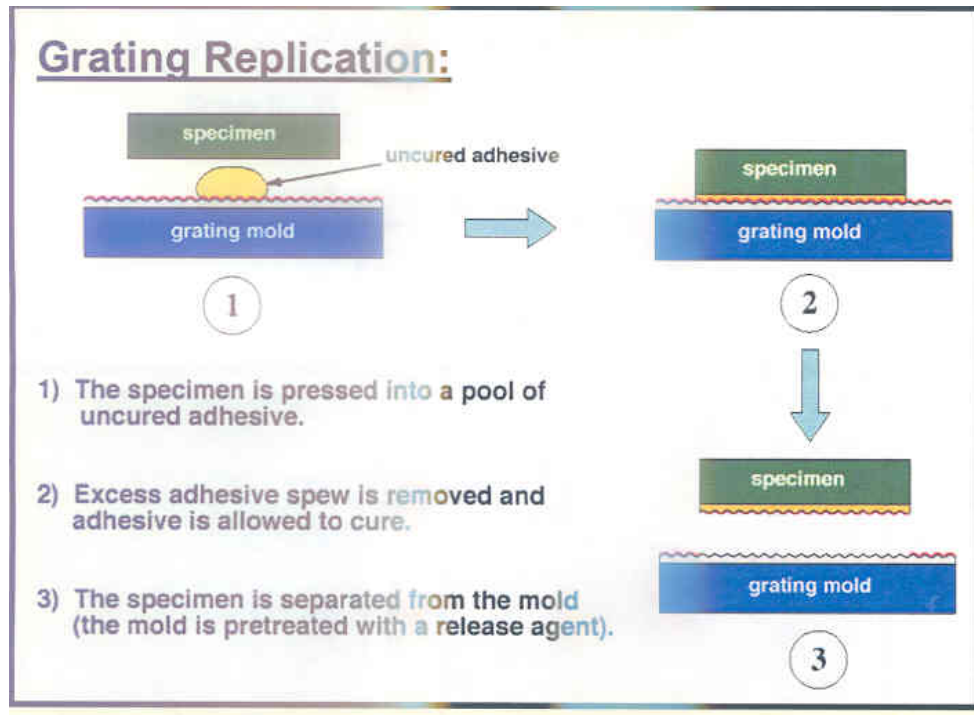


Figure 51. Steps involved in replication of diffraction grating (Mollenhauer).

Specimens #1 and #4 were selected from the scarf joint specimens because they had the most uniform bond line among the five specimens produced. This was determined by taking three bond line thickness measurements for each specimen: one from the left side, one from the middle, and one from the right side of the scarf repair bond line. Measurements were taken using a microscope with a digital coordinate output ($\pm 2.54 \mu\text{m}$ or $\pm 0.0001\text{in}$ accuracy). Using the three measurements for each specimen, the average bond line thickness and standard deviation were calculated and compared to one another to find the specimens with the most uniform bond line.

Specimens #3 and #4 were selected from the stepped-lap joint specimens. Since there was less warping and twisting during the machining of the stepped-lap repairs, the bond line was more consistent across the specimens produced. Specimens #3 and #4 were selected because they had the most identical width 2.565cm (1.010 inches) of the

five specimens, and provided the most uniform surface to polish on when butted against one another.

Before the diffraction grading was applied, the edges of the four selected specimens were polished to provide a flat surface for application. To accomplish this, the four specimens were butted against each other between several thick scrap specimens and clamped together (Figure 52).

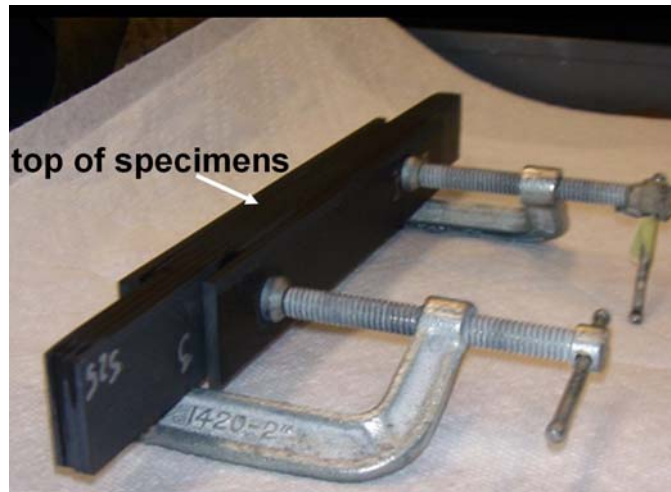


Figure 52. Clamped specimens for polishing.

It was thought that clamping several specimens together would ensure that the polished surface (top of specimens) for each individual test specimen would remain flat as shown in Figure 53 and not become rounded or angled during polishing.

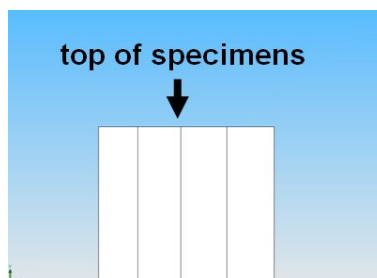


Figure 53. Desired surface of specimens for diffraction grating application.

At first, a radial disk polisher with 240 grid sandpaper was used to give a rough polish to the surface. The radial disk polisher used is shown in Figure 54. Small amounts of water were applied to the sandpaper disk throughout this process to wet sand the edge of the specimens until the surface was uniform.



Figure 54. Radial disk polisher.

Next, 320, 400, and 600 grit sandpaper was used to smooth and polish the edges in a wet sander tray, as shown in Figure 55.



Figure 55. Wet sander tray.

Excessive adhesive flashing was also removed from the top and bottom of the four specimens to give them the most uniform shape possible. Because the specimens were exposed to moisture during most of the polishing process, they were placed in a vacuum oven overnight at 63°C (145.4°F) and 711mm Hg (-28in Hg).

This polishing procedure described above did yield a polished surface that was very flat. However, inspection of the polished surfaces revealed that while the polished surface was flat, the specimens no longer had perpendicular edges, as shown in Figure 56.

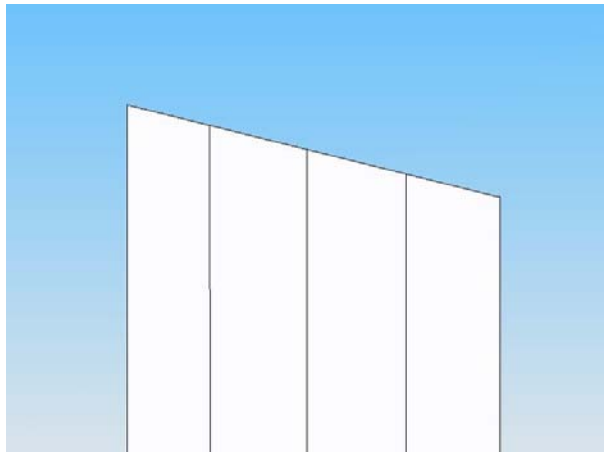


Figure 56. Exaggerated top view sketch of specimens after initial polishing.

This was a problem, as a specimen with perpendicular sides is necessary for the application of the diffraction grating. This was discovered after clamping the specimens again for replication of the diffraction grating, and using a flat metallic reflective plate to judge how flat and square the top edges of the specimens were. Since the specimens were not placed together in the exact same order as before some corners were higher than others (Figure 57). Using the flat metallic reflective plate, this problem was diagnosed after light leaked through cracks created by any specimen edges that were not exactly perpendicular.

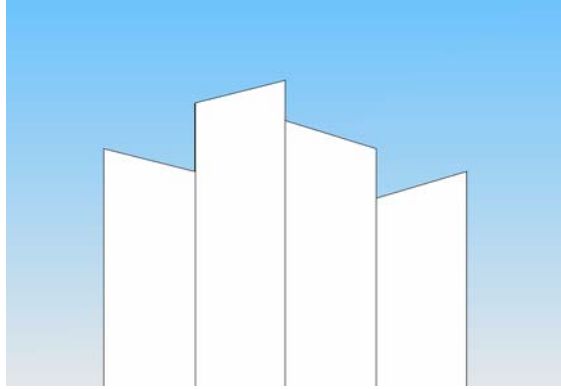


Figure 57. Exaggerated top view sketch of specimens placed together out of order.

To resolve this problem and square the specimens, the specimens were repolished in the same configuration that would be used for the application of the diffraction grating (Figure 58).



Figure 58. Clamped specimens in configuration used for replication of diffraction grating.

The specimens were polished again in a manner similar to the initial procedure, starting with 240 grit sandpaper and again working up to the 600 grit sandpaper. As a final check to make sure the specimens were flat and square with one another, a non-water soluble paint pen was used to mark the polished surfaces. It was thought that if the polished surface was flat and even, a couple swipes over the 600 grit sandpaper would completely remove the paint from the specimens. 600 grit sandpaper was selected to check if the surface was flat and even to minimize the amount of material removed, as it was the finest sandpaper available. When this was accomplished, the surfaces were deemed acceptable for application of the diffraction grating. Panoramic pictures of the polished repairs were then taken under a microscope (Figure 59).



Figure 59. Gathering coordinates for final polished edges.

After the repaired section of the specimen edges were polished, replication of the diffraction grating only required a few steps. The diffraction grating used for this thesis can be seen in Figure 60. The colors seen in the photograph of the metallic diffraction grating are simply a reflection of light off of its surface. However, while the overall

process of replicating the diffraction grating was brief, it was critical that every step taken in the replication process was as precise and accurate as possible. Similar to the machining of the scarf repairs, replication of the diffraction grating required a great deal of delicate craftsmanship and precise handling.

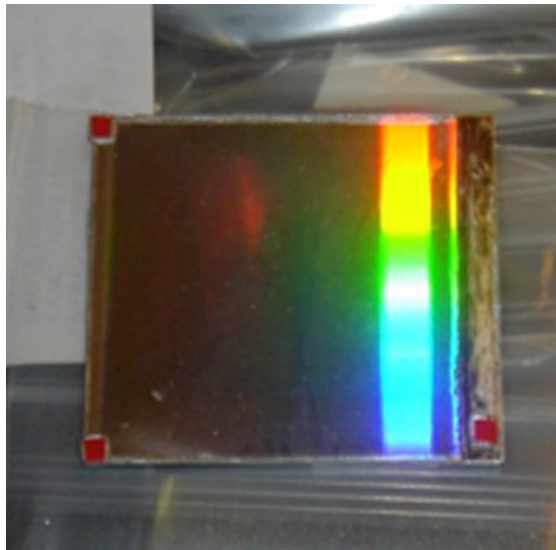


Figure 60. Photomechanics diffraction grating.

The first step was to make sure the grating was square with the specimen. To do this the grating was mounted to a surface using double-sided tape and then placed across from a laser. The grating contours deflect the laser light into two beams at about a 45° angle to either side. If the diffracted beams are at the same height on both sides of the specimen then it can be concluded that the grating is exactly perpendicular to the incoming laser light.



Figure 61. Determining position of reflected laser light.

To determine if the diffracted laser light was at the same height on both sides, the position of the reflected laser light on one side was marked by pencil on an unused object (such as the yellow tab used in Figure 61). By placing the marked unused object on the opposite side, the position of the diffracted laser light on that side could be compared to the marking. Adjustments to the orientation of the diffraction grating were then made until the position of the reflected laser light lined up with the pencil marking. A diagram of this process can be shown in Figure 62.

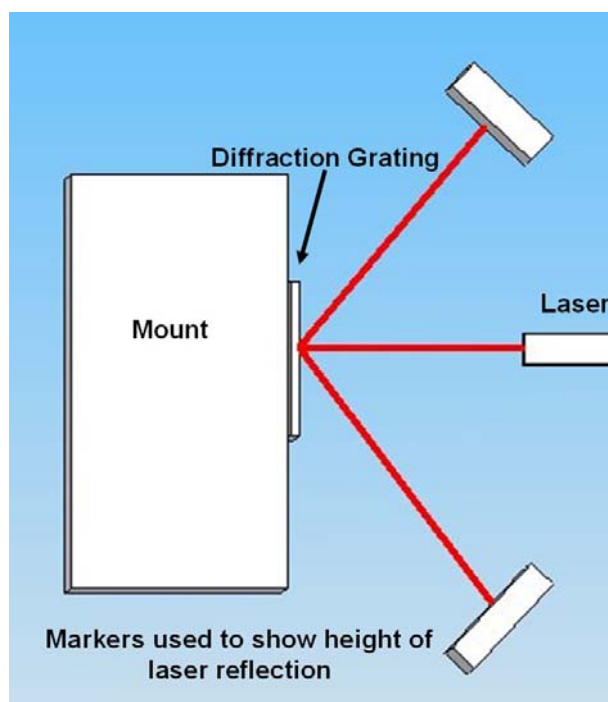


Figure 62. Using laser light reflection to square diffraction grating.

After the diffraction grating was oriented, a metal tab with perfectly parallel sides was fixed to the grating using double-side tape. This tab was used as a reference to orient the contours of the diffraction grating with the specimens.

The next step was to mix the resin that would be used to replicate the diffraction grating. To accomplish this, a 3:1 ratio (50g/17g) of Miller Stephenson EPON Resin 828 and Huntsman Jeffamine D-230 curing agent were mixed in a plastic beaker. The mixture was then transferred into another beaker and then into two vials. The two vials were placed in a centrifuge for approximately 10 minutes to eliminate any bubbles in the mixture.

After removing the vials from the centrifuge, a thin layer of the resin mixture was applied to the edges of the specimens in the region of the bonds. Using the metal tab to align the diffraction grating with specimen edges, the grating was then placed carefully

against the specimens (as shown in Figure 63). Special attention was taken throughout this process to make sure the replicated grating was both as thin and flat as possible.

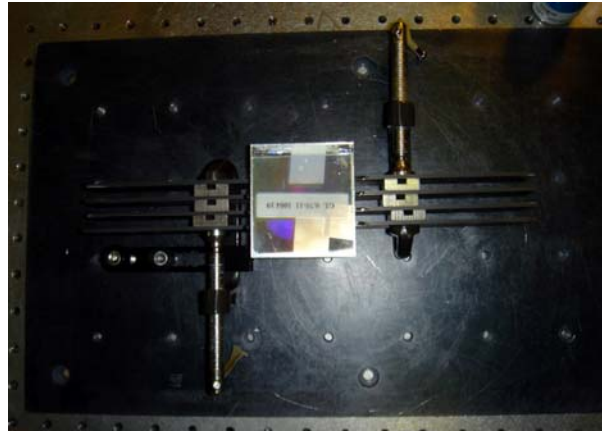


Figure 63. Diffraction grating placed against specimens.

The resin was left to dry for approximately a week before removing the grating. Overall, the diffraction grating came out very clean. There were no excessive bubbles and the grating surface was even on all four specimens. However, the epoxy did not fully replicate the diffraction grating on one of the four specimens. This was stepped-lap specimen #4 and was not used during experimentation. Pictures of the clamped specimens after removal of diffraction grating are shown below in Figure 64 and Figure 65.

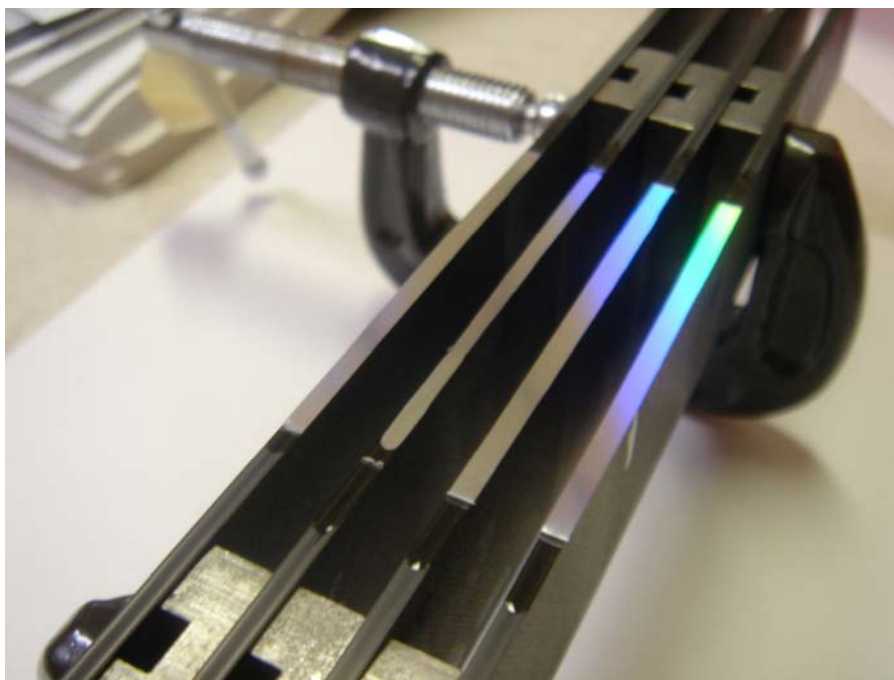


Figure 64. Diffraction grating replicated on test specimens.

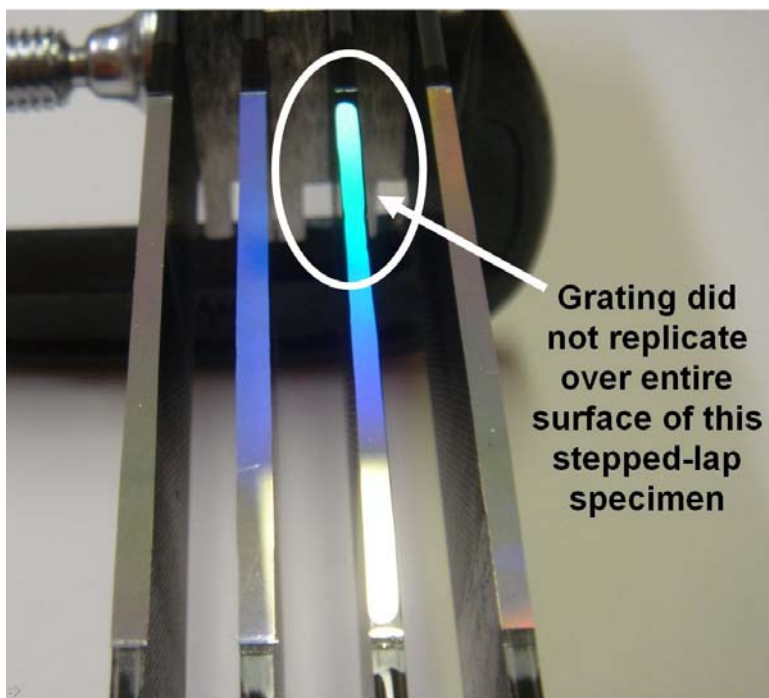
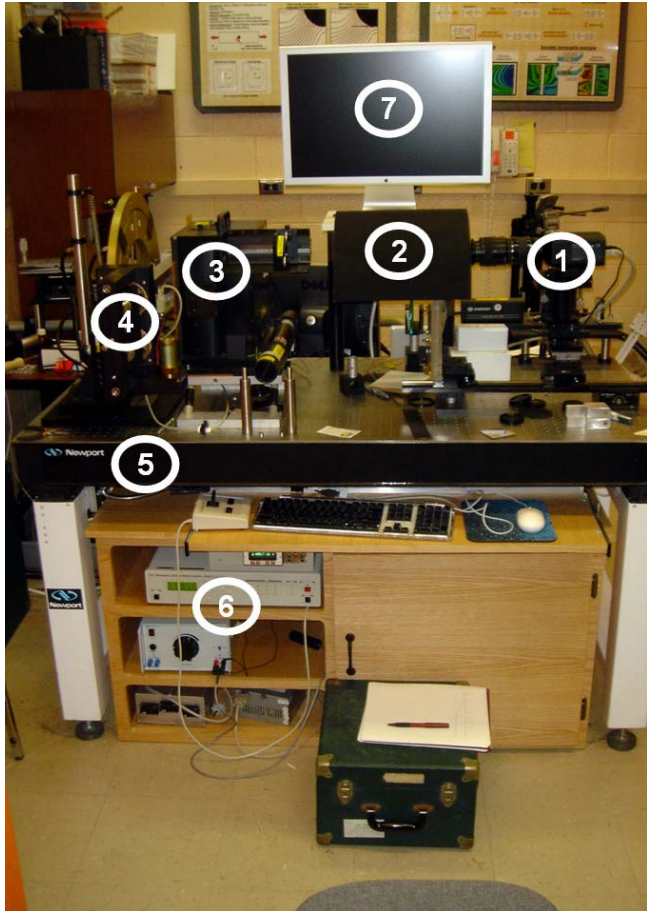


Figure 65. Flawed specimen.

Experimentation

Scarf specimen #4 and stepped-lap specimen #3 were selected for testing, as they had the most uniform and clean diffraction grating. The stepped-lap specimen was tested first and the scarf specimen was tested approximately a week later. Figure 66 gives an overall view of the moiré interferometry test set-up.



1. Camera used to photograph fringe patterns
2. Black (non-reflective box) containing opaque disk used to minimize glare and reduce number of ghost images
3. Box where collimated light is split and refracted
4. Screw driven load fixture
5. Pneumatic table used to dampen vibration
6. Units used to traverse load fixture and apply tensile load
7. Computer used to photograph and process fringe pattern images

Figure 66. Labeled diagram of moiré interferometry experimental test-set up

Before the specimens were statically loaded in the moiré interferometry experimental set-up, several steps were taken for final preparation. First, excess diffraction grating fringes were removed from the top and bottom edges of the specimens using sand paper on a glass surface. The purpose of removing excess fringe was to make

sure the edge of the grating was flush with the edge of the specimen, so that all experimental data obtained would correspond to an exact location on the specimen. Next, a mark on the top of each specimen was used to indicate the entire region of repair, as the diffraction grating made it difficult to see exactly where the adhesive repair ended on each specimen.

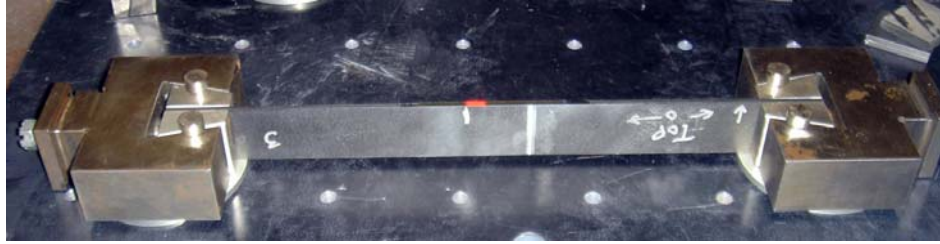


Figure 67. Clamping specimen prior to placing in load fixture.

Before placing the specimen in the load fixture, screw driven wedge grips with magnetic wedges were used to clamp the specimen as shown in Figure 67. After placing the specimen in the load fixture, the full range of motion over the entire region of repair was determined by traversing the movable load fixture across the view of the camera (Figure 68). Overall, it was concluded that five different segments of the stepped-lap and scarf repair would have to be photographed in order to create a full panoramic image of the stepped-lap and scarf repair regions.



Figure 68. Load fixture mount for moiré interferometry.

After fixing the stepped-lap specimen into the load fixture, null field fringe patterns were photographed at a tensile load of 5lbf. The small load was kept on the specimen throughout test set-up and initial calibration to ensure that it would not slip out of the clamps. After five (5) sets of null field fringe patterns were photographed across the bonded region at a negligible load, the specimen was given a static tensile load of 2000N (450lbf). The load fixture can be seen in Figure 69. Appendix C describes the methodology and testing completed to determine this load. Five (5) more sets of fringe pattern images were then photographed. This same procedure was used in acquiring data from the scarf specimen.



Figure 69. Fixture used to apply tensile load.

Fringe patterns were obtained both in the x -direction (across the width) and z -direction (through specimen thickness). This was done by changing the orientation of the collimated light refracting off the specimen grating. As shown in Figure 70, beams of light interacting with the grating could be controlled by blocking light with the removable wooden tabs surrounding the lens. By placing the tabs in two basic configurations, a combination of light could pass to produce a desired fringe pattern. For example, to photograph fringe patterns showing displacement in the x -direction, the wooden tabs to the left and right of the lens would be removed. This would allow focused light to refract off the specimen grating at angles from the left and from the right sides (as seen in the picture). To obtain fringe patterns showing displacement in the z -direction, the wooden tabs to the top and bottom of the lens would be removed. This would allow focused light to refract off the specimen grating at angles from the top and bottom.

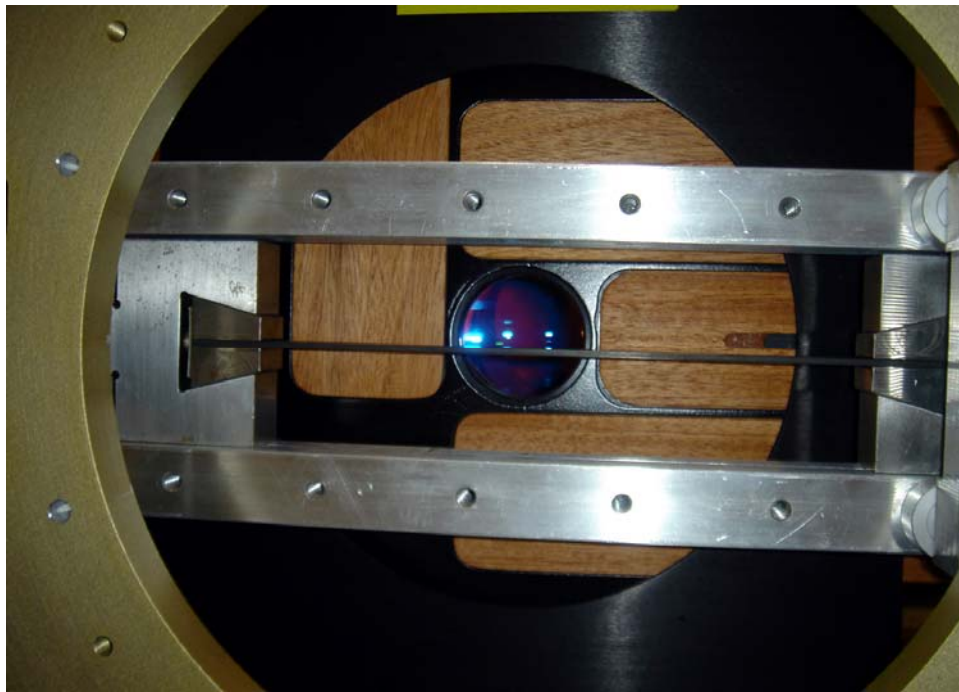


Figure 70. Tabs used to obtain desired fringe patterns.

Experimental strain data was extracted from the fringe patterns using a non-commercialized fringe pattern analysis code. This computer program essentially takes the fringe patterns and uses a light intensity scale to convert changes in fringes between photographs into displacements and then strains. This program has the ability to remove discontinuities in fringe pattern data sets that are a result of the “ 2π ” type ambiguities associated with data sets attained using sinusoidal functions. The matrices of data produced using the fringe pattern analysis code were then exported to a program called Transform, where the data could be converted again and visualized as a two-dimensional color coded strain map.

Dr. David Mollenhauer, an expert in moiré interferometry who works in the Air Force Research Laboratories at Wright Patterson Air Force Base, converted the photographed fringe patterns into strain data sets accessible in Transform (a software package). As part of this process, he “stitched” the fringe patterns taken at five different locations together to create a panoramic set of data stretching the entire length of both repairs. Figure 71 provides an example of three stitched fringe patterns from the stepped-lap specimen.

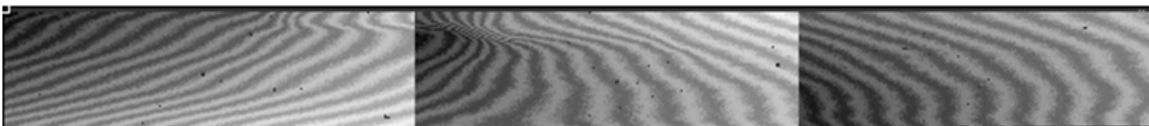


Figure 71. Stitching together of fringe patterns.

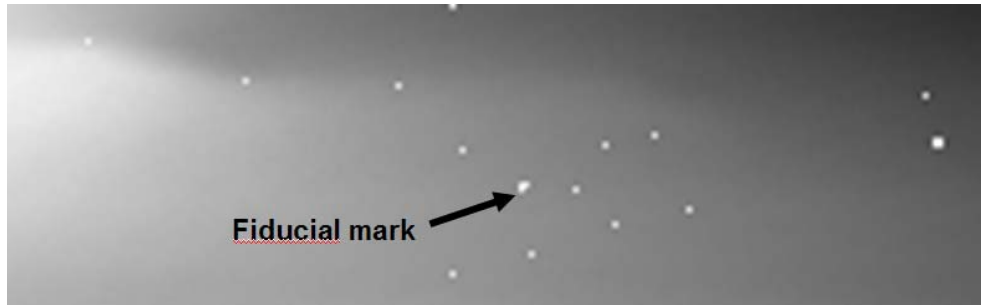


Figure 72. Example of fiducial mark on diffraction grating

To accomplish this, he used “fiducial” marks as reference points to match up overlapping fringe patterns. Fiducial marks are basically imperfections, such as a bubble, in the diffraction grating that are unique in shape and appearance and can be used to line up images (Figure 72). Because too few fiducial marks were present on the scarf specimen’s diffraction grating to line up all the fringe patterns, distinguishing marks were made on the top edge of the scarf specimen at 5mm intervals. These marks were made by taking a thin spring loaded wire and traversing the specimen in the load fixture until the tension in the spring became too high at which point it would nick or scratch the diffraction grating at the top edge of the specimen. There were a sufficient number of fiducial marks in the on the stepped-lap specimen to stitch the displacement fringe patterns together.

Generation of Plots

To produce the full-field strain images, data obtained from both the BSAM models and moiré interferometry was converted into Transform data files containing matrices of data representing strain information over the entire region of both repairs. Transform is a software package that can create images and plots from 2D data arrays. A screen capture of a data matrix in Transform can be seen in Figure 73. Full-field strain

images of the stepped-lap and scarf joint were then generated in Transform, as shown in Figure 74. When viewing one of the full-field strain images produced in Transform, the user is essentially looking at a large two-dimensional data matrix, where values are represented by a color map.

		-17.79875	-17.79384	-17.78893	-17.78402	-17.77911	-17.77420	-17.76929	-17.76438
1.12685	2.124e-005	2.152e-005	2.206e-005	2.287e-005	2.392e-005	2.518e-005	2.663e-005	2.825e-005	
1.12194	2.156e-005	2.184e-005	2.239e-005	2.321e-005	2.426e-005	2.554e-005	2.701e-005	2.865e-005	
1.11703	2.219e-005	2.248e-005	2.305e-005	2.388e-005	2.496e-005	2.627e-005	2.777e-005	2.944e-005	
1.11212	2.315e-005	2.344e-005	2.403e-005	2.489e-005	2.600e-005	2.735e-005	2.890e-005	3.062e-005	
1.10721	2.442e-005	2.472e-005	2.533e-005	2.623e-005	2.739e-005	2.879e-005	3.040e-005	3.219e-005	
1.10230	2.600e-005	2.632e-005	2.696e-005	2.789e-005	2.911e-005	3.058e-005	3.227e-005	3.414e-005	
1.09739	2.790e-005	2.824e-005	2.891e-005	2.989e-005	3.117e-005	3.271e-005	3.449e-005	3.646e-005	
1.09248	3.010e-005	3.046e-005	3.117e-005	3.221e-005	3.356e-005	3.519e-005	3.707e-005	3.915e-005	
1.08757	3.262e-005	3.300e-005	3.375e-005	3.485e-005	3.628e-005	3.800e-005	3.998e-005	4.218e-005	
1.08266	3.545e-005	3.585e-005	3.664e-005	3.780e-005	3.931e-005	4.114e-005	4.324e-005	4.556e-005	
1.07775	3.858e-005	3.900e-005	3.984e-005	4.107e-005	4.267e-005	4.460e-005	4.682e-005	4.928e-005	
1.07284	4.202e-005	4.247e-005	4.335e-005	4.466e-005	4.634e-005	4.838e-005	5.072e-005	5.332e-005	
1.06793	4.578e-005	4.625e-005	4.718e-005	4.855e-005	5.033e-005	5.248e-005	5.495e-005	5.768e-005	
1.06302	4.984e-005	5.034e-005	5.132e-005	5.276e-005	5.463e-005	5.688e-005	5.948e-005	6.235e-005	
1.05811	5.422e-005	5.474e-005	5.577e-005	5.728e-005	5.924e-005	6.160e-005	6.432e-005	6.732e-005	
1.05320	5.893e-005	5.947e-005	6.054e-005	6.212e-005	6.416e-005	6.663e-005	6.946e-005	7.260e-005	
1.04829	6.396e-005	6.453e-005	6.564e-005	6.728e-005	6.941e-005	7.197e-005	7.492e-005	7.818e-005	
1.04338	6.934e-005	6.992e-005	7.107e-005	7.277e-005	7.497e-005	7.763e-005	8.068e-005	8.406e-005	
1.03847	7.505e-005	7.565e-005	7.685e-005	7.860e-005	8.087e-005	8.361e-005	8.676e-005	9.025e-005	
1.03356	8.113e-005	8.174e-005	8.297e-005	8.477e-005	8.711e-005	8.993e-005	9.316e-005	9.675e-005	
1.02865	8.757e-005	8.820e-005	8.945e-005	9.130e-005	9.369e-005	9.658e-005	9.990e-005	1.036e-004	
1.02374	9.438e-005	9.503e-005	9.631e-005	9.820e-005	1.006e-004	1.036e-004	1.070e-004	1.107e-004	
1.01883	1.016e-004	1.023e-004	1.036e-004	1.055e-004	1.080e-004	1.109e-004	1.144e-004	1.182e-004	
1.01392	1.092e-004	1.099e-004	1.112e-004	1.131e-004	1.157e-004	1.187e-004	1.222e-004	1.260e-004	
1.00901	1.172e-004	1.179e-004	1.192e-004	1.212e-004	1.237e-004	1.268e-004	1.303e-004	1.342e-004	
1.00410	1.257e-004	1.264e-004	1.277e-004	1.297e-004	1.322e-004	1.353e-004	1.389e-004	1.428e-004	
0.99919	1.346e-004	1.352e-004	1.366e-004	1.386e-004	1.412e-004	1.443e-004	1.478e-004	1.518e-004	
0.99428	1.439e-004	1.446e-004	1.459e-004	1.479e-004	1.505e-004	1.536e-004	1.572e-004	1.612e-004	
0.98937	1.536e-004	1.543e-004	1.557e-004	1.577e-004	1.603e-004	1.634e-004	1.670e-004	1.710e-004	
0.98446	1.639e-004	1.645e-004	1.659e-004	1.679e-004	1.705e-004	1.736e-004	1.772e-004	1.812e-004	
0.97955	1.745e-004	1.752e-004	1.766e-004	1.786e-004	1.811e-004	1.843e-004	1.879e-004	1.919e-004	
0.97464	1.856e-004	1.863e-004	1.877e-004	1.897e-004	1.922e-004	1.954e-004	1.990e-004	2.029e-004	
0.96973	1.972e-004	1.978e-004	1.992e-004	2.012e-004	2.038e-004	2.069e-004	2.105e-004	2.145e-004	
0.96482	2.091e-004	2.098e-004	2.112e-004	2.131e-004	2.157e-004	2.188e-004	2.224e-004	2.264e-004	
0.95991	2.215e-004	2.222e-004	2.235e-004	2.255e-004	2.281e-004	2.312e-004	2.348e-004	2.388e-004	
0.95500	2.343e-004	2.349e-004	2.363e-004	2.383e-004	2.409e-004	2.440e-004	2.476e-004	2.516e-004	

Figure 73. Screen capture of moiré data set in Transform.

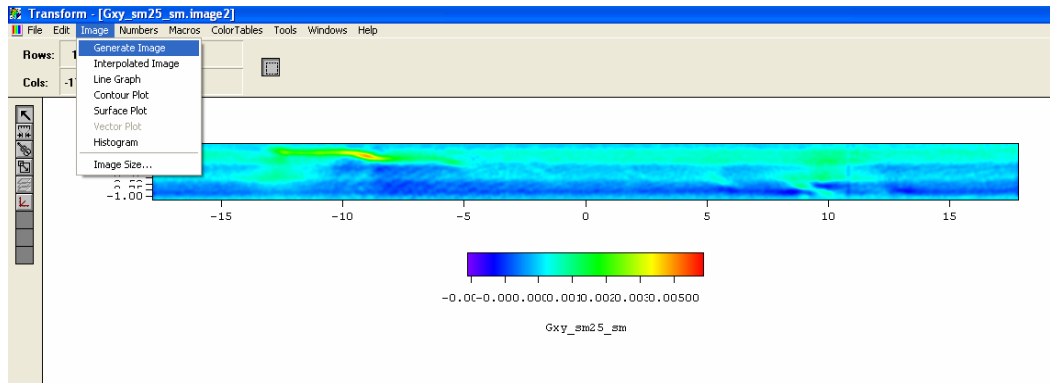


Figure 74. Screen capture of image being generated in Transform.

During the generation of these images, one major problem was encountered: for both the stepped-lap and scarf joint, the area modeled in BSAM was slightly smaller than the area that the experimental data covered. The result: the experimental data set was larger than the BSAM data set. This meant that the results could not be directly overlaid because the bond-lines did not line up when the images were superimposed upon one another.

To solve this problem, exact dimensions for the moiré and BSAM data matrices were needed to determine how much the BSAM data set would have to be shifted to line up with the moiré data set. An extensive explanation of this process is included in the following paragraphs for the scarf specimen, followed by a brief mathematical summary for the stepped-lap specimen. Overall, it was determined that 641 columns and 39 rows of null data needed to be added to the BSAM scarf data set, while 337 columns and 2 rows of null data needed to be added to the BSAM stepped-lap data set.

For the scarf specimen, the moiré data matrix was 494 rows (pixels) by 8680 columns (pixels). Moire data spanned 42.52692mm (1.674in) along the x-axis (across the width of the specimen) and 2.41569mm (0.0951in) through the thickness (z-axis). Dividing the range of data in the z-direction (2.41569mm) by the number of pixels in the

z-direction, it could be determined that each pixel was 0.0049mm (0.0049mm/pixel) in the z-direction. Dividing the range of data in the x-direction (42.52692mm) by the number of pixels in the x-direction (8680), it could be determined that each pixel was 0.0049mm (0.0049mm/pixel) in the x-direction.

Using the size of each pixel, the number of rows and columns that needed to be added to the BSAM data set could be calculated. The area modeled in BSAM for the scarf specimen was 39.389304mm (1.55076in) in the x-direction by 2.225548mm (0.08762in) in the z-direction, slightly smaller than the dimensions of the moiré data set. To match the resolution of the data sets in moiré, the dimensions of the BSAM model were divided by the size of each pixel (0.0049mm). This resulted in a strain matrix 455 rows by 8039 columns, compared to the moiré data matrix which was 494 rows by 8680 columns. Because the moiré data set was 641 columns wider and 39 rows thicker than the BSAM data set, that number of null (0) rows and columns had to be added to the BSAM data set in order precisely match the size and to line up the two sets of data.

Using the same process for the stepped-lap specimen, it was determined that 2 rows and 337 columns needed to be supplemented to the BSAM data set to equal the size of the moiré data set. This process is shown below:

Moiré data set (stepped-lap specimen)

$$\text{Size: } 460 \text{ (rows) by } 7250 \text{ (columns) pixels} \quad (33)$$

$$\text{Column: } x\text{-total} = 17.79875\text{mm} + 17.79499\text{mm} = 35.59374\text{mm} \quad (34)$$

$$\frac{35.59374\text{mm}}{7250\text{pixels}} = 0.00491\text{mm} / \text{pixel}$$

$$\text{Row: } z\text{-total} = 1.12685\text{mm} + 1.12685\text{mm} = 2.25369\text{mm} \quad (35)$$

$$\frac{2.25369mm}{460pixels} = 0.00491mm / pixel \quad (36)$$

BSAM data set (stepped-lap specimen)

Column: $x-total = 5.66412in - 4.32775in = 33.943798mm (1.33637in)$ (37)

$$\frac{33.943798mm}{0.00491mm / pixel} = 6913pixels \quad (38)$$

Row: $z-total = 0.08838in = 2.244852mm$ (39)

$$\frac{2.244852mm}{0.00491mm / pixel} = 458pixels \quad (40)$$

Size: 458 (rows) by 6913 (columns) pixels (41)

of additional columns needed for BSAM data set $= 7250 - 6913 = 337$ (42)

of additional rows needed for BSAM data set $= 460 - 458 = 2$ (43)

After going through these numbers, the BSAM data sets were shifted appropriately in the x-direction and z-direction so that the modeled bond-line lined up with the experimental bond-line. This was done for both the stepped-lap and scarf joint. To accomplish this, a null (0) matrix was inserted in either side of the BSAM results until the experimental bond-line matched up with the modeled bond-line. These “correction” matrices can be seen in either side of the full-field strain images, as indicated by the strips of solid color on the outside the BSAM strain images containing no strain variation (Figure 75).

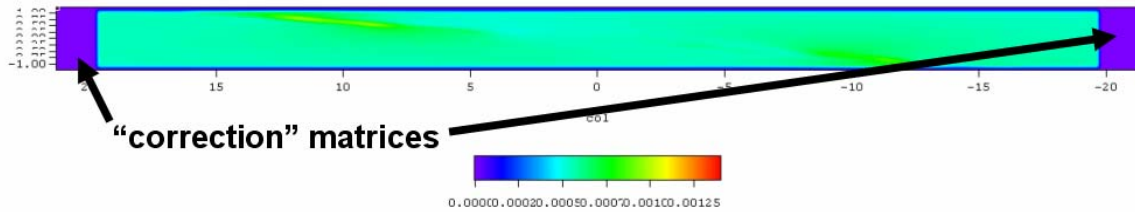


Figure 75. Shifted BSAM data set.

In addition to shifting the BSAM data sets, one other minor problem was encountered. The experimental scarf specimen orientation was different from the orientation modeled in BSAM. To reorient the experimental data set with the BSAM model, the moiré data set was “flipped” to match the modeled data set. This was achieved by performing a row flip and column flip execution in Transform.

To extract data at specific x-locations for the generation of line plots, data was extracted from the Transform file and opened and plotted using Microsoft Excel. This was done by highlighting the desired column, selecting the “numbers” tab from the menu, and selecting the “extract selection” option. Although data was saved in a textbook format, it could be opened and plotted using Excel.

In summary, data from the experimental test runs and BSAM computer program results were converted into Transform files. From these data files, full field strain images were generated and data at specific x-locations was extracted to make line plots in Microsoft Excel. This process yielded two problems. First of all, moiré data sets were larger than the size of the BSAM data sets, preventing an accurate comparison of corresponding strain fields. To solve this problem, the BSAM data set was shifted slightly in both the x-direction and z-direction through the use of “correction” matrices. Also, since the experimental orientation of the scarf specimen was different than that of the BSAM model, the moiré data set was “flipped” to realign the data.

V. Results and Analysis

This chapter compares the results from the BSAM models to experimental data obtained through moiré interferometry. Strain fields of three sets of data were produced and compared for both joints, including: (1) strain in the x-direction (ϵ_x), (2) strain in the z-direction (ϵ_z), and (3) shear strain in the x-z plane (γ_{xz}). Full-field strain images of these strain components can be seen for both the stepped-lap and scarf joint in this chapter. Overall, results from both BSAM models demonstrated strong correlation to experimental data. There was better correlation between the experimental and modeled scarf joint data than the stepped-lap data.

Full-field Strain Images

The images produced by Transform are essentially color-coded strain maps, in which a given color indicates a defined range of strain values. The range of strain for each figure is defined in its respective caption. It is important to note that the *final* sets of both experimental and numerical data were smoothed 250 times in Transform. Figure 76 shows the coordinate system defined for subsequent plots.

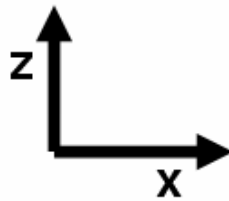


Figure 76. Coordinate system defined for full-field strain images.

Stepped-Lap Joint

Full-field strain images for the stepped-lap joint can be seen in Figure 77, Figure 79, and Figure 81. For these figures, the top image represents the strain field predicted by the BSAM computer program, while the bottom image represents the experimental

strain field found using moiré interferometry. Figure 77 shows a comparison of modeled and experimental strain in the x-direction (ϵ_x), Figure 79 shows a comparison of strain in the z-direction (ϵ_z), and Figure 81 shows a comparison of shear strain in the x-z plane (γ_{xz})

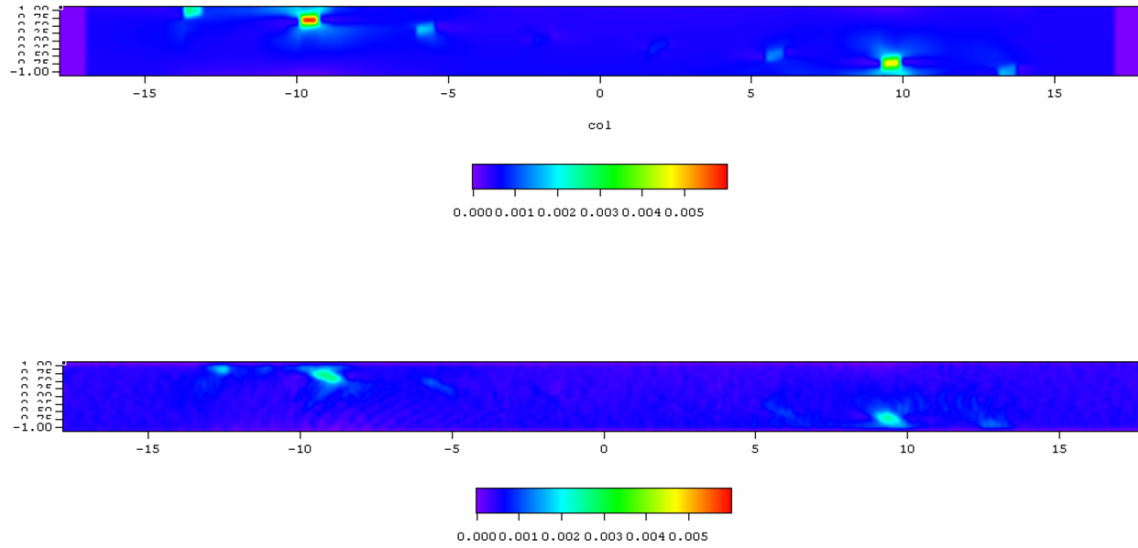


Figure 77. BSAM (top) and moiré (bottom) full field strain (ϵ_x) images of stepped-lap joint ($0 < \epsilon_x < 0.006$).

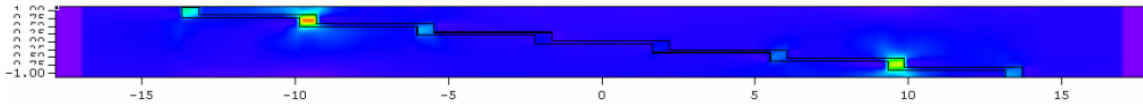


Figure 78. Overlap of stepped-lap bond-line contour onto BSAM strain (ϵ_x) field.

As Figure 77 illustrates, the BSAM strain (ϵ_x) field shows a good correlation to the experimental strain (ϵ_x) field. Both strain fields indicate a spike in strain in the x-direction approximately $\pm 9.6\text{mm}$ from the z-axis of the repair, although the peak magnitude of strain appears much higher in the BSAM model. By overlapping a contour image of the bond-line over the corresponding location on the BSAM strain field (Figure

78), it is evident that this spike in strain occurs at the step where the 0° plies interface in both the BSAM strain field and experimental results. There is also a smaller strain intensity present in both strain fields at about $\pm 13.5\text{mm}$ from the z-axis, or the step corresponding to the $+45^\circ$ plies.

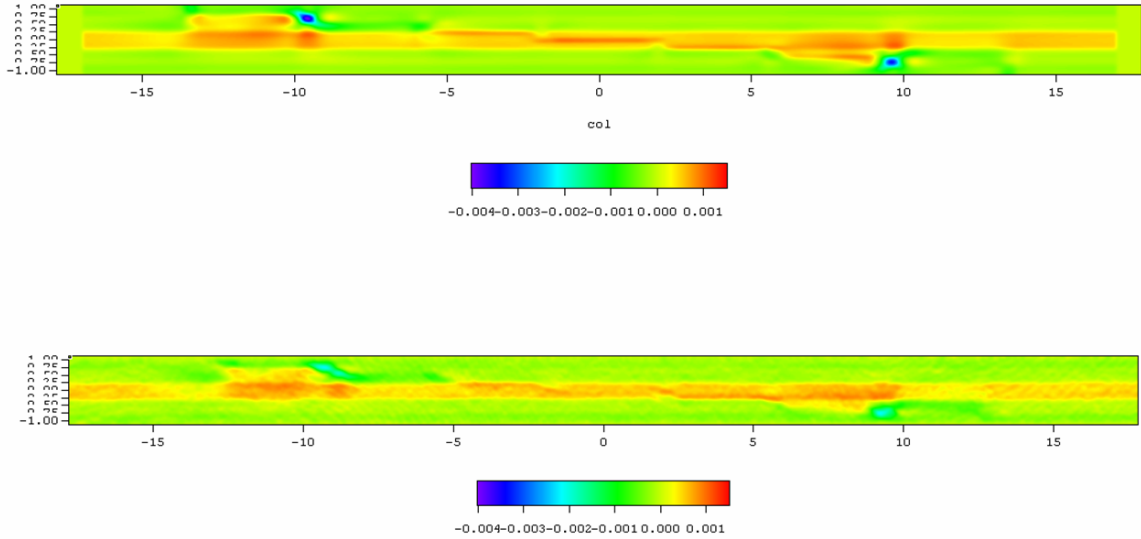


Figure 79. BSAM (top) and moiré (bottom) full field strain (ϵ_z) images of stepped-lap joint
($-0.004 < \epsilon_z < 0.0015$)

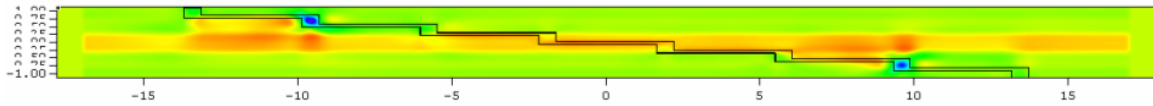


Figure 80. Overlap of stepped-lap bond-line contour onto BSAM strain (ϵ_z) field.

Figure 79 shows BSAM and experimental full field strain images for strain in the z-direction (ϵ_z). Visual inspection of the images again reveals a strong correlation in mechanical behavior between the modeled and experimental strain data. As the strain fields show, a positive strain in the z-direction is indicated through the 90° or middle plies of the laminate across the repair, while there are two negative peaks of strain (ϵ_z) in the

area of the bond-line corresponding to the 0° plies (Figure 80). However, the peak magnitude of strain again appears to be higher in the BSAM model when compared to experimental data, as indicated by the darker shade of blue in the bond-line at the intersection of the 0° plies.

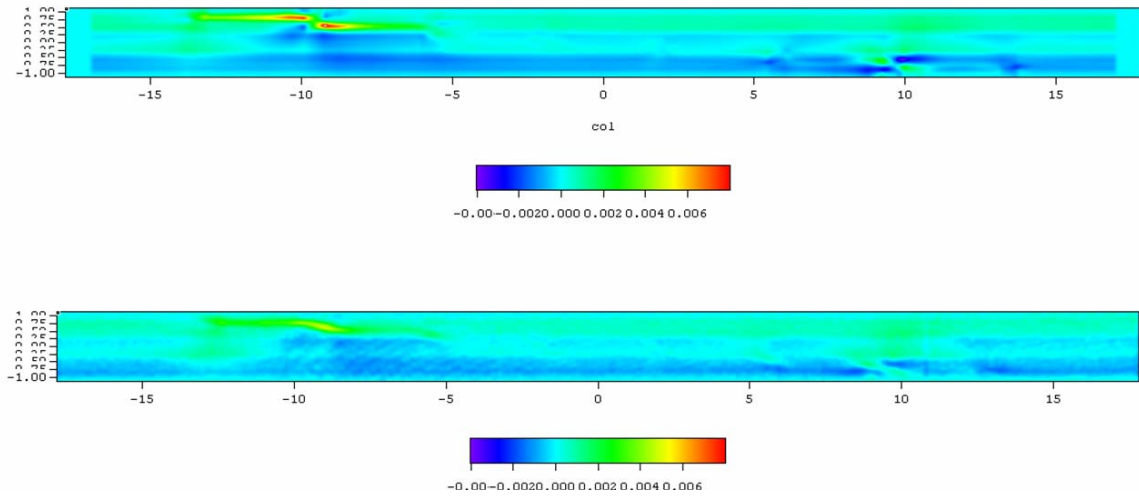


Figure 81. BSAM (top) and moiré (bottom) full field shear strain (γ_{xz}) images of stepped-lap joint

$$(-0.004 < \gamma_{xz} < 0.008)$$

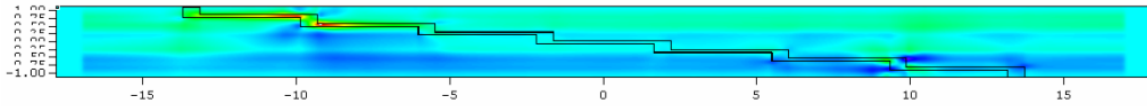


Figure 82. Overlap of stepped-lap bond-line contour onto BSAM shear strain (γ_{xz}) image.

Another strong correlation in experimental and modeled strain fields can be seen in Figure 81. The shear strain in the x-z plane not only has a range magnitude twice that of the other strain components, but also shows a great deal of similarity. For example, both strain fields reflect a shaded region of negative shear in the lower region of the cross-section of the specimen, while experiencing positive shear on the upper half of the

specimen. Once again, however, the peak magnitude of shear strain appears to be higher in the BSAM model than from experimental data. The bond-line through this strain component can be seen in Figure 82.

Scarf Joint

A similar qualitative comparison can be made with strain fields from the scarf joint, shown in Figure 83, Figure 84, and Figure 85. Like the stepped-lap strain images, the scarf strain fields showed remarkable similarities, with the shear strain component comparing most favorably. Unlike the stepped-lap strain images, the peak magnitudes of strain appear to match more closely between the predicted and experimental strain components for the scarf joint. This is especially evident in Figure 85.

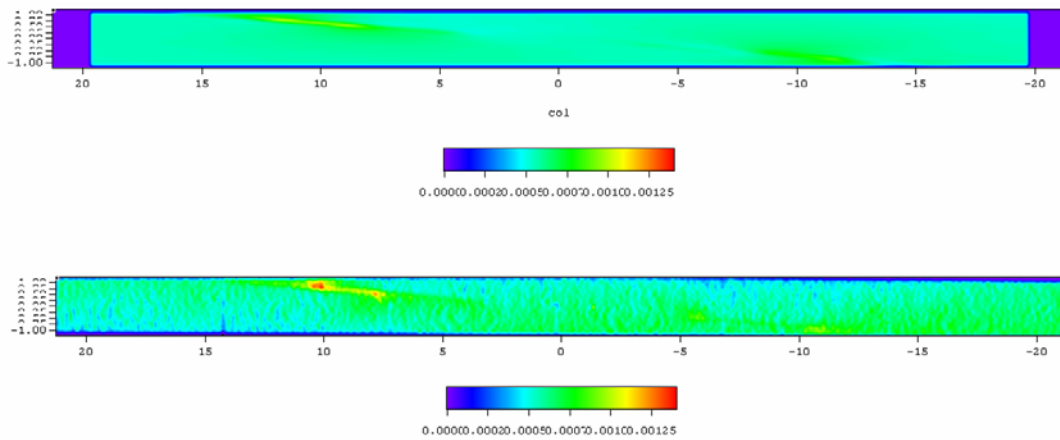


Figure 83. BSAM (top) and moiré (bottom) full field strain (ϵ_x) images of scarf joint ($0 < \epsilon_x < 0.0014$)

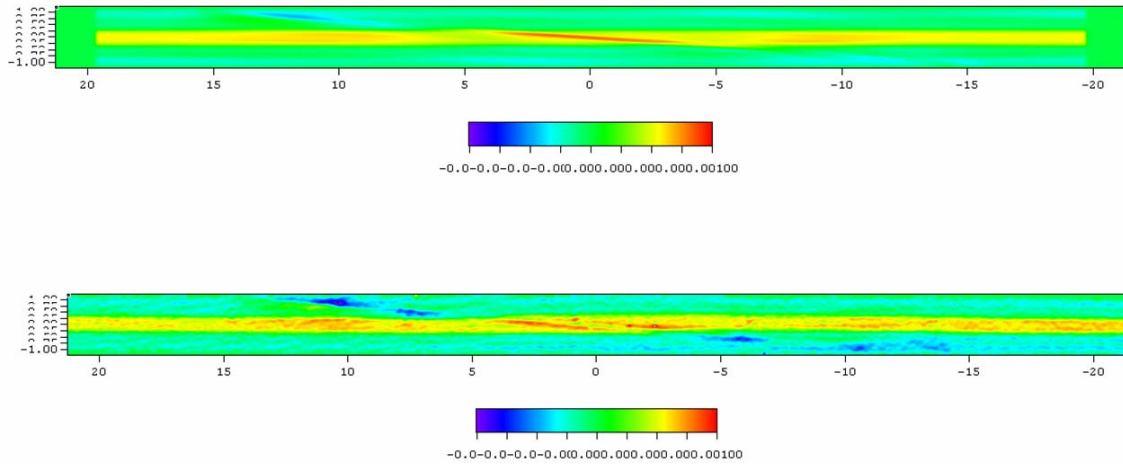


Figure 84. BSAM (top) and moiré (bottom) full field strain (ϵ_z) images of scarf joint

$$(-0.001 < \epsilon_z < 0.001)$$

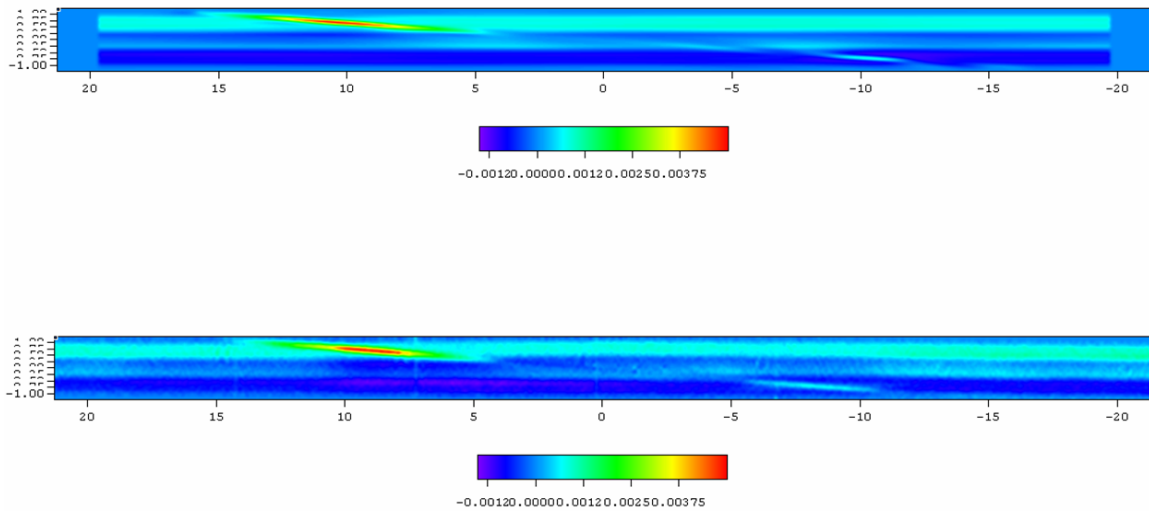


Figure 85. BSAM (top) and moiré (bottom) full field shear strain (γ_{xz}) images of scarf joint

$$(-0.0015 < \gamma_{xz} < 0.005)$$

Analysis of Results

To more accurately assess resultant strain fields, BSAM and moiré strain data was extracted from Transform at various corresponding x-locations and plotted against one

another. For the following line plots, the ranges of strain data are identical to the ranges of strain data in corresponding full-field strain images.

Line Plots: Stepped-Lap Joint

To get an initial idea of the correlation between the raw data predicted and experimental results, values of the three (3) strain components through the specimen thickness were extracted from Transform at the 5mm intervals across the region of the repair. These locations were: -15mm, -10mm, -5mm, 0mm, 5mm, 10mm, and 15mm (Figure 86). Line plots were made at 5mm intervals to obtain an overall comparison between the BSAM model and experimental results across the entire region of the repair. For all line plots, moiré data is represented in red while predicted BSAM values are shown in blue.

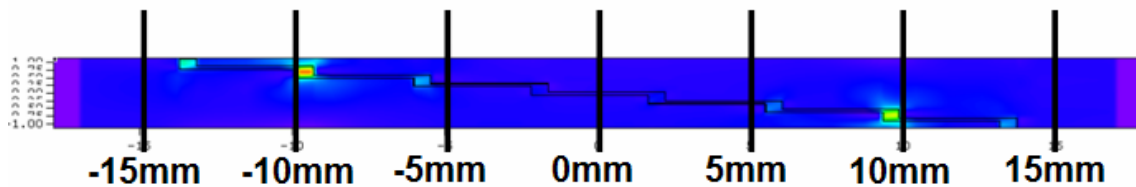


Figure 86. x-location of extracted stepped-lap strain data for line plots.

Initial correlation between modeled and experimental values was decent, but not conclusive. Initial line plots of the three strain components at $x = 0\text{mm}$ are shown in Figure 87, Figure 88, and Figure 89. The trends exhibited in plots at this x-location were representative of all of the initial line plots generated. No smoothing was done before initial plotting. As evident by these plots, general trends in the data sets corresponded but there was a fair amount of discrepancy in the behavior of the moiré and BSAM data. A complete set of preliminary line plots can be found in Appendix D.

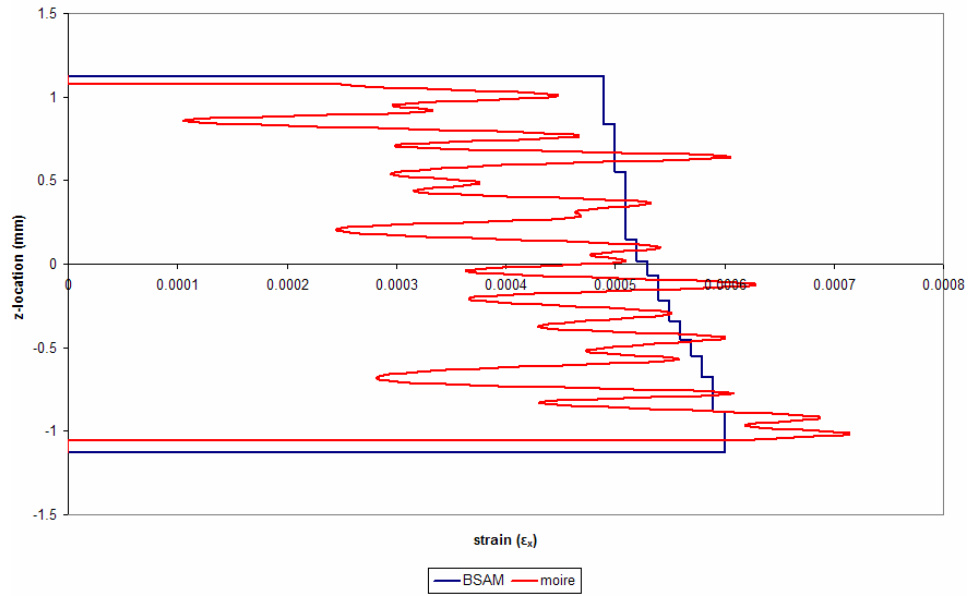


Figure 87. Stepped-Lap Joint: strain distribution (ϵ_x) through specimen thickness (z) at $x = 0\text{mm}$ (data not smoothed)

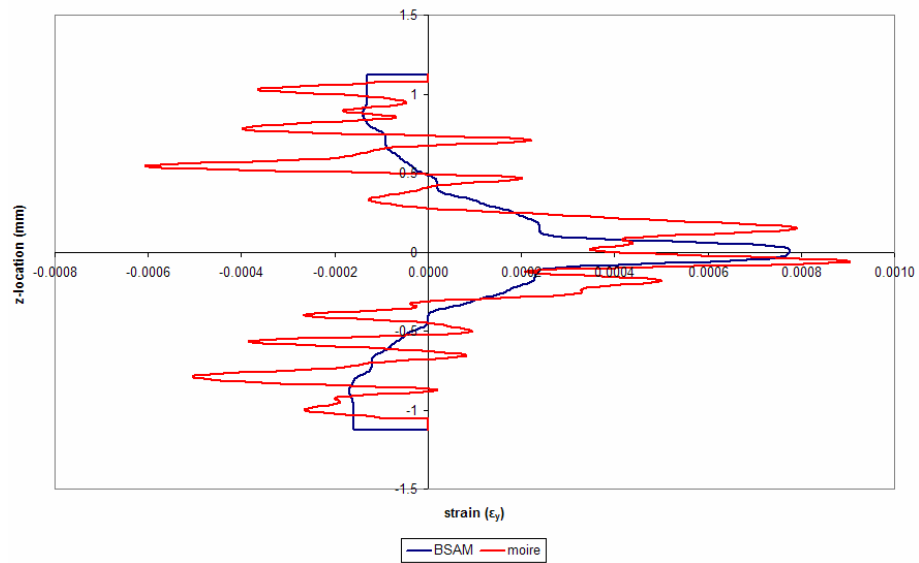


Figure 88. Stepped-Lap Joint: strain distribution (ϵ_y) through specimen thickness (z) at $x = 0\text{mm}$ (data not smoothed)

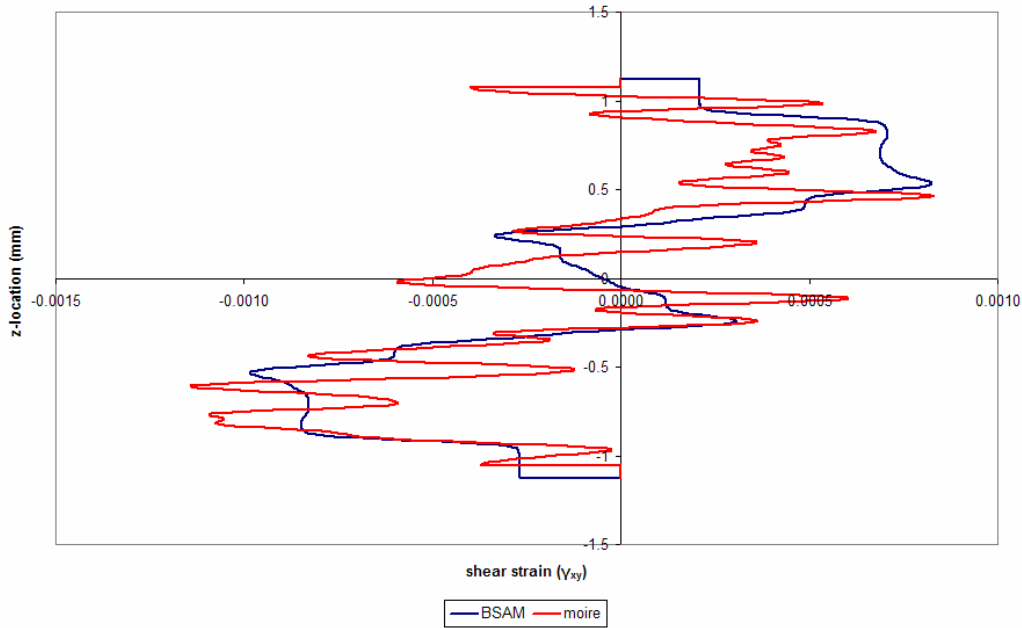


Figure 89. Stepped-Lap Joint: shear strain distribution (γ_{xy}) through specimen thickness (z) at

x = 0mm (data not smoothed)

After inspection of these initial plots, two steps were taken to attain a better comparison: (1) a refinement of the BSAM model and (2) smoothing of data sets. First of all, the degrees of polynomials used in the BSAM model were increased. The stepped-lap model in BSAM used linear basis functions during primary analysis. It was thought that this might explain the “blocky” behavior of the x-component of strain apparent in Figure 87 and the failure of BSAM to predict more of the “peaks” and “valleys” of strain seen in the moiré data. To create a model that would more accurately predict the strains, quadratic splines were used in the refined model instead of linear functions. Since the initial BSAM model already pushed the limits of the available computer memory with its complexity (80,000 degrees of freedom), the discretization was also altered to compensate for the addition of quadratic splines. While the preliminary discretization

was symmetric about the x-z plane, the refined discretization was biased toward the side of interest. It was thought that this might alter the strain intensities of that side, but it was necessary for the computer to be able to process the model. Figure 90 shows the refined discretization for the stepped-lap model.

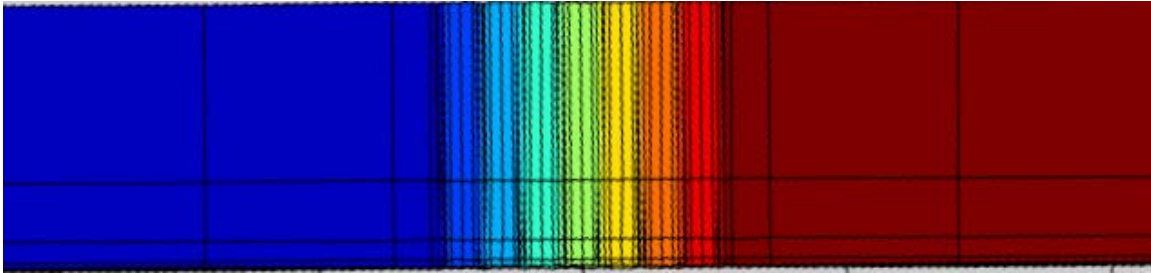


Figure 90. Refined discretization of BSAM stepped-lap model.

In addition to modifying the BSAM input file, the data sets produced by the new BSAM model and moiré were smoothed 250 times in Transform. It was thought that smoothing the data would eliminate any extraneous strain fluctuations or experimental noise in moiré data, while also allowing for a better comparison of trends between the predicted and experimental strains. Figure 91 illustrates the effect of smoothing in Transform. According to the Transform User's Guide and Reference Manual, smoothing is done by averaging every point with its eight neighbors. This process is repeated for the specified number of passes. An appropriate number of smoothing passes was determined to be 250 times, as this number of passes reduced any high frequency noise and phase errors that occurred during experimental data reduction, while also maintaining general trends in the data. This number of smoothing passes used in this study was not based off of an established procedure or prior experience; it was determined to be appropriate only in the context of this specific analysis. This is evident in Figure 91. In the figure, original data is indicated by the "no smooth" line.

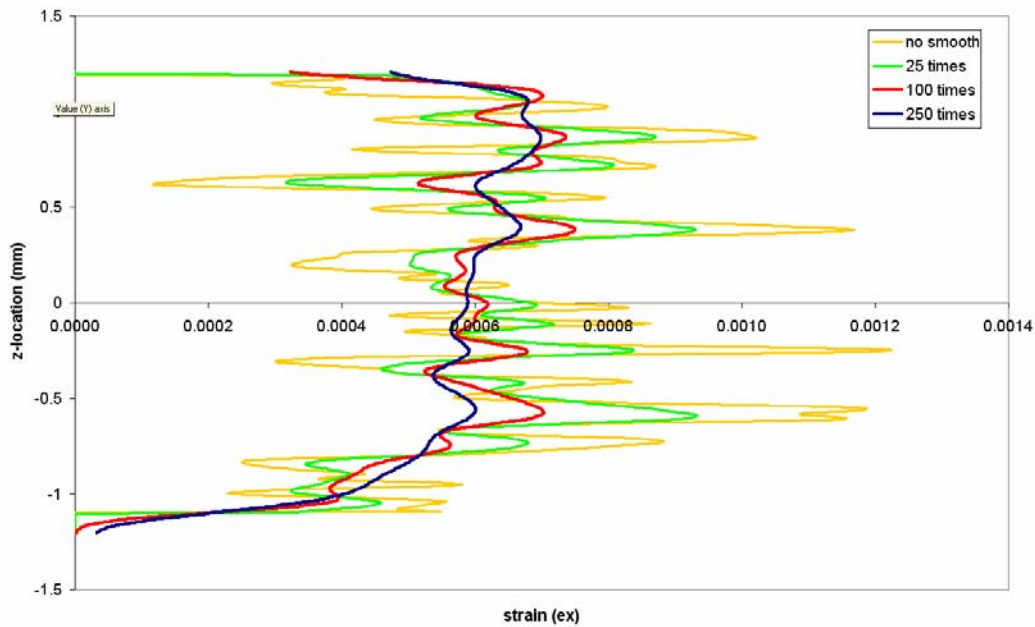
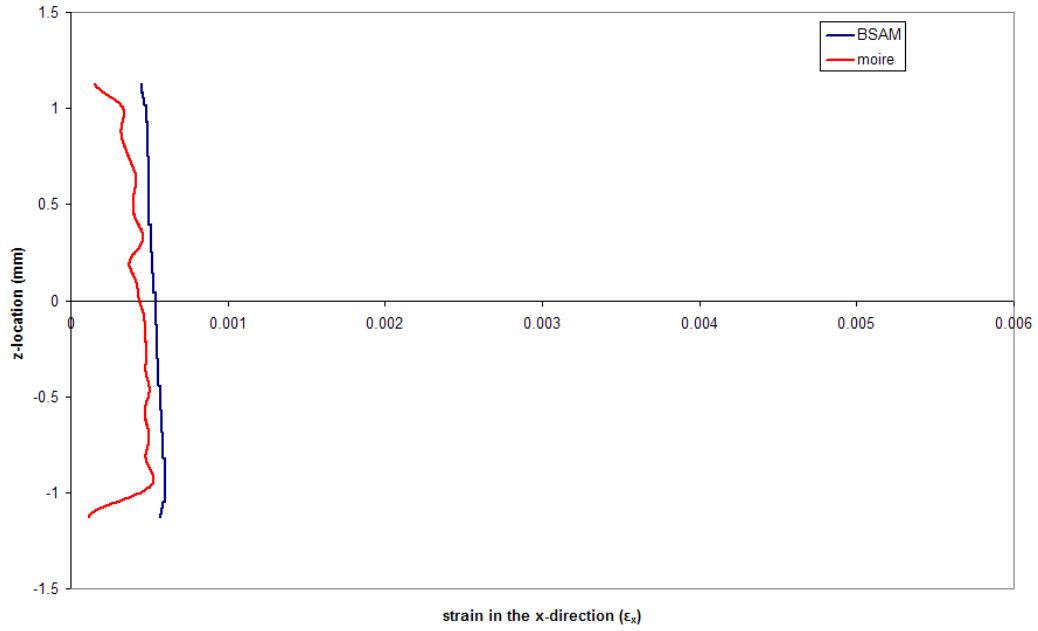


Figure 91. Effect of smoothing on data.

After (1) BSAM input files were refined and re-processed and (2) moiré data sets were smoothed, a second iteration of line plots was created. The correlation between modeled and experimental values in the revised plots was excellent for all three strain components through the entire thickness of the specimen. Refined line plots of the three strain components are shown at x-locations of 0mm and 5mm respectively in Figure 92 through Figure 97. A complete set of refined line-plots can be found in Appendix E.

After inspecting the line plots created at these locations, it was concluded that the predicted and experimental strains compared favorably throughout the thickness at x-locations away from vertical steps in the adhesive bond-line. Data from plots taken at -15mm, -5mm, 0mm, 5mm, and 15mm showed excellent correlation through the entire thickness of the specimen, as the respective figures in Appendix E indicate. They provide a representative example of the strong correlation between the experimental and

modeled results, in which both the magnitude and behavior of strain through the thickness is nearly identical.



**Figure 92. Stepped-lap Joint: strain (ϵ_x) through thickness (z) at $x = 0\text{mm}$
(data smoothed 250 times)**

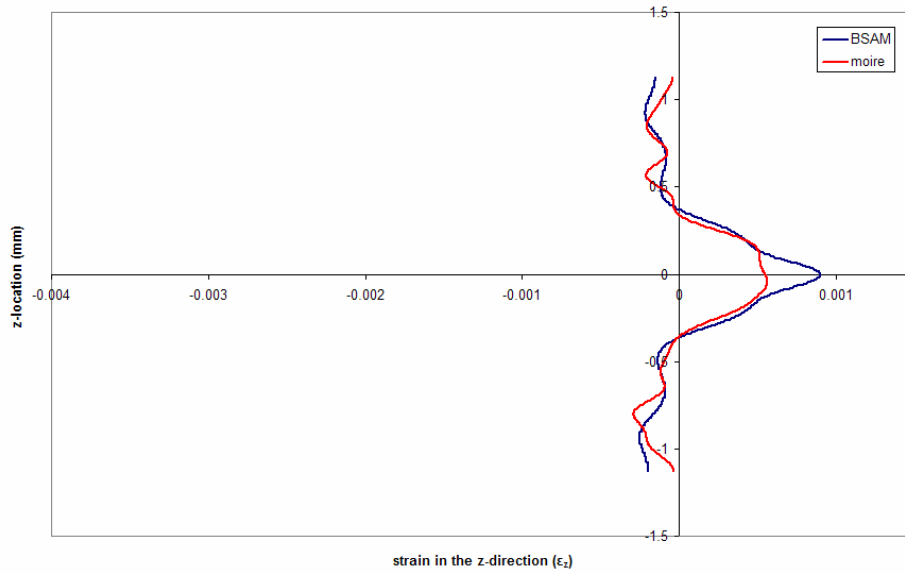


**Figure 93. Stepped-lap Joint: strain (ϵ_z) through thickness (z) at $x = 0\text{mm}$
(data smoothed 250 times)**

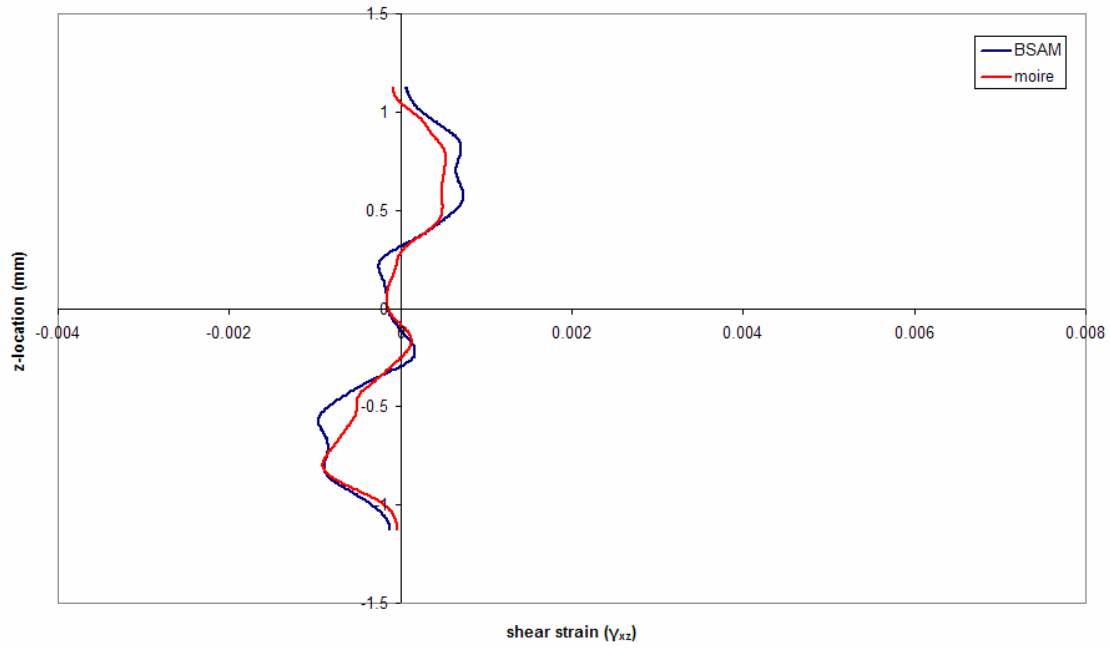


Figure 94. Stepped-lap Joint: shear strain (γ_{xz}) through thickness (z) at $x = 0\text{mm}$
(data smoothed 250 times)

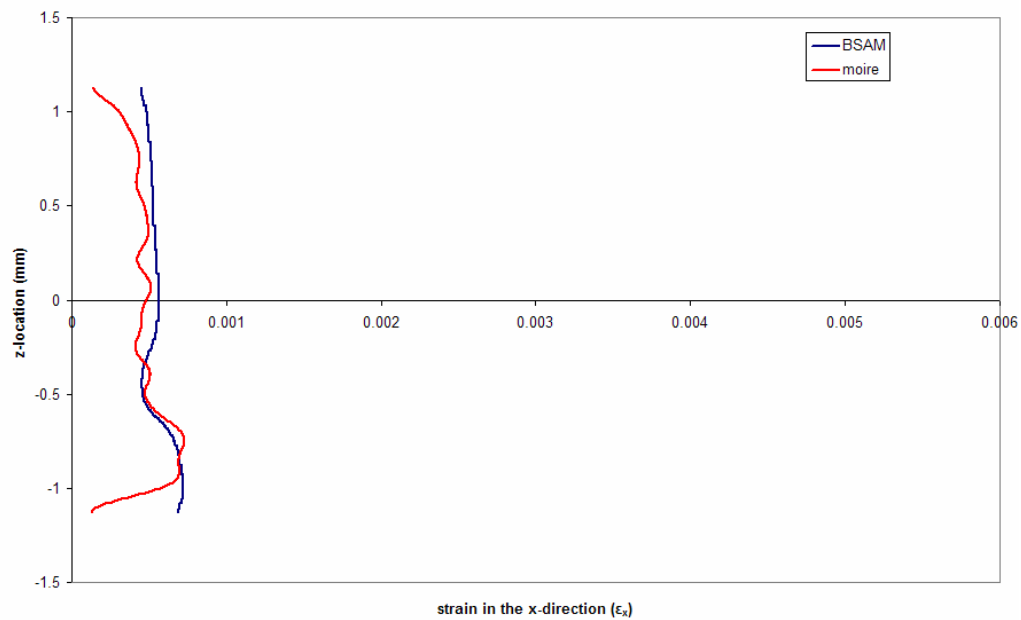


Figure 95. Stepped-lap Joint: strain (ϵ_x) through specimen thickness (z) at $x = 5\text{mm}$
(data smoothed 250 times)

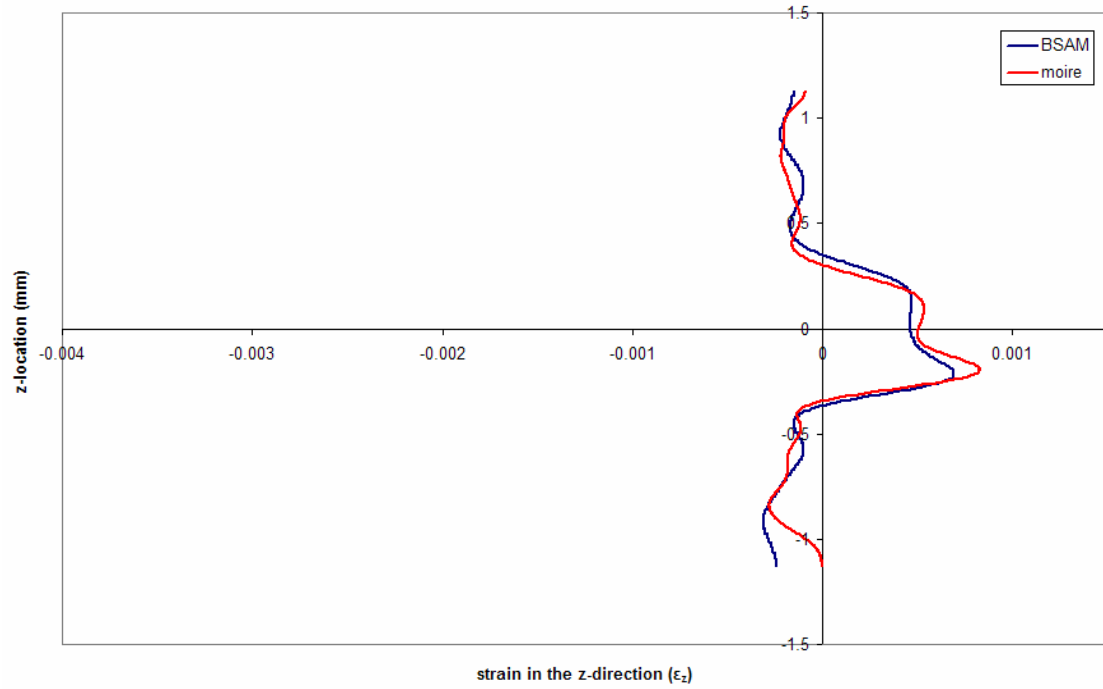


Figure 96. Stepped-lap Joint: strain (ϵ_z) through specimen thickness (z) at $x = 5\text{mm}$
(data smoothed 250 times)

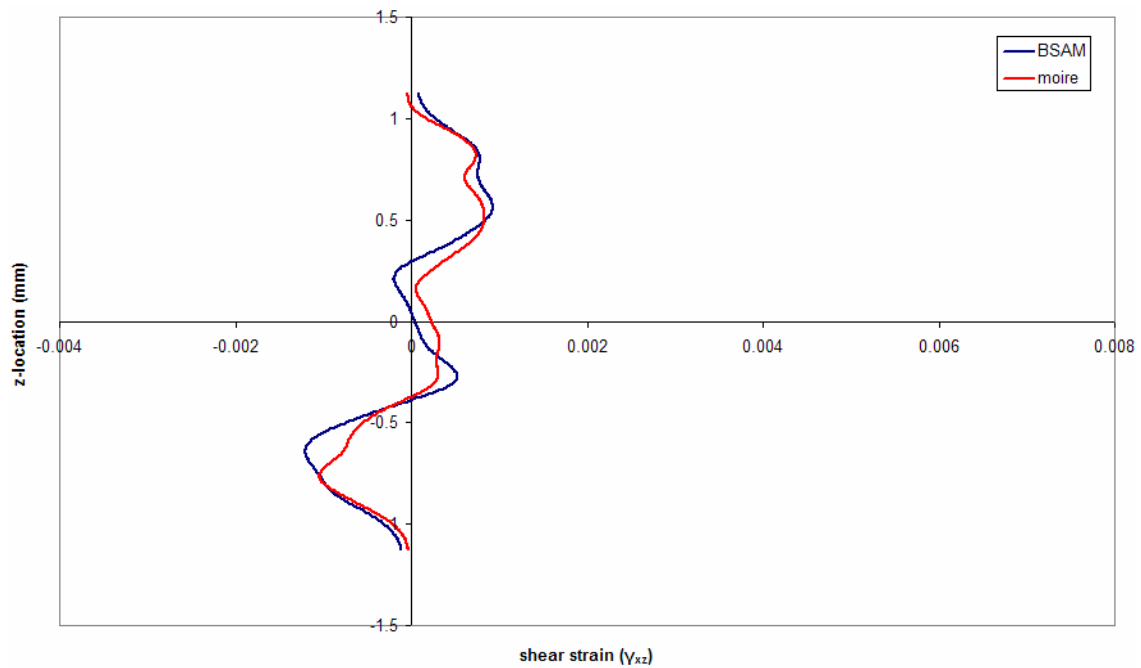


Figure 97. Stepped-lap Joint: strain (γ_{xz}) through specimen thickness (z) at $x = 5\text{mm}$
(data smoothed 250 times)

After generating line plots at 5mm intervals across the region of repair, additional line plots were made at x-locations of $\pm 9.6\text{mm}$ as shown in Figure 98, Figure 99, and Figure 100 in this chapter and corresponding plots in Appendix E. These two locations were selected as they corresponded to the peak locations of the strain components as indicated by the full-field strain images. This was also the x-location of the 0° step in the bond-line.

Upon examination of line plots of the strain components at these locations, the following conclusion was reached: while the strain components at x-locations away from vertical steps in the adhesive bond line compared favorably throughout the thickness, there was discrepancy in the line plots taken at x-locations in the vicinity of vertical steps in the adhesive bond line. This section contains line plots of the three strain components through the specimen thickness at -9.6mm demonstrating this behavior (Figure 98, Figure 99, and Figure 100). A grid representing the modeled plies of the laminate has been superimposed over the graph so that strain behavior can be correlated to a specific location and ply orientation through the thickness of the specimen.

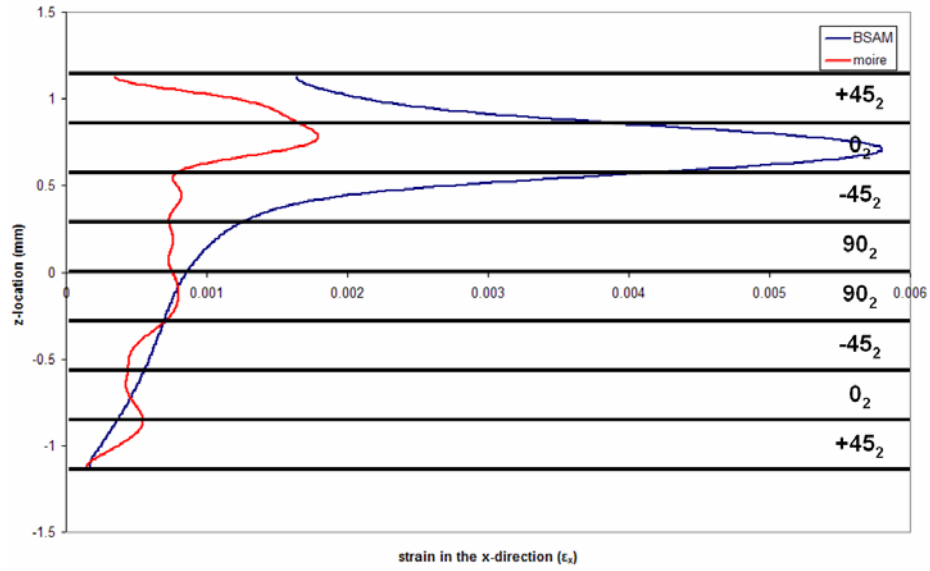


Figure 98. Stepped-lap Joint: strain (ϵ_x) through specimen thickness (z) at x = -9.6mm
(data smoothed 250 times)

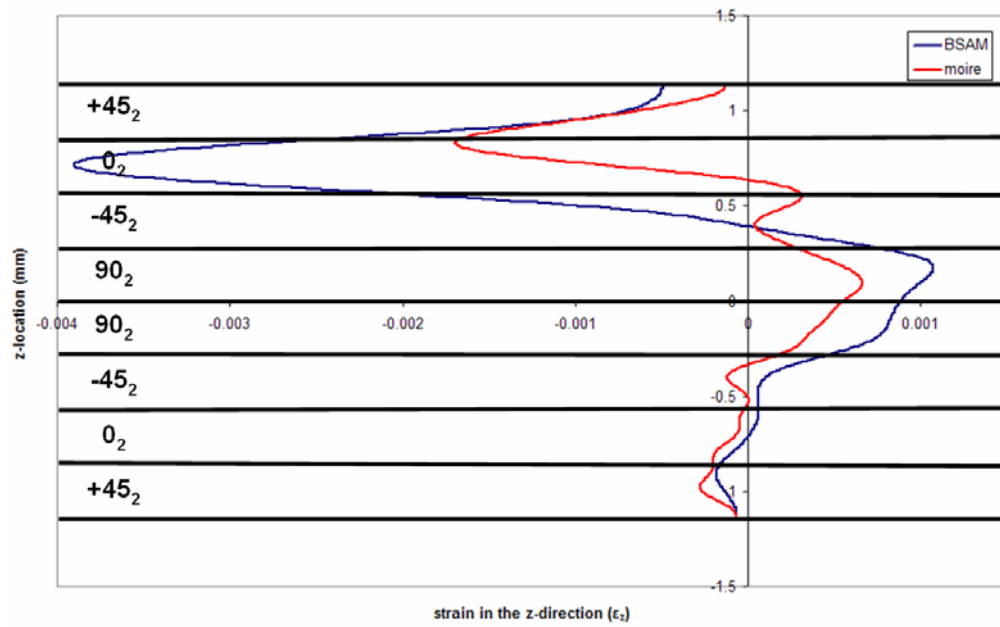


Figure 99. Stepped-lap Joint: strain (ϵ_z) through specimen thickness (z) at x = -9.6mm
(data smoothed 250 times)

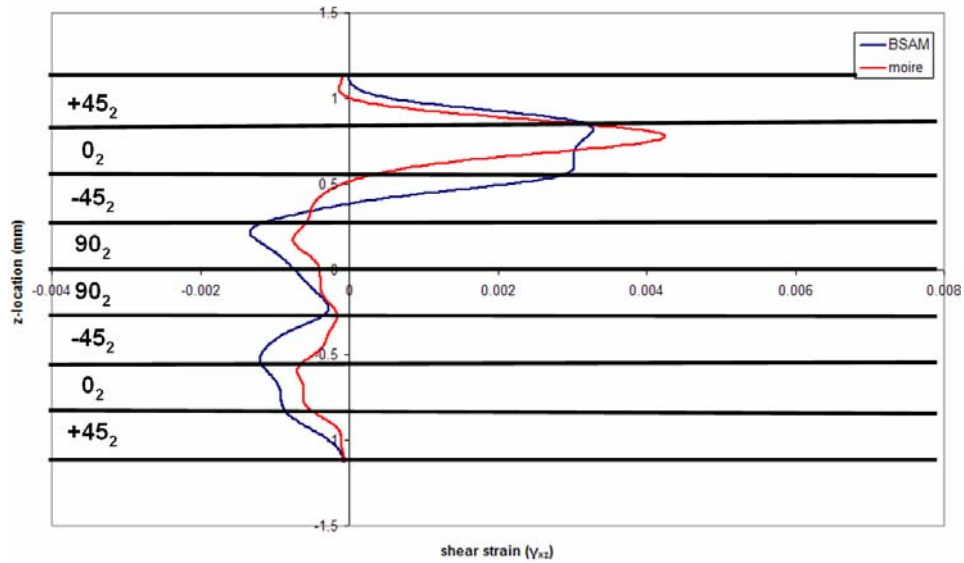


Figure 100. Stepped-lap Joint: shear strain (γ_{xz}) through specimen thickness (z) at $x = -9.6\text{mm}$ (data smoothed 250 times)

Overall, the largest discrepancies between the predicted and experimental data for the stepped-lap joint occurred at -9.6mm when compared to the other line plots produced. As a general trend, line plots taken in the vicinity of vertical adhesive steps seemed to have a greater disparity in peak strain intensities than other areas. As Figure 98 and Figure 99 indicate, the strain through the thickness of the specimen at -9.6mm exhibits the same general behavior in both the BSAM model and experimental results, but the peak magnitudes of strain are significantly different. The similarities in general behavior of the data are indicated by spikes in strain in the x -direction and z -direction in the upper 0° plies in the adhesive region, with strain decreasing through the thickness of the specimen. A large discrepancy between predicted and experimental results can be seen in the peak strain in the x -direction and z -direction. While BSAM predicted a strain of close to 0.006 in the x -direction and -0.004 in the z -direction, moiré interferometry

demonstrated a peak strain of less than 0.002 in the x-direction and -0.002 in the z-direction, or three times smaller than predicted values in both cases.

As a first step, a stress analysis was completed to try to get a different perspective that could explain the disparity of these peaks. Because the adhesive was modeled as an isotropic material, a two-dimensional stress analysis was conducted in the vicinity of the vertical steps in the bond line as another form of comparison between the BSAM model and experimental data. To perform this stress analysis, the following equations were used:

$$\begin{aligned}\sigma_{xx} &= \frac{E}{(1+\nu)(1-2\nu)} [(1-\nu)\epsilon_{xx} + \nu\epsilon_{zz}] \\ \sigma_{zz} &= \frac{E}{(1+\nu)(1-2\nu)} [(1-\nu)\epsilon_{zz} + \nu\epsilon_{xx}]\end{aligned}\tag{44}$$

In these equations, E was the adhesive modulus of elasticity and ν was the poisson's ratio for the adhesive. It was thought that although the strain components through the adhesive compared poorly, the stresses in these areas may compare more favorably. While BSAM offered a three dimensional strain analysis, it was determined that a two-dimensional stress analysis of these strains might provide a decent stress comparison with minimal effort. This stress analysis was conducted through adhesive material at +/-10mm and +/-9.6mm for the stepped-lap joint, or the areas with the greatest discrepancies in peak magnitude of strain.

Table 1 shows the overall results from the two-dimensional stress analysis. The values in the second and third columns are averages of stresses calculated in regions of the adhesive. Figure 101 and Figure 102 provide examples of the predicted and experimental 2D stresses plotted together. Overall, the two-dimensional stress analysis reinforced the notion that the predicted and experimental strain simply did not compare

well. Neither the stresses nor the strains compared favorably through the adhesive, so it concluded that the predicted and experimental peak strains were, in fact, different.

Table 1. Summary of results from 2D stress analysis through adhesive in stepped-lap model.

	x-location (mm)	BSAM	moire	% difference
σ_{xx}	10	430.1	277.7	55%
	9.6	429.6	306.4	40%
	-9.6	386.5	337.8	14%
	-10	368.4	276.9	33%
σ_{zz}	10	252.2	104.8	141%
	9.6	247.0	124.1	99%
	-9.6	227.8	152.0	50%
	-10	187.1	68.9	171%

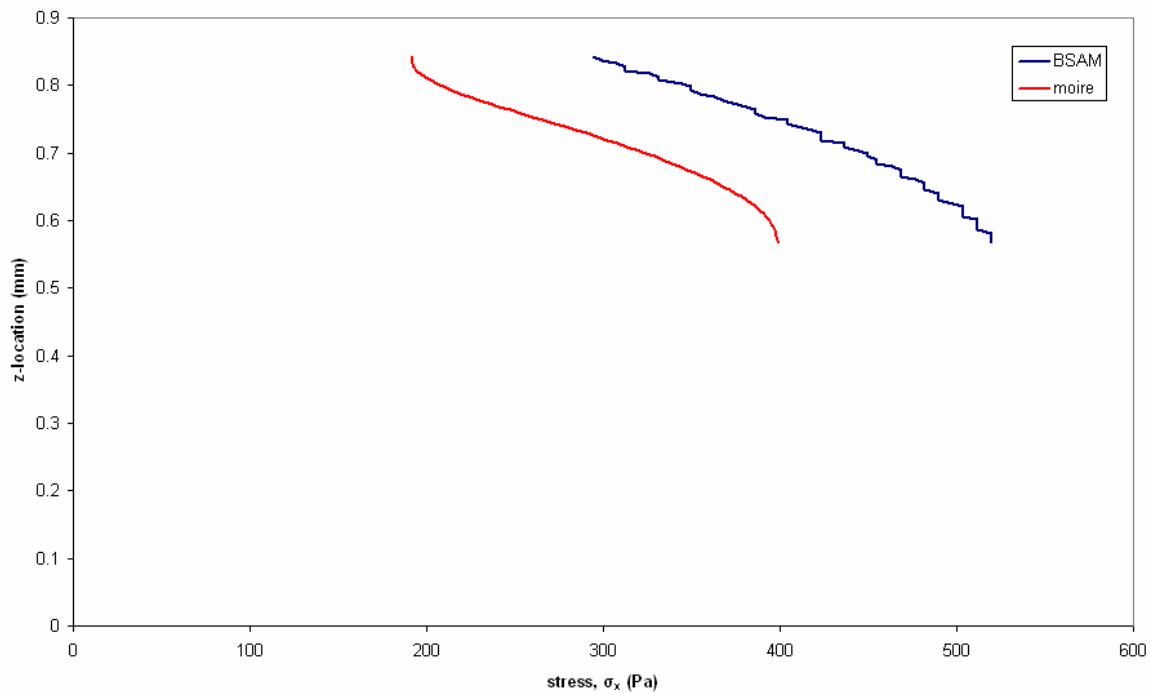


Figure 101. Two-dimensional stress (x) through the adhesive at x = 9.6mm

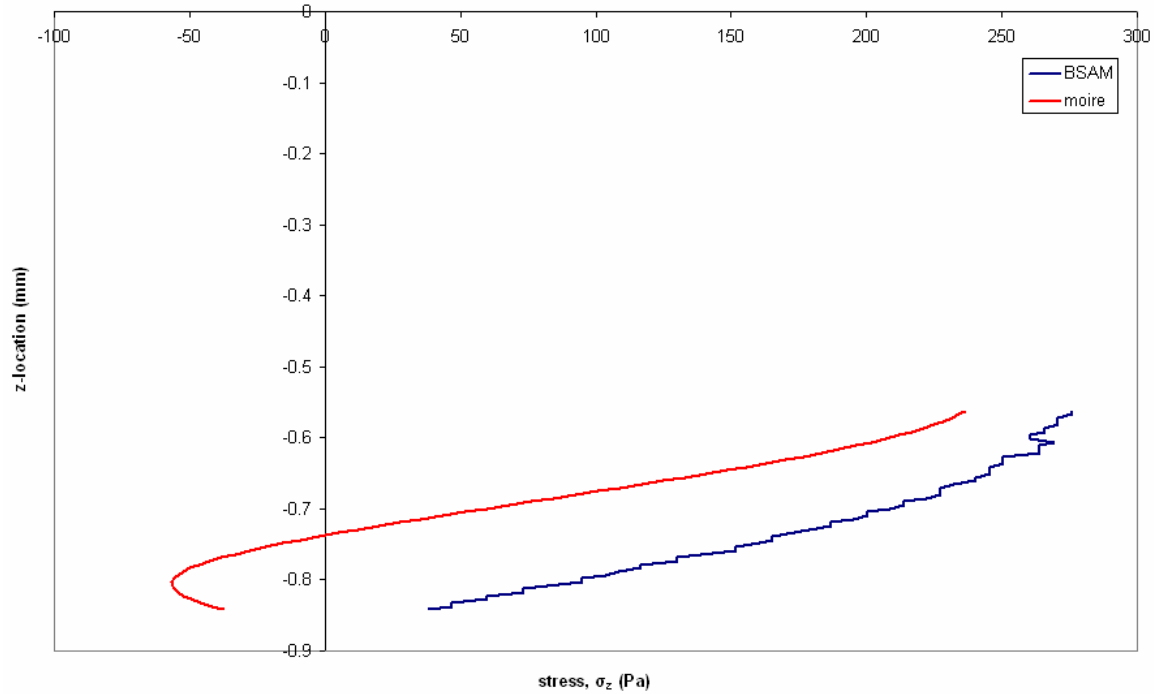


Figure 102. Two-dimensional stress (σ_z) through the adhesive at $x = 10\text{mm}$

At this point, two main conclusions had been reached: (1) strain data from line plots taken at -15mm, -5mm, 0mm, 5mm, and 15mm showed excellent correlation through the entire thickness of the specimen, (2) discrepancies between the predicted and experimental peak strain data for the stepped-lap joint occurred at $\pm 9.6\text{mm}$ and $\pm 10\text{mm}$ when compared to the other line plots produced. From here, effort was then focused toward trying to explain the discrepancies between predicted and experimental peak strain.

First, it was thought that the high strain intensities in the adhesive predicted by the BSAM program could be attributed to the theory behind the code. Theoretically, the stress at the interface between two dissimilar materials (the laminate and adhesive) at a free edge should be infinite. To model this singularity, the BSAM program is capable of using an asymptotic solution to provide accurate stress fields in the vicinity of the

interface. The development of this solution is explained extensively by Iarve and Pagano (1999). Although the asymptotic solution was not used here, the free-edge singularity still manifests itself in the three dimensional linear elastic solution. However, since the peak magnitudes of the strain components were much closer in the scarf model (discussed later), it was determined that the singularity only contributed a small amount of error (if any) in the stepped-lap model.

Next, the accuracy of the BSAM stepped-lap model was considered. While the stepped-lap model was developed with the assumption that the adhesive bond-line contained perfectly square steps, microscopic pictures of the bond-line showed otherwise. In reality, the steps were significantly rounded in the actual repair as shown in Figure 103.

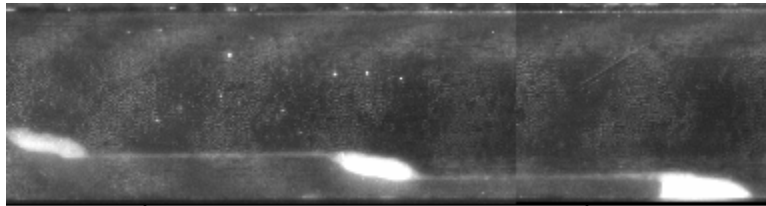


Figure 103. Portion of stepped-lap adhesive bondline.

A thorough explanation of the manufacture of the stepped-lap specimen, including factors contributing to rounding in the “steps,” is covered in the Methodology chapter of this thesis. Because of the complexity of the model, it was decided that the adhesive bond-line should be modeled using perfectly square corners, as shown in Figure 104.

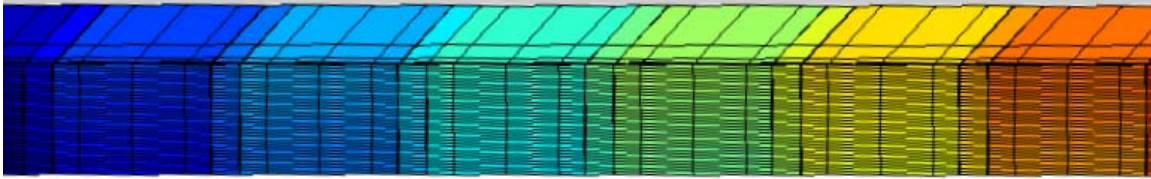


Figure 104. Screen capture of edge view of segment of BSAM stepped-lap model in Mat Lab.

A good illustration of the difference between the model and the actual specimen can be seen in overlapping a contour of the BSAM adhesive bond-line with an enlarged photograph of the specimen. This was done in Transform. In this case, the right side of the diffraction grating was wiped clean with hydrochloric acid to get a reference for the exact location of the bond-line after the moiré testing. Despite the small scale of the repair region, the BSAM model lined up closely with the actual specimen, as shown in Figure 105. As the figure indicates, the location of the steps in the model corresponded almost exactly with the location of adhesive steps in the actual stepped-lap specimen. However, it is apparent that although they are in the correct location, the modeled steps are not a good approximation of reality. The modeled steps have sharp, precise corners while in the actual adhesive steps were rounded and curved.

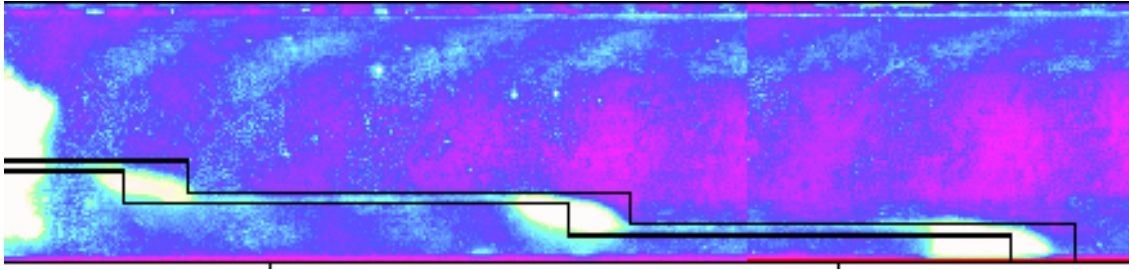


Figure 105. Comparison of BSAM stepped-lap model to experimental test specimen.

Interestingly, the location of the spike in strain, $\pm 9.6\text{mm}$, corresponds exactly to a 90° edge at the step in the 0° plies (Figure 106). It is clear that a higher strain concentration would be exhibited by a sharp corner than a rounded step. Therefore, it can be concluded that assumptions made in the modeling process offers an explanation of why the BSAM predicted a peak strain at this location is so much higher than the peak strain displayed by the moiré.

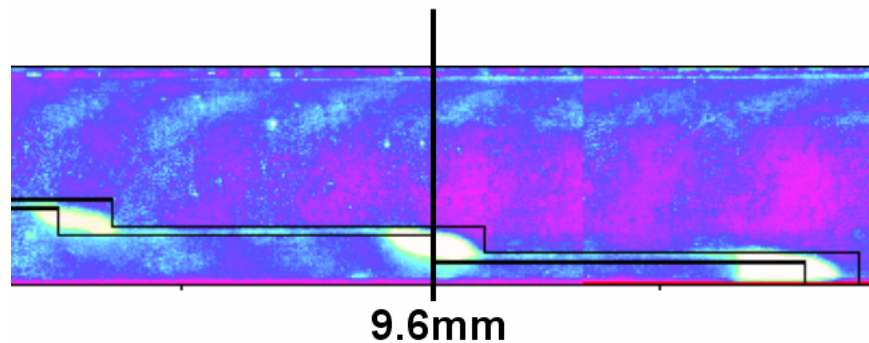


Figure 106. Location of strain peak disparity for stepped-lap joint.

Another factor considered was the presence of air pockets in the vertical steps of the final stepped-lap specimen. Panoramic pictures of the polished specimen edge taken under a high powered microscope revealed that several vertical steps contained pockets of air in the adhesive layer. This occurred because the adhesive pockets at the vertical steps were wider than anticipated. Because the steps were rounded at the bottom of each

step, there was a considerable gap between the two composite panels, even when butted flush against one another. The strips of film adhesive used did not completely fill the width of these gaps, resulting in the formation of air pockets during the curing process. It is assumed that these air pockets occurred with some frequency throughout the width of the stepped-lap specimens used for this thesis. It is not known what the effects of these irregular air pockets in the adhesive layer might be on resultant strain, but it is another factor that should be noted when considering the experimental results pertaining to the stepped-lap repair in this study.

Line Plots: Scarf Joint

Values of the three (3) strain components through the specimen thickness were extracted from Transform at the 5mm intervals across the region of the repair for the scarf joint. These locations were: -15mm, -10mm, -5mm, 0mm, 5mm, 10mm, and 15mm (Figure 107). For all line plots, moiré data is represented in red while predicted BSAM values are shown in blue.

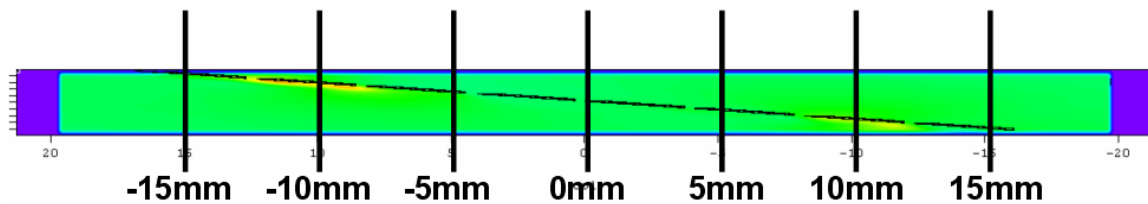


Figure 107. x-location of extracted scarf strain data for line plots.

Initial line plots of strain data for the scarf joint demonstrated similar trends to those seen in initial line plots generated for the stepped-lap joint (Appendix D). Preliminary line plots of the three strain components for the scarf joint at $x = 0\text{mm}$ are shown below. The trends exhibited in plots at this x-location were representative of all of the initial line plots generated. Like the stepped-lap joint, no smoothing was done before

initial plotting. As evident by Figure 108, Figure 109, and Figure 110, general trends in the data sets corresponded but there was a fair amount of discrepancy in the behavior of the moiré and BSAM data. Other initial line plots can be found in Appendix D.

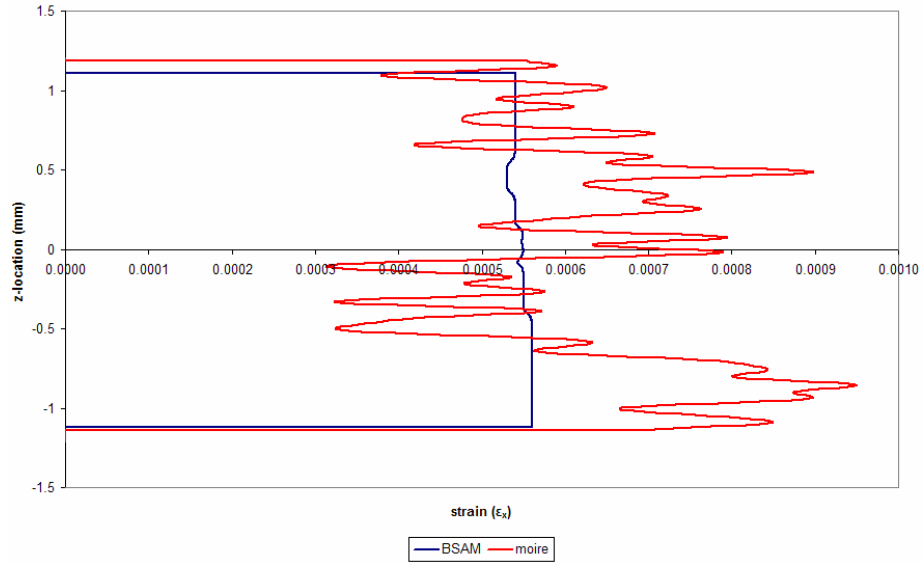


Figure 108. Scarf Joint: strain distribution (ϵ_x) through specimen thickness (z) at $x = 0\text{mm}$

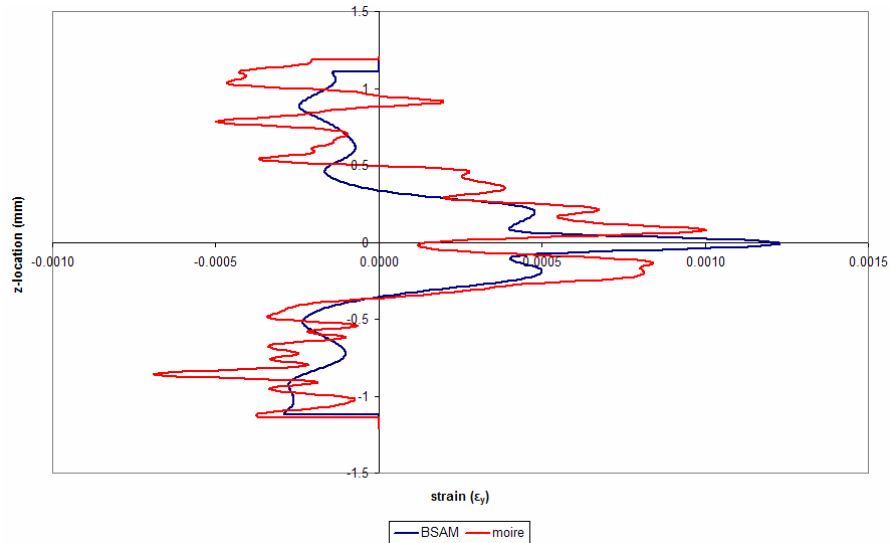


Figure 109. Scarf Joint: strain distribution (ϵ_y) through specimen thickness (z) at $x = 0\text{mm}$

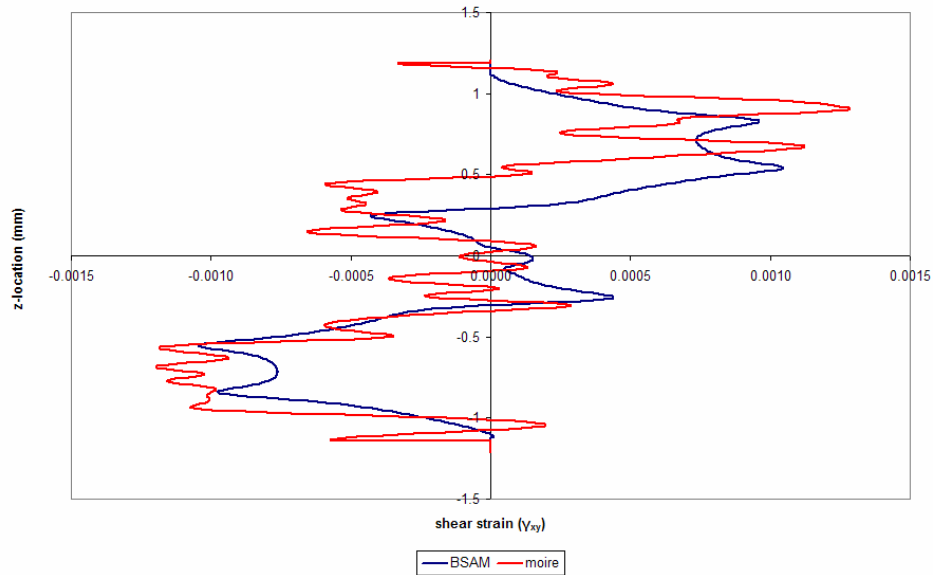


Figure 110. Scarf Joint: shear strain distribution (γ_{xy}) through specimen thickness (z) at $x = 0\text{mm}$

After inspection of these initial plots, it was determined that data should be smoothed, like the stepped-lap data, to obtain a better comparison of the results. While the scarf joint input file was reviewed, it was left unchanged as higher order splines (cubic) were already in place. Data for the scarf joint was smoothed in a manner identical to data from the stepped-lap joint.

Like the stepped-lap joint, the correlation between modeled and experimental values in the revised plots improved for all three strain components through the entire thickness of the specimen. Refined line plots of the three strain components are shown at x -locations of 0mm and 5mm. A complete set of refined line-plots can be found in Appendix E.

After inspecting the line plots created at these locations, it was concluded that the predicted and experimental strains compared favorably across the width of the repair. Data from plots taken at -15mm, -5mm, 0mm, 5mm, and 15mm showed even better

correlation through the entire thickness of the specimen than the stepped-lap joint. The line plots generated at these locations provide a representative example of the strong correlation between the experimental and modeled results, in which both the magnitude and behavior of strain through the thickness is nearly identical.

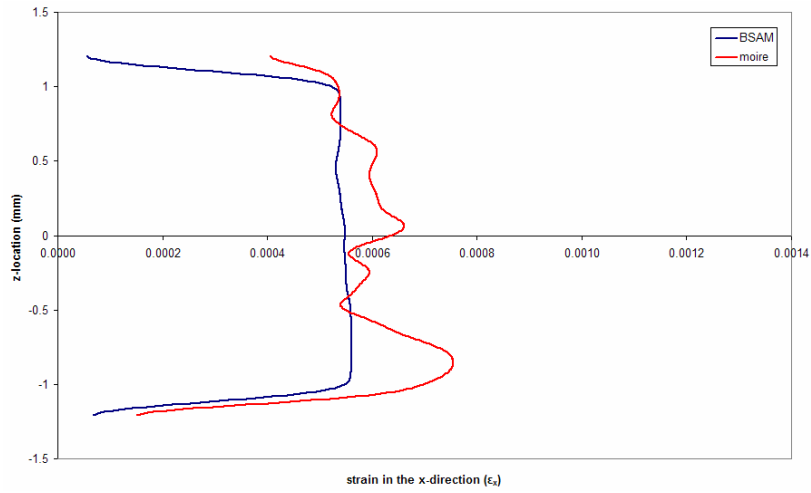


Figure 111. Scarf Joint: strain (ϵ_x) through thickness (z) at $x = 0\text{mm}$

(data smoothed 250 times)

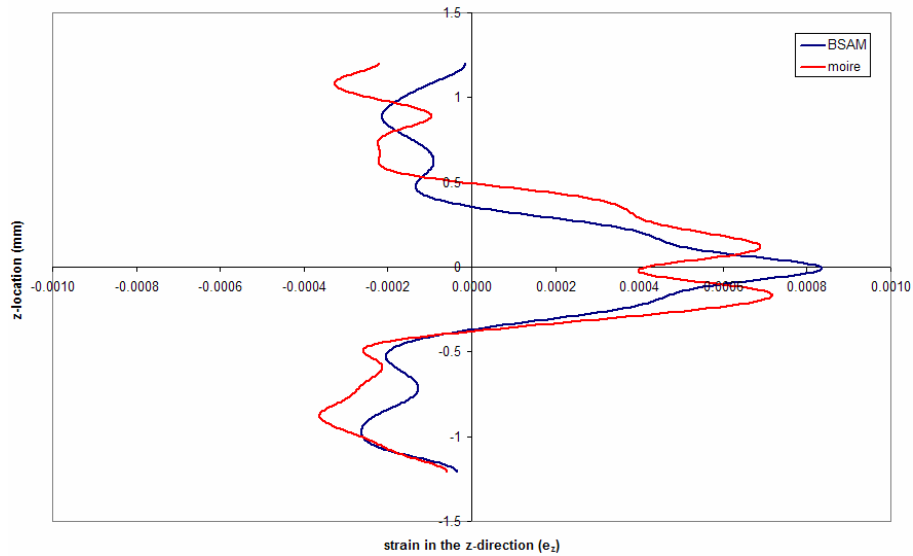
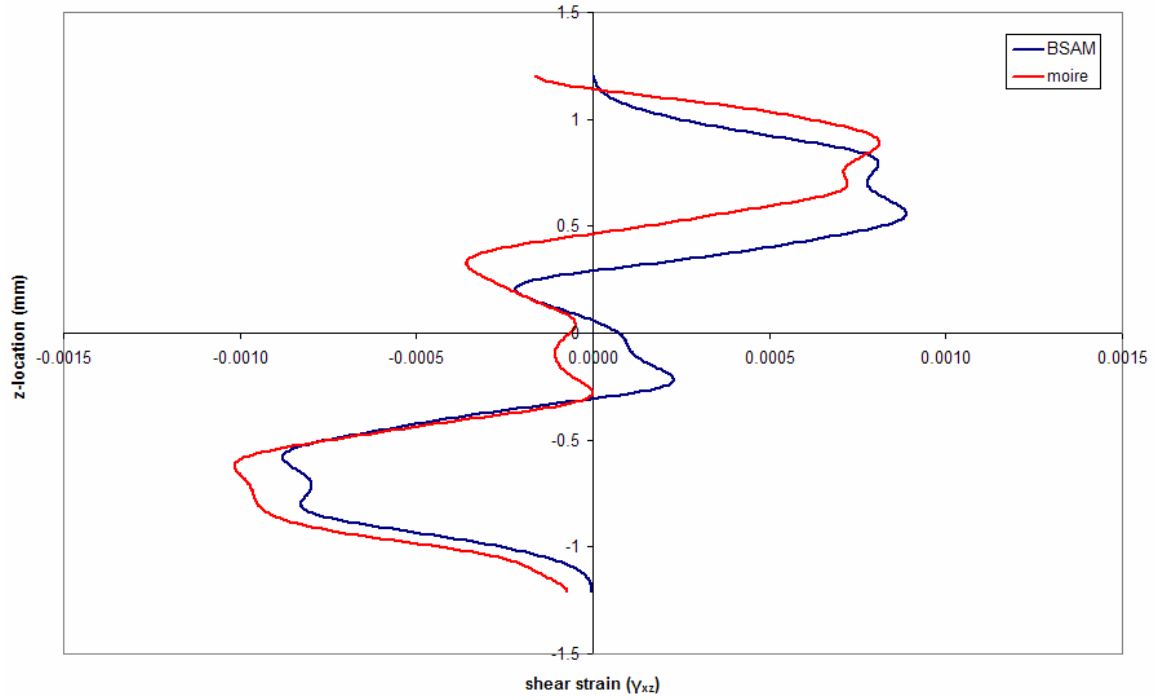
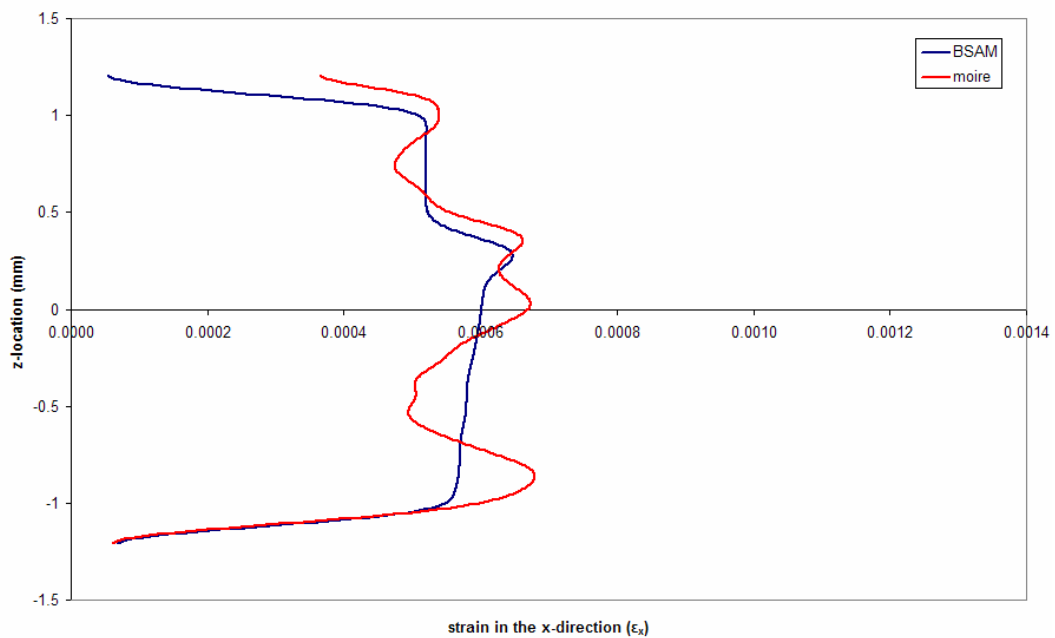


Figure 112. Scarf Joint: strain (ϵ_z) through thickness (z) at $x = 0\text{mm}$

(data smoothed 250 times)



**Figure 113. Scarf Joint: shear strain (γ_{xz}) through thickness (z) at $x = 0\text{mm}$
(data smoothed 250 times)**



**Figure 114. Scarf Joint: strain (ϵ_x) through thickness (z) at $x = 5\text{mm}$
(data smoothed 250 times)**

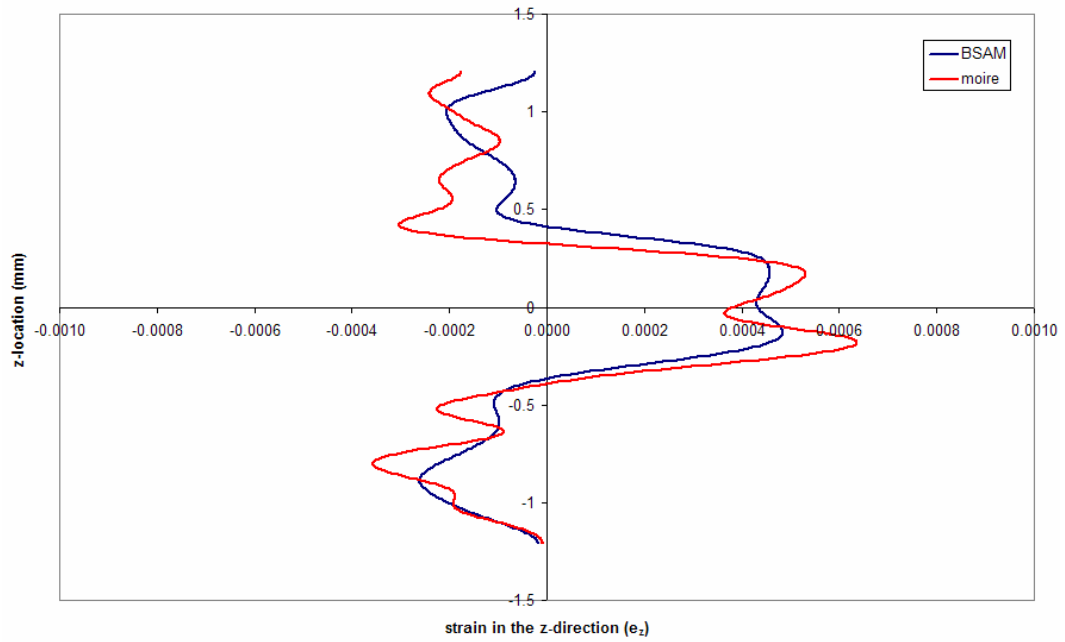


Figure 115. Scarf Joint: strain (ϵ_z) through thickness (z) at $x = 5\text{mm}$
(data smoothed 250 times)

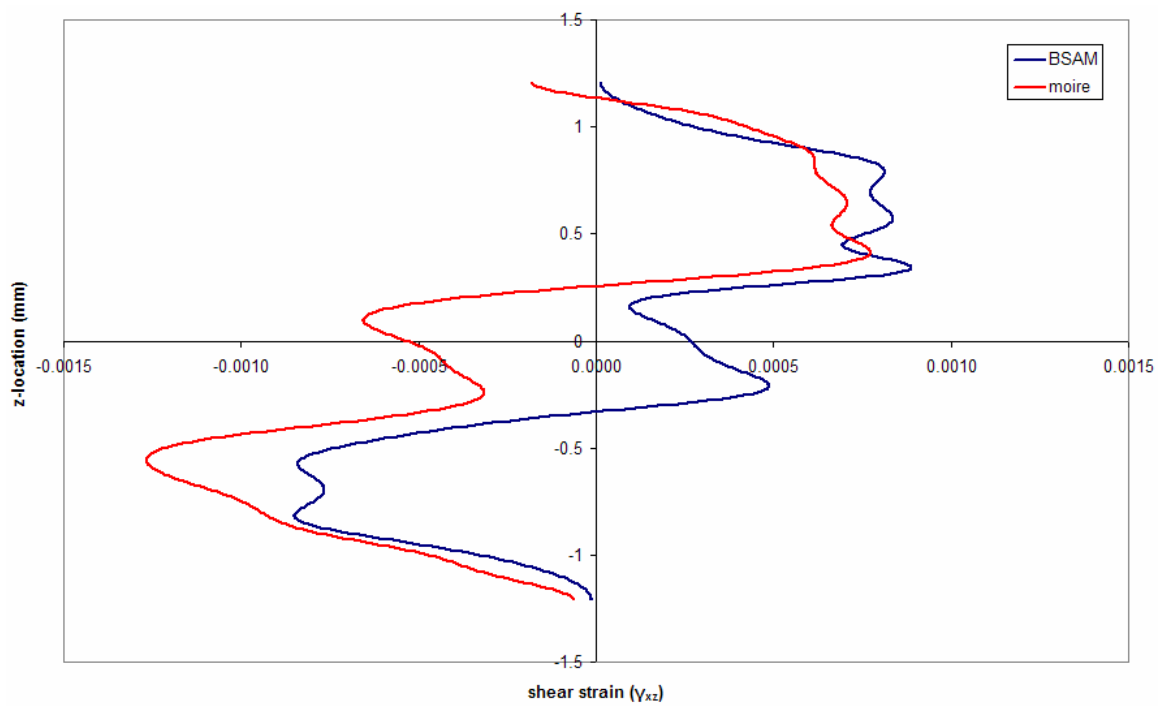


Figure 116. Scarf Joint: shear strain (γ_{xz}) through thickness (z) at $x = 5\text{mm}$
(data smoothed 250 times)

While strain data from the stepped-lap joint displayed a high discrepancy in peak values through the adhesive at x-locations in the vicinity of peak strain, this was not true of the scarf joint for the left side of the repair. Line plots of the three strain components of the scarf joint at the x-location of -10.3mm are included as Figure 117, Figure 118, and Figure 119. Peak strains from the full-field strain images correlated to this location (-10.3mm), so it was thought if there was a considerable difference between peak magnitudes of strain through the thickness of the specimen, it would occur at this x-location. However, after comparing the line plots of the strain components at this location, it was clear that the predicted and experimental data had excellent correlation in both behavioral trends and strain magnitudes.

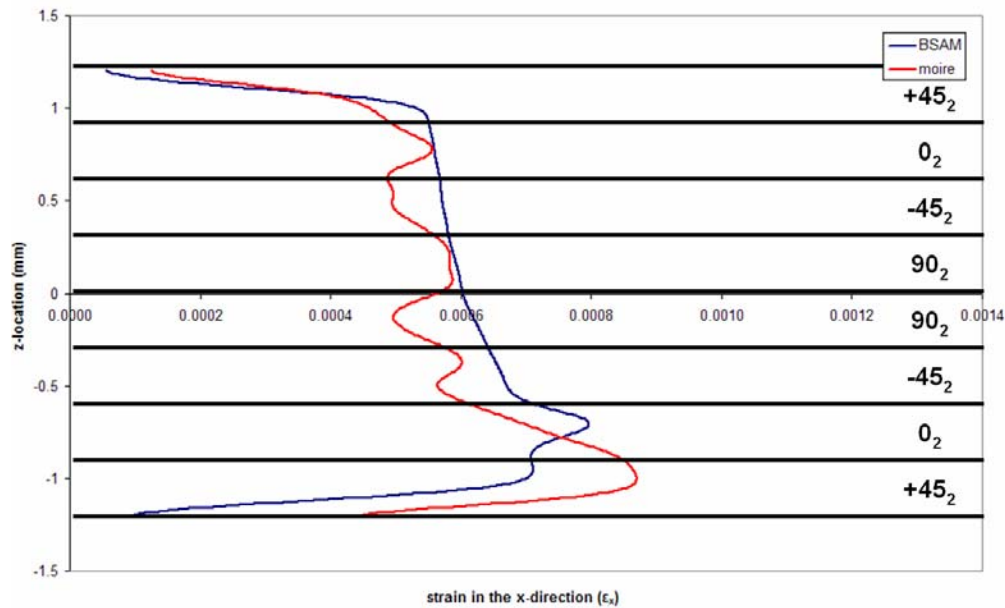


Figure 117. Scarf Joint: strain (ϵ_x) through specimen thickness (z) at x = -10.3mm
(data smoothed 250 times)

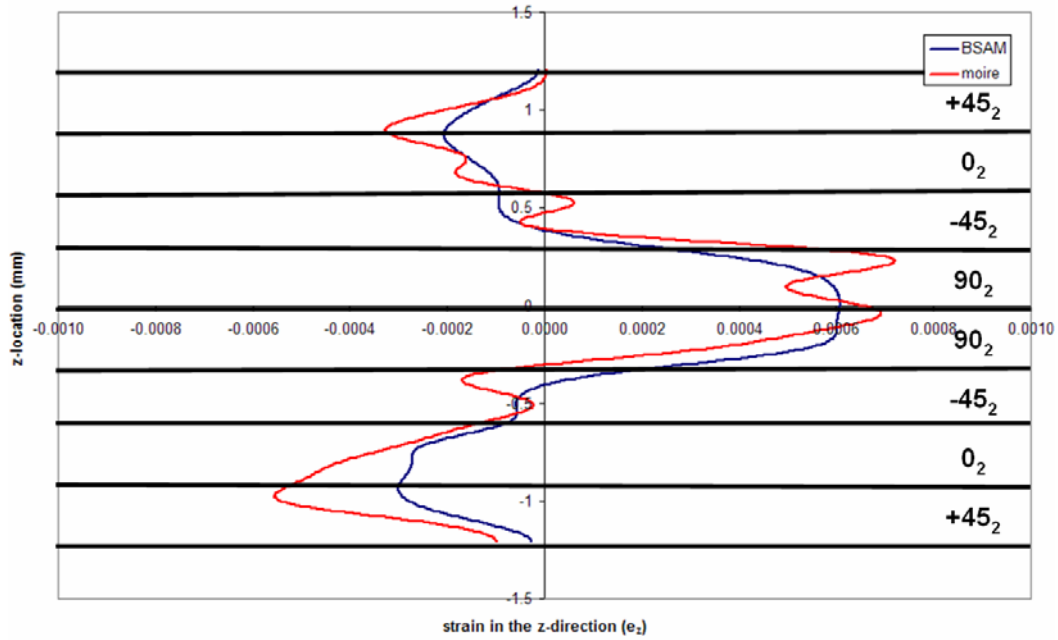


Figure 118. Scarf joint: strain (ϵ_z) through specimen thickness (z) at $x = -10.3\text{mm}$
(data smoothed 250 times)

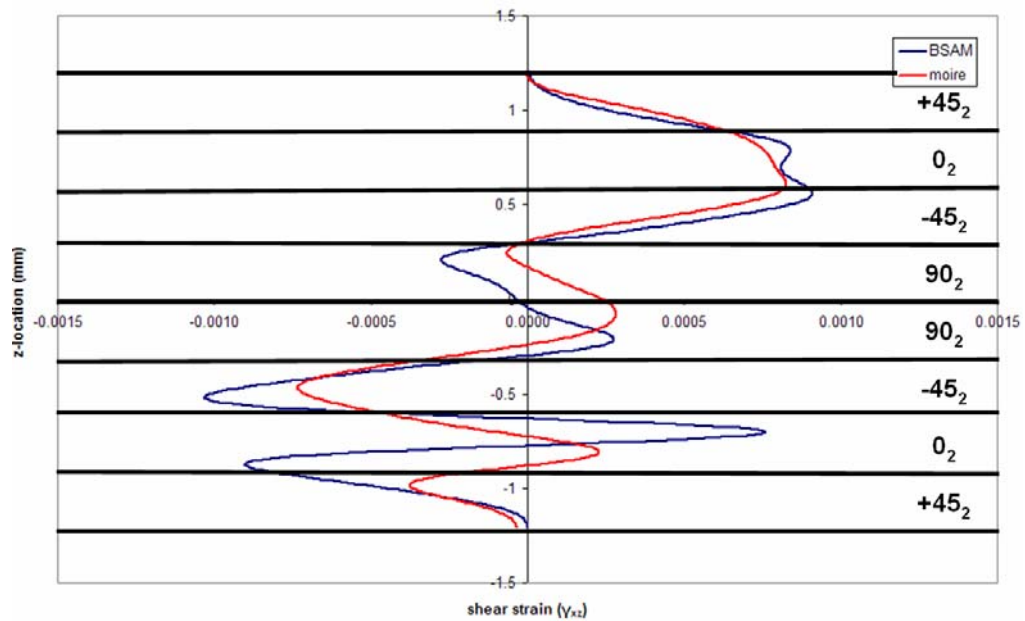
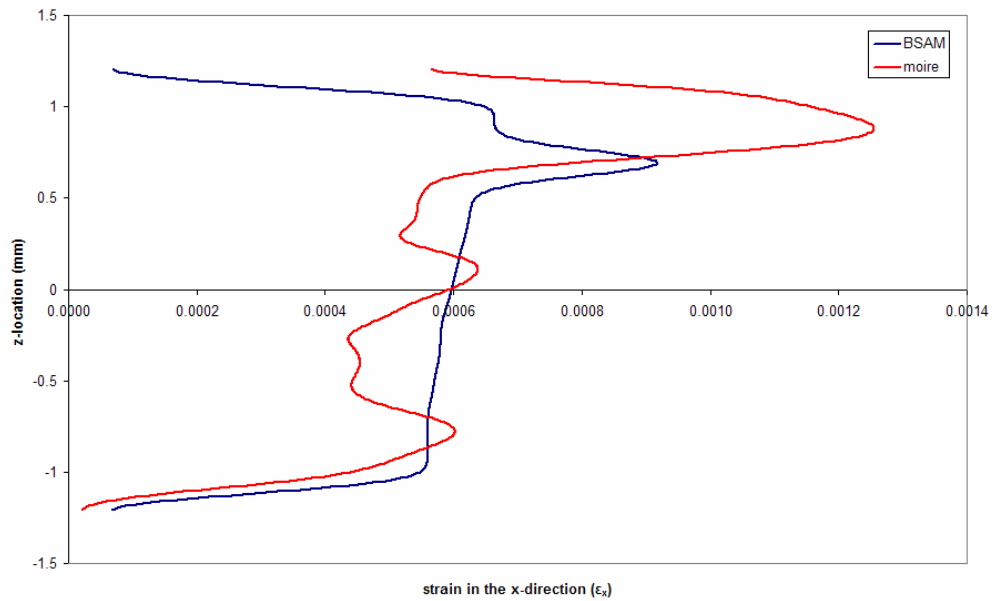
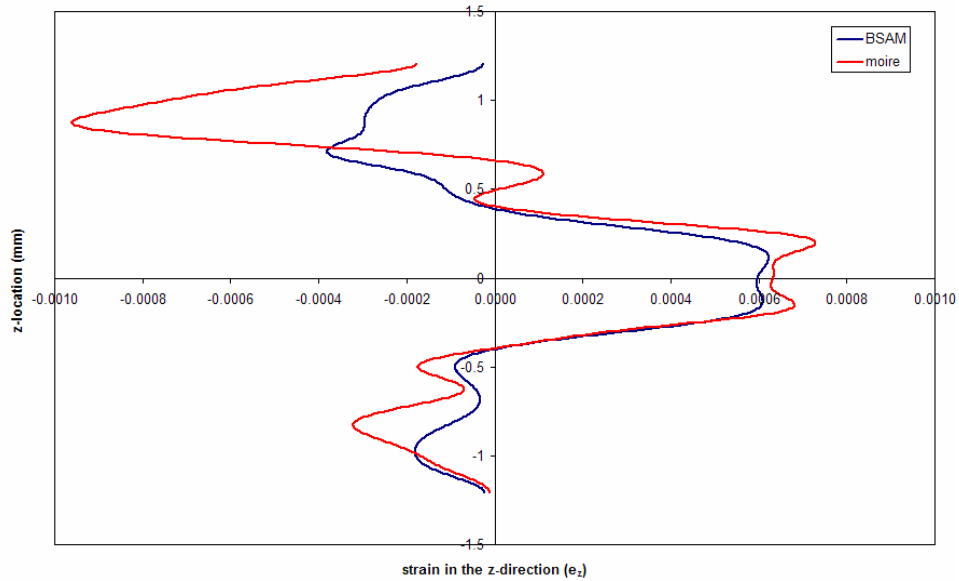


Figure 119. Scarf joint: shear strain (γ_{xz}) through specimen thickness (z) at $x = -10.3\text{mm}$
(data smoothed 250 times)

However, there was some discrepancy in peak strains in components for the scarf joint at 10.3mm, as evident in Figure 120 and Figure 121. Unlike the stepped-lap joint, the peak strain components at this x-location were actually higher in the moiré data set. While the peak moiré strain in the x-direction was over 0.0012, BSAM predicted a peak strain of approximately 0.0009. Similarly, while the peak moiré strain in the z-direction was almost -0.0010, a peak strain of less than -0.0004 was predicted.



**Figure 120. Scarf Joint: strain (ϵ_x) through thickness (z) at $x = 10.3\text{mm}$
(data smoothed 250 times)**



**Figure 121. Scarf Joint: strain (ϵ_z) through thickness (z) at $x = 10.3\text{mm}$
(data smoothed 250 times)**

Another issue in the strain data for the scarf joint was that the z -location of strain peaks did not match. Overall, the BSAM computer program seemed to be predicting peak strains in slightly offset locations when compared to the experimental results. In most cases, strain peaks in the moiré data were shifted slightly in the z -location as compared to the predicted strain peaks in BSAM. Examples of these “shifts” are shown in Figure 122 and Figure 123.

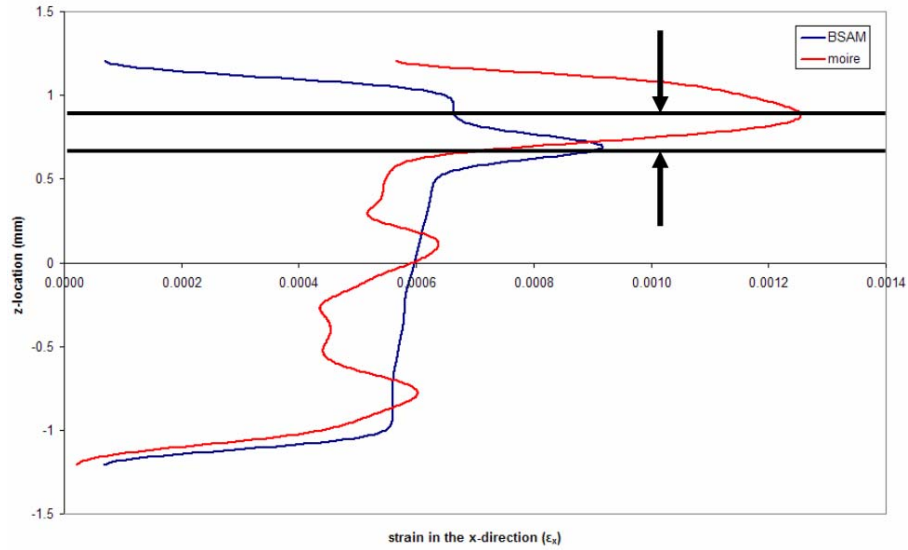


Figure 122. Example of shift in z-location of peak strain for scarf joint

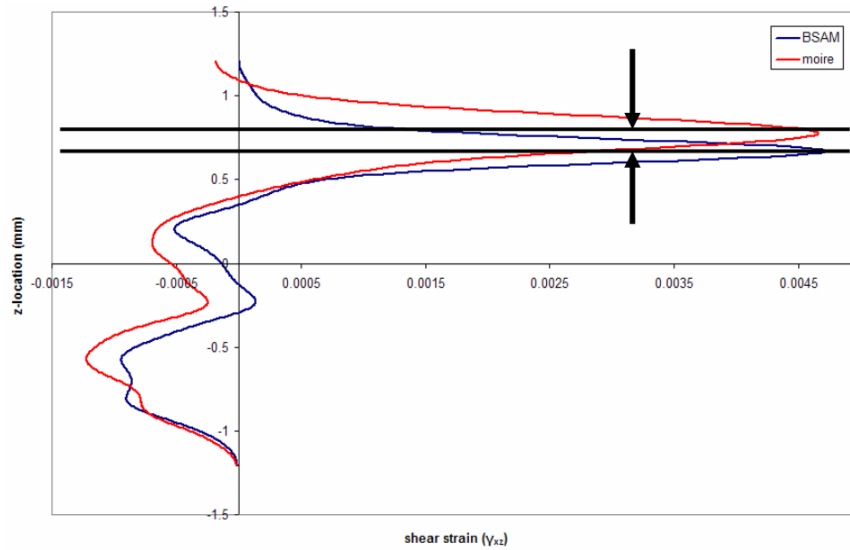


Figure 123. Second example of shift in z-location for scarf joint.

Although data compared favorably, it was apparent that there were two minor inconsistencies with the data at this point: (1) the magnitude of the experimental peak strain at $x = 10.3\text{mm}$ was significantly higher than the strain predicted, and (2) many experimental strain peaks had “shifted” z-locations compared to their predicted

counterparts. To investigate the potential causes for these discrepancies in strain data for the scarf joint, an approach similar to the strain data analysis for the stepped-lap joint was taken. Overall, three arguments were considered to explain differences in modeled and experimental data. These arguments assessed (1) the variation in the adhesive bond line, (2) the accuracy of the scarf angle, and (3) a size comparison of the resultant data matrices.

The first approach consisted of checking the adhesive bond line of the scarf joint for accuracy. This was done because while a linear adhesive bond line was modeled, the actual bond line was not exactly linear and varied through the thickness. As mentioned in the chapter II, the thickness of the modeled bond line was found by taking the average of three points across the width of the bond line and the slope of the repair was found using coordinates obtained using a microscope. While it was hoped that these assumptions would provide an accurate model of the actual repair, any variation between the two would result in inconsistent peak strain magnitudes and locations. These deviations can be better seen in a magnified outline of the actual scarf joint bond line, as shown in Figure 124.

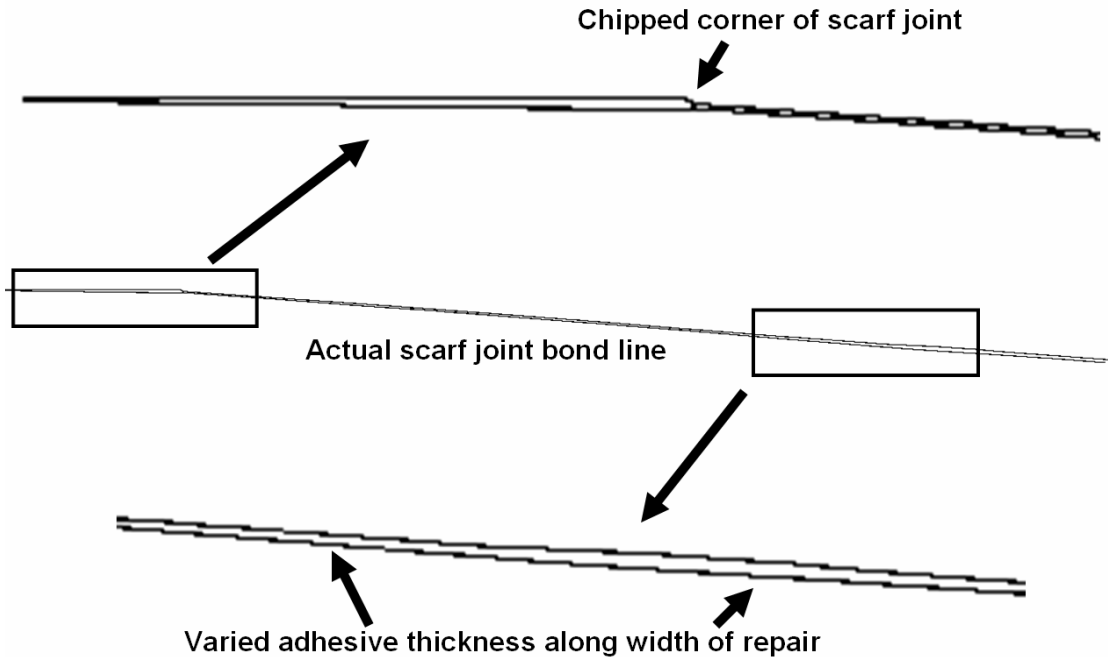


Figure 124. Deviations between actual scarf bond line and idealized model.

As Figure 124 indicates, the bond line was not uniform across the width of the repair. The varied thickness of the bond line provides a good explanation for why the experimental strain was higher than predicted strain at 10mm and 10.3mm. Looking to Figure 124, it is clear that the adhesive bond line is much thicker around 10mm and 10.3mm when compared with the rest of the bond line. This illustrates a clear example of when the model created did not match the reality of the bond line. To reiterate, the adhesive layer was the thickest region corresponding to an x-location of approximately 10mm and 10.3mm. Because the BSAM model did not capture this deviation, this provides a potential explanation for why the experimental and predicted strains did not match in this region of the repair.

While the non-uniform bond-line provides a solid explanation for inconsistencies between predicted and experimental peak strain *magnitudes* at 10mm and 10.3mm, two explanations were then considered to explain for the discrepancies in peak strain *location*.

The first thought was to compare the modeled scarf angle to the actual scarf angle. It was thought that a comparison between the modeled and actual scarf angle might be able to explain the minor discrepancies in the data. At first, an effort was made in overlaying the modeled scarf joint with the moiré scarf joint, as shown in Figure 125. The red line indicates the experimental bond line, while the black line represents the bond line modeled in BSAM.

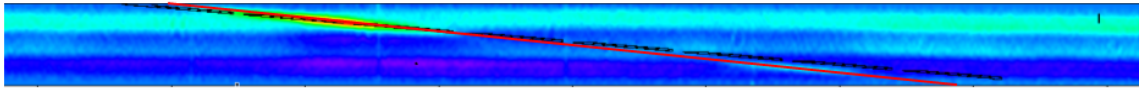


Figure 125. Comparison of experimental and modeled scarf joint.

Because of the small scale of the repair, it was still difficult to compare the bond lines after overlapping them in Transform. The next attempt to get a comparison of the scarf angles involved estimating the bond line angles by extracting peak strain data along the bond line. A plot was made by selecting corresponding regions of peak strain in both the modeled and moiré strain fields, selecting two points and running a line fit through the two selected points in the bond line. It was hoped that this method would provide a fairly accurate estimation for the difference in the modeled and experimental scarf angle.

By using these points to generate estimated bond lines, it was estimated that the angle of moiré repair, $\theta_{moiré}$, was 4.5699° , while the angle of the BSAM model, θ_{BSAM} , was 3.3593° , a difference of 1.2106° . To verify the accuracy of this method, the θ_{BSAM} found by fitting a line through two points of peak strain from the full-field strain images was compared to the actual angle modeled in BSAM (as verified through the defined geometries). The actual angle modeled in BSAM was 3.8678° , roughly 0.5° off of the θ_{BSAM} estimated. While this disparity is notable, it was assumed that the difference

between bond line angles would be most accurate if determined by the same method. Therefore, the estimated angles of 4.5699° ($\theta_{moiré}$) and 3.3593° (θ_{BSAM}) were used for the remainder of this section of analysis. The estimated difference in the bond lines determined by this method is depicted in Figure 126.

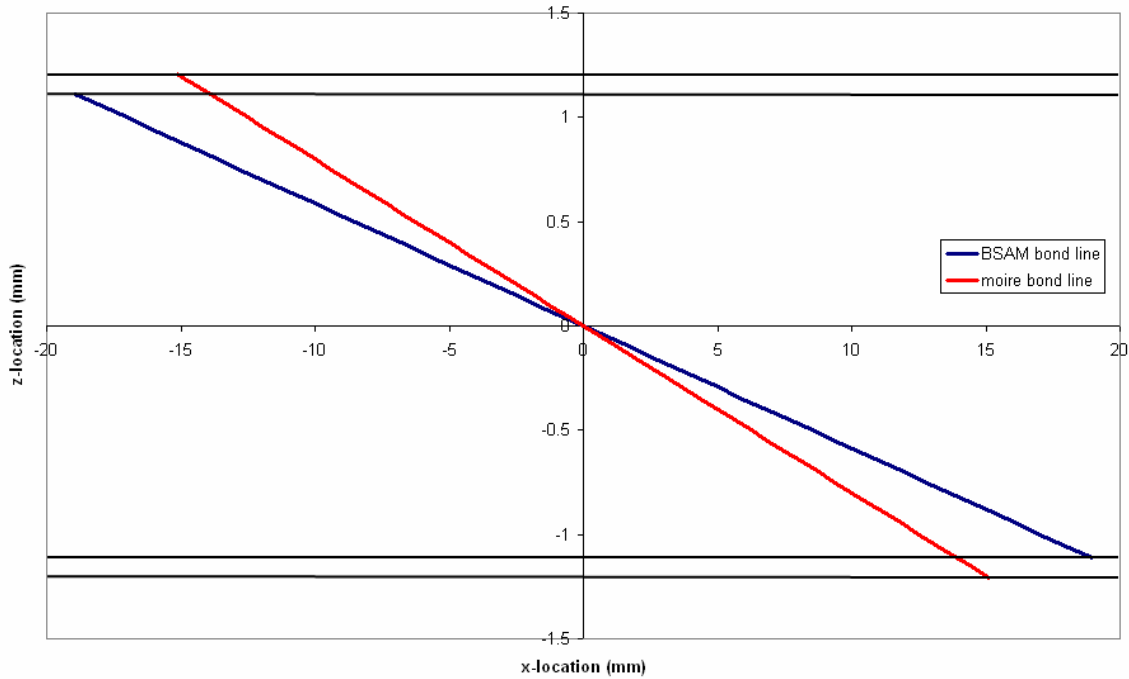


Figure 126. Comparison of modeled and experimental bond line (not to scale).

Even though the difference in scarf angles may not have been as high as this method estimated, any slight difference in angles would provide a potential explanation for the “shifted” peak strain locations in the z-axis. For example, referring again to Figure 126, if data is extracted at an x-location of -10mm, the bond line would intersect a z-location of 0.8mm for the actual repair but only 0.6mm for the BSAM model. This would result a shift of peak strain in the z-direction by 0.2mm and provide a feasible explanation to why the z-locations of the peaks do not match. Figure 126 indicates the general trend that the peak strain from moiré data should occur at greater z-distances

from the laminate's plane of symmetry than the BSAM peak strain across the width of the repair, depending on the exact x-location where data is extracted. Looking to the Transform data matrix at an x-location of -10mm (Figure 122), it can be seen that the exact difference in z-locations of the peak strains is 0.186mm. This value compares very closely to the 0.2mm disparity between the model and actual repair at $x = -10\text{mm}$. This provides an example that the misalignment (shifted z-location) of peak strain values might be indicative of inaccuracies in the model.

This potential explanation was then put to the test. To find a better comparison between the peak strain magnitudes in the moiré and BSAM, x-locations corresponding to the same z-location (through the laminate thickness) were calculated. It was hoped that if there was a difference between the modeled and actual scarf angles, that strain data could be extracted from different x-locations to provide a more favorable comparison of peak strain magnitude and location. This is shown in Figure 127, where it can be seen that the adhesive based intersects a z-location of 0.6mm at different x-locations in the two data sets (based on the *estimated* scarf angles).

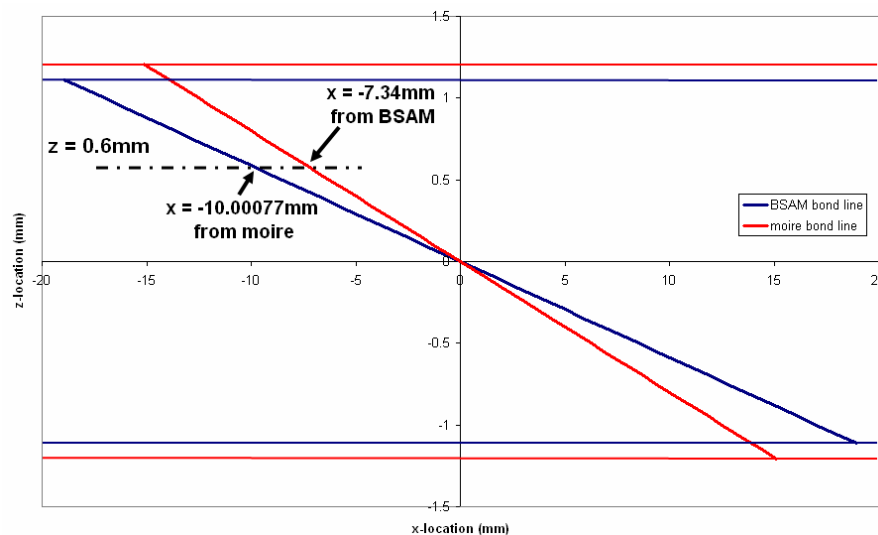


Figure 127. x-locations from BSAM and moiré corresponding to same z-location

Data was then extracted from Transform at these x-locations and plotted (Figure 128). As expected, the peak strain magnitudes compared much more favorably using these corrected or “shifted” locations (compare Figure 128 and Figure 120).

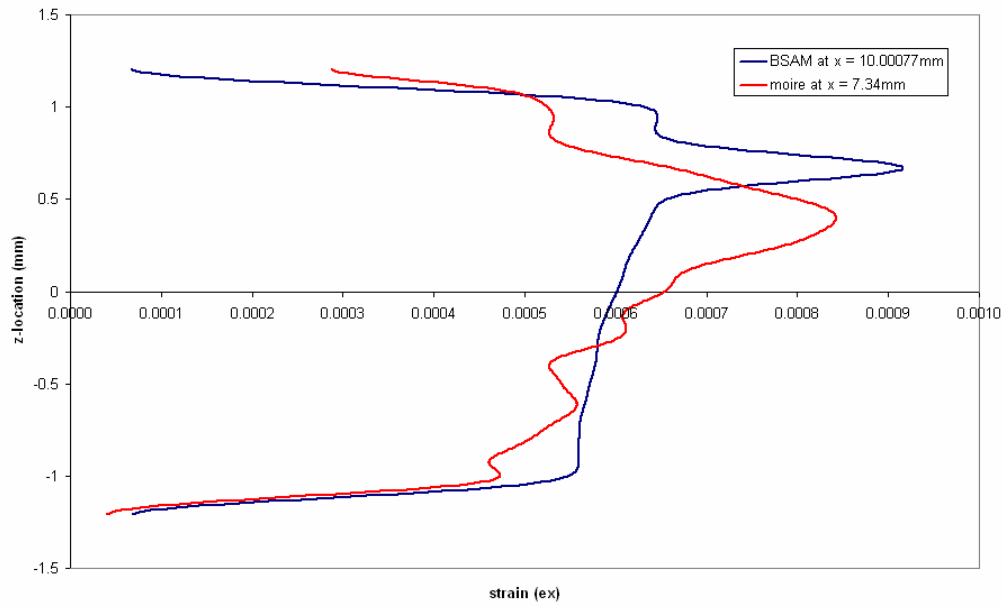


Figure 128: Scarf Joint: Comparison of peak strain magnitudes at corrected x-locations.

This result supports the implication that the angle of the modeled bond line and actual bond line were not exactly the same. However, although the strain peak magnitudes compared more favorably, the z-location of the peak strains still did not correspond well. This time, the experimental strain peak occurred at a z-location *below* the predicted strain peak, indicating that the modeled and predicted angles were probably not off by as much as estimated. Two sources may have contributed to overestimating the angle of the scarf repair from this analysis: (1) any error in finding the bond line angles from two data points extracted from Transform, or (2) the fact that the actual bond line was not exactly linear and there was considerable variation in adhesive thickness

across the region of repair. Because the experimental strain peak occurred at a z-location below the predicted strain peak, it is likely that the method used to determine the scarf angles overestimated their difference. From this analysis, it can be concluded that while the predicted and experimental angles were probably not exactly the same, they were definitely closer than this procedure estimated. It can also be concluded that any slight difference between the modeled and actual scarf angle would have resulted in slightly different strain peak locations, providing a feasible explanation for the shifted strain peak locations observed in the scarf joint line plots.

A second explanation was also considered to account for the differences in z-locations of peak strain. For this argument, it was thought that inconsistencies made while reducing the data for comparison in Transform might explain the slight disparities between the geometry of the model and geometry of the actual test repair. For this second explanation, the experimental and modeled data matrices were again considered.

As noted in the methodology chapter of this thesis, the moiré data matrix in Transform was slightly larger than the original BSAM data matrix. While moiré data spanned 42.52692mm by 2.41569mm, the data matrix from the BSAM model covered only 39.389304mm by 2.225548mm. In this sense, the BSAM specimen modeled was only 92% as “big” as the actual specimen. It was thought that 641 columns and 39 rows of null data could be added in order to “correct” the BSAM matrix so that it could be overlaid onto the moiré data matrix for comparison. In reality, shifting the data matrix in Transform did allow for a better comparison by centering the two data matrices, but it did not correct for this size difference. The simple fact remained that the BSAM data matrix was smaller than the moiré data matrix, and although the center of the bond line could be

matched up, an exact comparison could still not be made because of the size disparity.

To attain a better comparison, all scarf data should have been scaled rather than shifted.

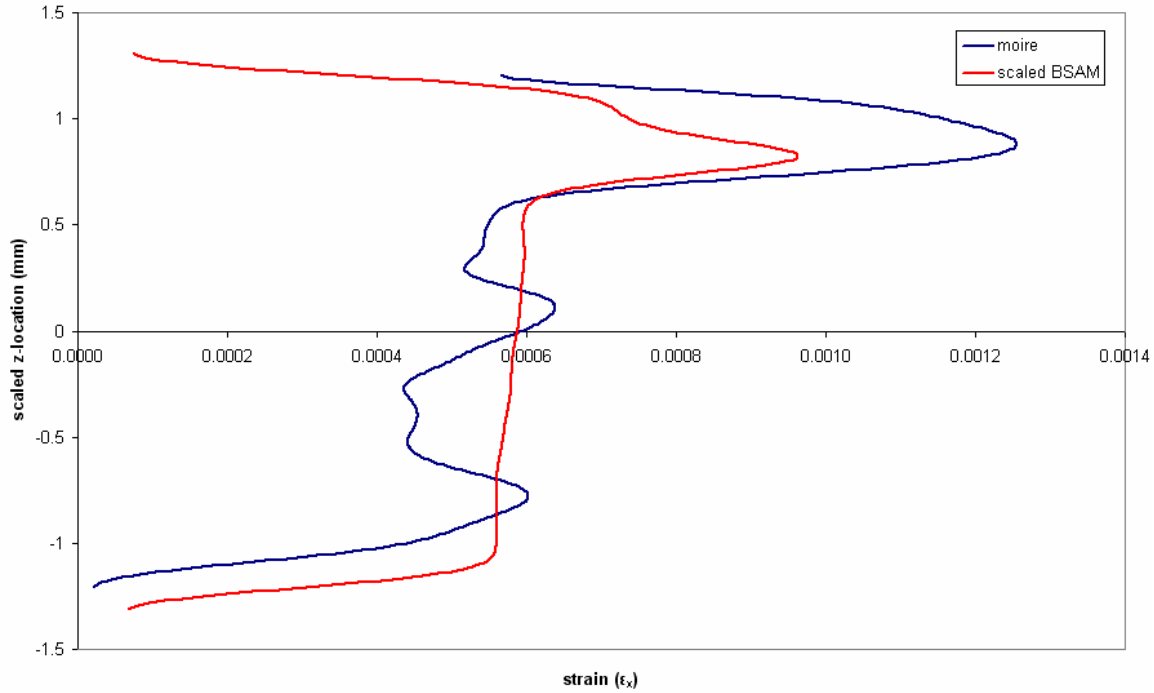


Figure 129. Comparison of scaled BSAM strain data with unaltered moiré strain data.

To validate the merit of this argument, strain results from BSAM were scaled and compared to unaltered experimental moiré data, as shown in Figure 129. To achieve this comparison, the coordinate system for the BSAM model was scaled by a factor of 1.0854 (or 2.41569mm/2.225548mm) in both the x and z directions. Therefore, moiré data at an x -location of 10.3mm was compared to BSAM data at an x -location of 11.18mm. As Figure 129 indicates, the z -location of the peak strain matched much better than the comparison of raw data (Figure 122). Even with scaling the strain data in the x -direction, however, the difference in peak magnitudes between the moiré and scaled BSAM data remained sizable.

After looking over all three of these arguments, it was concluded that discrepancies between the moiré and BSAM line plots for the scarf joint at an x-location of 10.3mm could be attributed to a combination of factors. While no single argument completely explained or accounted for differences between modeled and experimental results, it could be seen that all three might have contributed to inaccuracies in the results at $x = 10.3\text{mm}$.

In summary, there is a strong correlation between the modeled and experimental data extracted across the width of the scarf repair. While there were minor disparities in the strain components at an x-location of 10.3mm, they can be explained by accounting for several factors. Specifically:

1. A linear bond line was modeled in BSAM, while the actual bond line was not exactly straight. Also, a uniform adhesive layer was modeled in BSAM, while the actual adhesive layer varied in thickness across the length of the repair. Most notably, the adhesive was substantially thicker in the area of the repair corresponding to an x-location of 10mm and 10.3mm. This was also the location of the greatest disparity between experimental and modeled results.
2. According to analysis of the scarf angles, the scarf angle modeled in BSAM was slightly less than the actual scarf angle. While it was concluded that the method used in the analysis overestimated the difference between experimental and modeled angles, *any* difference between modeled and experimental scarf angles would have resulted in strain components that did not match exactly in location through the thickness of the specimens.

3. The BSAM model was 92% the size of the experimental data matrix. Because the modeled specimen was smaller than the actual specimen, the BSAM data should be scaled to attain a better comparison between predicted and experimental strain results.

While slight inaccuracies in both the stepped-lap and scarf BSAM models may account for significant discrepancies between the predicted and experimental data sets, it also should be noted that B-spline analysis method carries out a linear analysis. In this sense, it does not take into account any non-linear response or behavior of the adhesive or adherents. While a strong majority of the literature reviewed also assumed the adhesive layer to behave as a linear elastic material, the fact remains that most polymeric structural adhesives behave non-linearly (Mortensen). Therefore, while the BSAM linear analysis has demonstrated that it can provide fairly accurate strain intensity magnitudes and locations in spite of inaccuracies in the model, the limitations of a linear analysis should be considered (Butkus).

VI. Conclusions and Recommendations

The objective of this thesis was to apply a non-commercialized spline-based computer program (BSAM) to model and predict strain fields in two composite repairs, a scarf joint and a stepped-lap joint, subjected to static tensile loading. It was hoped that modeling these repairs would test the ability of BSAM computer program, developed at Wright Patterson AFB, to handle and accurately predict strains in scenarios containing both composite and adhesive materials with complex geometries. After analysis of experimental results (attained through moiré interferometry) and data output from the BSAM program, the following overall conclusion was reached: BSAM accurately predicted the mechanical behavior of both the scarf and stepped-lap repair under a static tensile load when compared to experimental data attained through moiré interferometry.

Overall, strain data compared favorably in both full field strain images created in Transform and line plots generated from data extracted at specific locations across the width of the repair. Any discrepancies between predicted and experimental peak strain magnitudes and locations for both repairs were rare and could be attributed to inaccuracies of the model developed for the BSAM computer program. It was also noted that although polymeric structural adhesives behave non-linearly, the adhesive layer was assumed to behave as a linear elastic material for this study. More specifically, the following conclusions were reached:

1. Stepped-Lap Joint

Strain data from line plots taken at -15mm, -5mm, 0mm, 5mm, and 15mm showed excellent correlation in both strain magnitude and location through the entire thickness of the specimen. Discrepancies between the predicted and experimental

peak strain data magnitude occurred at $\pm 9.6\text{mm}$ and $\pm 10\text{mm}$ when compared to other line plots produced. In the end, it was concluded that the accuracy (or lack of accuracy) of the BSAM predictions are attributed to inaccuracies in representing the exact geometry of the experimental test specimen at these locations. While the actual bond-line had a rounded bond-line with no sharp corners, the bond-line was modeled with perfectly square steps, resulting in high strain concentrations predicted by BSAM at the corners of these steps.

2. Scarf Joint

Strain data from line plots created from data taken at -15, -10.3, -10, -5, 0, 5, and 15mm compared favorably through the entire thickness of the specimen.

Discrepancies between the predicted and experimental peak strain magnitude occurred at 10mm and 10.3mm when compared to other line plots produced, as the disparity between predicted and experimental peak strain data magnitude was the highest there. Another trend consistent across the scarf joint plots was that the z-locations of the strain peaks did not always match. Again, a combination of inaccuracies in the model provided the main explanation for these inconsistencies. First of all, while the actual bond-line was not exactly straight and had an adhesive layer that varied in thickness, the bond-line modeled in BSAM was linear with a uniform adhesive layer. Second, a slight difference between the modeled and actual scarf angle provides a possible explanation for the differences between the predicted and experimental peak strain magnitudes and z-locations. Finally, the size difference between the BSAM and moiré data matrices also attributed to the “shifted” z-location of the strain distributions. In summary, the slight variation between the model and

reality resulted in strain peaks with offset z-locations and inconsistencies in magnitudes in regions of peak strain at an x-location of 10mm and 10.3mm.

While inaccuracies in modeling the exact specimen geometry proved to be the main reason for differences between modeled data and experimental results, the disparity was small when compared to overall results. As the full-field strain images and line plots indicate, the models developed for both repairs were very accurate for the most part and predicted the actual strain fields with undeniable accuracy.

When looking to the precision of the models, two main factors should be considered. First of all, the size of the repair modeled should be considered. In this case, both repairs were less than 2.54mm (0.1in) thick and 35mm (1.38in) wide. While great care was taken in making the models as close as possible to the actual specimens, the reality was that even enlarging microscopic images has its limitations. Second, the complexity of the models produced was also a factor. Even with the assumptions and simplifications made, both the scarf and stepped-lap joint pushed the processing capability of the computers available for analysis. Over one gigabyte of text files was necessary to produce BSAM output at the desired resolution, while the output files contained around 700 to 800 megabytes of strain data. The 374 clusters of the stepped-lap model ended up having over 80,000 degrees of freedom. According to one of the original programmers of the BSAM computer program, the models produced for this thesis were the most complicated models developed for and processed by BSAM up to this point.

This is not to say that no improvements could have been made in the execution of this thesis. On the contrary, the approach taken in both the computational and

experimental sides of this study could have been, and still can be, improved in several areas:

Manufacture of straight scarf joint

As this study proved, the quality of the scarf repair machined is pivotal to the accuracy of the results. This is especially the case when an experimental technique with high resolution, such as moiré interferometry, is used. While the thicker 16-ply laminate used in this thesis did provide a surface sufficient for the replication of diffraction grating, a $[+45_2/0_2/-45_2/90_2]_s$ lay-up is not appropriate when an extremely linear, straight scarf surface is desired. It is recommended that $[+45/0/-45/90]_{2s}$, or some kind of lay-up symmetric about the “quarter-plane,” should be used in future studies to minimize the effects of warping and curling during machining. Also, unless a skilled technician with extensive composite repair experience machines the repairs, some type of apparatus (such as the one made for this thesis) should be used. The fixture created for this study not only allows someone with minimal experience to machine a uniform scarf surface in a laboratory/research environment, but also ensures that each panel machined has an identical angle of the repair.

Theory versus reality of stepped-lap joints

While an ideal stepped-lap joint theoretically has perfectly square corners, the reality is that each step will have rounded corners. Even in a laboratory/research environment using diamond coated bits submerged in a water bath on a flat panel with a drill-bit accurate up to $(+/-)0.0005\text{in}$, the assumption that the resultant stepped-lap joint will have perfect 90° corners and steps is simply not true. To attain a more accurate comparison between strain data produced by BSAM and experimental data, every effort

should be made to accurately model rounded steps despite the scale and increased complexity of such a model.

Continue to refine the BSAM computer program's graphical user interface (GUI)

While the analytical capabilities of the BSAM computer program are impressive and robust, its current graphical user interface is marginal at best. While the program is not commercialized and continues to acquire new capability, developing a model in the program can be tedious, especially for the first time user. An advantage of the current input file system is that an existing model can easily be corrected and refined. However, with new models of increased complexity, generating the hundreds or thousands of lines of text style input files is a challenge. Because of this, it is recommended that the BSAM computer programmers continue to improve the program, specifically its graphical user interface in the immediate future.

As a final note, while the BSAM computer program provides a linear analysis and is able to approximate displacements, the experimental data should be considered to be more accurate of the two data sets (if further analysis of any data obtained in this study is desired). Although the experimental and analytical data compared favorably in this study, it is important to emphasize that the experimental data obtained through moiré interferometry was based off of actual displacement measurements, while analytical data produced by the BSAM computer program was a result of a model and theoretical approximations. Because of this, any discrepancies between predicted and experimental strain data should error in favor of experimental values. These experimental values provide the most accurate representation of the specimens' true mechanical behavior.

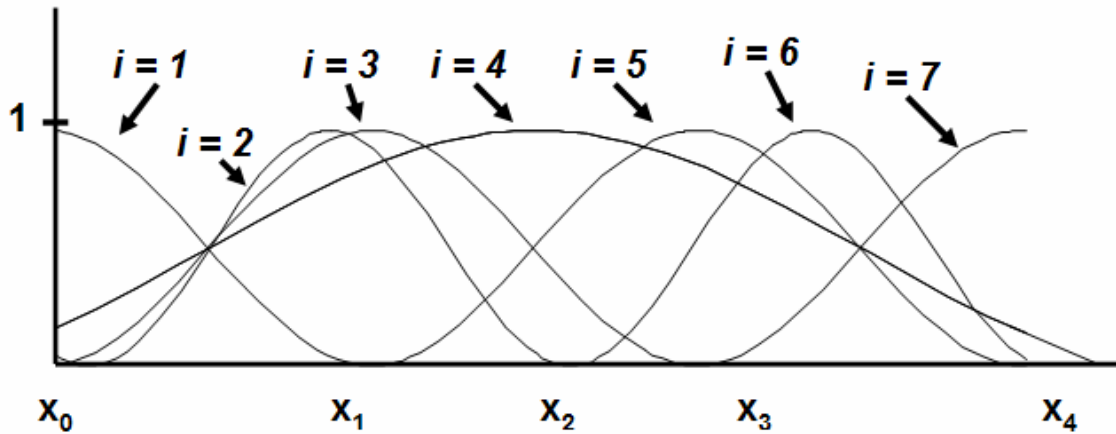
Appendix A: B-Spline Analysis Method: Theory, Equation Development, and Examples

The equations and spline developments contained in this appendix come from an informal handwritten document produced by Dr. Greg Schoeppner, a researcher at Air Force Research Laboratories at Wright-Patterson Air Force Base who contributed heavily the development of the BSAM computer program. The handout was converted into a Word document with the hope that it can be used as a reference guide for future users of the program as they attempt to learn the logic behind the BSAM computer program. It explains how displacements, strains, and stresses are solved for using the B-spline analysis method, stepping the reader through one-dimensional and two-dimensional examples using linear splines. With the exception of a few clarifying annotations, this document contains all of its original wording and grammar, so it remains informal in this sense.

We use cubic polynomials that are non-zero over an entire interval (except at the node). Why make them zero except over the 4 intervals of their local support? The reason is that if we make their local support small, then the stiffness matrix will be narrowly banded. It can be proven that using a basic support of 4 for cubic splines will give a total function that is twice continuously differentiable.

This results in a narrowly banded stiffness matrix that is easy to solve. The function itself is defined over the entire interval and is twice continuously differentiable.

For example:



$$u_x(x) = \sum x_i(x)C_i$$

$$u_x(x) = C_1X_1(x) + C_2X_2(x) + C_3X_3(x) + \dots + C_7X_7(x)$$

$X_i(x)$'s are the cubic spline functions built according to the recurrent procedure and C_i 's are constants that are to be determined. Given the displacements on the boundary, for example:

$$u_x(x_0) = 5 \quad \text{and} \quad u_x(x_4) = -5$$

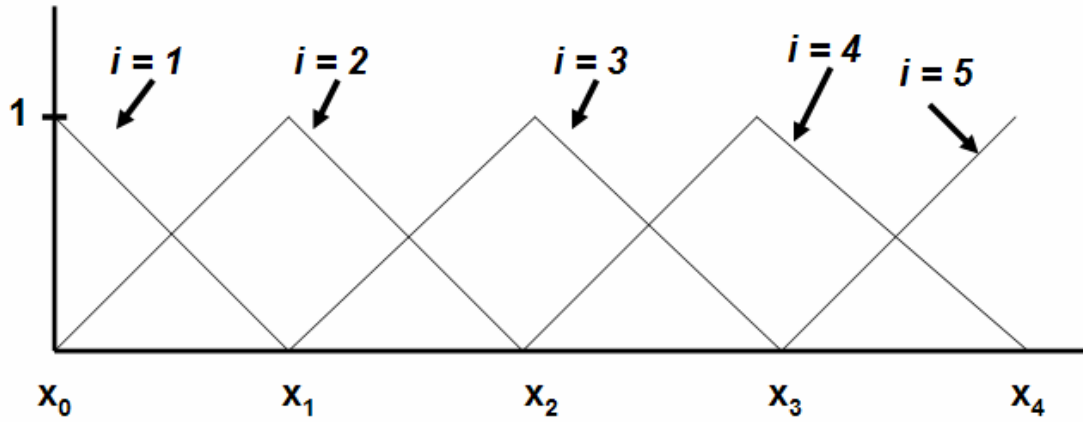
C_1 will be 5 and C_7 will be -5.

$C_2, C_3, C_4, C_5,$ and C_6 will be determined by the integral

$$\int \sigma_{ij} \epsilon_{ij} dV = \pi$$

As in the finite element method, displacements (u) are differentiated to get strains (ϵ_{ij}) and then Hooke's law is applied to get stresses (σ_{ij}). This integral can be done in closed form over each interval. Since we are actually solving $\delta\pi = 0$, we perturb each node an arbitrary amount and therefore this comes down to a set of linear equations for the C_i 's.

Example: Assume we have linear splines over $x_0 \leq x \leq x_4$



$$X_{1,1} = 1 - \frac{x - x_0}{x_1 - x_0} \quad \text{from } x_0 \leq x \leq x_1$$

$$X_{1,1} = 0 \quad \text{elsewhere}$$

$$X_{1,2} = \frac{x - x_0}{x_1 - x_0} \quad \text{from } x_0 \leq x \leq x_1$$

$$X_{1,2} = 1 - \frac{x_2 - x_1}{x_2 - x_1} \quad \text{from } x_1 \leq x \leq x_2$$

$$X_{1,2} = 0 \quad \text{elsewhere}$$

$$X_{1,3} = \frac{x - x_1}{x_2 - x_1} \quad \text{from } x_1 \leq x \leq x_2$$

$$X_{1,3} = \frac{x - x_2}{x_3 - x_2} \quad \text{from } x_2 \leq x \leq x_3$$

$$X_{1,3} = 0 \quad \text{elsewhere}$$

$$X_{1,4} = \frac{x - x_2}{x_3 - x_2} \quad \text{from } x_2 \leq x \leq x_3$$

$$X_{1,4} = \frac{x - x_3}{x_4 - x_3} \quad \text{from } x_3 \leq x \leq x_4$$

$$X_{1,4} = 0 \quad \text{elsewhere}$$

$$X_{1,5} = \frac{x - x_3}{x_4 - x_3} \quad \text{from } x_3 \leq x \leq x_4$$

$$X_{1,5} = 0 \quad \text{elsewhere}$$

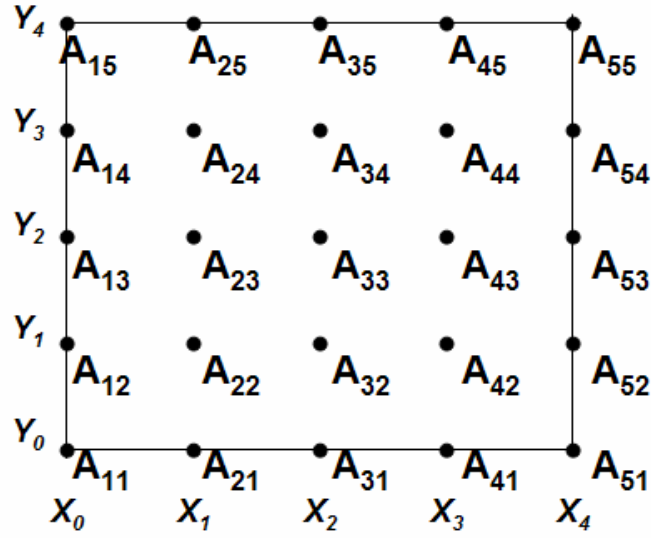
For these shape functions, $X_{j,i}$ where j represents the polynomial or spline function being used (in this case, 1 represents a linear approximation) and i represents the shape function segment being defined.

From these shape functions,

$$\begin{aligned}
 x_0 \leq x \leq x_1 \quad u_x(x) &= A_1 \left[1 - \frac{x-x_0}{x_1-x_0} \right] + A_2 \left[\frac{x-x_0}{x_1-x_0} \right] \\
 x_1 \leq x \leq x_2 \quad u_x(x) &= A_2 \left[1 - \frac{x-x_1}{x_2-x_1} \right] + A_3 \left[\frac{x-x_1}{x_2-x_1} \right] \\
 x_2 \leq x \leq x_3 \quad u_x(x) &= A_3 \left[1 - \frac{x-x_2}{x_3-x_2} \right] + A_4 \left[\frac{x-x_2}{x_3-x_2} \right] \\
 x_3 \leq x \leq x_4 \quad u_x(x) &= A_4 \left[1 - \frac{x-x_3}{x_4-x_3} \right] + A_5 \left[\frac{x-x_3}{x_4-x_3} \right]
 \end{aligned}$$

We can specify displacement at any node. For example, if $u_x(x_3) = 10$ is specified as a boundary condition then $A_4 = 10$. So any number of nodes can have a force or displacement.

Suppose we have a 2-D body (again with linear splines)



$u_x = \sum_{i=1}^5 \sum_{j=1}^5 A_{ij} X_{1,i} Y_{1,j}$ where $X_{1,i}$ are the same as previously described and $Y_{1,j}$ have a similar form.

Then

$$\begin{aligned}
 u_x = & A_{11} X_{1,1} Y_{1,1} + A_{12} X_{1,1} Y_{1,2} + A_{13} X_{1,1} Y_{1,3} + A_{14} X_{1,1} Y_{1,4} + A_{15} X_{1,1} Y_{1,5} \\
 & + A_{21} X_{1,2} Y_{1,1} + A_{22} X_{1,2} Y_{1,2} + \dots \\
 & + \dots \\
 & + \dots \\
 & + A_{51} X_{1,5} Y_{1,1} + \dots \qquad \dots + A_{55} X_{1,5} Y_{1,5}
 \end{aligned}$$

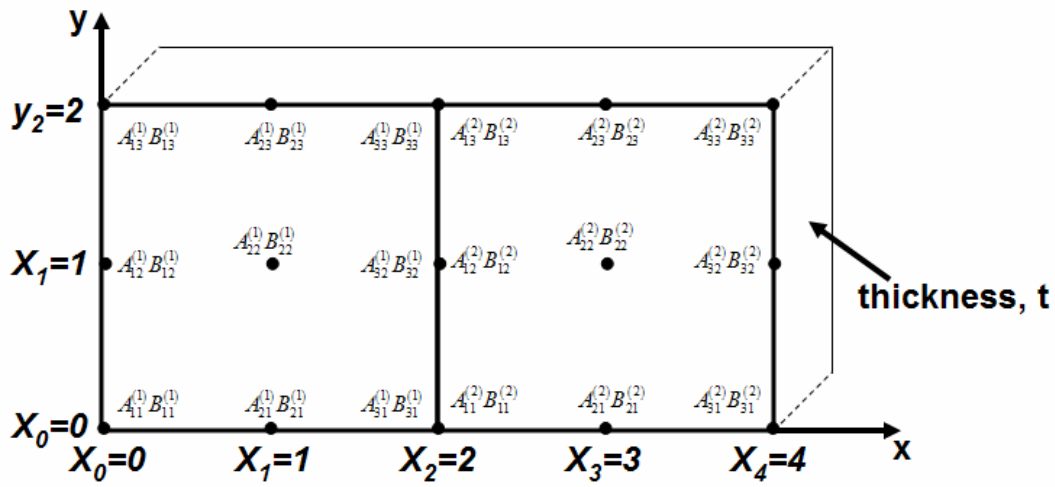
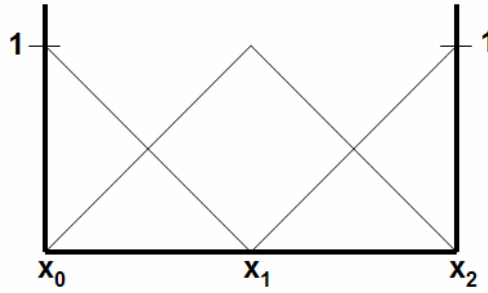
For the area $x_0 \leq x \leq x_1$
 $y_0 \leq y \leq y_1$

We have

$$\begin{aligned}
 u_x = & A_{11} \left[1 - \frac{x - x_0}{x_1 - x_0} \right] \left[1 - \frac{y - y_0}{y_1 - y_0} \right] + A_{12} \left[1 - \frac{x - x_0}{x_1 - x_0} \right] \left[\frac{y - y_0}{y_1 - y_0} \right] \\
 & + A_{21} \left[\frac{x - x_0}{x_1 - x_0} \right] \left[1 - \frac{y - y_0}{y_1 - y_0} \right] + A_{22} \left[\frac{x - x_0}{x_1 - x_0} \right] \left[\frac{y - y_0}{y_1 - y_0} \right]
 \end{aligned}$$

We can prescribe displacement boundary conditions at any of these nodal points. Assume linear splines.

Suppose we have 2 isotropic plates, plate 1 with E_1, ν_1 and plate 2 with E_2, ν_2



Let $u_x = 0$ on $x = 0$ and $u_x = 0.001m$ on $x = x_4$
and $u_y = 0$ on $x = 0$ and $u_y = 0$ on $x = x_4$

For plate 1:

$$X_{1,1}^{(1)} = 1 - \frac{x - x_0}{x_1 - x_0} = 1 - x \quad \text{from } x_0 \leq x \leq x_1$$

$$X_{1,1}^{(1)} = 0 \quad \text{elsewhere}$$

$$X_{1,2}^{(1)} = \frac{x - x_0}{x_1 - x_0} = x \quad \text{from } x_0 \leq x \leq x_1$$

$$X_{1,2}^{(1)} = 1 - \frac{x - x_1}{x_2 - x_1} = 2 - x \quad \text{from } x_1 \leq x \leq x_2$$

$$X_{1,2}^{(1)} = 0 \quad \text{elsewhere}$$

$$X_{1,3}^{(1)} = \frac{x - x_1}{x_2 - x_1} = x - 1 \quad \text{from} \quad x_1 \leq x \leq x_2$$

$$X_{1,3}^{(1)} = 0 \quad \text{elsewhere}$$

For plate 2:

$$X_{1,1}^{(2)} = 1 - \frac{x - x_2}{x_3 - x_2} = 3 - x \quad \text{from} \quad x_2 \leq x \leq x_3$$

$$X_{1,1}^{(2)} = 0 \quad \text{elsewhere}$$

$$X_{1,2}^{(2)} = 1 - \frac{x - x_2}{x_3 - x_2} = x - 2 \quad \text{from} \quad x_2 \leq x \leq x_3$$

$$X_{1,2}^{(2)} = 1 - \frac{x - x_3}{x_4 - x_3} = 4 - x \quad \text{from} \quad x_3 \leq x \leq x_4$$

$$X_{1,2}^{(2)} = 0 \quad \text{elsewhere}$$

$$X_{1,3}^{(2)} = \frac{x - x_3}{x_4 - x_3} = x - 3 \quad \text{from} \quad x_3 \leq x \leq x_4$$

$$X_{1,3}^{(2)} = 0 \quad \text{elsewhere}$$

For Plate 1:

$$Y_{1,1}^{(1)} = 1 - y \quad y_0 \leq y \leq y_1$$

$$Y_{1,1}^{(1)} = 0 \quad \text{elsewhere}$$

$$Y_{1,2}^{(1)} = y \quad y_0 \leq y \leq y_1$$

$$Y_{1,2}^{(1)} = 2 - y \quad y_1 \leq y \leq y_2$$

$$Y_{1,2}^{(1)} = 0 \quad \text{elsewhere}$$

$$Y_{1,3}^{(1)} = y - 1 \quad y_1 \leq y \leq y_2$$

$$Y_{1,3}^{(1)} = 0 \quad \text{elsewhere}$$

For Plate 2:

$$Y_{1,1}^{(2)} = 1 - y \quad y_0 \leq y \leq y_1$$

$$Y_{1,1}^{(2)} = 0 \quad \text{elsewhere}$$

$$Y_{1,2}^{(2)} = y \quad y_0 \leq y \leq y_1$$

$$Y_{1,2}^{(2)} = 2 - y \quad y_1 \leq y \leq y_2$$

$$Y_{1,2}^{(2)} = 0 \quad \text{elsewhere}$$

$$Y_{1,3}^{(2)} = y - 1 \quad y_1 \leq y \leq y_2$$

$$Y_{1,3}^{(2)} = 0 \quad \text{elsewhere}$$

$$u^{(1)}(x, y) = \sum_{i=1}^3 \sum_{j=1}^3 A_{ij}^{(1)} X_{1,i}^{(1)} Y_{1,j}^{(1)}$$

$$u^{(1)}(x, y) = A_{11}^{(1)} X_{1,1}^{(1)} Y_{1,1}^{(1)} + A_{12}^{(1)} X_{1,1}^{(1)} Y_{1,2}^{(1)} + A_{13}^{(1)} X_{1,1}^{(1)} Y_{1,3}^{(1)}$$

$$+ A_{21}^{(1)} X_{1,2}^{(1)} Y_{1,1}^{(1)} + A_{22}^{(1)} X_{1,2}^{(1)} Y_{1,2}^{(1)} + A_{23}^{(1)} X_{1,2}^{(1)} Y_{1,3}^{(1)}$$

$$+ A_{31}^{(1)} X_{1,3}^{(1)} Y_{1,1}^{(1)} + A_{32}^{(1)} X_{1,3}^{(1)} Y_{1,2}^{(1)} + A_{33}^{(1)} X_{1,3}^{(1)} Y_{1,3}^{(1)}$$

$$u^{(1)}(x, y) = A_{11}^{(1)} X_{1,1}^{(1)} Y_{1,1}^{(1)} + A_{12}^{(1)} X_{1,1}^{(1)} Y_{1,2}^{(1)} + A_{21}^{(1)} X_{1,2}^{(1)} Y_{1,1}^{(1)} + A_{22}^{(1)} X_{1,2}^{(1)} Y_{1,2}^{(1)} \quad x_0 \leq x \leq x_1 \quad y_0 \leq y \leq y_1$$

$$+ A_{13}^{(1)} X_{1,1}^{(1)} Y_{1,3}^{(1)} + A_{22}^{(1)} X_{1,2}^{(1)} Y_{1,2}^{(1)} + A_{23}^{(1)} X_{1,2}^{(1)} Y_{1,3}^{(1)} \quad x_0 \leq x \leq x_1 \quad y_1 \leq y \leq y_2$$

$$+ A_{21}^{(1)} X_{1,2}^{(1)} Y_{1,1}^{(1)} + A_{22}^{(1)} X_{1,2}^{(1)} Y_{1,2}^{(1)} + A_{31}^{(1)} X_{1,3}^{(1)} Y_{1,1}^{(1)} + A_{32}^{(1)} X_{1,3}^{(1)} Y_{1,2}^{(1)} \quad x_1 \leq x \leq x_2 \quad y_0 \leq y \leq y_1$$

$$+ A_{22}^{(1)} X_{1,2}^{(1)} Y_{1,2}^{(1)} + A_{23}^{(1)} X_{1,2}^{(1)} Y_{1,3}^{(1)} + A_{32}^{(1)} X_{1,3}^{(1)} Y_{1,2}^{(1)} + A_{33}^{(1)} X_{1,3}^{(1)} Y_{1,3}^{(1)} \quad x_1 \leq x \leq x_2 \quad y_1 \leq y \leq y_2$$

$$u^{(1)}(x, y) = A_{11}^{(1)}(1-x)(1-y) + A_{12}^{(1)}(1-x)(y) + A_{21}^{(1)}(x)(1-y) + A_{22}^{(1)}(x)(y) \quad x_0 \leq x \leq x_1 \quad y_0 \leq y \leq y_1$$

$$+ A_{12}^{(1)}(1-x)(2-y) + A_{13}^{(1)}(1-x)(y-1) + A_{22}^{(1)}(x)(2-y) + A_{23}^{(1)}(x)(y-1) \quad x_0 \leq x \leq x_1 \quad y_1 \leq y \leq y_2$$

$$+ A_{21}^{(1)}(2-x)(1-y) + A_{22}^{(1)}(2-x)(y) + A_{31}^{(1)}(x-1)(1-y) + A_{32}^{(1)}(x-1)(y) \quad x_1 \leq x \leq x_2 \quad y_0 \leq y \leq y_1$$

$$+ A_{22}^{(1)}(2-x)(2-y) + A_{23}^{(1)}(2-x)(y-1) + A_{32}^{(1)}(x-1)(2-y) + A_{33}^{(1)}(x-1)(y-1) \quad x_1 \leq x \leq x_2 \quad y_1 \leq y \leq y_2$$

We know $u_x = 0$ on $x = 0 \rightarrow A_{11}^{(1)} = A_{12}^{(1)} = A_{13}^{(1)} = 0$

Therefore,

$$u^{(1)}(x, y) = A_{21}^{(1)}(x)(1-y) + A_{22}^{(1)}(x)(y) \quad x_0 \leq x \leq x_1 \quad y_0 \leq y \leq y_1$$

$$+ A_{22}^{(1)}(x)(2-y) + A_{23}^{(1)}(x)(y-1) \quad x_0 \leq x \leq x_1 \quad y_1 \leq y \leq y_2$$

$$+ A_{21}^{(1)}(2-x)(1-y) + A_{22}^{(1)}(2-x)(y) + A_{31}^{(1)}(x-1)(1-y) + A_{32}^{(1)}(x-1)(y) \quad x_1 \leq x \leq x_2 \quad y_0 \leq y \leq y_1$$

$$+ A_{22}^{(1)}(2-x)(2-y) + A_{23}^{(1)}(2-x)(y-1) + A_{32}^{(1)}(x-1)(2-y) + A_{33}^{(1)}(x-1)(y-1) \quad x_1 \leq x \leq x_2 \quad y_1 \leq y \leq y_2$$

Similarly, because $v_y = 0$ on $x = 0 \rightarrow B_{11}^{(1)} = B_{12}^{(1)} = B_{13}^{(1)} = 0$

$$v^{(1)}(x, y) = B_{21}^{(1)}(x)(1-y) + B_{22}^{(1)}(x)(y) \quad x_0 \leq x \leq x_1 \quad y_0 \leq y \leq y_1$$

$$+ B_{22}^{(1)}(x)(2-y) + B_{23}^{(1)}(x)(y-1) \quad x_0 \leq x \leq x_1 \quad y_1 \leq y \leq y_2$$

$$+ B_{21}^{(1)}(2-x)(1-y) + B_{22}^{(1)}(2-x)(y) + B_{31}^{(1)}(x-1)(1-y) + B_{32}^{(1)}(x-1)(y) \quad x_1 \leq x \leq x_2 \quad y_0 \leq y \leq y_1$$

$$+ B_{22}^{(1)}(2-x)(2-y) + B_{23}^{(1)}(2-x)(y-1) + B_{32}^{(1)}(x-1)(2-y) + B_{33}^{(1)}(x-1)(y-1) \quad x_1 \leq x \leq x_2 \quad y_1 \leq y \leq y_2$$

Strains

$$\varepsilon_x^{(1)}(x, y) = \frac{\partial u}{\partial x}$$

$$\begin{aligned} \varepsilon_x^{(1)}(x, y) &= A_{21}^{(1)}(1-y) + A_{22}^{(1)}(y) & x_0 \leq x \leq x_1 & \quad y_0 \leq y \leq y_1 \\ &+ A_{22}^{(1)}(2-y) + A_{23}^{(1)}(y-1) & x_0 \leq x \leq x_1 & \quad y_1 \leq y \leq y_2 \\ &+ A_{21}^{(1)}(-1)(1-y) + A_{22}^{(1)}(-1)(y) + A_{31}^{(1)}(1-y) + A_{32}^{(1)}(y) & x_1 \leq x \leq x_2 & \quad y_0 \leq y \leq y_1 \\ &+ A_{22}^{(1)}(-1)(2-y) + A_{23}^{(1)}(-1)(y-1) + A_{32}^{(1)}(2-y) + A_{33}^{(1)}(y-1) & x_1 \leq x \leq x_2 & \quad y_1 \leq y \leq y_2 \end{aligned}$$

$$\varepsilon_y^{(1)}(x, y) = \frac{\partial v}{\partial y}$$

$$\begin{aligned} v^{(1)}(x, y) &= B_{21}^{(1)}(x)(-1) + B_{22}^{(1)}(x) & x_0 \leq x \leq x_1 & \quad y_0 \leq y \leq y_1 \\ &+ B_{22}^{(1)}(x)(-1) + B_{23}^{(1)}(x) & x_0 \leq x \leq x_1 & \quad y_1 \leq y \leq y_2 \\ &+ B_{21}^{(1)}(2-x)(-1) + B_{22}^{(1)}(2-x) + B_{31}^{(1)}(x-1)(-1) + B_{32}^{(1)}(x-1) & x_1 \leq x \leq x_2 & \quad y_0 \leq y \leq y_1 \\ &+ B_{22}^{(1)}(2-x)(-1) + B_{23}^{(1)}(2-x) + B_{32}^{(1)}(x-1)(-1) + B_{33}^{(1)}(x-1) & x_1 \leq x \leq x_2 & \quad y_1 \leq y \leq y_2 \end{aligned}$$

$$\varepsilon_{xy}^{(1)}(x, y) = \frac{\partial u}{\partial y} + \frac{\partial v}{\partial x}$$

$$\begin{aligned} \varepsilon_{xy}^{(1)}(x, y) &= A_{21}^{(1)}(x)(-1) + A_{22}^{(1)}(x) + B_{21}^{(1)}(1-y) + B_{22}^{(1)}(y) & x_0 \leq x \leq x_1 & \quad y_0 \leq y \leq y_1 \\ &+ A_{22}^{(1)}(x)(-1) + A_{23}^{(1)}(x) + B_{22}^{(1)}(2-y) + B_{23}^{(1)}(y-1) & x_0 \leq x \leq x_1 & \quad y_1 \leq y \leq y_2 \\ &+ A_{21}^{(1)}(2-x)(-1) + A_{22}^{(1)}(2-x) + A_{31}^{(1)}(x-1)(-1) + A_{32}^{(1)}(x-1) & x_1 \leq x \leq x_2 & \quad y_0 \leq y \leq y_1 \\ &+ B_{21}^{(1)}(-1)(1-y) + B_{22}^{(1)}(-1)(y) + B_{31}^{(1)}(1-y) + B_{32}^{(1)}(y) & & \\ &+ A_{22}^{(1)}(2-x)(-1) + A_{23}^{(1)}(2-x) + A_{32}^{(1)}(x-1)(-1) + A_{33}^{(1)}(x-1) & x_1 \leq x \leq x_2 & \quad y_1 \leq y \leq y_2 \\ &+ B_{22}^{(1)}(-1)(2-y) + B_{23}^{(1)}(-1)(y-1) + B_{32}^{(1)}(2-y) + B_{33}^{(1)}(y-1) & & \end{aligned}$$

For plane stress $\varepsilon_{zz} = -\frac{\nu}{E}(\sigma_{xx} + \sigma_{yy})$, $\sigma_{zz} = \sigma_{yz} = \sigma_{xz} = 0$

$$\text{And } \begin{Bmatrix} \sigma_{xx} \\ \sigma_{yy} \\ \sigma_{xy} \end{Bmatrix} = \frac{E}{1-\nu^2} \begin{bmatrix} 1 & \nu & 0 \\ \nu & 1 & 0 \\ 0 & 0 & 1/2(1-\nu) \end{bmatrix} \begin{Bmatrix} \varepsilon_{xx} \\ \varepsilon_{yy} \\ \varepsilon_{xy} \end{Bmatrix}$$

For plate 2 we determine the displacements $u^{(2)}$ and $v^{(2)}$ with prescribed displacements

$$\begin{aligned}
u^{(2)}(x, y) &= A_{11}^{(2)}(3-x)(1-y) + A_{12}^{(2)}(3-x)(y) + A_{21}^{(2)}(x-2)(1-y) + A_{22}^{(2)}(x-2)(y) & x_2 \leq x \leq x_3 \quad y_0 \leq y \leq y_1 \\
&+ A_{12}^{(2)}(3-x)(2-y) + A_{13}^{(2)}(3-x)(y-1) + A_{22}^{(2)}(x-2)(2-y) + A_{23}^{(2)}(x-2)(y-1) & x_2 \leq x \leq x_3 \quad y_1 \leq y \leq y_2 \\
&+ A_{21}^{(2)}(4-x)(1-y) + A_{22}^{(4)}(4-x)(y) + (0.001)(x-3)(1-y) + (0.001)(x-3)(y) & x_3 \leq x \leq x_4 \quad y_0 \leq y \leq y_1 \\
&+ A_{22}^{(2)}(4-x)(2-y) + A_{23}^{(2)}(4-x)(y-1) + (0.001)(x-3)(2-y) + (0.001)(x-3)(y-1) & x_3 \leq x \leq x_4 \quad y_1 \leq y \leq y_2 \\
\\
v^{(2)}(x, y) &= B_{11}^{(2)}(3-x)(1-y) + B_{12}^{(2)}(3-x)(y) + B_{21}^{(2)}(x-2)(1-y) + B_{22}^{(2)}(x-2)(y) & x_2 \leq x \leq x_3 \quad y_0 \leq y \leq y_1 \\
&+ B_{12}^{(2)}(3-x)(2-y) + B_{13}^{(2)}(3-x)(y-1) + B_{22}^{(2)}(x-2)(2-y) + B_{23}^{(2)}(x-2)(y-1) & x_2 \leq x \leq x_3 \quad y_1 \leq y \leq y_2 \\
&+ B_{21}^{(2)}(4-x)(1-y) + B_{22}^{(4)}(4-x)(y) & x_3 \leq x \leq x_4 \quad y_0 \leq y \leq y_1 \\
&+ B_{22}^{(2)}(4-x)(2-y) + B_{23}^{(2)}(4-x)(y-1) & x_3 \leq x \leq x_4 \quad y_1 \leq y \leq y_2
\end{aligned}$$

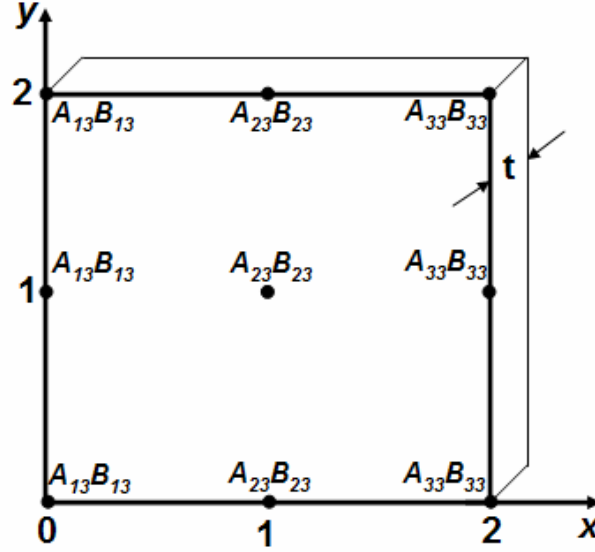
If we want displacement continuity between the plates, we must have

$$\begin{aligned}
u\text{-cont} \quad & A_{31}^{(1)} = A_{11}^{(2)}; \quad A_{32}^{(1)} = A_{12}^{(2)}; \quad A_{33}^{(1)} = A_{13}^{(2)} \\
v\text{-cont} \quad & B_{31}^{(1)} = B_{11}^{(2)}; \quad B_{32}^{(1)} = B_{12}^{(2)}; \quad B_{33}^{(1)} = B_{13}^{(2)}
\end{aligned}$$

We then apply the principle of minimum potential energy

$$\int_V (\delta \varepsilon_{xx} \sigma_{xx} + \delta \varepsilon_{yy} \sigma_{yy} + \delta \varepsilon_{xy} \sigma_{xy}) dx dy = \int_{\partial R_i} (\delta u t_x + \delta v t_y) dA$$

Solve a simple plane stress problem of stretching of an isotropic plate with E, ν (linear splines)



$$u = 0 \text{ on } x = 0$$

$$u = 0.001 \text{ on } x = 2$$

$$v = 0 \text{ on } x = 0 \text{ \& } x = 2$$

$$u(x, y) = A_{21}(x)(1-y) + A_{22}(x)(y) \quad 0 \leq x \leq 1 \quad 0 \leq y \leq 1$$

$$+ A_{22}(x)(2-y) + A_{23}(x)(y-1) \quad 0 \leq x \leq 1 \quad 1 \leq y \leq 2$$

$$+ A_{21}(2-x)(1-y) + A_{22}(2-x)(y) + 0.001(x-1)(1-y) + 0.001(x-1)(y) \quad 1 \leq x \leq 2 \quad 0 \leq y \leq 1$$

$$+ A_{22}(2-x)(2-y) + A_{23}(2-x)(y-1) + 0.001(x-1)(2-y) + 0.001(x-1)(y-1) \quad 1 \leq x \leq 2 \quad 1 \leq y \leq 2$$

$$v(x, y) = B_{21}(x)(1-y) + B_{22}(x)(y) \quad 0 \leq x \leq 1 \quad 0 \leq y \leq 1$$

$$+ B_{22}(x)(2-y) + B_{23}(x)(y-1) \quad 0 \leq x \leq 1 \quad 1 \leq y \leq 2$$

$$+ B_{21}(2-x)(1-y) + B_{22}(2-x)(y) \quad 1 \leq x \leq 2 \quad 0 \leq y \leq 1$$

$$+ B_{22}(2-x)(2-y) + B_{23}(2-x)(y-1) \quad 1 \leq x \leq 2 \quad 1 \leq y \leq 2$$

$$\varepsilon_x(x, y) = A_{21}(1-y) + A_{22}(y) \quad 0 \leq x \leq 1 \quad 0 \leq y \leq 1$$

$$+ A_{22}(2-y) + A_{23}(y-1) \quad 0 \leq x \leq 1 \quad 1 \leq y \leq 2$$

$$+ A_{21}(-1)(1-y) + A_{22}(-1)(y) + 0.001(1-y) + 0.001(y) \quad 1 \leq x \leq 2 \quad 0 \leq y \leq 1$$

$$+ A_{22}(-1)(2-y) + A_{23}(-1)(y-1) + 0.001(2-y) + 0.001(y-1) \quad 1 \leq x \leq 2 \quad 1 \leq y \leq 2$$

$$\begin{aligned}
\varepsilon_y(x, y) &= B_{21}(x)(-1) + B_{22}(x) & 0 \leq x \leq 1 & \quad 0 \leq y \leq 1 \\
&+ B_{22}(x)(-1) + B_{23}(x) & 0 \leq x \leq 1 & \quad 1 \leq y \leq 2 \\
&+ B_{21}(2-x)(-1) + B_{22}(2-x) & 1 \leq x \leq 2 & \quad 0 \leq y \leq 1 \\
&+ B_{22}(2-x)(-1) + B_{23}(2-x) & 1 \leq x \leq 2 & \quad 1 \leq y \leq 2
\end{aligned}$$

$$\begin{aligned}
\varepsilon_{xy}(x, y) &= A_{21}(x)(-1) + A_{22}(x) + B_{21}(1-y) + B_{22}(y) & 0 \leq x \leq 1 & \quad 0 \leq y \leq 1 \\
&+ A_{22}(x)(-1) + A_{23}(x) + B_{22}(2-y) + B_{23}(y-1) & 0 \leq x \leq 1 & \quad 1 \leq y \leq 2 \\
&+ A_{21}(2-x)(-1) + A_{22}(2-x) + 0.001(x-1)(-1) + 0.001(x-1) & 1 \leq x \leq 2 & \quad 0 \leq y \leq 1 \\
&+ B_{21}(1-y)(-1) + B_{22}(-1)(y) & & \\
&+ A_{22}(2-x)(-1) + A_{23}(2-x) + 0.001(x-1)(-1) + 0.001(x-1) & 1 \leq x \leq 2 & \quad 1 \leq y \leq 2 \\
&+ B_{22}(-1)(2-y) + B_{23}(-1)(y-1) & &
\end{aligned}$$

$$\sigma_x = \frac{E}{1-\nu^2}(\varepsilon_x + \nu\varepsilon_y)$$

$$\begin{aligned}
\sigma_x(x, y) &= \frac{E}{1-\nu^2}[A_{21}(1-y) + A_{22}(y) - \nu B_{21}(x) + \nu B_{22}(x) & 0 \leq x \leq 1 & \quad 0 \leq y \leq 1 \\
&+ A_{22}(2-y) + A_{23}(y-1) - \nu B_{22}(x) + \nu B_{23}(x) & 0 \leq x \leq 1 & \quad 1 \leq y \leq 2 \\
&- A_{21}(1-y) - A_{22}(y) + 0.001\nu(1-y) + 0.001\nu(y) & 1 \leq x \leq 2 & \quad 0 \leq y \leq 1 \\
&- \nu B_{21}(2-x) + \nu B_{22}(2-x) & & \\
&- A_{22}(2-y) - A_{23}(y-1) + 0.001\nu(2-y) + 0.001\nu(y-1) & 1 \leq x \leq 2 & \quad 1 \leq y \leq 2 \\
&- B_{22}(2-x) + B_{23}(2-x)] & &
\end{aligned}$$

$$\begin{aligned}
\sigma_y(x, y) &= \frac{E}{1-\nu^2}[\nu A_{21}(1-y) + \nu A_{22}(y) - B_{21}(x) + B_{22}(x) & 0 \leq x \leq 1 & \quad 0 \leq y \leq 1 \\
&+ \nu A_{22}(2-y) + \nu A_{23}(y-1) - B_{22}(x) + B_{23}(x) & 0 \leq x \leq 1 & \quad 1 \leq y \leq 2 \\
&- \nu A_{21}(1-y) - \nu A_{22}(y) + 0.001(1-y) + 0.001(y) & 1 \leq x \leq 2 & \quad 0 \leq y \leq 1 \\
&- B_{21}(2-x) + B_{22}(2-x) & & \\
&- \nu A_{22}(2-y) - \nu A_{23}(y-1) + 0.001(2-y) + 0.001(y-1) & 1 \leq x \leq 2 & \quad 1 \leq y \leq 2 \\
&- B_{22}(2-x) + B_{23}(2-x)] & &
\end{aligned}$$

$$\begin{aligned}
\sigma_{xy}(x, y) = & G[-A_{21}(x) + A_{22}(x) + B_{21}(1-y) + B_{22}(y) & 0 \leq x \leq 1 \quad 0 \leq y \leq 1 \\
& + A_{22}(x) + A_{23}(x) - B_{22}(2-y) + B_{23}(y-1) & 0 \leq x \leq 1 \quad 1 \leq y \leq 2 \\
& - A_{21}(2-x) - A_{22}(2-x) - 0.001(x-1) + 0.001(x-1) & 1 \leq x \leq 2 \quad 0 \leq y \leq 1 \\
& - B_{21}(1-y) - B_{22}(y) \\
& - A_{22}(2-x) - A_{23}(2-x) - 0.001(x-1) + 0.001(x-1) & 1 \leq x \leq 2 \quad 1 \leq y \leq 2 \\
& - B_{22}(2-y) - B_{23}(y-1)]
\end{aligned}$$

Principle of minimum potential energy

$$\delta\pi = \int_0^1 \int_0^1 \int_0^2 (\delta\varepsilon_x \sigma_x + \delta\varepsilon_y \sigma_y + \delta\varepsilon_{xy} \sigma_{xy}) dx dy dz - \int_{\partial R} (\delta u t_x + \delta v t_y) dA = 0$$

$$\begin{aligned}
\delta\pi = & \int_0^1 \int_0^1 \left[\frac{E}{1-\nu^2} (A_{21}(1-y) + A_{22}y - \nu B_{21}x + \nu B_{22}x) (\delta A_{21}(1-y) + \delta A_{22}y) \right. \\
& + \frac{E}{1-\nu^2} (\nu A_{21}(1-y) + \nu A_{22}y - B_{21}x + B_{22}x) (-\delta B_{21}x + \delta B_{22}y) \\
& + G(-A_{21}x + A_{22}x + B_{21}(1-y) + B_{22}y) (-\delta A_{21}x + \delta A_{22}y + \delta B_{21}(1-y) + \delta B_{22}y) \Big] dx dy \\
& + \int_0^1 \int_1^2 \left[\frac{E}{1-\nu^2} (A_{22}(2-y) + A_{23}(y-1) - \nu B_{22}x + \nu B_{23}x) (\delta A_{22}(2-y) + \delta A_{23}(y-1)) \right. \\
& + \frac{E}{1-\nu^2} (\nu A_{22}(2-y) + \nu A_{23}(y-1) - B_{22}x + B_{23}x) (-\delta B_{22}x + \delta B_{23}y) \\
& + G(-A_{22}x + A_{23}x + B_{22}(2-y) + B_{23}(y-1)) (-\delta A_{22}x + \delta A_{23}x + \delta B_{22}(2-y) + \delta B_{23}(y-1)) \Big] dx dy \\
& + \int_1^2 \int_0^1 \left[\frac{E}{1-\nu^2} (-A_{21}(1-y) - A_{22}(y) + 0.001\nu - \nu B_{21}(2-x) + \nu B_{22}(2-x)) (-\delta A_{21}(1-y) - \delta A_{22}(y)) \right. \\
& + \frac{E}{1-\nu^2} (-\nu A_{21}(1-y) - \nu A_{22}(y) + 0.001 - B_{21}(2-x) + B_{22}(2-x)) (-\delta B_{21}(2-x) + \delta B_{22}(2-x)) \\
& + G(-A_{21}(2-x) + A_{23}(2-x) - \cancel{0.001(x-1)} + \cancel{0.001(x-1)} - B_{21}(1-y) - B_{22}y)^* \\
& \left. (-\delta A_{21}(2-x) + \delta A_{22}(2-x) + \delta B_{21}(1-y) - \delta B_{22}(y)) \right] dx dy \\
& + \int_1^2 \int_1^2 \left[\frac{E}{1-\nu^2} (-A_{22}(2-y) - A_{23}(y-1) + 0.001\nu - \nu B_{22}(2-x) + \nu B_{23}(2-x)) (-\delta A_{22}(2-y) - \delta A_{23}(2-x)) \right. \\
& + \frac{E}{1-\nu^2} (-\nu A_{22}(2-y) - \nu A_{23}(y-1) + 0.001 - B_{22}(2-x) + B_{23}(2-x)) (-\delta B_{22}(2-x) + \delta B_{23}(2-x)) \\
& + G(-A_{22}(2-x) + A_{23}(2-x) - \cancel{0.001(x-1)} + \cancel{0.001(x-1)} - B_{22}(2-y) - B_{23}(y-1))^* \\
& \left. (-\delta A_{22}(2-x) + \delta A_{23}(2-x) + \delta B_{22}(2-y) - \delta B_{23}(y-1)) \right] dx dy
\end{aligned}$$

$$\begin{aligned}
\delta\pi = & t \int_0^1 \int_0^1 \left[\frac{E}{1-v^2} \left((1-y)^2 A_{21} \delta A_{21} + y(1-y) A_{22} \delta A_{21} - v(1-y) B_{21} x \delta A_{21} \right. \right. \\
& + (1-y) y A_{21} \delta A_{22} + y^2 A_{22} \delta A_{22} - vxy B_{21} \delta A_{22} + vxy B_{22} \delta A_{22} \\
& - v(1-y) x A_{21} \delta B_{21} - vxy A_{22} \delta B_{21} + x^2 B_{21} \delta B_{21} - x^2 B_{22} \delta B_{21} \\
& + v(1-y) x A_{21} \delta B_{22} + vxy A_{22} \delta B_{21} - x^2 B_{21} \delta B_{22} + x^2 B_{22} \delta B_{22} \Big) \\
& + G(x^2 A_{21} \delta A_{21} - x^2 A_{22} \delta A_{21} - (1-y) x B_{21} \delta A_{21} - xy B_{22} \delta B_{22} \\
& - x^2 A_{21} \delta A_{22} + x^2 A_{22} \delta A_{22} - (1-y) x B_{21} \delta A_{22} + xy B_{22} \delta A_{22} \\
& - (1-y) x A_{21} \delta B_{21} + (1-y) x A_{22} \delta B_{21} - (1-y)^2 B_{21} \delta B_{21} + (1-y) y B_{22} \delta B_{21} \\
& - xy A_{21} \delta B_{22} + xy A_{22} \delta B_{22} + (1-y) y B_{21} \delta B_{22} + y^2 B_{22} \delta B_{22} \Big) dx dy \\
& + t \int_0^1 \int_1^2 \left[\frac{E}{1-v^2} \left((2-y)^2 A_{22} \delta A_{22} + (y-1)(2-y) A_{23} \delta A_{22} - v(2-y) x B_{22} \delta A_{22} + v(2-y) x B_{23} \delta A_{22} \right. \right. \\
& + (2-y)(y-1) A_{22} \delta A_{23} + (y-1)^2 A_{23} \delta A_{23} - v(y-1) x B_{22} \delta A_{23} + v(y-1) x B_{23} \delta A_{23} \\
& - v(2-y) x A_{22} \delta B_{22} - v(y-1) x A_{23} \delta B_{22} + x^2 B_{22} \delta B_{22} - x^2 B_{23} \delta B_{22} \\
& + v(2-y) x A_{22} \delta B_{23} + v(y-1) x A_{23} \delta B_{23} + x^2 B_{22} \delta B_{23} + x^2 B_{23} \delta B_{23} \Big) \\
& + G(x^2 A_{22} \delta A_{22} - x^2 A_{23} \delta A_{22} - (2-y) x B_{22} \delta A_{22} - (y-1) x B_{23} \delta A_{22} \\
& - x^2 A_{22} \delta A_{23} + x^2 A_{23} \delta A_{23} + (2-y) x B_{22} \delta A_{23} + (y-1) x B_{23} \delta A_{23} \\
& - (2-y) x A_{22} \delta B_{22} + (2-y) x A_{23} \delta B_{22} + (2-y)^2 B_{22} \delta B_{22} + (1-y)(2-y) B_{23} \delta B_{22} \\
& - (y-1) x A_{22} \delta B_{23} + (y-1) x A_{23} \delta B_{23} + (2-y)(y-1) B_{22} \delta B_{23} + (y-1)^2 B_{23} \delta B_{23} \Big) dx dy \\
& + t \int_1^2 \int_0^1 \left[\frac{E}{1-v^2} \left((1-y)^2 A_{21} \delta A_{21} + y(1-y) A_{22} \delta A_{21} - 0.001(1-y) \delta A_{21} + v(1-y)(2-x) B_{21} \delta A_{21} \right. \right. \\
& - v(1-y)(2-x) B_{22} \delta A_{21} + (1-y) y A_{21} \delta A_{22} - y^2 A_{22} \delta A_{22} \\
& - 0.001vy \delta A_{22} - vy(2-x) B_{21} \delta A_{22} - vy(2-x) B_{22} \delta A_{22} \\
& + v(1-y)(2-x) A_{21} \delta B_{21} + vy(2-x) A_{22} \delta B_{21} - 0.001v(2-x) \delta B_{21} \\
& + (2-x)^2 B_{21} \delta B_{21} + (2-x)^2 B_{22} \delta B_{21} - v(1-y)(2-x) A_{21} \delta B_{22} \\
& + vy(2-x) A_{22} \delta B_{22} + 0.001v(2-x) \delta B_{22} - (2-x)^2 B_{21} \delta B_{22} + (2-x)^2 B_{22} \delta B_{22} \Big) \\
& + G((2-x)^2 A_{21} \delta A_{21} - (2-x)^2 A_{22} \delta A_{21} + (1-y)(2-x) B_{21} \delta A_{21} + y(2-x) B_{22} \delta A_{21} \\
& - (2-x)^2 A_{21} \delta A_{22} + (2-x)^2 A_{22} \delta A_{22} - (1-y)(2-x) B_{21} \delta A_{22} - y(2-x) B_{22} \delta A_{22} \\
& + (1-y)(2-x) A_{21} \delta B_{21} - (1-y)(2-x) A_{22} \delta B_{21} + (1-y)^2 B_{21} \delta B_{21} \\
& + y(1-y) B_{22} \delta B_{21} + y(2-x) A_{21} \delta B_{22} - (2-x) A_{22} \delta B_{22} \\
& + (1-y) y B_{21} \delta B_{22} + y^2 B_{22} \delta B_{22} \Big) dx dy
\end{aligned}$$

cont...

$$\begin{aligned}
& + t \int_1^2 \int_1^2 \left[\frac{E}{1-v^2} ((2-y)^2 A_{22} \delta A_{22} + (2-y)(y-1) A_{23} \delta A_{22} - 0.001(2-y) \delta A_{22} \right. \\
& + v(2-y)(2-x) B_{22} \delta A_{22} - v(2-y)(2-x) B_{23} \delta A_{22} + (2-y)(y-1) A_{22} \delta A_{23} \\
& + (y-1)^2 A_{23} \delta A_{23} - 0.001v(y-1) \delta A_{23} + v(y-1)(2-x) B_{22} \delta A_{23} \\
& - v(y-1)(2-x) B_{23} \delta A_{23} + v(2-y)(2-x) A_{22} \delta B_{22} + v(y-1)(2-x) A_{23} \delta B_{22} \\
& - 0.001v(2-x) \delta B_{22} + (2-x)^2 B_{22} \delta B_{22} - (2-x)^2 B_{23} \delta B_{22} - v(2-y)(2-x) A_{22} \delta B_{23} \\
& - v(y-1)(2-x) A_{23} \delta B_{23} + 0.001v(2-x) \delta B_{23} - (2-x)^2 B_{22} \delta B_{23} + (2-x)^2 B_{23} \delta B_{23}) \\
& + G((2-x)^2 A_{22} \delta A_{22} - (2-x)^2 A_{23} \delta A_{22} - (2-y)(2-x) B_{22} \delta A_{22} \\
& + (y-1)(2-x) B_{23} \delta A_{22} - (2-x)^2 A_{22} \delta A_{23} + (2-x)^2 A_{23} \delta A_{23} \\
& - (2-y)(2-x) B_{22} \delta A_{23} - (y-1)(2-x) B_{23} \delta A_{23} + (2-y)(2-x) A_{22} \delta B_{22} \\
& - (2-y)(2-x) A_{23} \delta B_{22} + (2-y)^2 B_{22} \delta B_{22} + (2-y)(y-1) B_{23} \delta B_{22} \\
& + (y-1)(2-x) A_{22} \delta B_{23} - (y-1)(2-x) A_{23} \delta B_{23} - (y-1)(2-y) B_{22} \delta B_{23} \\
& \left. + (y-1)^2 B_{23} \delta B_{23}) \right] dx dy
\end{aligned}$$

$$\begin{aligned}
\delta\pi = & t \left[\frac{E}{1-v^2} \left(\frac{1}{3} A_{21} \delta A_{21} + \frac{1}{6} A_{22} \delta A_{21} - \frac{v}{4} B_{21} \delta A_{21} + \frac{v}{4} B_{22} \delta A_{21} \right. \right. \\
& + \frac{1}{6} A_{21} \delta A_{22} + \frac{1}{3} A_{22} \delta A_{22} - \frac{v}{4} B_{21} \delta A_{22} + \frac{v}{4} B_{22} \delta A_{22} \\
& - \frac{v}{4} A_{21} \delta B_{21} - \frac{v}{4} A_{22} \delta B_{21} + \frac{1}{3} B_{21} \delta B_{21} - \frac{1}{3} B_{22} \delta B_{21} \\
& + \frac{v}{4} A_{21} \delta B_{22} + \frac{v}{4} A_{22} \delta B_{21} - \frac{1}{3} B_{21} \delta B_{22} + \frac{1}{3} B_{22} \delta B_{22} \left. \right) \\
& + G \left(\frac{1}{3} A_{21} \delta A_{21} - \frac{1}{3} A_{22} \delta A_{21} - \frac{1}{4} B_{21} \delta A_{21} - \frac{1}{4} B_{22} \delta A_{21} \right. \\
& - \frac{1}{3} A_{21} \delta A_{22} + \frac{1}{3} A_{22} \delta A_{22} + \frac{1}{4} B_{21} \delta A_{22} + \frac{1}{4} B_{22} \delta A_{22} \\
& - \frac{1}{4} A_{21} \delta B_{21} + \frac{1}{4} A_{22} \delta B_{21} + \frac{1}{3} B_{21} \delta B_{21} + \frac{1}{6} B_{22} \delta B_{21} \\
& - \frac{1}{4} A_{21} \delta B_{22} + \frac{1}{4} A_{22} \delta B_{22} + \frac{1}{6} B_{21} \delta B_{22} + \frac{1}{3} B_{22} \delta B_{22} \left. \right) \\
& + \frac{E}{1-v^2} \left(\frac{1}{3} A_{22} \delta A_{22} + \frac{1}{6} A_{23} \delta A_{22} - \frac{v}{4} B_{22} \delta A_{22} + \frac{v}{4} B_{23} \delta A_{22} \right. \\
& + \frac{1}{6} A_{22} \delta A_{23} + \frac{1}{3} A_{23} \delta A_{23} - \frac{v}{4} B_{22} \delta A_{23} + \frac{v}{4} B_{23} \delta A_{23} \\
& - \frac{v}{4} A_{22} \delta B_{22} - \frac{v}{4} A_{23} \delta B_{22} + \frac{1}{3} B_{22} \delta B_{22} - \frac{1}{3} B_{23} \delta B_{22} \\
& + \frac{v}{4} A_{22} \delta B_{23} + \frac{v}{4} A_{23} \delta B_{23} - \frac{1}{3} B_{22} \delta B_{23} + \frac{1}{3} B_{23} \delta B_{23} \left. \right) \\
& + G \left(\frac{1}{3} A_{22} \delta A_{22} - \frac{1}{3} A_{23} \delta A_{22} - \frac{1}{4} B_{22} \delta A_{22} - \frac{1}{4} B_{23} \delta A_{22} \right. \\
& - \frac{1}{3} A_{22} \delta A_{23} + \frac{1}{3} A_{23} \delta A_{23} + \frac{1}{4} B_{22} \delta A_{23} + \frac{1}{4} B_{23} \delta A_{23} \\
& - \frac{1}{4} A_{22} \delta B_{22} + \frac{1}{4} A_{23} \delta B_{22} + \frac{1}{3} B_{22} \delta B_{22} + \frac{1}{6} B_{23} \delta B_{22} \\
& - \frac{1}{4} A_{22} \delta B_{23} + \frac{1}{4} A_{23} \delta B_{23} + \frac{1}{6} B_{22} \delta B_{23} + \frac{1}{3} B_{23} \delta B_{23} \left. \right)
\end{aligned}$$

Continued...

$$\begin{aligned}
& + \frac{E}{1-v^2} \left(\frac{1}{3} A_{21} \delta A_{21} + \frac{1}{6} A_{22} \delta A_{21} - \frac{1}{2} 0.001 \delta A_{21} + \frac{v}{4} B_{21} \delta A_{21} \right. \\
& - \frac{v}{4} B_{22} \delta A_{21} + \frac{1}{6} A_{21} \delta A_{22} - \frac{1}{3} A_{22} \delta A_{22} \\
& - 0.001 \left(\frac{1}{2} \right) \delta A_{22} - \frac{v}{4} B_{21} \delta A_{22} - \frac{v}{4} B_{22} \delta A_{22} \\
& + \frac{v}{4} A_{21} \delta B_{21} + \frac{v}{4} A_{22} \delta B_{21} - 0.001 \left(\frac{1}{2} \right) \delta B_{21} \\
& + \frac{1}{3} B_{21} \delta B_{21} - \frac{1}{3} B_{22} \delta B_{21} - \frac{v}{4} A_{21} \delta B_{22} \\
& - \frac{v}{4} A_{22} \delta B_{22} + 0.001 \left(\frac{1}{2} \right) \delta B_{22} - \frac{1}{3} B_{21} \delta B_{22} + \frac{1}{3} B_{22} \delta B_{22} \Big) \\
& + G \left(\frac{1}{3} A_{21} \delta A_{21} - \frac{1}{3} A_{22} \delta A_{21} + \frac{1}{4} B_{21} \delta A_{21} + \frac{1}{4} B_{22} \delta A_{21} \right. \\
& - \frac{1}{3} A_{21} \delta A_{22} + \frac{1}{3} A_{22} \delta A_{22} - \frac{1}{4} B_{21} \delta A_{22} - \frac{1}{4} B_{22} \delta A_{22} \\
& + \frac{1}{4} A_{21} \delta B_{21} - \frac{1}{4} A_{22} \delta B_{21} + \frac{1}{3} B_{21} \delta B_{21} \\
& + \frac{1}{6} B_{22} \delta B_{21} + \frac{1}{4} A_{21} \delta B_{22} - \frac{1}{4} A_{22} \delta B_{22} \\
& + \frac{1}{6} B_{21} \delta B_{22} + \frac{1}{3} B_{22} \delta B_{22} \Big) \\
& + \frac{E}{1-v^2} \left(\frac{1}{3} A_{22} \delta A_{22} + \frac{1}{6} A_{23} \delta A_{22} - 0.001 \left(\frac{1}{2} \right) \delta A_{22} \right. \\
& + \frac{v}{4} B_{22} \delta A_{22} - \frac{v}{4} B_{23} \delta A_{22} + \frac{1}{6} A_{22} \delta A_{23} \\
& + \frac{1}{3} A_{23} \delta A_{23} - 0.001 \left(\frac{1}{2} \right) \delta A_{23} + \frac{v}{4} B_{22} \delta A_{22} \\
& - \frac{v}{4} B_{23} \delta A_{23} + \frac{v}{4} A_{22} \delta B_{22} + \frac{v}{4} A_{23} \delta B_{22} \\
& - 0.001 \left(\frac{1}{2} \right) \delta B_{22} + \frac{1}{3} B_{22} \delta B_{22} - \frac{1}{3} B_{23} \delta B_{22} - \frac{v}{4} A_{22} \delta B_{23} \\
& - \frac{v}{4} A_{23} \delta B_{23} + 0.001 \left(\frac{1}{2} \right) \delta B_{23} - \frac{1}{3} B_{22} \delta B_{23} + \frac{1}{3} B_{23} \delta B_{23} \Big)
\end{aligned}$$

Continued...

$$\begin{aligned}
& +G(\frac{1}{3}A_{22}\delta A_{22}-\frac{1}{3}A_{23}\delta A_{22}+\frac{1}{4}B_{22}\delta A_{22}+\frac{1}{4}B_{23}\delta A_{22} \\
& -\frac{1}{3}A_{22}\delta A_{23}+\frac{1}{3}A_{23}\delta A_{23}-\frac{1}{4}B_{22}\delta A_{23}-\frac{1}{4}B_{23}\delta A_{23} \\
& +\frac{1}{4}A_{22}\delta B_{22}-\frac{1}{4}A_{23}\delta B_{22}+\frac{1}{3}B_{22}\delta B_{22}+\frac{1}{6}B_{23}\delta B_{22} \\
& +\frac{1}{4}A_{22}\delta B_{23}-\frac{1}{4}A_{23}\delta B_{23}+\frac{1}{6}B_{22}\delta B_{23}+\frac{1}{3}B_{23}\delta B_{23})]
\end{aligned}$$

$$\begin{aligned}
\delta\pi = & t[\frac{E}{1-v^2}(\frac{1}{3}A_{21}+\frac{1}{6}A_{22}-\frac{v}{4}B_{21}+\frac{v}{4}B_{22}+\frac{1}{3}A_{21}+\frac{1}{6}A_{22}-\left(\frac{1}{2}\right)0.001+\frac{v}{4}B_{21}-\frac{v}{4}B_{22}) \\
& +G(\frac{1}{3}A_{21}-\frac{1}{3}A_{22}-\frac{1}{4}B_{21}-\frac{1}{4}B_{22}+\frac{1}{3}A_{21}-\frac{1}{3}A_{22}+\frac{v}{4}B_{21}-\frac{v}{4}B_{22})]\delta A_{21} \\
& +[\frac{E}{1-v^2}(\frac{1}{6}A_{21}+\frac{1}{3}A_{22}-\frac{v}{4}B_{21}+\frac{v}{4}B_{22}+\frac{1}{3}A_{22}+\frac{1}{6}A_{23}-\frac{v}{4}B_{22}+\frac{v}{4}B_{23} \\
& +\frac{1}{6}A_{21}+\frac{1}{3}A_{22}-\left(\frac{1}{2}\right)0.001+\frac{v}{4}B_{21}-\frac{v}{4}B_{22}+\frac{1}{3}A_{22}+\frac{1}{6}A_{23}-\left(\frac{1}{2}\right)0.001+\frac{v}{4}B_{22}-\frac{v}{4}B_{23}) \\
& +G(-\frac{1}{3}A_{21}+\frac{1}{3}A_{22}+\frac{1}{4}B_{21}+\frac{1}{4}B_{22}+\frac{1}{3}A_{22}-\frac{1}{3}A_{23}-\frac{1}{4}B_{22}-\frac{1}{4}B_{23} \\
& -\frac{1}{3}A_{21}+\frac{1}{3}A_{22}-\frac{1}{4}B_{21}-\frac{1}{4}B_{22}+\frac{1}{3}A_{22}-\frac{1}{3}A_{23}+\frac{1}{4}B_{22}+\frac{1}{4}B_{23})]\delta A_{22} \\
& +[\frac{E}{1-v^2}(\frac{1}{6}A_{22}+\frac{1}{3}A_{23}-\frac{v}{4}B_{22}+\frac{v}{4}B_{23}+\frac{1}{6}A_{22}+\frac{1}{3}A_{23}-\left(\frac{1}{2}\right)0.001+\frac{v}{4}B_{22}-\frac{v}{4}B_{23}) \\
& +G(-\frac{1}{3}A_{22}+\frac{1}{3}A_{23}+\frac{1}{4}B_{22}+\frac{1}{4}B_{23}-\frac{1}{3}A_{22}+\frac{1}{3}A_{23}-\frac{1}{4}B_{22}-\frac{1}{4}B_{23})]\delta A_{23} \\
& +[\frac{E}{1-v^2}(-\frac{v}{4}A_{21}-\frac{v}{4}A_{22}+\frac{1}{3}B_{21}-\frac{1}{3}B_{22}+\frac{v}{4}A_{21}+\frac{v}{4}A_{22}-\left(\frac{1}{2}\right)0.001+\frac{1}{3}B_{21}-\frac{1}{3}B_{22}) \\
& +G(-\frac{1}{4}A_{21}+\frac{1}{4}A_{22}+\frac{1}{3}B_{21}+\frac{1}{6}B_{22}+\frac{1}{4}A_{21}-\frac{1}{4}A_{22}+\frac{1}{3}B_{21}+\frac{1}{6}B_{22})]\delta B_{21}
\end{aligned}$$

Continued...

$$\begin{aligned}
& + [\frac{E}{1-v^2} (\cancel{\frac{v}{4}A_{21}} + \cancel{\frac{v}{4}A_{22}} - \frac{1}{3}B_{21} + \frac{1}{3}B_{22} - \cancel{\frac{v}{4}A_{22}} - \cancel{\frac{v}{4}A_{23}} + \frac{1}{3}B_{22} - \frac{1}{3}B_{23} \\
& - \cancel{\frac{v}{4}A_{21}} - \cancel{\frac{v}{4}A_{22}} + \cancel{\frac{v}{2}0.001} - \frac{1}{3}B_{21} + \frac{1}{3}B_{22} + \cancel{\frac{v}{4}A_{22}} + \cancel{\frac{v}{4}A_{23}} - \cancel{\frac{v}{2}0.001} \\
& + \frac{1}{3}B_{21} - \frac{1}{3}B_{22}) \\
& + G(-\cancel{\frac{1}{4}A_{21}} + \cancel{\frac{1}{4}A_{22}} + \frac{1}{6}B_{21} + \frac{1}{3}B_{22} - \cancel{\frac{1}{4}A_{22}} + \cancel{\frac{1}{4}A_{23}} + \frac{1}{3}B_{22} + \frac{1}{6}B_{23} \\
& + \cancel{\frac{1}{4}A_{21}} - \cancel{\frac{1}{4}A_{22}} + \frac{1}{6}B_{21} + \frac{1}{3}B_{22} + \cancel{\frac{1}{4}A_{22}} - \cancel{\frac{1}{4}A_{23}} + \frac{1}{3}B_{22} + \frac{1}{6}B_{23})\delta B_{22} \\
& + [\frac{E}{1-v^2} (\cancel{\frac{v}{4}A_{22}} + \cancel{\frac{v}{4}A_{23}} - \frac{1}{3}B_{22} + \frac{1}{3}B_{23} - \cancel{\frac{v}{4}A_{22}} - \cancel{\frac{v}{4}A_{23}} + \left(\frac{1}{2}\right)0.001 - \frac{1}{3}B_{22} + \frac{1}{3}B_{23}) \\
& + G(-\cancel{\frac{1}{4}A_{22}} + \cancel{\frac{1}{4}A_{23}} + \frac{1}{6}B_{22} + \frac{1}{3}B_{23} + \cancel{\frac{1}{4}A_{22}} - \cancel{\frac{1}{4}A_{23}} + \frac{1}{6}B_{22} + \frac{1}{3}B_{23})\delta B_{23}
\end{aligned}$$

$$\begin{aligned}
\delta\pi = & t[\frac{E}{1-v^2} (\frac{2}{3}A_{21} + \frac{1}{3}A_{22} - \left(\frac{1}{2}\right)0.001) + G(\frac{2}{3}A_{21} - \frac{2}{3}A_{22})]\delta A_{21} \\
& + [\frac{E}{1-v^2} (\frac{1}{3}A_{21} + \frac{4}{3}A_{22} + \frac{1}{3}A_{23} - 0.001) + G(-\frac{2}{3}A_{21} + \frac{4}{3}A_{22} - \frac{2}{3}A_{23})]\delta A_{22} \\
& + [\frac{E}{1-v^2} (\frac{1}{3}A_{22} + \frac{2}{3}A_{23} - \left(\frac{1}{2}\right)0.001) + G(-\frac{2}{3}A_{22} + \frac{2}{3}A_{23})]\delta A_{23} \\
& + [\frac{E}{1-v^2} (\frac{2}{3}B_{21} - \frac{2}{3}B_{22} - \left(\frac{1}{2}\right)0.001) + G(\frac{2}{3}B_{21} + \frac{1}{3}B_{22})]\delta B_{21} \\
& + [\frac{E}{1-v^2} (-\frac{2}{3}B_{21} + \frac{4}{3}B_{22} + \frac{2}{3}B_{23}) + G(\frac{1}{3}B_{21} + \frac{4}{3}B_{22} + \frac{1}{3}B_{23})]\delta B_{22} \\
& + [\frac{E}{1-v^2} (-\frac{2}{3}B_{22} + \frac{2}{3}B_{23} + \left(\frac{1}{2}\right)0.001) + G(\frac{1}{3}B_{22} + \frac{2}{3}B_{23})]\delta B_{23}
\end{aligned}$$

$$\begin{bmatrix}
\frac{2}{3}\left(\frac{E}{1-v^2}+G\right) & \frac{1}{3}\left(\frac{E}{1-v^2}-2G\right) & 0 & 0 & 0 & 0 \\
\frac{1}{3}\left(\frac{E}{1-v^2}-2G\right) & \frac{4}{3}\left(\frac{E}{1-v^2}+G\right) & \frac{1}{3}\left(\frac{E}{1-v^2}-2G\right) & 0 & 0 & 0 \\
0 & \frac{1}{3}\left(\frac{E}{1-v^2}-2G\right) & \frac{2}{3}\left(\frac{E}{1-v^2}+G\right) & 0 & 0 & 0 \\
0 & 0 & 0 & \frac{2}{3}\left(\frac{E}{1-v^2}+G\right) & \frac{1}{3}\left(-2\frac{E}{1-v^2}+G\right) & 0 \\
0 & 0 & 0 & \frac{1}{3}\left(-2\frac{E}{1-v^2}+G\right) & \frac{4}{3}\left(\frac{E}{1-v^2}+G\right) & \frac{1}{3}\left(-2\frac{E}{1-v^2}+G\right) \\
0 & 0 & 0 & 0 & \frac{1}{3}\left(-2\frac{E}{1-v^2}+G\right) & \frac{2}{3}\left(\frac{E}{1-v^2}+G\right)
\end{bmatrix}
\begin{bmatrix}
A_{21} \\
A_{22} \\
A_{23} \\
B_{21} \\
B_{22} \\
B_{23}
\end{bmatrix}
=
\begin{bmatrix}
\frac{1}{2}(0.001) \\
(0.001) \\
\frac{1}{2}(0.001) \\
\frac{v}{2}(0.001) \\
0 \\
-\frac{v}{2}(0.001)
\end{bmatrix}$$

Appendix B: Computational Modeling of Specimens

The following appendix outlines the modification of the BSAM computer program input files for the scarf and stepped-lap specimens analyzed in this thesis. While the BSAM program is very capable and has refined analytical capabilities, it is not a commercialized code. Because of this, it has an undeveloped graphical user interface (GUI) and little documentation exists on the modification or creation of input files. As such, only a limited number of individuals currently have the knowledge of and experience with BSAM to tackle complex problems. The purpose of this appendix is to explain how BSAM input files were modified to model the stepped-lap and scarf joints analyzed in this thesis. Furthermore, it is hoped that this document will provide some insight into the logic and modification of a BSAM input file and provide future users with an example for reference purposes.

According to one of the BSAM computer code's programmers, the most efficient way to generate a BSAM input file is to build or modify the input file from the bottom up, starting at the end of the input file and working backward. While it may seem counterintuitive, the segments at the end of the input file build the foundation for the model. Starting from the bottom or back of the input file, each input block supplies information for preceding input blocks or sections. In other words, looking from the opposite direction (from top to bottom) each input block/section draws upon information and variables contained in subsequent blocks. A flowchart that shows how these building blocks build a foundation for the program eventually leading to the process can be seen Figure 130.

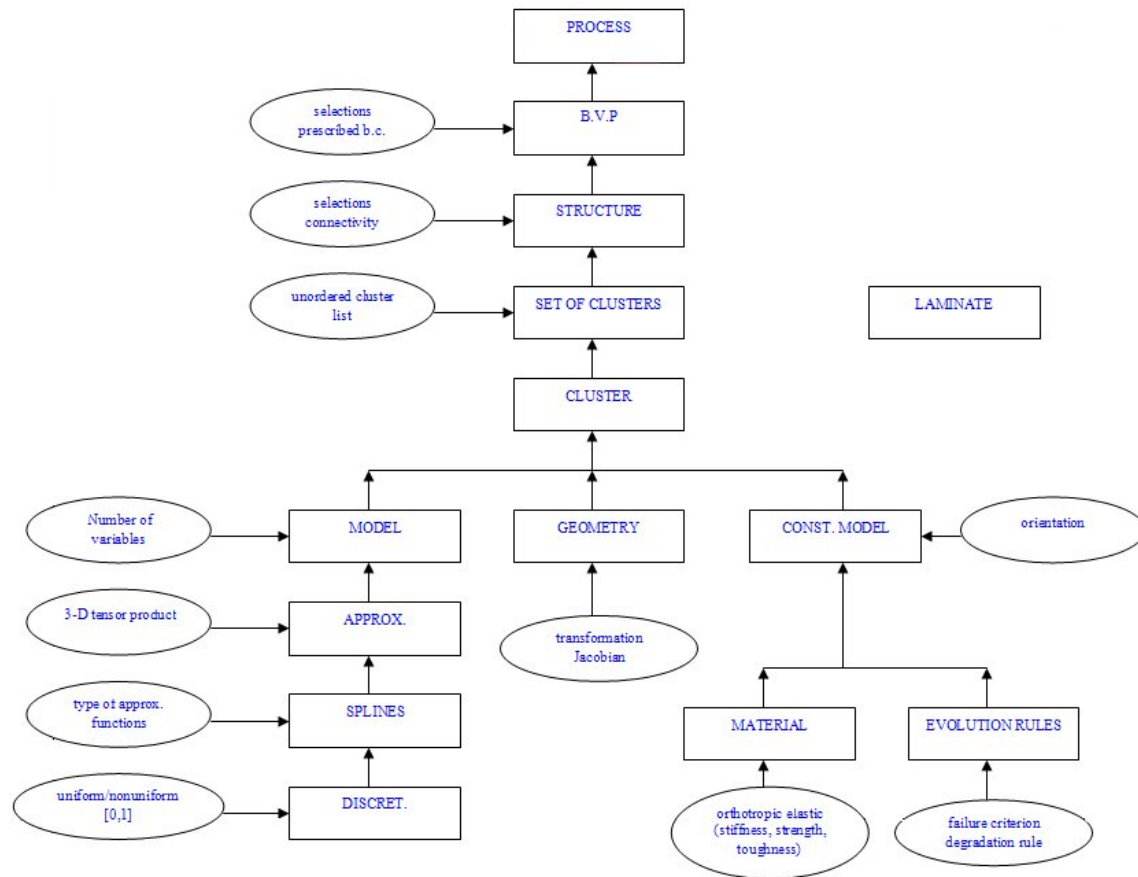


Figure 130. Flow chart of BSAM input file

It is important to note that this appendix gives information for the specific modification of an existing BSAM input file. It does not provide information for the creation of a new BSAM input file. It is also important to note that the purpose of this appendix is to explain steps taken in the building of models of the scarf and stepped-lap repairs analyzed in this thesis. Because of this, it does not provide guidance for the development of a model with different parameters. More extensive and general information regarding development of a BSAM input file is available through Endel Iarve, Greg Schoeppner, or David Mollenhauer at the Air Force Research Laboratories of Wright-Patterson Air Force Base in Dayton, OH.

Problem Summary

The problem addressed in this thesis includes the modification of BSAM input files to model 10 inch by 1 inch specimens with straight stepped-lap and scarf repairs.

Specimens are manufactured from IM6/3501-6 carbon epoxy material with a 16-ply, $[45_2/0_2/-45_2/90_2]_s$ lay-up. The stepped-lap repair consists of eight equal steps. All material properties and specimen dimensions are given. Adhesive stress is low, such that a linear elastic model is applicable. One stepped-lap specimen and one scarf specimen is subjected to a tensile load of 1000N (450lb).

The first section of this appendix will explain the modification of the foundation for the BSAM input file, including the three components illustrated in the flowchart in Figure 130. The components will be addressed in the following order:

1. Evolution Rules, Material, Constitutive Model
2. Geometry
3. Discretization, Splines, Approximation, Model

The second section of this document will explain the modification of the remaining input blocks of the BSAM input file.

Failure Input Block (Evolution Rules)

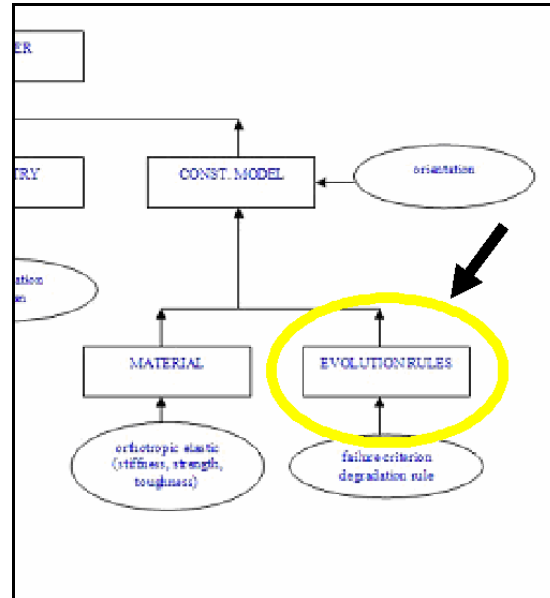


Figure 131. Evolution Rules on flowchart.

Since this study consisted of a strain analysis (not failure analysis) of composite repairs, the last section of the input file titled “failure,” shown in Figure 132, was not modified for either model as it was not necessary for the process.

```

FAILURE
1 type
1.e-0 1.e-0 1.e-0 1.e-0 1.e-0 1.e-0 1.e-0 1.e-0 1.e-0 1
1.e-0 1.e-0 1.e-0 1.e-0 1.e-0 1.e-0 1.e-0 1.e-0 1.e-0 2
1.e-0 1.e-0 1.e-0 1.e-0 1.e-0 1.e-0 1.e-0 1.e-0 1.e-0 3
1.e-0 1.e-0 1.e-0 1.e-0 1.e-0 1.e-0 1.e-0 1.e-0 1.e-0 3
1.e-0 1.e-0 1.e-0 1.e-0 1.e-0 1.e-0 1.e-0 1.e-0 1.e-0 5
1.e-0 1.e-0 1.e-0 1.e-0 1.e-0 1.e-0 1.e-0 1.e-0 1.e-0 6
1.e-0 1.e-0 1.e-0 1.e-0 1.e-0 1.e-0 1.e-0 1.e-0 1.e-0 7
1.e-0 1.e-0 1.e-0 1.e-0 1.e-0 1.e-0 1.e-0 1.e-0 1.e-0 8
1.e-0 1.e-0 1.e-0 1.e-0 1.e-0 1.e-0 1.e-0 1.e-0 1.e-0 3
1.e-0 1.e-0 1.e-0 1.e-0 1.e-0 1.e-0 1.e-0 1.e-0 1.e-0 10
END FAILURE
*****
***** END BSAM INPUT FILE *****
*****

```

Figure 132. Failure block of BSAM input file.

Material Input Block

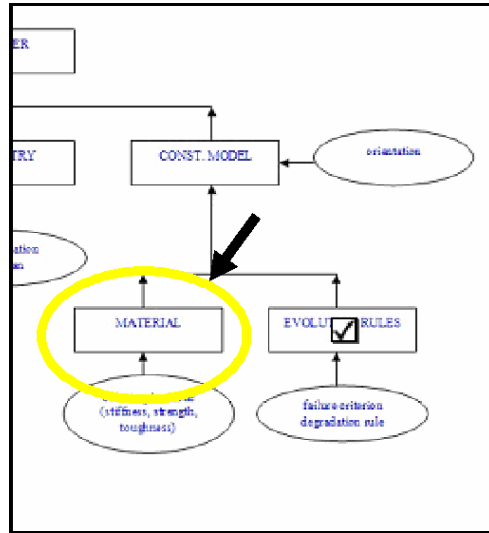


Figure 133. Material input block on flowchart

The “material” input block of the file describes the material properties for use by each cluster. For both the stepped-lap and scarf model, two materials were defined: (1) the carbon-epoxy parent material and (2) the adhesive used for bonding the repair.

The rest of this section (describing the material input block) explains how each specific material property value is input into BSAM. If the reader is familiar with programs with notepad style input files and undeveloped graphical user interfaces, it may be more helpful to simply refer to Figure 134 at the end of this portion of the chapter.

The same will be true for other portions of this chapter.

Overall, the notepad style BSAM input file requires that all values are placed in an appropriate row or column. The following paragraphs describe the significance of each of the values listed in the material input block. First, the parent material was defined. Starting from the upper left corner, the “1” to the left of each material described the type of material being modeled. In this case, type 1 is used to describe a linear elastic

orthotropic material. Everything to the right of this number is for programmer comments and not used by the BSAM computer program. In this case, the first material describes the specific type of composite used in this thesis.

```
1 Material IM6/3501-6 (US) (strengths from Ran Kim) material # 1
```

The next three lines of code in the material input block include two main components:

1. The modulus of elasticity in each direction (E_{11} , E_{22} , E_{33})
2. The tensile and compressive strengths of the material in the x and y directions (X_t , X_c , Y_t , Y_c)

Looking to the lines below, the number in the first row and first column is the modulus of elasticity in the 1, 1 direction or E_{11} (corresponding to the **E11** comment in row 1, column 4). The number in the first row and second column is the tensile strength of the material in the 1 direction or X_t (corresponding to the **Xt** comment in row 1, column 5). The number in row 1, column 3 is the compression strength of the material in the 1 direction or X_c (corresponding to the **Xc** comment in row 1, column 6) and so on. Since the model being produced is not being used for failure analysis, dummy values for X_c and Y_c can be included into this section for the input file to run.

```
25420000.0 366640.0 0.00 E11, Xt, Xc
1420000.0 6414.0 0.00 E22, Yt, Yc
1420000.0 E33
```

The following three lines of code in the material input block contains:

1. Poisson's Ratio (ν_{13} , ν_{23} , ν_{12})
2. Critical Energy Release Rates (G_{1c} , G_{11c} , G_{111c})

The values for Poisson's Ratio are listed in the first column of each row, as shown in the lines below, corresponding to comments **Nu13**, **Nu23**, and **Nu12** in column 4 for

each row. Critical Energy Release Rates (**G1c**, **G11c**, and **G111c**) were not modified for this model because they are values only applicable in failure. Overall, these inputs follow the same logic as the three lines preceding them (containing the modulus of elasticity and material strength in each direction).

```
0.33      1.25      3.2      0      Nu13,      G1c,      G11c,      G111c;
0.45
0.33      Nu23
      Nu12
```

The final 6 lines of the material input block include information regarding:

1. The shear moduli of elasticity (G_{13} , G_{23} , and G_{12})
2. Material density (ρ)
3. The coefficients of thermal expansion (α_{11} and α_{22}).

Values entered for these fields were consistent with the pattern described for other lines. The material density on row 4 can be left as zero, as the strain analysis for this thesis is not a dynamic problem and does not factor in mass.

```
800000.0      G13
490000.0      G23      ***      calculated
800000.0      13500      13500      G12,      S,      S13

0.00      Density
0.2E-6      Alpha11
14.9E-6      Alpha22
```

The FM-300M epoxy adhesive was the second material necessary for the model. To define parameters for this material, the same approach was used. The adhesive section of the material input block is shown below.


```

1 Material FM-300M .05 (Elastic orthotropic) material # 2
453000.0 0.00 0.00 E11, Xt, Xc
453000.0 0.00 0.00 E22, Yt, Yc
453000.0 E33
0.377 0.00 0.00 0.00 Nu13, G1c, G11c, G111c; "
0.377 Nu23
0.377 Nu12
164000.0 G13
164000.0 G23
164000. 0.00 0.00 G12, S, S13
0.00 Density
34.8E-6 Alpha11
34.8E-6 Alpha22

```

Figure 134. Material block of BSAM input file.

Because the same parent material and adhesive was used for both the stepped-lap and scarf repairs, the material input block was identical for both scarf and stepped-lap BSAM input files.

Constitutive Model Input Block

Figure 135. Constitutive model input block on flowchart.

The purpose of the constitutive section is to describe the constitutive law and ply orientation used for a given cluster. Again, if the reader is familiar with programs with notepad style input files and undeveloped graphical user interfaces, it may be more helpful to simply refer to Figure 136 at the end of this portion of the appendix.

focused on a composite panel with a $[45_2/0_2/-45_2/90_2]_s$ ply lay-up, the 45 listed in this input slot refers to the 45 degree layers of the composite.

```
CONSTITUTIVE
1      type - constitutive law 1-elastic orthotrop Constitutive
1 1 45. material#, Failure criter., and orientation
```

In summary, the input lines shown directly above describe the constitutive law, material type, failure criterion, and ply orientation used for each unique building block of the model.

To describe the composite panels and adhesive for this thesis, a total of five different two line description blocks were required for the constitutive input section. The first four description blocks defined the different ply orientations of the composite material: $[45_2/0_2/-45_2/90_2]_s$. The final description block defined the adhesive layer. Since it was assumed that the adhesive was isotropic, its orientation was not important and was left arbitrarily as 00.

```
CONSTITUTIVE
1      type - constitutive law 1-elastic orthotrop Constitutive
1 1 45. material#, Failure criter., and orientation
1      type - constitutive law 1-elastic orthotrop Constitutive
1 1 00. material#, Failure criter., and orientation
1      type - constitutive law 1-elastic orthotrop Constitutive
1 1 -45. material#, Failure criter., and orientation
1      type - constitutive law 1-elastic orthotrop Constitutive
1 1 90. material#, Failure criter., and orientation
1      type - constitutive law 1-elastic orthotrop Constitutive
2 1 00. material#, Failure criter., and orientation
END CONSTITUTIVE
```

Figure 136. Constitutive input block for BSAM program

Because the same parent material lay-up and adhesive was used for both the stepped-lap and scarf repairs, the constitutive input block was identical for both BSAM input files.

Geometry Input Block

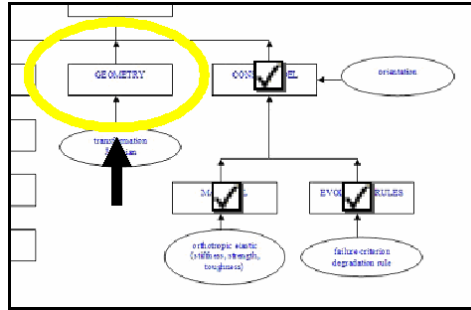


Figure 137. Geometry input block on flow chart

The second component of the foundation of the BSAM input file is the geometry input block. The purpose of the geometry input section is to define the geometry, or shape, associated with each cluster. One geometry can be used to define more than one cluster if desired. Because of this, it is only necessary to define unique geometries or shapes in the model.

The geometry input section for the stepped-lap model will be explained in detail during this section. The same logic and process was applied in creating the geometry input section for the scarf model.

To understand the geometry shapes needed to model the stepped-lap joint, it is critical to visualize the repair in the specimen. The figure below illustrates the anatomy of the modeled stepped-lap joint.

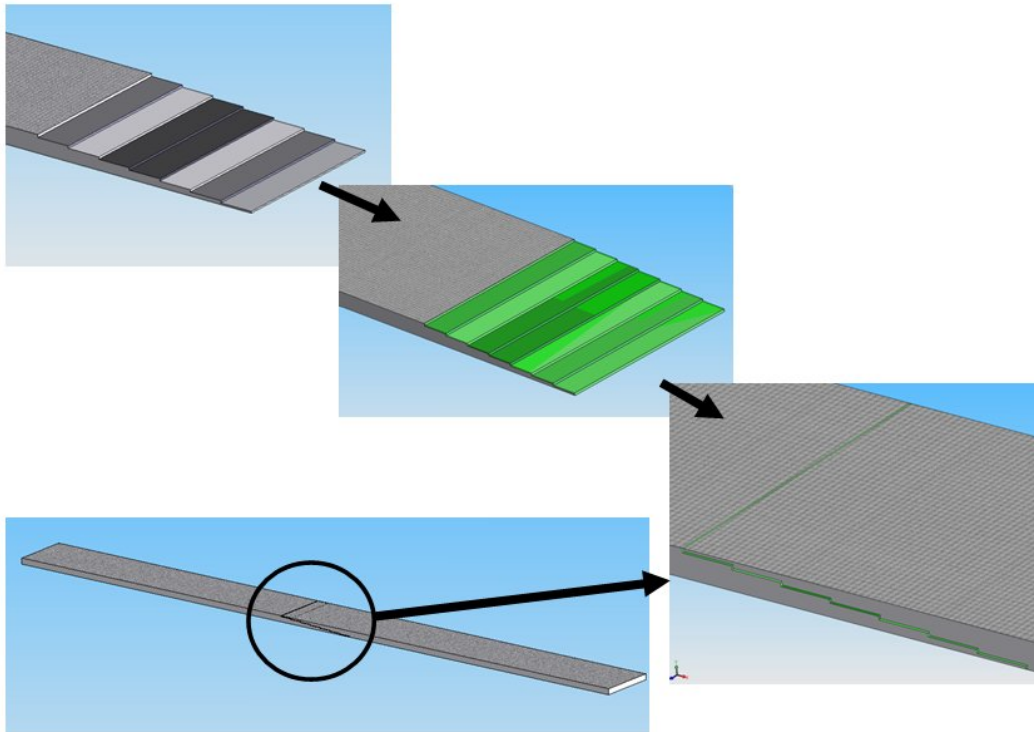


Figure 138. Anatomy of stepped-lap joint

Zooming in on the repaired section, it is evident that there are eight equal steps exposing the surfaces of seven plies (of the 16-ply laminate).

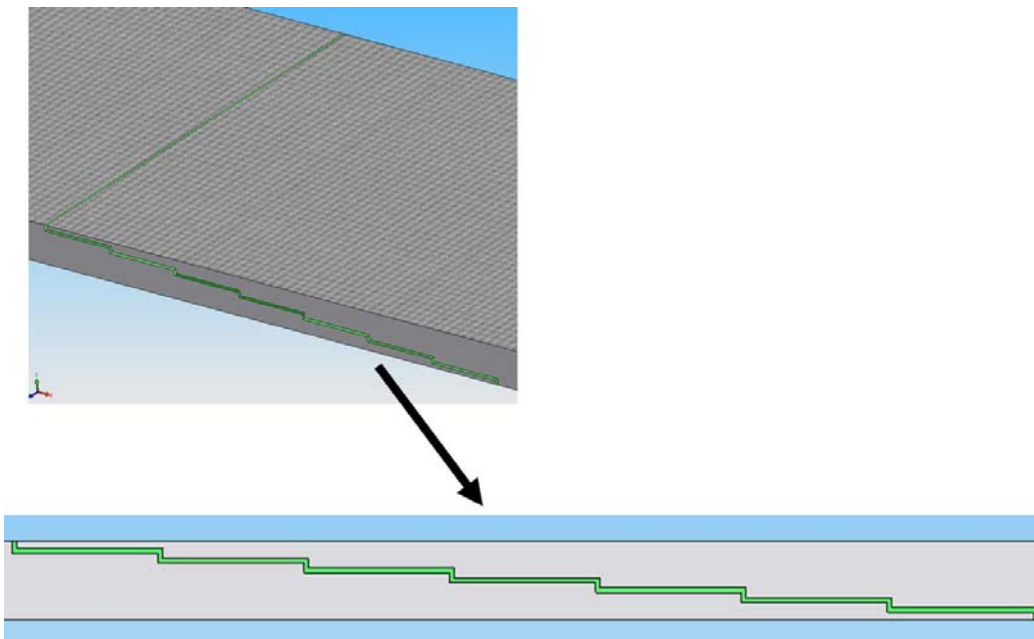


Figure 139. Cross sectional view of stepped-lap joint.

All adjoining sides of adjacent clusters in BSAM are required to be coincident. A couple examples of cluster configurations that BSAM cannot process, as well as an acceptable cluster/grid configuration, are shown in Figure 140.

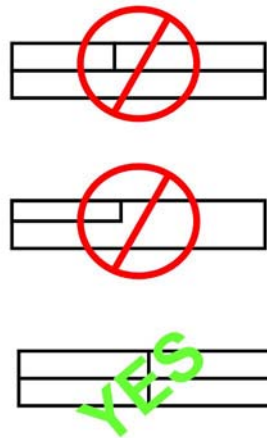


Figure 140. Acceptable cluster/grid configuration.

Because of this requirement, the grid created for the stepped-lap repair could not have any free hanging corners, and clusters that did not fit flush with one another. The simplest grid that could model the stepped-lap repair and fit this requirement is shown in Figure 141. It contained 374 clusters or geometries.



Figure 141. Grid of geometries required for stepped-lap model

As mentioned earlier, one geometry can be used to define more than one cluster. Referring to a closer view of a portion of the stepped-lap repair shown in Figure 142, it becomes apparent that some shapes are repeated.



Figure 142. Closer view of portion of stepped-lap repair

Taking an even closer look at the repair, patterns in the geometry dimensions are evident. While there are 22 clusters through the thickness of the grid, it can be seen that some clusters have the same thickness. In fact, there are only three different thicknesses that have to be modeled for the clusters: two clusters with a $\frac{3}{4}$ ply thickness (very top and very bottom), six clusters with a $\frac{1}{2}$ ply thickness, and 14 clusters with a $\frac{1}{4}$ ply thickness (adhesive layers). These dimensions are illustrated in Figure 143.

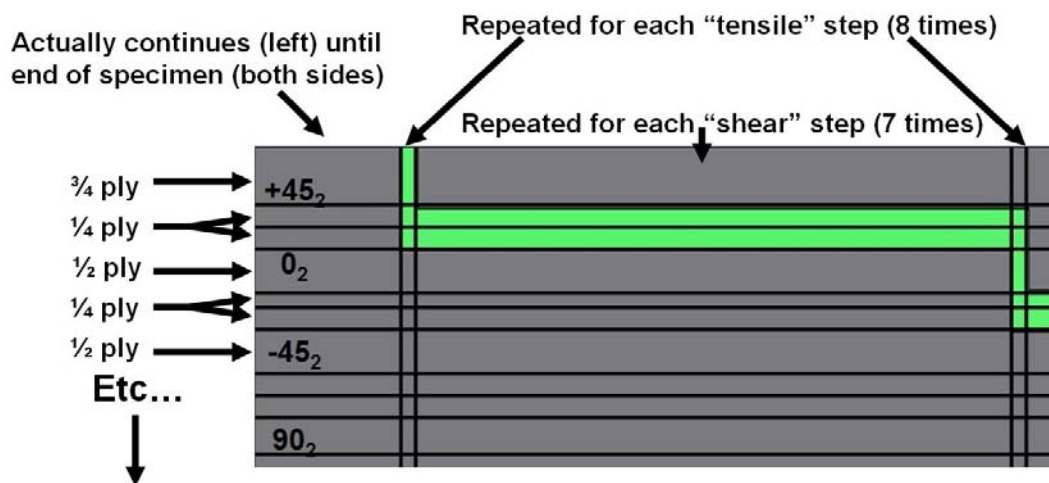


Figure 143. Patterns emerging in stepped-lap geometries.

A similar pattern can be found across the length of the repair. While there are 17 clusters across the length of the grid, it can be seen that some clusters have the same width. For example, assuming each “tensile” step has the same width, there are eight clusters across the length that share that same dimension. If it is assumed that each “shear” step has the same width, there are seven clusters across the length that share that same dimension. The two final clusters represent the portion of the specimen to the right and to the left of the repair. Because the repair lies in the middle of the specimen, it can be assumed that the length from the far end of the specimen to the repair is the same on both sides.

Overall, it was possible to identify 9 unique geometries from the 374 clusters needed to model the stepped-lap repair. These 9 geometries are identified below in Figure 144.

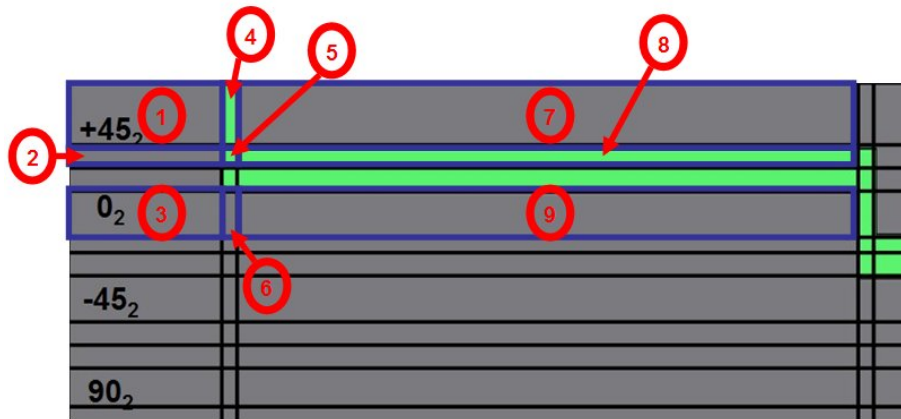


Figure 144. Unique geometries in stepped-lap model.

After identifying the geometries necessary to model the stepped-lap joint, the next step was to determine an appropriate geometry shape. There are many shapes available in the BSAM program in order to accurately define the cluster modeled. The number

directly below **GEOMETRY** in the first column of the input block below (**83**) indicates the shape chosen to describe the cluster.

GEOMETRY		Slanted Geometry	type,	x1,	x2,	x3,	x4,	Ly,	Lz		g1
83		4.361098249	4.361098249	0.0				1			0.0091125
1	0										

The shape or geometry number is determined by referring to a BSAM reference file (in Excel) and determining which shape best defines the cluster needed for the model. Geometry 83 is shown in the figure below, where x1, x2, x3, and x4 are the x-coordinates of the shape. Referring to the input block for the first geometry in the stepped-lap model, x1 = 0 in, x2 = 4.361098249 in, x3 = 4.361098249 in, and x4 = 0 in respectively.

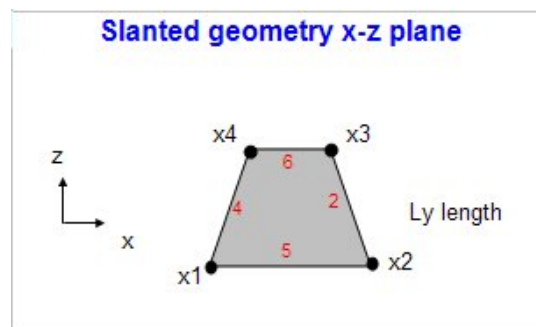


Figure 145. Geometry type used for stepped-lap and scarf models.

The number in the next column (**1**) indicates the width of the cluster, and the final number indicates the height of the cluster in the z-direction. All dimensional values are defined in inches. Dimensional values were defined for each geometry. This can be seen in the complete GEOMTERY input block shown below, as 9 geometries are defined to generate the clusters required for the stepped-lap model (see g1-g9 on the far right side of Figure 146).

Coordinates of stepped-lap repairs were found by taking a panoramic photograph of the polished edge of the specimen, placing a grid over it, and using known dimensions (such as the thickness) to find the exact location of any given point in the repair.

Measurements taken from the grid were then used to accurately model the actual specimen.

```

GEOMETRY
83          Slanted Geometry      type, x1, x2, x3, x4, Ly, Lz      g1
1          0          4.455590909  4.455590909  0.0          1.0045  0.008296875
83          g2
1          0          4.455590909  4.455590909  0          1.0045  0.002765625
83          g3
1          0          4.455590909  4.455590909  0          1.0045  0.00553125
83          g4
1          0          0.023298295  0.023298295  0          1.0045  0.008296875
83          g5
1          0          0.023298295  0.023298295  0          1.0045  0.002765625
83          g6
1          0          0.023298295  0.023298295  0          1.0045  0.00553125
83          g7
1          0          0.127769481  0.127769481  0          1.0045  0.008296875
83          g8
1          0          0.127769481  0.127769481  0          1.0045  0.002765625
83          g9
1          0          0.127769481  0.127769481  0          1.0045  0.00553125
END GEOMETRY

```

Figure 146. Geometry input block for stepped-lap model

Geometry 83 was selected because it could be used to accurately describe all the building blocks necessary for both the scarf and stepped-lap model.

The same methodology was used in modifying the geometry input block for the scarf joint. The scarf joint model required 17 unique geometries to build the 24 cluster model. As the figure below illustrates, clusters 9-16 could be considered to be the same geometry with the assumption of a linear bond line. The geometry input block for the scarf model is shown in Figure 149.

45°	Cluster 8	C16	Cluster 24
0°	Cluster 7	C15	Cluster 23
-45°	Cluster 6	C14	Cluster 22
90°	Cluster 5	C13	Cluster 21
90°	Cluster 4	C12	Cluster 20
-45°	Cluster 3	C11	Cluster 19
0°	Cluster 2	C10	Cluster 18
45°	Cluster 1	C9	Cluster 17

Figure 147. Clusters for scarf model.

45°	G8	G9	Geometry 17
0°	Geometry 7	G9	Geometry 16
-45°	Geometry 6	G9	Geometry 15
90°	Geometry 5	G9	Geometry 14
90°	Geometry 4	G9	Geometry 13
-45°	Geometry 3	G9	Geometry 12
0°	Geometry 2	G9	Geometry 11
45°	Geometry 1	G9	Geometry 10

Figure 148. Geometries for scarf model.

```

GEOMETRY
83      slanted Geometry      type, x1, x2, x3, x4, Ly, Lz      g1
1      0.0      5.6471      5.485325      0.0      1.004      0.010938000      g2
83
1      0.0      5.485325      5.32355      0.0      1.004      0.010938000      g3
83
1      0.0      5.32355      5.161775      0.0      1.004      0.010938000      g4
83
1      0.0      5.161775      5      0.0      1.004      0.010938000      g5
83
1      0.0      5      4.838225      0.0      1.004      0.010938000      g6
83
1      0.0      4.838225      4.67645      0.0      1.004      0.010938000      g7
83
1      0.0      4.67645      4.514675      0.0      1.004      0.010938000      g8
83
1      0.0      4.514675      4.3529      0.0      1.004      0.010938000      g9
83
1      5.6471      5.703533141      5.541758141      5.485325      1.004      0.010938000      g10
83
1      5.7035331      10.0      10.0      5.5417581      1.004      0.010938000      g11
83
1      5.5417581      10.0      10.0      5.3799831      1.004      0.010938000      g12
83
1      5.3799831      10.0      10.0      5.2182081      1.004      0.010938000      g13
83
1      5.2182081      10.0      10.0      5.0564331      1.004      0.010938000      g14
83
1      5.0564331      10.0      10.0      4.8946581      1.004      0.010938000      g15
83
1      4.8946581      10.0      10.0      4.7328831      1.004      0.010938000      g16
83
1      4.7328831      10.0      10.0      4.5711081      1.004      0.010938000      g17
83
1      4.5711081      10.0      10.0      4.4093331      1.004      0.010938000
END GEOMETRY

```

Figure 149. Geometry input block for scarf model

Several steps were taken to model each of the five scarf specimens. First of all, the joint endpoint coordinates were found under a microscope with an accuracy of +/- 0.0001. For Figure 150 (specimen #1), it can be seen that the coordinates from the microscope were (0, 0.0872) and (1.1804, 0).

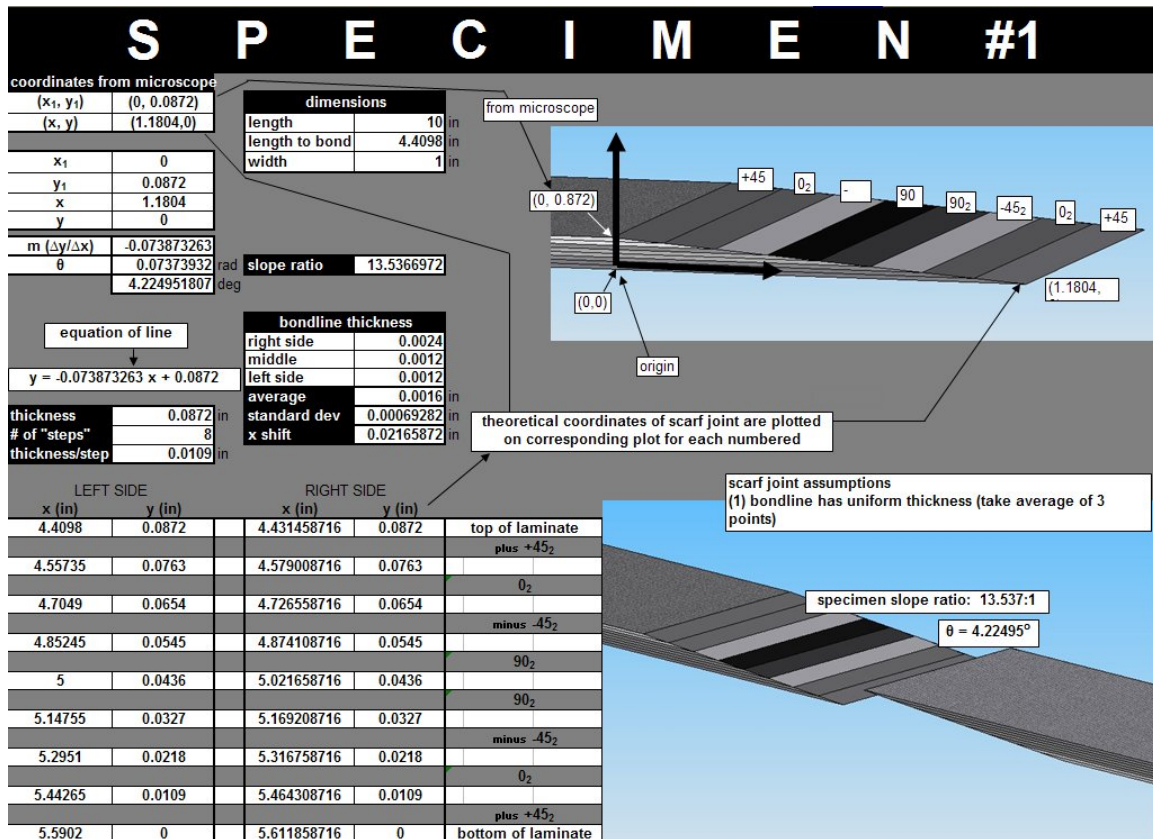


Figure 150. Modeling the adhesive bond-line for scarf specimen #1.

These points were used to determine the equation of the line for the scarf repair, as well as the angle of repair (assuming the bond-line was linear). For specimen #1, it could be seen that the equation of the line to describe the scarf joint was $y = -0.073873263 x + 0.0872$, and the angle of repair was 4.22° . Three adhesive thickness measurements were taken to determine the average bond-line thickness. The average bond-line thickness and equation of the scarf joint line were then used to determine theoretical points along the bond line which could be modeled in BSAM.

Because the scarf repair was not perfectly flush and even across the width of the panel, each specimen was modeled individually. Data regarding all five specimens is attached in appendix.

The third component of the foundation of the BSAM input file includes the Discretization, Splines, Approximation, and Model blocks (shown in Figure 151).

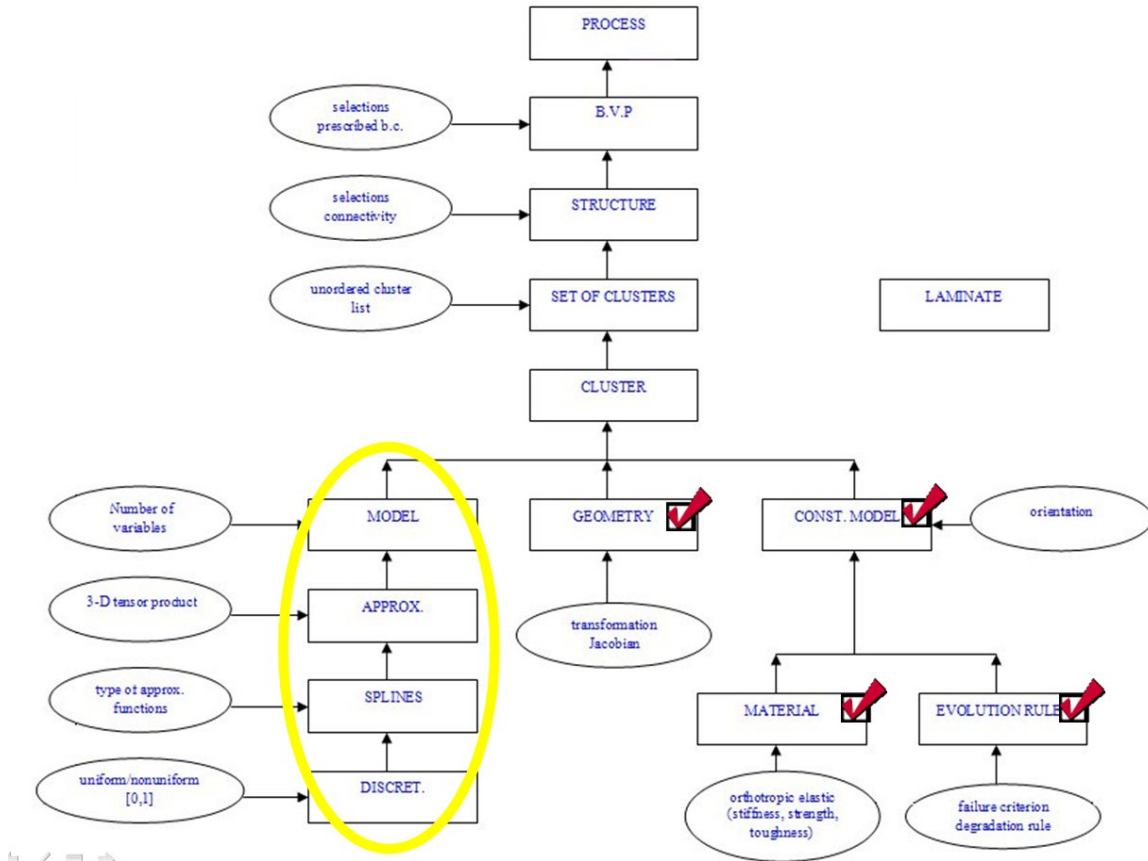


Figure 151. Discretization, splines, approximation, and model blocks from flowchart Discretization Input Block

This input section defines the discretization associated with each spline. For both models created for this thesis, special care was taken to create a finer mesh in the area of the repairs on the edges of the specimens. Building a finer mesh in the area of the repairs allowed the BSAM program to produce more accurate theoretical strain fields along the edge of the specimen in the area of interest.

To achieve this objective, it was determined that five discretizations would be appropriate for the scarf joint, while eight discretizations would be appropriate for the stepped lap joint.

Looking to the section of code in Figure 152, there were five spline discretizations available for the scarf model: three (3) in the x-plane (x1, x2, and x3), one (1) in the y-plane (y1), and one (1) in the z-plane (z1).

```
DISCRETIZATION
  2 10  #3  x1
  0.6
  1 2   #2  x2
  2 10  #3  x3
  1.4
  3 10  #4  y1
  2.2
  1 4   #5  z1
END DISCRETIZATION
```

Figure 152. Discretization input block.

Looking to the section of code in Figure 153, there were eight spline discretizations available for the stepped-lap model: four (4) in the x-plane (x1, x2, x3, and x4), one (1) in the y-plane (y1), and three (3) in the z-plane (z1, z2, z3).

```
DISCRETIZATION
  2 10  #1  x1
  0.6
  1 1   #2  x2
  3 5   #3  x3
  2
  2 10  #4  x4
  1.4
  3 10  #5  y1
  2.2
  1 1   #6  z1 (3/4 ply)
  1 1   #7  z2 (1/2 ply)
  1 1   #8  z3 (1/4 ply)
END DISCRETIZATION
```

Figure 153. Splines highlighted in discretization input block

There are three input options to describe each discretization. The first input indicates the discretization type.

Type → 2 10 #3 x1
0.6

There are four types available: (1) uniformly discretized, (2) 1-way biasing of discretization, (3) 2-way biasing of discretization, and (4) hand assigned intervals. For the example above, a 1-way biasing of discretization was assigned. The first three discretization types are shown below.

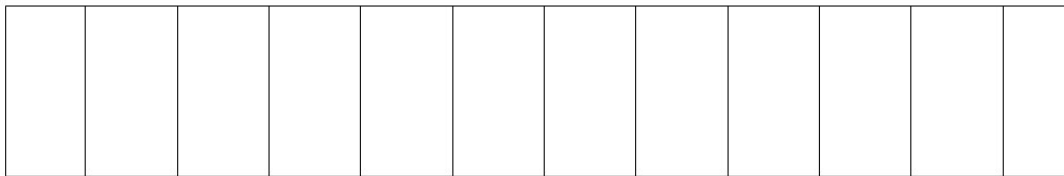


Figure 154. Type I: uniformly discretized

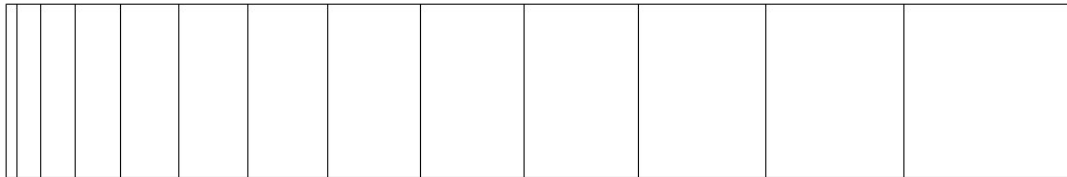


Figure 155. Type II: 1-way biasing of discretization



Figure 156. Type III: 2-way biasing of discretization

The second input indicates the number of intervals for each discretization. The example shown below is split into ten segments or intervals.

2 10 #3 x1
0.6 # of intervals

The third input indicates the bias ratio of each discretization. A number greater than 1 biases the intervals to the left side and a number less than 1 biases the intervals to the right side. The further the number is from 1, the greater the extremity of the biasing.

2 10 #3 x1
0.6 Bias ratio



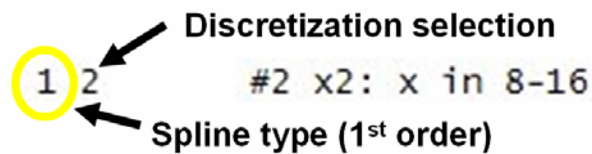
Figure 157. Bias ratio < 1



Figure 158. Bias ratio > 1

Spline Input Block

This block defines the polynomials to be used in each direction and selects the discretization. There are two important inputs in this block: (1) the polynomial type and (2) the discretization assigned to the spline. The line below identifies that a cubic order spline will be assigned to the 2nd discretization (as defined in order) from the discretization block.



For the scarf model, cubic order splines were assigned for each of the five discretization types. Quadratic splines were assigned for the stepped-lap model; the exception was that the cubic splines were used in the y-direction. Many other spline types are available and listed in Excel and Word reference documents produced for BSAM. The SPLINE input block for the scarf model is shown in Figure 159.

```
SPLINES
1 1 #1 x1: x in 1-8
1 2 #2 x2: x in 8-16
1 3 #3 x3: x in 17-24
1 4 #4 y1: y in all clusters
1 5 #5 z1: z in all clusters
END SPLINES
```

The code block is shown with a yellow oval highlighting the five spline definitions (lines 1-5).

Figure 159. Spline input block for scarf model

The spline input block for the stepped-lap model is shown in Figure 160.

```

SPLINES
2 1      #1 x1: x in 1-22
2 2      #2 x2: x in 23-44, 67-88, 111-132, 155-176, 199-220, 243-264, 287-308, 331-352
2 3      #3 x3: x in 45-66, 89-110, 133-154, 177-198, 221-242, 265-288, 309-330
2 4      #4 x4: x in 353-374
2 5      #5 y1: y in all clusters
2 6      #6 z1: z in 3/4 ply clusters
2 7      #7 z2: z in 1/2 ply clusters
2 8      #8 z3: z in 1/4 ply clusters
END SPLINES

```

Figure 160. Spline input block for stepped-lap model

The comments to the right of the spline type and discretization selection are reference comments for the user. They are not used in the program, and simply help the user refer to the clusters each spline is associated with. For example, looking to the spline input block for the scarf model, the first spline (#1) is associated with clusters 1-8 in the x-direction. The second spline (#2) is associated with clusters 8-16 in the x-direction, and so on.

Approximation Input Block

The purpose of the approximation block was to define approximations for each spline combination. There are several approximations available in the BSAM program: Type 1, or a standard 3D non periodic spline, was used for both stepped-lap and scarf models. The type of approximation was defined on the first line of the section.

```
APPROXIMATION
1 type of approximation x, y, z subdivision / approx 1
5 1 9 z,y,x -dir, approx, # of select
101 1 type, edge app.selections
101 2 type
101 3 type
101 4 type
101 5 type
101 6 type
101 7 type
101 8 type
101 9 type
```

The number of approximations required by the models corresponded directly to the number of spline permutations or combinations possible.

From the spline input block from the scarf model (shown in previous section), it is evident that there are three splines in the x-direction (x1, x2, x3), one spline in the y-direction (y1), and one spline in the z-direction (z1). These splines can be referenced in BSAM by calling them in the order they appear. For example, y1 is the fourth spline defined, so it can be called simply by putting the number 4 into the appropriate line of the approximation block.

X1 = 1
x2 = 2
x3 = 3
y1 = 4
z1 = 5

From these splines, it can be seen that there are three “z, y, x” permutations available.

Possible permutations

z	y	x
z1	y1	x1
z1	y1	x2
z1	y1	x3

By replacing the spline with its appropriate reference number, it can be seen that these permutations can be expressed in the BSAM input file as:

z	y	x
5	4	1
5	4	2
5	4	3

Since there are three permutations possible from the splines, three approximations are necessary for this model.

```

APPROXIMATION
1  type of approximatin  x, y,z subdivision / approx 1
5 4 1  z,y,x -dir, approx, # of select
101 1  type, edge app.selections
101 2  type
101 3  type
101 4  type
101 5  type
101 6  type
101 7  type
101 8  type
101 9  type
1  type of approximatin  x, y,z subdivision / approx 2
5 4 2  z,y,x -dir, approx, # of select
101 1  type, edge app.selections
101 2  type
101 3  type
101 4  type
101 5  type
101 6  type
101 7  type
101 8  type
101 9  type
1  type of approximatin  x, y,z subdivision / approx 3
5 4 3  z,y,x -dir, approx, # of select
101 1  type, edge app.selections
101 2  type
101 3  type
101 4  type
101 5  type
101 6  type
101 7  type
101 8  type
101 9  type
END APPROXIMATION

```

Figure 161. Approximation input block for scarf joint

The block of numbers associated with each approximation (i.e. the 101 1, 101 2, etc) refer to the type of spline and the edge or face corresponding to that specific spline. In this case, 101 is listed as the type of each spline. Reference BSAM documents show that the edges and faces of each cluster are defined as follows:

- 1 = face 1 ($y = 0$)
- 2 = face 2 ($x = 1$)
- 3 = face 3 ($y = 1$)
- 4 = face 4 ($x = 0$)
- 5 = face 5 ($z = 0$)
- 6 = face 6 ($z = 1$)
- 7 = point 7 ($x = y = z = 0$)
- 8 = point 8 ($x = z = 0, y = 1$)
- 9 = point 9 ($y = z = 0, z = 1$)

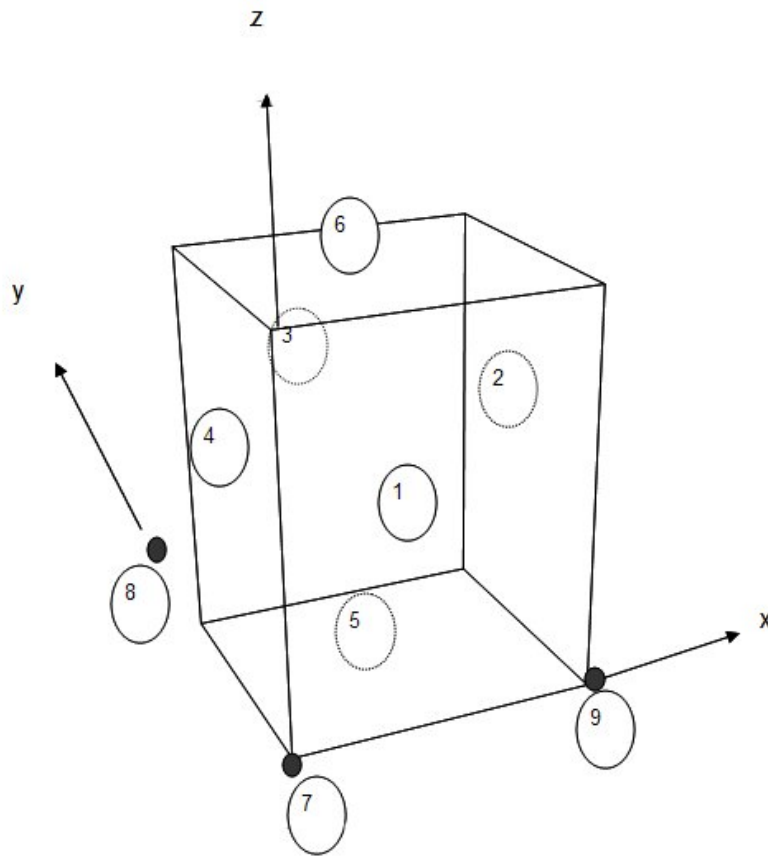


Figure 162. Cluster faces and edges defined

For the stepped lap model, twelve approximations were needed as more splines were defined.

```

SPLINES
2 1      #1 x1: x in 1-22
2 2      #2 x2: x in 23-44, 67-88, 111-132, 155-176, 199-220, 243-264, 287-308, 331-352
2 3      #3 x3: x in 45-66, 89-110, 133-154, 177-198, 221-242, 265-288, 309-330
2 4      #4 x4: x in 353-374
2 5      #5 y1: y in all clusters
2 6      #6 z1: z in 3/4 ply clusters
2 7      #7 z2: z in 1/2 ply clusters
2 8      #8 z3: z in 1/4 ply clusters
END SPLINES

```

Figure 163. Splines input block for stepped-lap model

From the spline input block from the stepped-lap model (shown above), it is evident that there are four splines in the x-direction (x1, x2, x3, x4), one spline in the y-direction (y1), and three spline in the z-direction (z1, z2, z3). These splines can be referenced in BSAM by calling them in the order they appear. For example, y1 is the fifth spline defined, so it can be called simply by putting the number 5 into the appropriate line of the approximation block.

```

X1 = 1
x2 = 2
x3 = 3
x4 = 4
y1 = 5
z1 = 6
z2 = 7
z3 = 8

```

From these splines, it can be seen that there are 12 “z, y, x” permutations available.

Possible permutations

z	y	x
z1	y1	x1
z1	y1	x2
z1	y1	x3
z1	y1	x4
z2	y1	x1
z2	y1	x2
z2	y1	x3
z2	y1	x4
z3	y1	x1
z3	y1	x2
z3	y1	x3
z3	y1	x4

By replacing the spline with its appropriate reference number, it can be seen that these permutations can be expressed in the BSAM input file as:

z	y	x
6	5	1
6	5	2
6	5	3
6	5	4
7	5	1
7	5	2
7	5	3
7	5	4
8	5	1
8	5	2
8	5	3
8	5	4

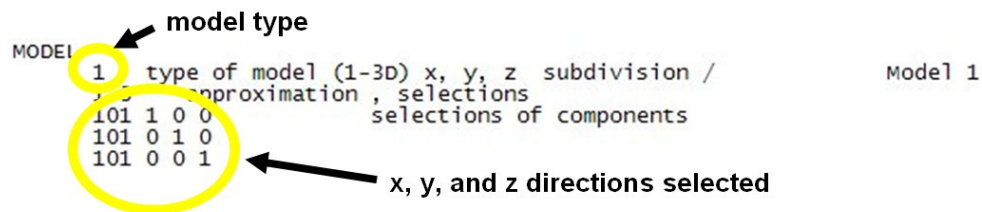
Since there are 12 permutations possible from the splines, 12 approximations are necessary for this model.

More surfaces of each cluster, such as specific edges, can be also be defined.

Model Input Block

A model is needed for every approximation. A model describes the number of variables and serves as a bridge between the approximation input block and the cluster input block. Three approximations were required for the scarf model, and 12 models were required for the stepped-lap model. Therefore, three models were required for the scarf model, and 12 models were required for the stepped-lap model.

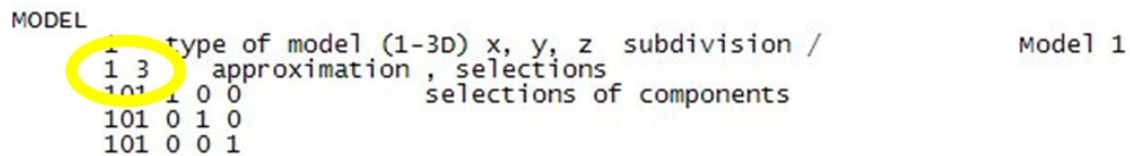
The “model type” entry indicates the type of model selected. In this case, model type 1 indicates a 3D parametric model. The bottom three lines for each model indicate the spline direction selected for that model. In this case, values are calculated in all three directions, so the x, y, and z directions are selected.



The diagram shows a model input block with the following text: MODEL 1 type of model (1-3D) x, y, z subdivision / approximation, selections selections of components Model 1. The number 1 is circled in yellow, with an arrow pointing to it labeled "model type". The three lines "101 1 0 0", "101 0 1 0", and "101 0 0 1" are circled in yellow, with an arrow pointing to them labeled "x, y, and z directions selected".

```
MODEL 1 type of model (1-3D) x, y, z subdivision /
      1 approximation, selections
      101 1 0 0 selections of components
      101 0 1 0
      101 0 0 1
```

The line above the selected directions indicates the approximation modeled and the number of selections that will follow. In this case, model 1 calls on approximation 1 and three directions (x, y, and z) are selected.



The diagram shows a model input block with the following text: MODEL 1 type of model (1-3D) x, y, z subdivision / approximation, selections selections of components Model 1. The line "1 3" is circled in yellow, with an arrow pointing to it.

```
MODEL 1 type of model (1-3D) x, y, z subdivision /
      1 3 approximation, selections
      101 1 0 0 selections of components
      101 0 1 0
      101 0 0 1
```

The model input block for the scarf model is shown below.

MODEL	1	type of model (1-3D) x, y, z	subdivision /	Model 1
	1 3	approximation ,	selections	
	101 1 0 0		selections of components	
	101 0 1 0			
	101 0 0 1			
	1	type of model (1-3D) x, y, z	subdivision /	Model 2
	2 3	approximation ,	selections	
	101 1 0 0		selections of components	
	101 0 1 0			
	101 0 0 1			
	1	type of model (1-3D) x, y, z	subdivision /	Model 3
	3 3	approximation ,	selections	
	101 1 0 0		selections of components	
	101 0 1 0			
	101 0 0 1			
END MODEL				

Figure 164. Model input block for scarf model.

Cluster Input Block

After completing the model input block for both the scarf and stepped-lap model, the foundation for the BSAM was complete (as shown in Figure 165). The parameters defined in these input sections were then used to build the cluster input block.

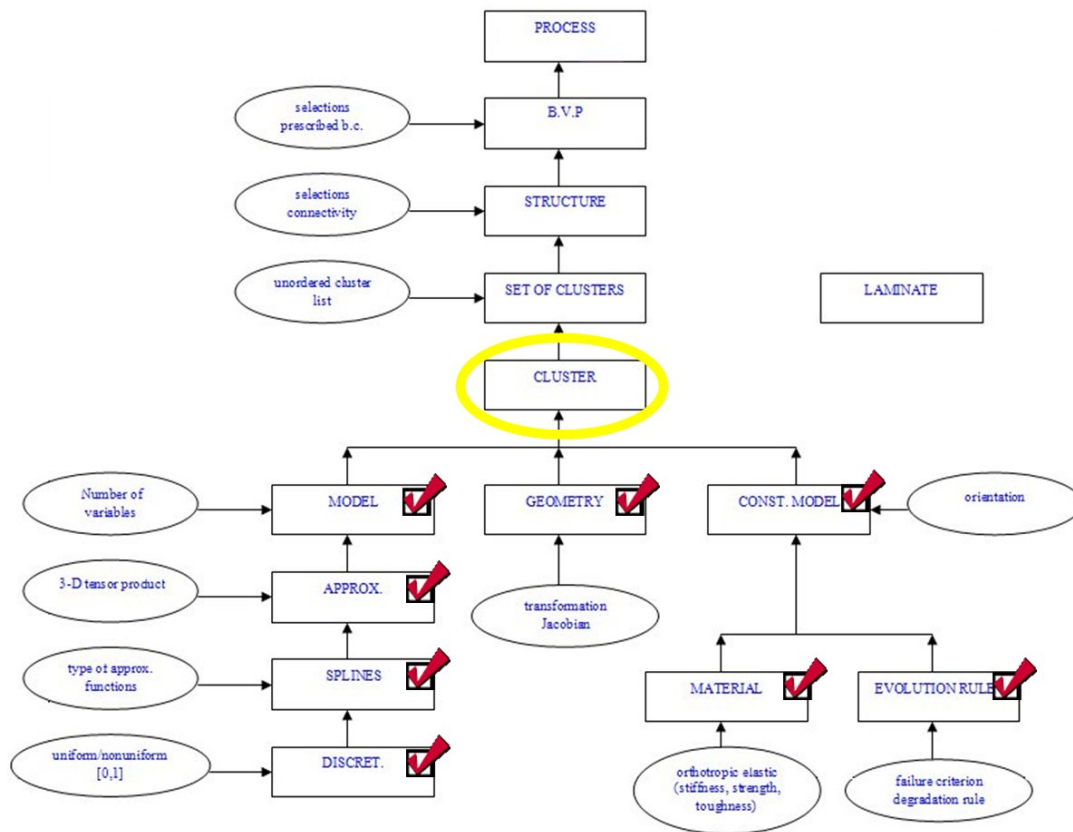
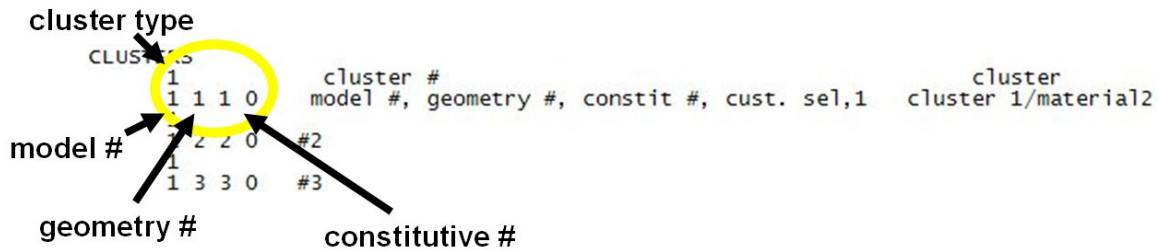


Figure 165. Completion of BSAM flow chart foundation

The purpose of the cluster input block is to define clusters by assigning a model, a geometry, and a constitutive law number to each one. As the example shown below indicates, there are four variables required to define each cluster: (1) cluster type, (2) model number, (3) geometry number, and (4) constitutive number. Cluster type 1 defines a standard cluster. The other three variables call directly on a specific model defined in

the model input block, a specific geometry defined in the geometry input block, and a specific constitutive law number defined in the constitutive model input block.



The highlighted example (cluster #1) above defines a standard cluster with the characteristics defined by model #1, geometry #1, and constitutive model #1 (45° ply made of IM6/3501-6).

24 clusters were required for the scarf model, as shown below. While only unique geometries need to be defined, every cluster has to be defined individually.

45° Cluster 1	C9	Cluster 17
0° Cluster 2	C10	Cluster 18
-45° Cluster 3	C11	Cluster 19
90° Cluster 4	C12	Cluster 20
90° Cluster 5	C13	Cluster 21
-45° Cluster 6	C14	Cluster 22
0° Cluster 7	C15	Cluster 23
45° Cluster 8	C16	Cluster 24

Figure 166. Cluster number assignment convention for scarf model

A breakdown of how the cluster input block was formed for the scarf model is shown in the illustration below. The first eight clusters defined (clusters #1 - #8) represented the left side of the scarf repair. The next eight clusters (#9 - #16) represented the adhesive bond line. The last eight clusters (#17 - #24) represented the right side of the scarf repair.

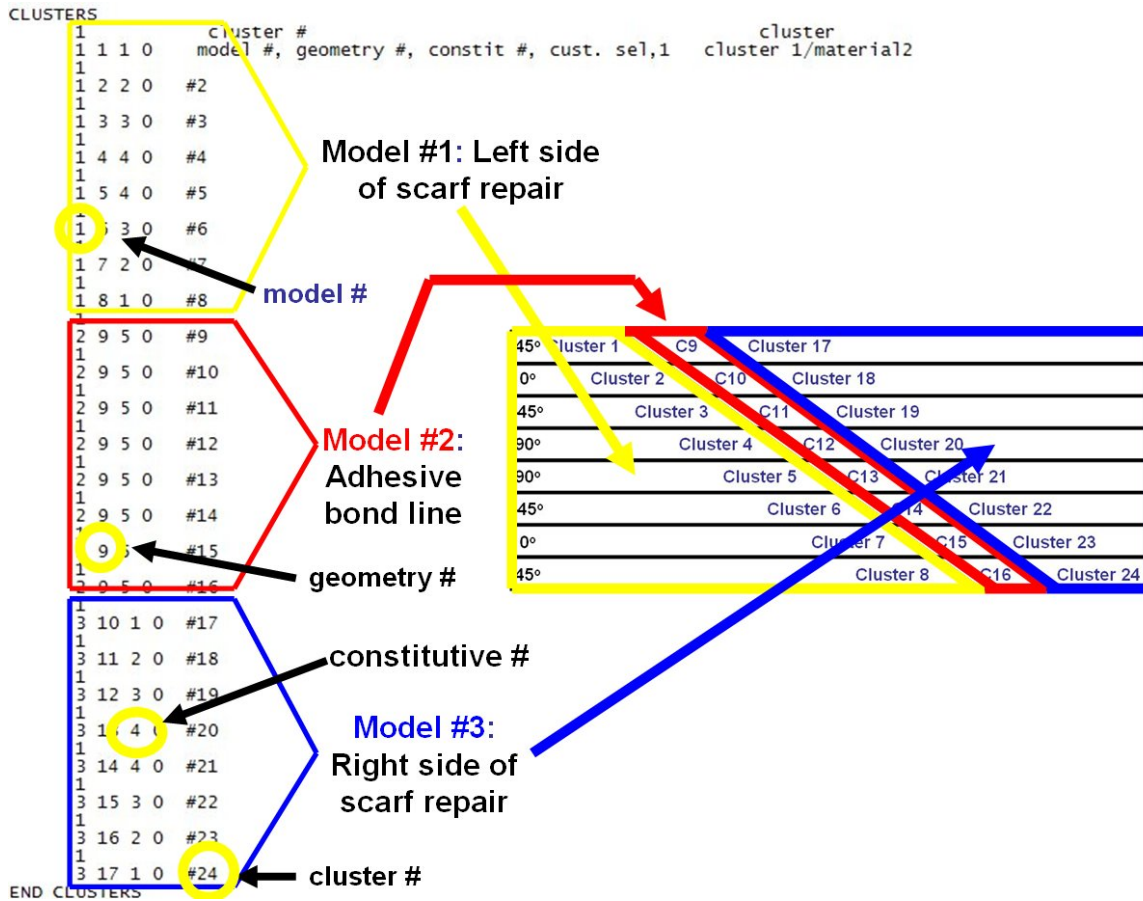


Figure 167. Development of clusters input block for scarf model

374 clusters were required to build the stepped-lap model, as shown in Figure 168

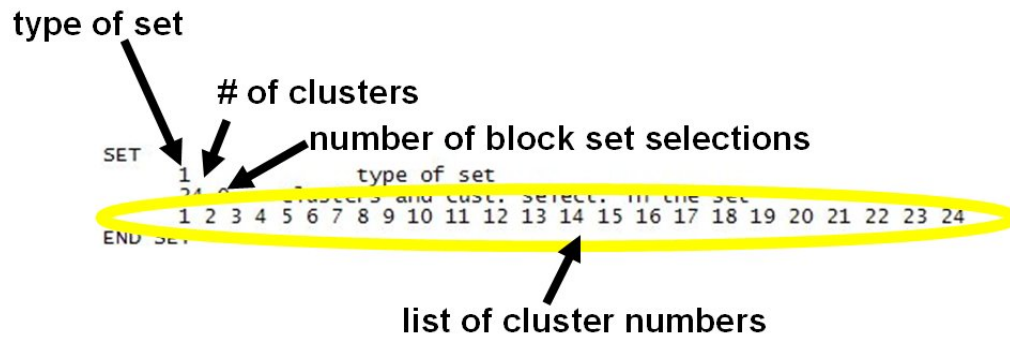


Figure 168. Clusters required to build stepped-lap model

The same methodology and process used in the scarf model was used to develop the cluster input block for the stepped-lap model. However, because of its length (374 clusters defined) and redundancy, its development will not be discussed in this section.

Set Input Block

The purpose of the set block is to select the clusters that will be included in the analysis. In the scarf model example shown below, there are several variables defined in this section: (1) the type of set, (2) the number of clusters, (3) the number of block set selections, and (4) a list of cluster numbers.



The set input block for the stepped-lap model is similar to the scarf, except that there are 374 clusters selected and listed. The set input block for the stepped-lap model is shown below.

```

SET
1 374 0
type of set clusters and cust. select. in the set
1 2 3 4 5 6 7 8 9 10 11 12
13 14 15 16 17 18 19 20 21 22 23 24
25 26 27 28 29 30 31 32 33 34 35 36
37 38 39 40 41 42 43 44 45 46 47 48
49 50 51 52 53 54 55 56 57 58 59 60
61 62 63 64 65 66 67 68 69 70 71 72
73 74 75 76 77 78 79 80 81 82 83 84
85 86 87 88 89 90 91 92 93 94 95 96
97 98 99 100 101 102 103 104 105 106 107 108
109 110 111 112 113 114 115 116 117 118 119 120
121 122 123 124 125 126 127 128 129 130 131 132
133 134 135 136 137 138 139 140 141 142 143 144
145 146 147 148 149 150 151 152 153 154 155 156
157 158 159 160 161 162 163 164 165 166 167 168
169 170 171 172 173 174 175 176 177 178 179 180
181 182 183 184 185 186 187 188 189 190 191 192
193 194 195 196 197 198 199 200 201 202 203 204
205 206 207 208 209 210 211 212 213 214 215 216
217 218 219 220 221 222 223 224 225 226 227 228
229 230 231 232 233 234 235 236 237 238 239 240
241 242 243 244 245 246 247 248 249 250 251 252
253 254 255 256 257 258 259 260 261 262 263 264
265 266 267 268 269 270 271 272 273 274 275 276
277 278 279 280 281 282 283 284 285 286 287 288
289 290 291 292 293 294 295 296 297 298 299 300
301 302 303 304 305 306 307 308 309 310 311 312
313 314 315 316 317 318 319 320 321 322 323 324
325 326 327 328 329 330 331 332 333 334 335 336
337 338 339 340 341 342 343 344 345 346 347 348
349 350 351 352 353 354 355 356 357 358 359 360
361 362 363 364 365 366 367 368 369 370 371 372
373 374
END SET

```

Structure Input Block

The structure input block assembles the set of clusters into a structure. Overall, it connects clusters together, and can be thought of as an element connectivity section.

Boundary conditions and origins were also defined in this input block.

The first parameter necessary in defining the structure was the type of structure. In this case, a single body structure (option 1) was modeled for both the scarf and stepped lap joints. From the scarf model structure block below, it can be seen that 37 connections were required to connect the 24 clusters defined in the cluster input block.

```
STRUCTURE
1 type of structure
1 37 2 set #, # of connections ,#f select structure
0. 0. 0. 0. 0. 0. origin
5 1 2 Type of conn. (5 -sides 6 and 5), clusters 1,2 connectivity
5 2 3
5 3 4
5 4 5
5 5 6
5 6 7
5 7 8
2 1 9
5 9 10
2 2 10
5 10 11
2 3 11
5 11 12
2 4 12
5 12 13
```

After defining the origin (0. 0. 0. 0. 0. 0.), the connections were then defined for the structure. As the highlighted numbers indicate, the number in the left column represented the connection type, while the two adjacent columns indicated the two clusters that were being connected. For both the scarf and stepped-lap models, only two connection types were used: type 2 and type 5.

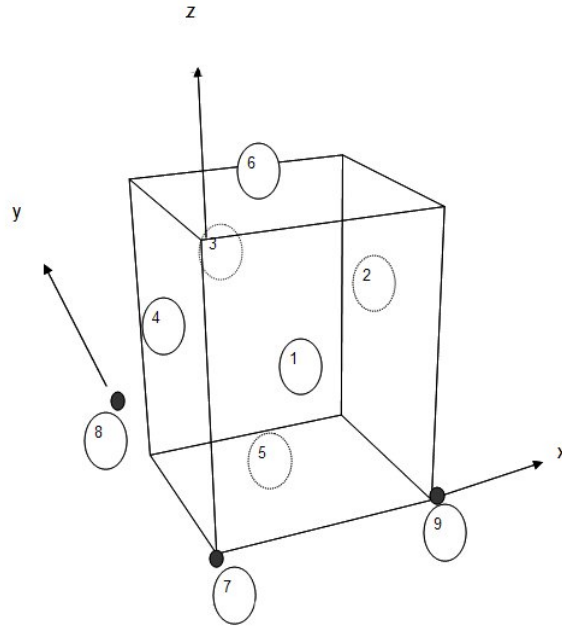


Figure 169. Sides and edges of cluster defined.

If the assigned numbers on the cube above are considered, a type 2 connection linked “side 2” to “side 4”, while a type 5 connection linked “side 6” to “side 5.” The figures shown below provide a better illustration of this.

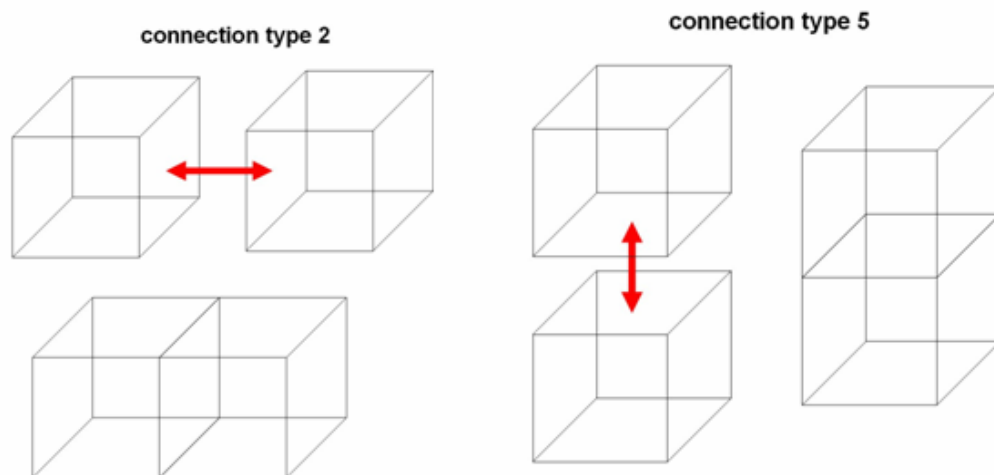


Figure 170. Connection type 2 and 5.

The connections needed for the scarf model are shown below. The connections for the stepped-lap model were developed in a similar fashion; however, because 709 connections were needed to put the stepped-lap model together, they will not be listed here.

```

5 1 2
5 2 3
5 3 4
5 4 5
5 5 6
5 6 7
5 7 8
2 1 9
5 9 10
2 2 10
5 10 11
2 3 11
5 11 12
2 4 12
5 12 13
2 5 13
5 13 14
2 6 14
5 14 15
2 7 15
5 15 16
2 8 16
2 9 17
5 17 18
2 10 18
5 18 19
2 11 19
5 19 20
2 12 20
5 20 21
2 13 21
5 21 22
2 14 22
5 22 23
2 15 23
5 23 24
2 16 24

```

The second half of the structure input block holds information pertaining to parameters for boundary and loading conditions. For example, the rigid body displacements section (shown below) outlines the clusters that are fixed or constrained in the model. Referring to Figure 169, the “4” edge of all clusters on the left side of the scarf joint (clusters 1-8) are constrained in the x-direction, cluster 1 at point “7” is

constrained in the y and z directions, and cluster 1 point “8” is constrained in the z-direction. These clusters are indicated by the far left column.

```

101 11    rigid body displs (struct selection 2)
1 2 4
2 2 4
3 2 4
4 2 4
5 2 4
6 2 4
7 2 4
8 2 4
1 4
1 3
1 4

```

constraint in z-direction

y

z

The applied displacements section (shown below for scarf model) outlines the clusters that are loaded and which direction they are loaded in. In the case of the scarf model, the clusters on the right side of the model (clusters 17-24) are loaded in the 2, or x, direction. Load is applied to eight clusters in the scarf model.

```

101 8    applied displs (struct selection 3)
17 2 2
18 2 2
19 2 2
20 2 2
21 2 2
22 2 2
23 2 2
24 2 2

```

For the stepped-lap model, the rigid body displacements and applied displacements sections were modified in a similar manner. The clusters on the far left side of the model (clusters 1-22) were constrained, while load was placed on the clusters on the far right side (clusters 353-374). These sections from the stepped-lap model will not be shown, as 25 constraints and 22 applied displacements were required.

Verifying accuracy of model

At this point in the construction of the two models, it was possible to plot the connected clusters to verify the geometrical accuracy of the model. This was done using Mat Lab. Generating a visual image of the entire model at this point allows the user to verify that they have properly defined model size, discretization type, geometries, connections, and orientation. The colors on the generated image are arbitrary.

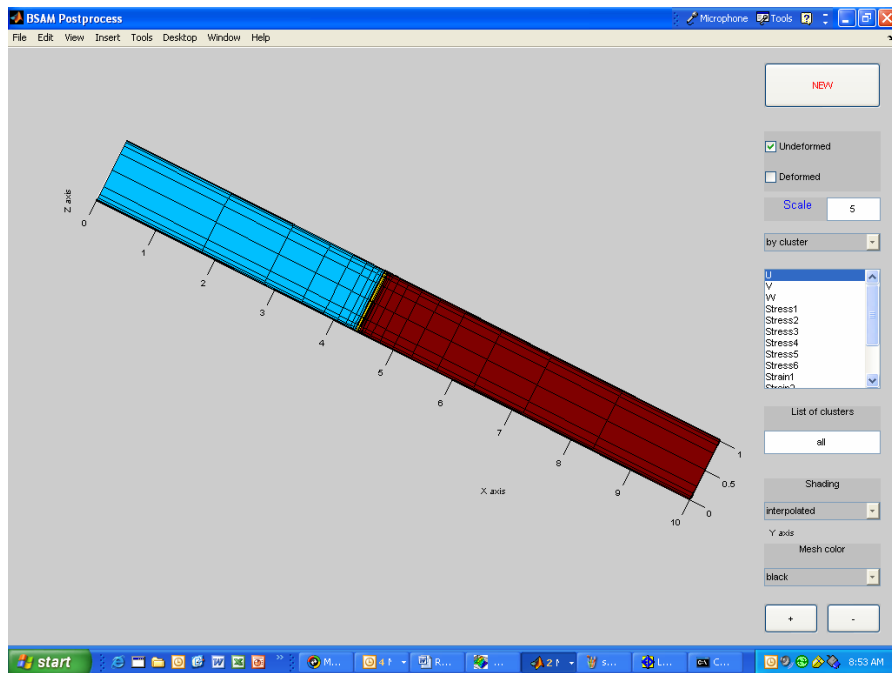


Figure 171. Screen capture of top view of BSAM scarf model in Mat Lab.

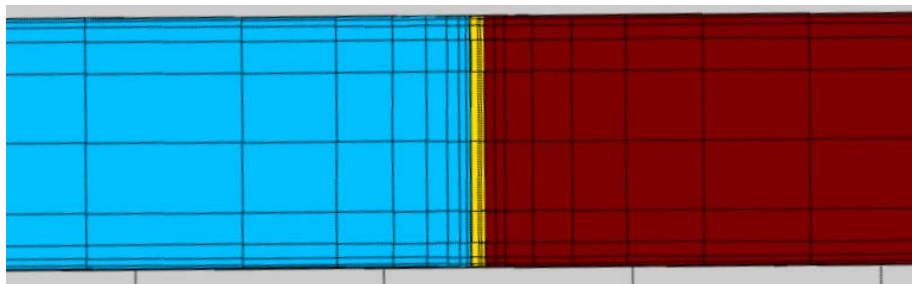


Figure 172. Screen capture of top view of segment of BSAM scarf model in Mat Lab.

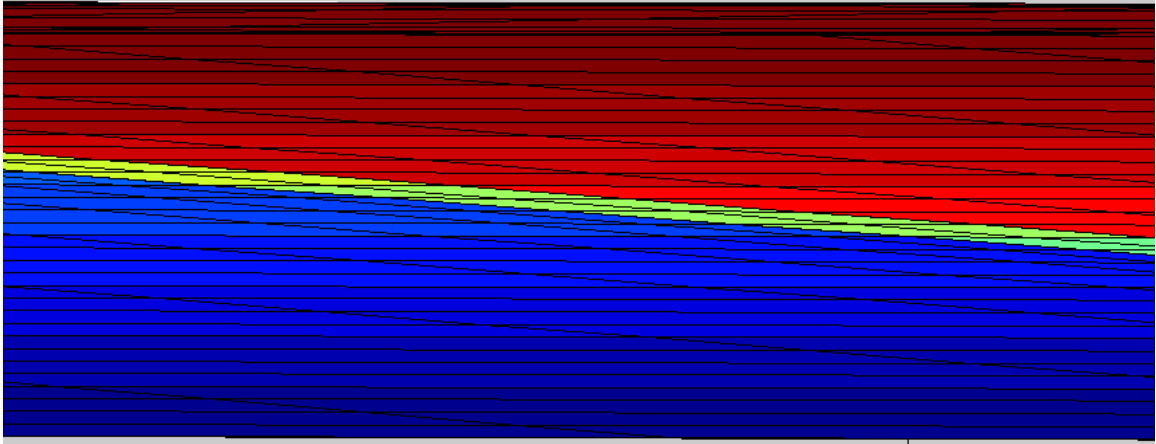


Figure 173. Screen capture of edge view of segment of BSAM scarf model in Mat Lab.

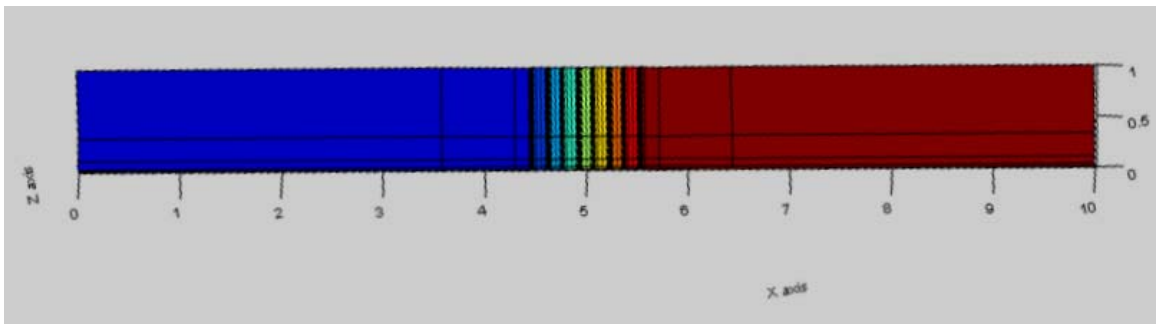


Figure 174. Screen capture of BSAM stepped-lap model in Mat Lab.

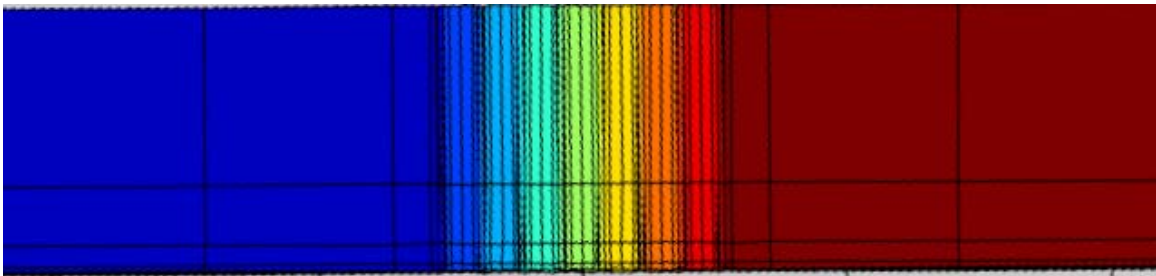


Figure 175. Screen capture of top view of segment of BSAM stepped-lap model in Mat Lab.

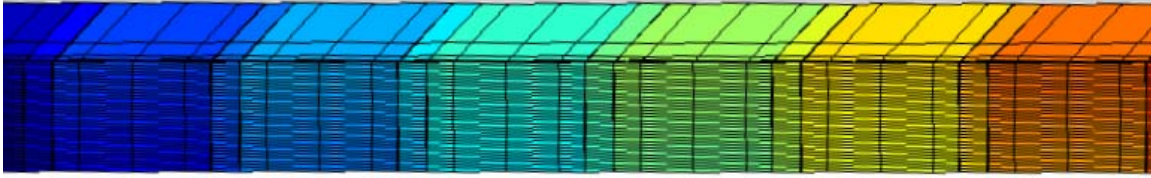


Figure 176. Screen capture of edge view of segment of BSAM stepped-lap model in Mat Lab.

Boundary Conditions Block

This block defines the boundary conditions of the model and was used for both models to find the average traction and corresponding displacement of each specimen. There were several steps taken to find the actual displacement of the specimens. First of all, the BSAM computer program was run given a unit displacement of 1.0 inches.

```
BOUNDARY
1 Boundary Condition Type (1=Mechanical, 2=Thermo-Mechanical)
1 2 Structure #, # of Conditions
2 2 0 BC Type, structure selection #
0.0 value
2 3 0 BC Type, structure selection #
5.4899214724e-3 value
END B
```

Enter 1.0"

While this value was much greater than the actual displacement, the program processed the model using this displacement and provided an average traction (T_x). While the traction calculated was extremely high (on the order of 10^6), it could be used with the unit displacement to find a set ratio between displacement and average traction for the model. Using this ratio and the traction calculated from the actual load and cross-sectional area of the specimens, the actual displacement of the specimen was determined. Below is an example of this process from the scarf model.

$$\frac{\text{unit displacement}}{\text{traction calculated in BSAM corresponding to unit displacement}} = \frac{\text{actual displacement}}{\text{actual traction}}$$

$$\text{actual traction} = \frac{\text{load}}{\text{area}} = \frac{450\text{lb}}{0.0885\text{in} * 1.0045\text{in}} = 5122\text{psi}$$

$$\frac{1.0}{10^6} = \frac{\text{actual displacement}}{5122 \text{ psi}}$$

$$\text{actual displacement} = 0.005496466 \text{ in}$$

The actual displacement (0.005496466in) was then plugged back into the boundary input block. Using the actual displacement, the BSAM computer program was rerun to calculate appropriate strains and displacements. This process was done for both the stepped-lap and scarf models.

Output Block

The purpose of this block is to set the desired outputs. The sections of the output input file block concerning moiré output are unique in the fact that they call upon separate text (.txt) files in order to execute. These text files contain information regarding the local coordinates for each cluster where values or output will be calculated. This block can contain several types of desired outputs, including moiré output (option 4), Mat Lab output (option 7), or average traction output (option 2). Figure 177 and Figure 178 show the input block segments containing information calling Mat Lab output and average traction output.

```
7  MatLab output option                                output1
1  0                                     not used yet
0  1  1      #of clusters to output -> next line=cluster list
0
```

Figure 177. Mat Lab Output Option

```
2 type of output: average tractions                    output 91
1 0  structr., solve-# b.c.p./postproc-0
8 2  0 number of clustrs, side,   coordinate system
17 18 19 20 21 22 23 24
```

Figure 178. Average Traction Output Option

To match the resolution of the experimental data acquired through moiré interferometry, it was decided that 500 data points should be calculated through the thickness for both the stepped-lap (2.2479mm or 0.0885in) and scarf (2.2226mm or 0.087504in) models. This resulted in the spacing between data points of 4.44 μ m (0.000177in) for the stepped-lap model and 4.496 μ m (0.000175in) for the scarf model. Using the same intervals between data points across the width of the repairs, this meant that roughly 3.8 million data points had to be calculated for the stepped-lap model, while 4.4 million data points were used for the scarf model.

Since the stepped-lap model contained 3.8 million data points and the scarf model contained 4.4 million data points, text files defining the localized coordinates of all of these data points had to be produced. This portion of the code modification was very tedious and time-consuming as several steps were involved. The steps required to create these text files are outlined in the following paragraphs.

Overall, each output text file created for moiré output contains four columns of information: (1) a point reference number, (2) the local x-coordinate of each data point, (3) the local y-coordinate of each data point, and (4) the local z-coordinate of each data point. To achieve a high level of resolution in the BSAM computer program moiré output (as described above), only data points in the region of the repairs were defined for output. For the stepped-lap model, it was decided that the local coordinates in the region $\pm 3.245\text{mm}$ ($\pm 0.1277\text{in}$) from the ends of the stepped-lap joint would be defined. The region of output can be seen in Figure 179. In terms of the global coordinates of the entire stepped-lap specimen, output was requested from 109.93mm (4.3278in) to 143.87mm (5.6641in) in the x-direction.

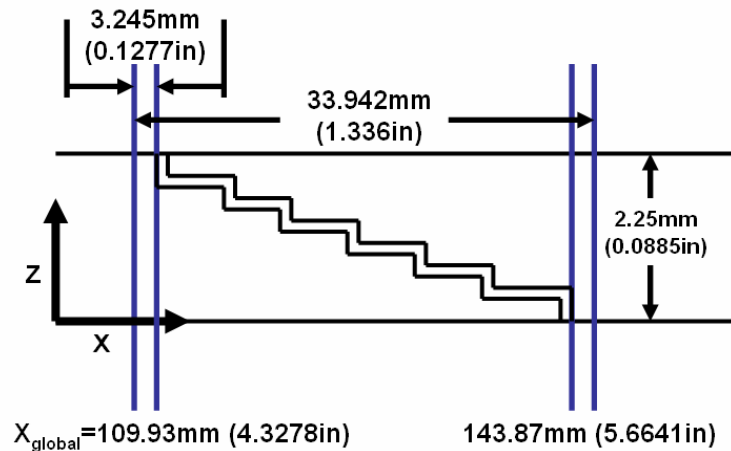


Figure 179. Region defined for BSAM output for stepped-lap model (not to scale).

Referring to the region defined in Figure 179, the grid for the stepped-lap model measured 33.942mm (1.336in) in the x-direction and 2.25mm (0.0885in) in the z-direction. Data points had a spacing of 4.44 μ m (0.000177in) for the stepped-lap model in both the x-direction and z-direction.

For the scarf joint, it was decided that the local coordinates in the region +/- 2.54mm (+/-0.1in) from the ends of the scarf joint would be defined. The region of output can be seen in Figure 180. In terms of the global coordinates of the entire scarf specimen, output was requested in a fine grid of data points from 108.02mm (4.2529in) to 147.41mm (5.8035in) in the x-direction. While the entire repair was modeled for both the stepped-lap and scarf joint, the region of repair was limited by the capability of the computer used.

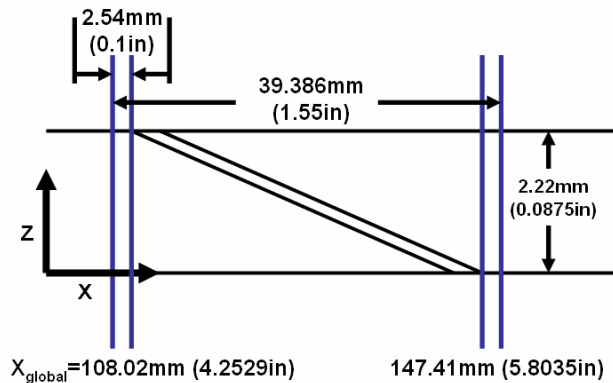


Figure 180. Region defined for BSAM output for scarf model (not to scale).

Referring to the region defined in Figure 180, the grid for the scarf model measured 39.386mm (1.55in) in the x-direction and 2.22mm (0.0875in) in the z-direction. Data points had a spacing of 4.496 μ m (0.000175in) for the scarf model in both the x-direction and z-direction. Because of the sheer number of data points for both models, the output files produced by the BSAM computer program were extremely large (on the magnitude of 600MB to 800MB) and difficult to handle on computers with limited RAM.

After defining the region of output, the next step was to convert the global coordinates of each geometry to local coordinates scaled between 0 and 1. This was done in Microsoft Excel. Figure 181 shows the geometries used to build the stepped-lap model, with the shaded blocks indicating the adhesive and the white blocks indicating the composite panels (not to scale).

Figure 181. Geometries of stepped-lap model (not to scale).

For an example, the process of converting the global coordinates to non-dimensionalized local coordinates for geometry 7 of the stepped-lap model will be described. Referring to the geometry input block section of this chapter, it can be seen that the width (x-direction) of geometry 7 is 3.245mm (0.127769in) while the height (z-direction) is 0.2107mm (0.08296875in). Using a spacing of 4.44 μ m (0.000177in) between each data point, it could be determined that roughly 34,000 data points were required for output in this geometry. Dividing the height of the geometry by the spacing between data points, it is evident that 46 data points will be calculated through the thickness. Using Microsoft Excel to create an incremental pattern in both x and z directions, global coordinates for each data point can be determined.

Because the geometries in the stepped-lap model are perfectly square or rectangular, converting from global coordinates to localized coordinates can be done by simply dividing each x or z global coordinate by the width (x -direction) or the height (z -direction) of geometry 7. For example, for a data point with global coordinates of ($x = 2.76\text{mm}$, $y = 0$, $z = 0.07\text{mm}$), the local coordinates would be ($x = 0.85$, $y = 0$, $z = 0.332$). These local coordinates were found by dividing 2.76mm by 3.245mm (local x coordinate), 0mm by 25.4mm (local y coordinate), and 0.07mm by 0.2107mm (local z coordinate), respectively.

Columns of data containing the local coordinates for geometry 7 were then converted into a text file and labeled appropriately. Figure 182 shows the segment of the output input block corresponding to geometry 7. As the block describes, moiré output (option 4) is desired for structural post-processing (option 1, then option 0).

```

4      Moire output
1 0    structr., solve-# b.c.p./postproc-0      output8
14 33934 0 number of clustrs, # of points,    coordinate system
    45      66
    89     110
   133     154
   177     198
   221     242
   265     286
   309     330      cluster numbers
geometry 7 clusters.txt

```

Figure 182. Moire output block from input file for geometry 7 clusters

Cross referencing Figure 183 with Figure 181, it can be seen that geometry 7 is used in 14 different clusters of the stepped-lap model and that 33,934 data points are defined in the separate text file. These clusters are listed in two columns toward the bottom of Figure 182. The text file is appropriately labeled “geometry 7 clusters.txt.”

22	44	66	88	110	132	154	176	198	220	242	264	286	308	330	352	374
21	43	65	87	109	131	153	175	197	219	241	263	285	307	329	351	373
20	42	64	86	108	130	152	174	196	218	240	262	284	306	328	350	372
19	41	63	85	107	129	151	173	195	217	239	261	283	305	327	349	371
18	40	62	84	106	128	150	172	194	216	238	260	282	304	326	348	370
17	39	61	83	105	127	149	171	193	215	237	259	281	303	325	347	369
16	38	60	82	104	126	148	170	192	214	236	258	280	302	324	346	368
15	37	59	81	103	125	147	169	191	213	235	257	279	301	323	345	367
14	36	58	80	102	124	146	168	190	212	234	256	278	300	322	344	366
13	35	57	79	101	123	145	167	189	211	233	255	277	299	321	343	365
12	34	56	78	100	122	144	166	188	210	232	254	276	298	320	342	364
11	33	55	77	99	121	143	165	187	209	231	253	275	297	319	341	363
10	32	54	76	98	120	142	164	186	208	230	252	274	296	318	340	362
9	31	53	75	97	119	141	163	185	207	229	251	273	295	317	339	361
8	30	52	74	96	118	140	162	184	206	228	250	272	294	316	338	360
7	29	51	73	95	117	139	161	183	205	227	249	271	293	315	337	359
6	28	50	72	94	116	138	160	182	204	226	248	270	292	314	336	358
5	27	49	71	93	115	137	159	181	203	225	247	269	291	313	335	357
4	26	48	70	92	114	136	158	180	202	224	246	268	290	312	334	356
3	25	47	69	91	113	135	157	179	201	223	245	267	289	311	333	355
2	24	46	68	90	112	134	156	178	200	222	244	266	288	310	332	354
1	23	45	67	89	111	133	155	177	199	221	243	265	287	309	331	353

Figure 183. Cluster numbering system for stepped-lap model.

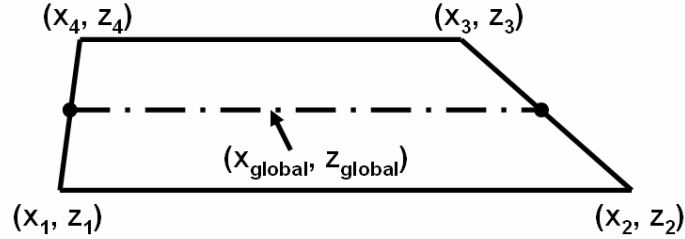
The same general process was used to identify data points for BSAM moiré output for the remaining geometries, resulting in the creation of twelve (12) text files referencing all 374 clusters of the stepped-lap model. Although only nine (9) unique geometries existed for the stepped-model, geometries 1, 2, and 3, on the far right and left sides of the repair had to be modeled separately to access the appropriate range of localized data coordinates.

Developing the separate text files for the scarf model was a little more complicated. While the geometries for the stepped-lap model had square corners resulting in an easy conversion from global to local coordinates, the geometries for the scarf model were not square, as shown in Figure 184.

45°	G8	G9	Geometry 17
0°	Geometry 7	G9	Geometry 16
-45°	Geometry 6	G9	Geometry 15
90°	Geometry 5	G9	Geometry 14
90°	Geometry 4	G9	Geometry 13
-45°	Geometry 3	G9	Geometry 12
0°	Geometry 2	G9	Geometry 11
45°	Geometry 1	G9	Geometry 10

Figure 184. More complex shape of scarf model geometries.

The local z-coordinates could be calculated similarly to the geometries modeled in the stepped-lap model, but linear equations were derived to find the localized x-coordinates for the scarf model. These equations are shown below in Figure 185.



$$x_{RIGHT} = \frac{x_3 - x_2}{z_3 - z_2} * z_{global} + x_2$$

$$x_{LEFT} = \frac{x_4 - x_1}{z_4 - z_1} * z_{global} + x_1$$

$$x_{LOCAL} = \frac{x_{global} - x_{LEFT}}{x_{RIGHT} - x_{LEFT}}$$

Figure 185. Determining local coordinates for scarf model.

Local coordinates were again calculated from global coordinates in Excel. Using a spacing of 4.496 μ m (0.000175in) between each data point, it could be determined that a about 4.5 million data points would need to be defined to cover the region of interest. This was important to note, because although 3.8 million data points were spread over 374 clusters in the stepped-lap model, 4.5 million data points had to be spread over only 24 clusters in the scarf model. In the end, all of the geometries in the scarf model exceeded the worksheet capacity of Microsoft Excel (roughly 65,500), so multiple worksheets were created for each geometry. This meant that while a small group of separate text files (12) couple be applied to multiple clusters in the stepped-lap model, multiple text files had to be assigned to each cluster for the scarf model.

45°	Cluster 8	C16	Cluster 24
0°	Cluster 7	C15	Cluster 23
-45°	Cluster 6	C14	Cluster 22
90°	Cluster 5	C13	Cluster 21
90°	Cluster 4	C12	Cluster 20
-45°	Cluster 3	C11	Cluster 19
0°	Cluster 2	C10	Cluster 18
45°	Cluster 1	C9	Cluster 17

Figure 186. Clusters in scarf model.

Table 2 gives an idea of the number of text files generated for scarf model moiré output of 4.5 million data points spread over 24 clusters. The far left column indicates the clusters in the scarf model, while each row corresponding to the cluster numbers show (1) the number of data points in each text file and (2) the number of text files created for each cluster. Overall, 4.5 million data points were distributed over 89 text files.

Table 2. Text files generated for scarf model moiré output.

cluster	number of data points in each text file									
1	65472	65408	65472	65408	65408	65408	64923	22903		
2	65408	65344	65344	65280	65280	65274	29208			
3	65344	65280	65280	65216	65216	35664				
4	65280	65216	65216	65152	41554	387				
5	65216	65152	65152	46717	1428					
6	65152	65088	51205	3080						
7	65088	54935	5310							
8	58115	8074								
9	18729	2091								
10	18729	2091								
11	18729	2091								
12	18729	2091								
13	18729	2091								
14	18729	2091								
15	18729	2091								
16	18729	2091								
17	35176	31488								
18	35176	64960	26176							
19	35240	65024	65024	20672						
20	35304	65088	65088	65024	15104					
21	35368	65152	65152	65088	65088	6336	3008			
22	35432	65216	65216	65152	65152	65216	3456			
23	35432	65216	65216	65152	65152	65152	58688	4086		
24	35624	65344	65408	17088	65344	65344	65344	51968	51968	768

An important step in the generation of text files with localized coordinates was to remove all data points with localized coordinates of greater than 1 or less than 0. Localized coordinates in these ranges occurred whenever the global coordinate exceeded the bounds of the cluster.

To illustrate how multiple text files were created for a given cluster, cluster 3 will be used as an example. Referencing cluster 3 in Table 2, it can be seen that six text files containing between 35,664 and 65,344 data points were necessary for moiré output at the spacing or resolution desired. In order to generate output from the data points in all six text files, each text file has to be called individually in the OUTPUT input block. The section of the output block corresponding to cluster 3 can be seen in Figure 187. As Figure 187 indicates, each text file related to cluster 3 is given an output block (labeled 17-22). Each output block segment lists the number of data points defined in each text file, such as 65,344 data points for output 17, 65,280 data points for output 18, and so on. Finally, the last line of each output segment lists the specific text file containing localized data coordinates. This is listed as “cluster3_1.txt”, “cluster3_2.txt”, and so on. Using this process for the remaining text files, it can be seen that 89 output segments had to be defined for moiré output in BSAM across the entire region of interest.

4	Moire output		
1	0 structr., solve-# b.c.p./postproc-0		
1	65344 0 number of clustrs, # of points,	coordinate system	output17
3	cluster numbers		
	cluster3_1.txt		
4	Moire output		
1	0 structr., solve-# b.c.p./postproc-0		
1	65280 0 number of clustrs, # of points,	coordinate system	output18
3	cluster numbers		
	cluster3_2.txt		
4	Moire output		
1	0 structr., solve-# b.c.p./postproc-0		
1	65280 0 number of clustrs, # of points,	coordinate system	output19
3	cluster numbers		
	cluster3_3.txt		
4	Moire output		
1	0 structr., solve-# b.c.p./postproc-0		
1	65216 0 number of clustrs, # of points,	coordinate system	output20
3	cluster numbers		
	cluster3_4.txt		
4	Moire output		
1	0 structr., solve-# b.c.p./postproc-0		
1	65216 0 number of clustrs, # of points,	coordinate system	output21
3	cluster numbers		
	cluster3_5.txt		
4	Moire output		
1	0 structr., solve-# b.c.p./postproc-0		
1	35664 0 number of clustrs, # of points,	coordinate system	output22
3	cluster numbers		
	cluster3_6.txt		

Figure 187. Output block for cluster 3 in stepped-lap model.

Process Input Block

The final input block for the BSAM computer program is the process block. As Figure 188 indicates, every other input block of the BSAM input file must be defined before the process block can be executed. Overall, the purpose of the process block is to set the type of process, the number of boundary conditions, and the number of outputs.

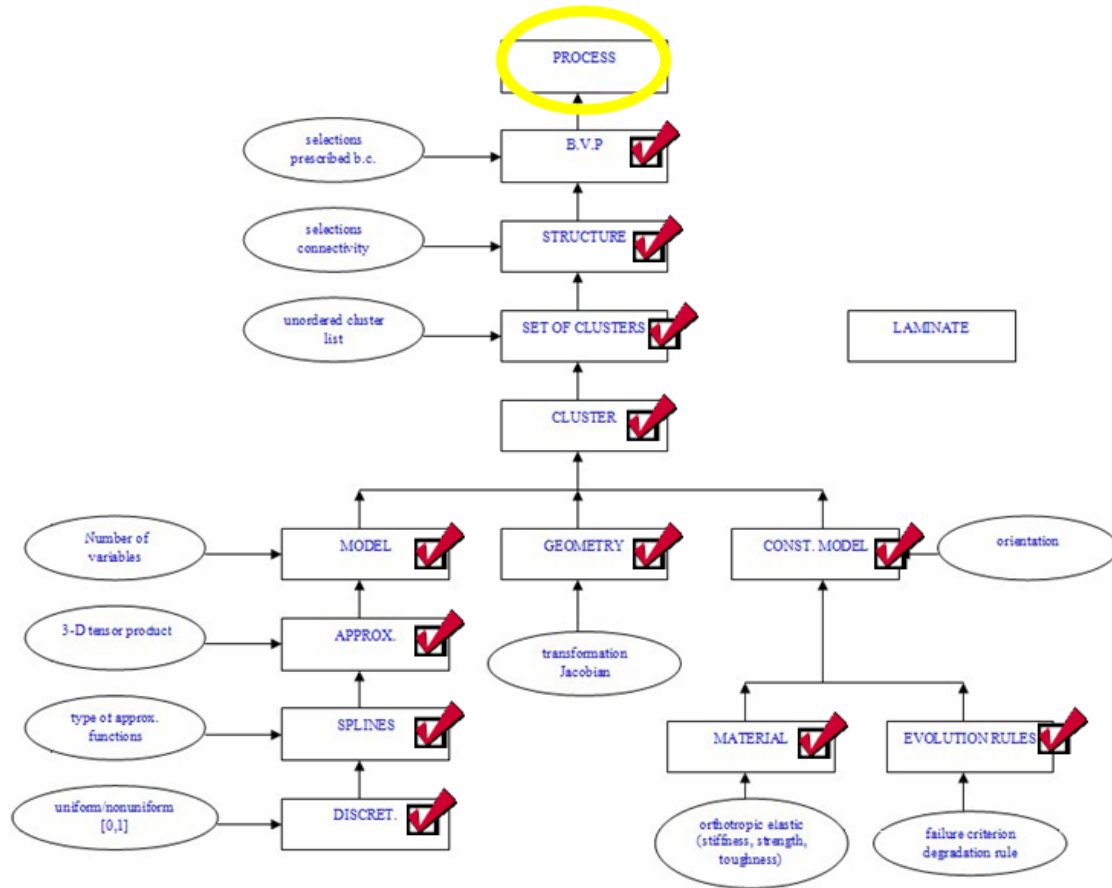


Figure 188. Location of process input block on BSAM input file flowchart.

Figure 189 shows the process input block for the scarf model. The type of process selected for both the stepped-lap and scarf model was 1, or static loading. The first set of boundary conditions were selected for both models, and while various run options were used at different points in processing the models, the post-processing option

was used for all moiré output files. Finally, the bottom portion of the process block defines the output segments to output. As Figure 189 indicates, output segments 1 through 22 were selected for processing. While 91 output segments were present in the scarf model, the size of the output files dictated the number of segments that could be processed in any given run of BSAM computer program. Because of the complexity of the models created in this study, output was produced in multiple processing runs to ensure the size of resultant data files were manageable.

```

|8
8 *****
8 ***** BEGIN BSAM INPUT FILE *****
8 *****
8
INPUT
1
END INPUT
PROCESS
1 Type of process: 1 = static loading
1 2 ID of BC; Run option: 0 = new start, 1 = restart, -1 = mesh output, 2 = postprocess
22 1 # of outputs at each step; total # of steps
1 2 3 4 5 6 7 8 9 10 11 12 13 14 15 16 17 18 19 20 21 22 List of Outputs to Process
END PROCESS
OUTPUT

```

Figure 189. Process input block for scarf model.

In summary, the BSAM computer program is a non-commercial code that lacks a developed graphical user interface. This chapter outlined the process used to modify the BSAM input files developed for this thesis. While a BSAM input file can be modified or created in any order, it is recommended that the user approach problems from the bottom up, defining material properties and geometries first, and then building a specific model from there.

Appendix C: Determination of appropriate loading for moiré fringe pattern visualization

The ideal tensile load for this study was one that is near the linear elastic limit while not causing any cracking or damage in the material. By loading the specimens enough to produce a significant strain field, it would be easier to compare the experimental fringe pattern results to the strain field modeled in the B-spline analysis method (BSAM) program. A load too small would produce a strain field that would be difficult to see, making a comparison of experimental and theoretical displacement and strain maps difficult. A tensile load too high would have caused cracking in the specimen, resulting in an inaccurate strain field and most likely damaging the replicated grating.

Plastic deformation or cracking in the test specimens would require remanufacturing of test specimens. To minimize overloads in the specimens with diffraction gratings, several extra specimens were fitted with acoustic emission sensors and tested to failure to determine the damage incidence load for the test specimens.

Overall, three pieces of information attained in these tests helped determine an appropriate load for moiré fringe pattern visualization:

1. The ultimate strength of $[45_2/0_2/-45_2/90_2]_s$ IM-6/3501-6 carbon epoxy virgin, scarf repaired, and stepped-lap repaired specimens
2. The mechanical behavior of virgin and repaired specimens, in the form of load versus displacement plots
3. A history of acoustic emissions produced by the specimens during testing

In the end, it was concluded that a load of approximately 450lb_f should be used for moiré fringe pattern visualization. This section outlines the process in which this conclusion was reached.

Background on acoustic emissions

Acoustic emission was monitored during these tensile tests to detect any early signs of cracking. Composites, like most materials, emit energy in the form of mechanical vibrations as a result of a defect related event, such as cracking. These sounds propagate from the source and can be detected electronically using an acoustic sensor, which is basically a piezo-electric transducer fixed to the specimen during testing. This sensor converts mechanical shock waves, caused by damage like cracking, into an electronic signal that is amplified and processed (Carlos).



Figure 190. Acoustic sensor attached to specimen.

Monitoring acoustic emission is advantageous in determining the load at which the specimens begin to experience cracking or plastic deformation, as acoustic emissions track defect propagation in real time, as it is occurring. This characteristic makes acoustic emission unique to all other nondestructive test methods (Carlos).

Usually, acoustic emission systems operate in a range of 1kHz to 2MHz or greater in frequency. The lower frequency limit depends on background noises such as friction, outside impacts, or process generated signals. The upper frequency limit is based by attenuation, which is the decrease in amplitude of an electric signal. Since acoustic emission generally occurs in discrete bursts, these bursts are processed and tracked by their amplitude, duration, rise time, and count (number of acoustic emissions) (Carlos). Two acoustic emission behavior patterns were tracked for this set of tests: (1) number of acoustic emissions (counts) with load and (2) rate of acoustic emissions (count rate) with load.

From the 15 manufactured specimens, a total of seven tensile specimen tests were conducted to determine appropriate loading needed to produce visible strain fields in the moiré technique. First, three virgin specimens were tested to get an idea of the original strength of the specimens. Then, two scarf repaired specimens and two stepped-lap repaired specimens were tested. Acoustic sensors were used during all tests.

Test Procedure

Tensile tests were completed using an MTS test machine with load increasing at a constant rate of 10lb_f/sec. This rate was appropriate, as tensile test durations ranged between five and 15 minutes before specimen failure. While a minimum pneumatic grip pressure of 324psi was calculated based on the anticipated failure load ($0.036 \times$ maximum anticipated load = minimum grip pressure), a grip pressure of 700psi was used to ensure the specimens would not slip during testing. For precautionary measures, tabs were taped to the ends of each specimen to prevent damage from the grip pressure, and a

gallon size zipped-lock bag was taped around the testing area to protect people from material debris when the specimen failed. The test set-up can be seen in Figure 191.



Figure 191. Test set-up.

Tests 1-3: Virgin (unrepaired) Specimens

The first virgin specimen, specimen #5, was used for a test run to make sure sensors and equipment were hooked up and running properly. During this test run, it was determined that the acoustic sensor software was not connected properly with the MTS machine software. In the process of solving this problem, specimen #5 was loaded and unloaded several times before all equipment was running correctly. While preliminary loading was not high enough to cause delamination, the numbers generated during this test run were not used for further analysis.

After properly setting up the test, two more virgin specimens were tested to failure. Virgin specimen #1 fractured at 9036.12 lb_f, while virgin specimen #2 fractured

at 9047.12 lb_f. The load versus displacement behavior of both virgin specimens is shown in Figure 192. As Figure 192 indicates, the mechanical behavior of both specimens was nearly identical.

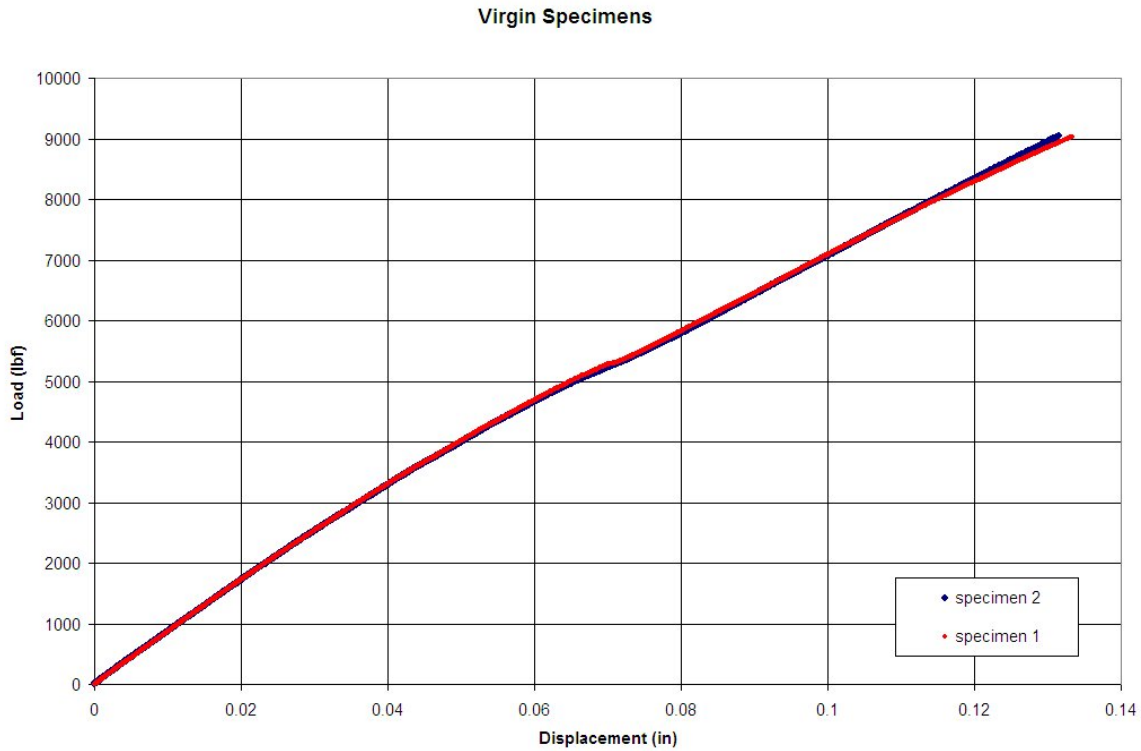


Figure 192. Load versus displacement of virgin specimens.

Photographs of the fractured specimens also indicated similar fracture surfaces, as both specimens delaminated along the 90° plies. These photographs can be seen below in Figure 193, Figure 194, and Figure 195.



Figure 193. Fractured virgin specimen 1 in MTS machine.

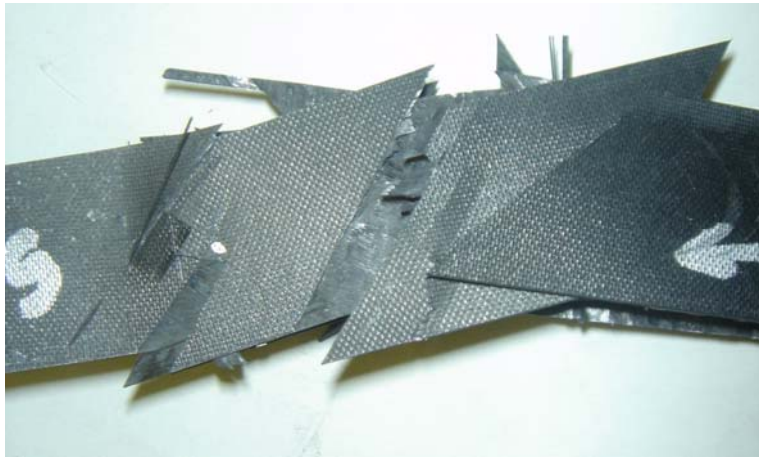


Figure 194. Fractured surface of virgin specimen #1.



Figure 195. Fracture surface of virgin specimen #2.

Initial acoustic emission was detected in virgin specimen #1 at a load of approximately 1900 lb_f, as shown in Figure 196. Delamination of virgin specimen #1 occurred at around 5400 lb_f as indicated by the peak count rate location in Figure 197.

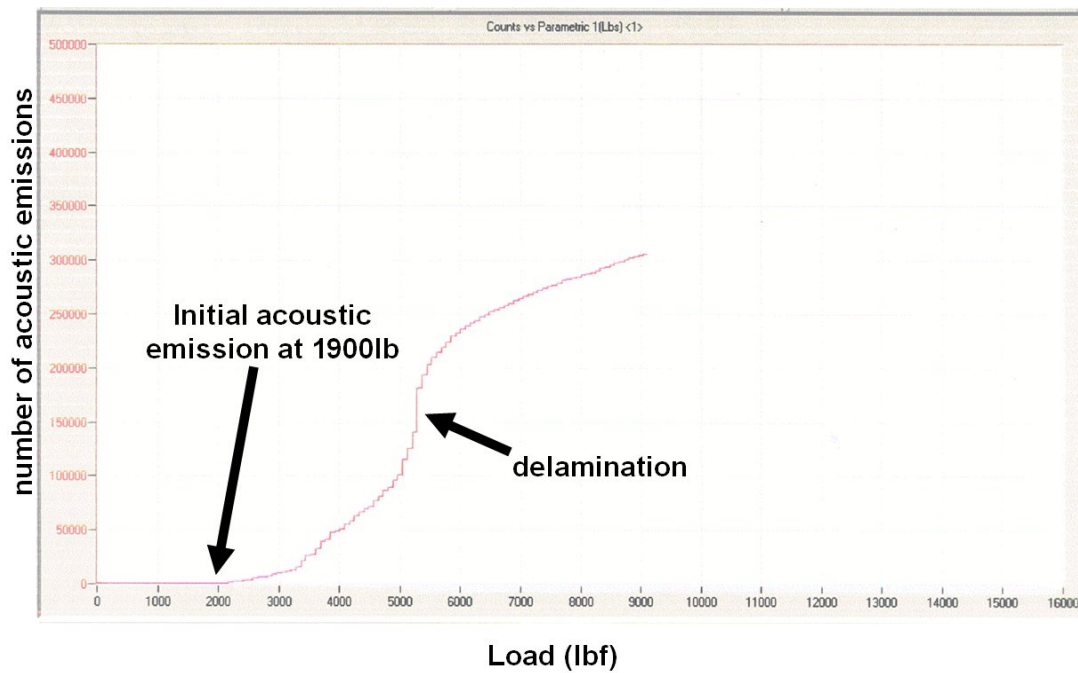


Figure 196. Counts versus load (lb_f) chart for virgin specimen #1.

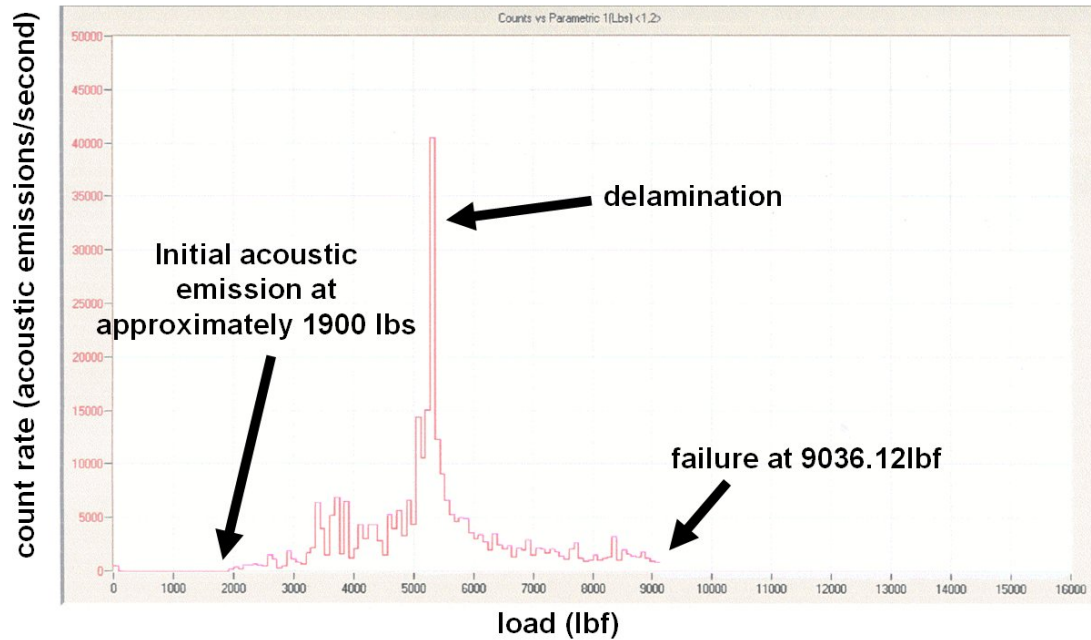


Figure 197. Count rate versus load (lb_f) chart for virgin specimen #1.

Initial acoustic emission was detected in virgin specimen #2 at a load of approximately 1700 lb_f, as shown in Figure 198. Delamination of virgin specimen #2 occurred at around 5100 lb_f as indicated in Figure 199.

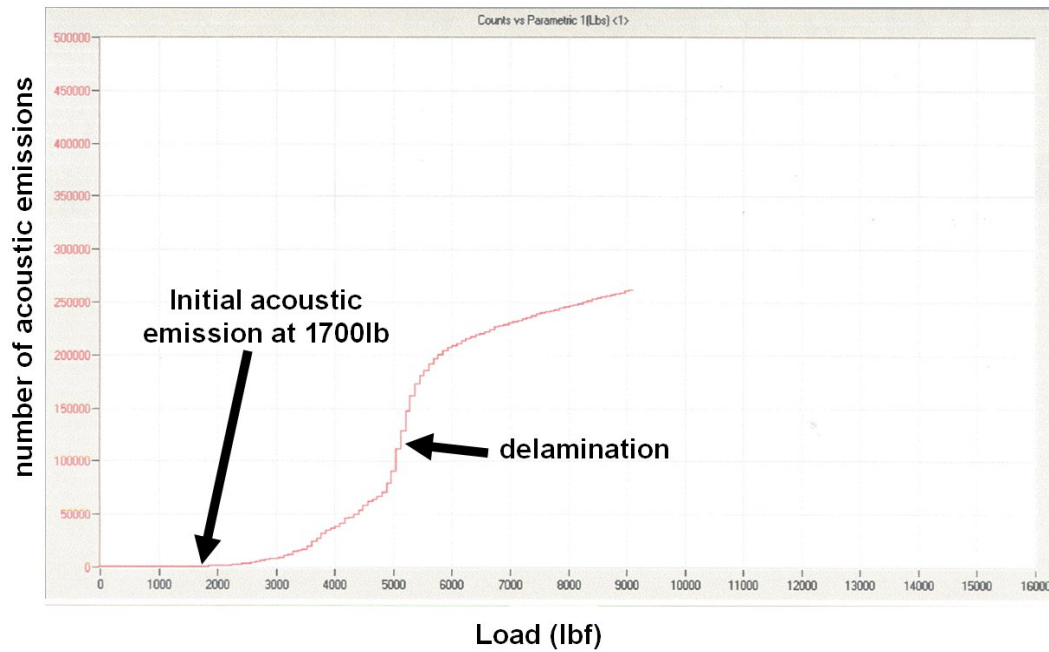


Figure 198. Counts versus load (lbf) of virgin specimen #2.

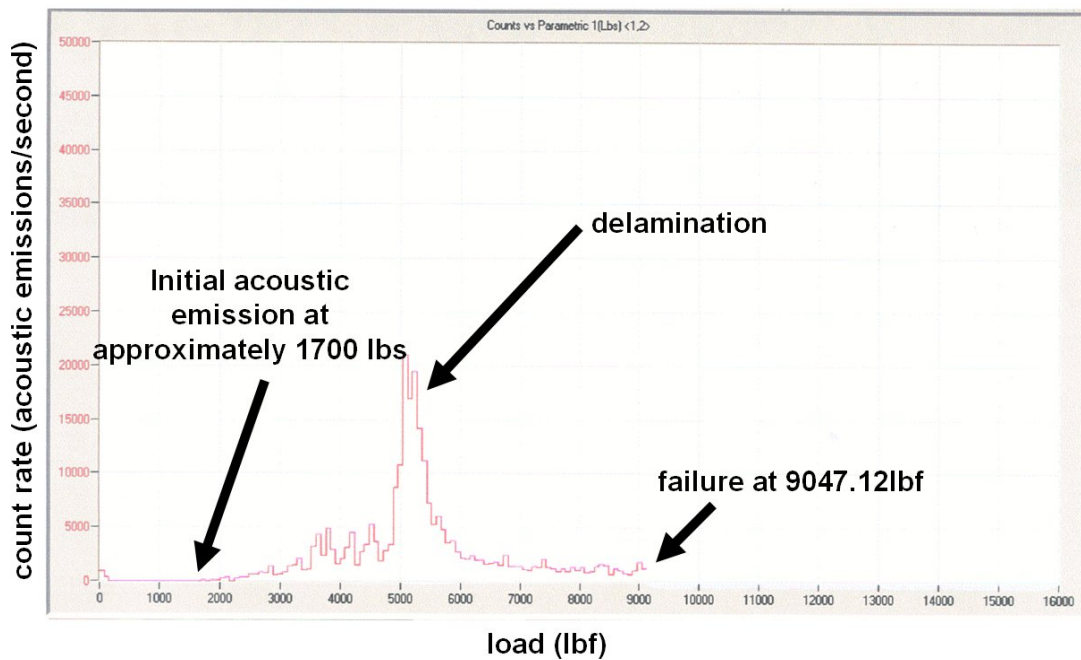


Figure 199. Count rate versus load (lbf) of virgin specimen #2.

Tests 4-5: Stepped-lap Specimens

Two stepped-lap specimens were tested to failure. Stepped-lap specimen #1 fractured at 2466.14 lb_f, or about 27.3% of the virgin specimen strength. Stepped-lap specimen #5 fractured at 2679.65 lb_f, or 29.6% of the virgin specimens strength. The load versus displacement behavior of both stepped-lap specimens is shown in Figure 200.

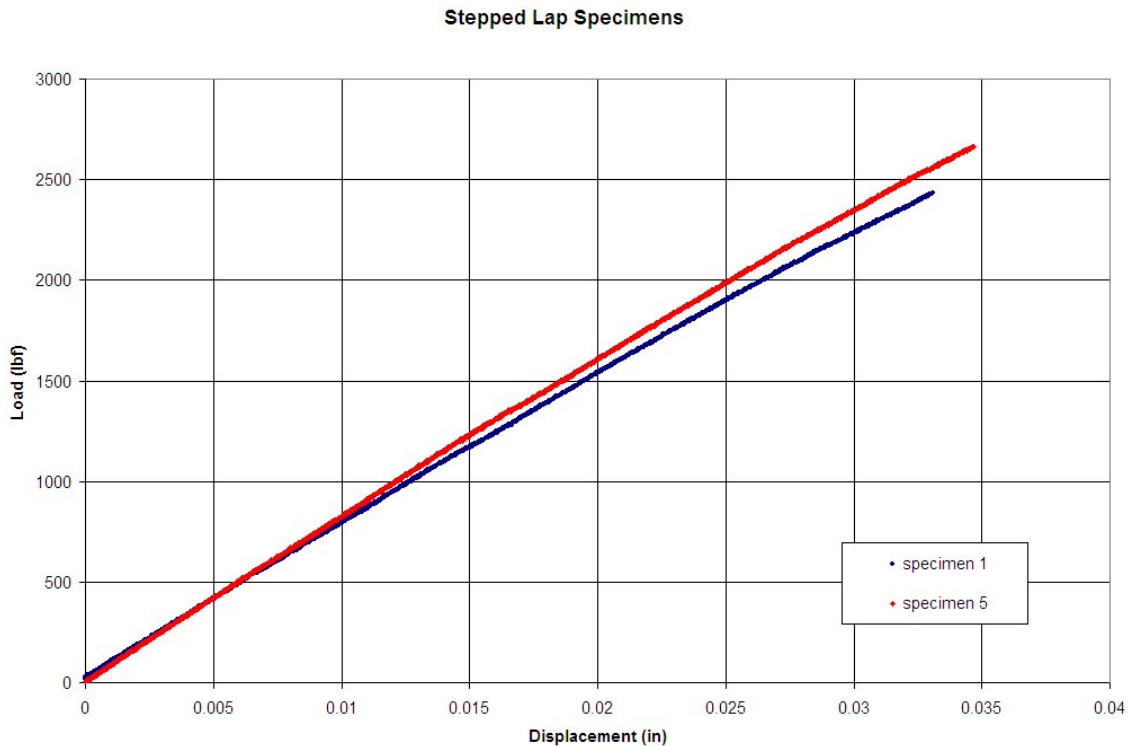


Figure 200. Load versus displacement of stepped-lap specimens.

From the photographs of the fractured stepped-lap specimens, it was concluded that the failure occurred in the parent material in the 90° plies, the adhesive material in the 0° plies, and a combination of the parent material and the adhesive in the +/-45° plies.

Overall, it was observed that failure occurred in the region of repair.

According to the manufacturer, FM 300M (0.05psf) has a tensile shear strength of 5340 psi at 75°F. Stepped-lap specimen #1 had a width of 0.9426 inches and a repair

length of 1.0888 inches, while stepped-lap specimen #5 had a width of 0.98915 and a width of 1.0888 inches. From these measurements, the exposed area of adhesive loaded in tensile shear was 1.0263 in^2 for stepped-lap specimen #1 and 1.0779 in^2 for stepped-lap specimen #5, respectively.

Since both repairs had approximately 1 in^2 of exposed adhesive, it might be assumed that the theoretical strength of repair should have been about 5340lbs, or the tensile shear strength of the adhesive. However, because of the ply orientation of the laminate, only some of the exposed adhesive actually carries the load. For instance, 90° plies have little resistance to transverse loading, so failure in those plies occurs before failure in the adhesive. Since three of the steps in the stepped-lap repairs were adjacent to 90° plies, the area of those steps cannot be considered in the strength estimate of the repair. Steps adjacent to only $\pm 45^\circ$ and 0° plies actually can be considered when loading exceeds the transverse strength of the composite laminate. Since this occurred in four of the seven steps, the actual load bearing area of the adhesive was about 0.5865 in^2 in stepped-lap specimen #1 and 0.6154 in^2 in stepped-lap specimen #5. Using these effective areas, it can be estimated that the theoretical strength of the stepped-lap specimens should have been around 3200lb_f.

Therefore, while the stepped-lap specimens only retained 28.5% of their original strength, the stepped-lap specimens actually demonstrated 80% of predicted strength based on the area of repair and adhesive tensile shear strength. Fracture surfaces demonstrating these trends can be seen in Figure 201, Figure 202, and Figure 203.

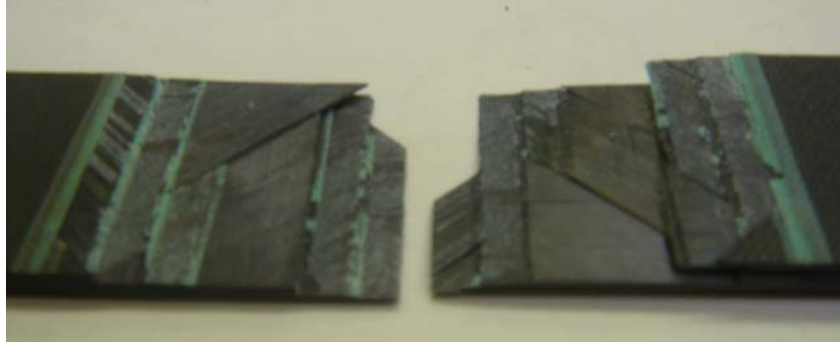


Figure 201. Fracture surface of stepped-lap specimen #1.

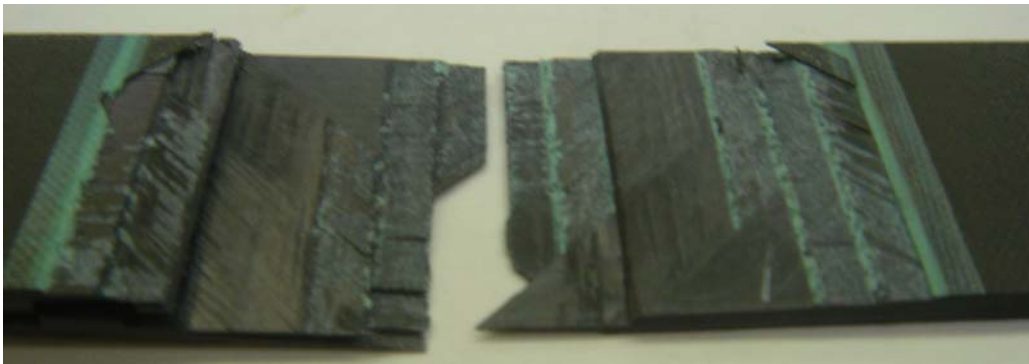


Figure 202. Fracture surface of stepped-lap specimen #5.

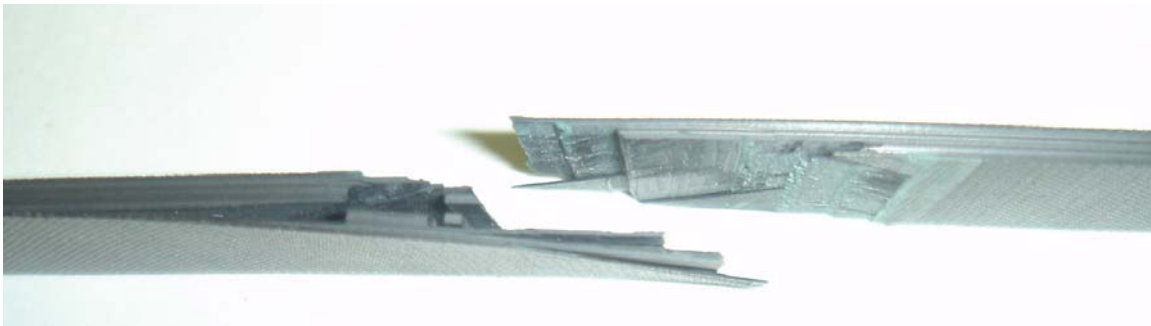


Figure 203. Profile of fracture surface of stepped-lap specimen #5.

Initial acoustic emission was detected in stepped-lap specimen #1 at a load of approximately 900 lb_f, as shown in Figure 204. While it is evident that there was some acoustic emission from specimen #1 at the beginning of the test, it was assumed that this noise was a result of initial settling of the tabs or shifting of the grips on the tab surface.

Fracture surfaces indicated that there was no delamination in the adherends of the stepped lap specimens.

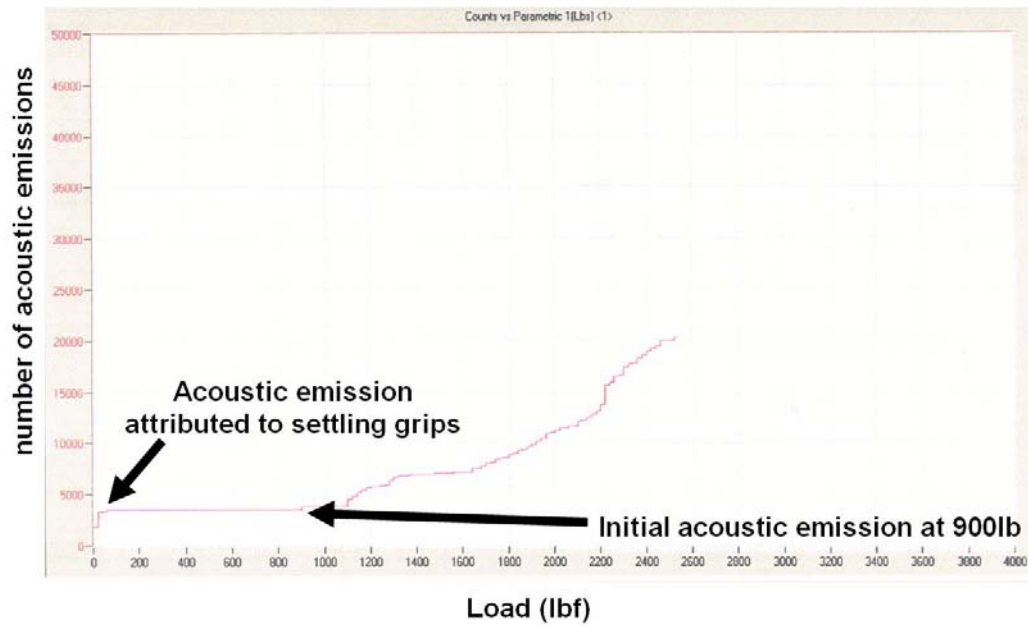


Figure 204. Counts versus load (lbf) for stepped-lap specimen #1.

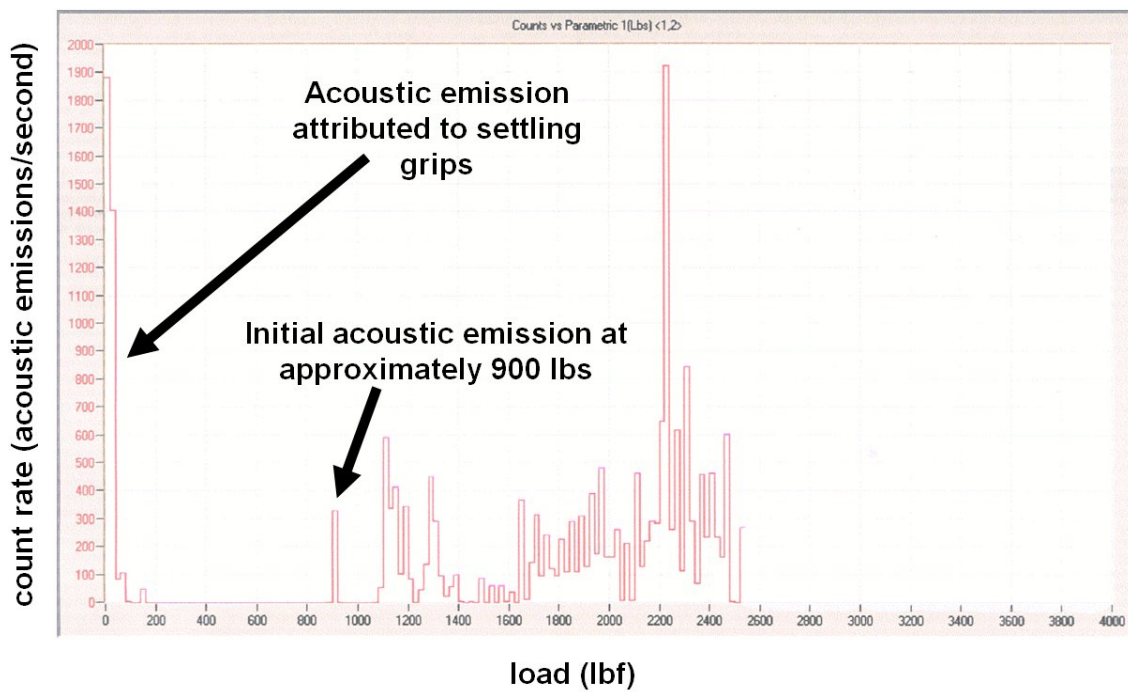


Figure 205. Count rate versus load (lbf) for stepped-lap specimen #1.

Initial acoustic emission was detected in stepped-lap specimen #5 at a load of approximately 750 lb_f, as shown in Figure 204. While there was some acoustic emission before this point in specimen #5, it was again assumed that it was a result of noise from settling grips and tabs.

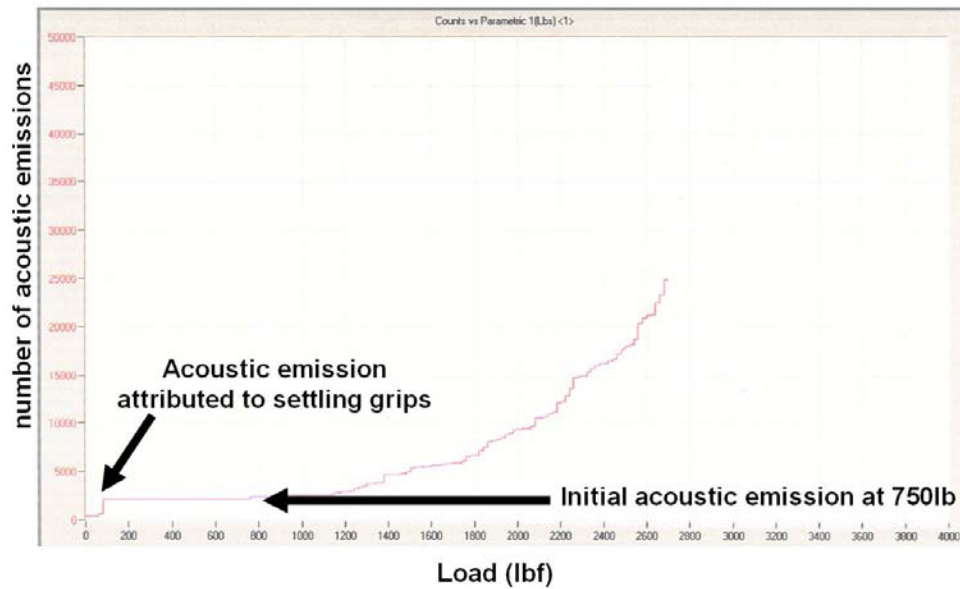


Figure 206. Counts versus load (lb_f) for stepped-lap specimen #5.

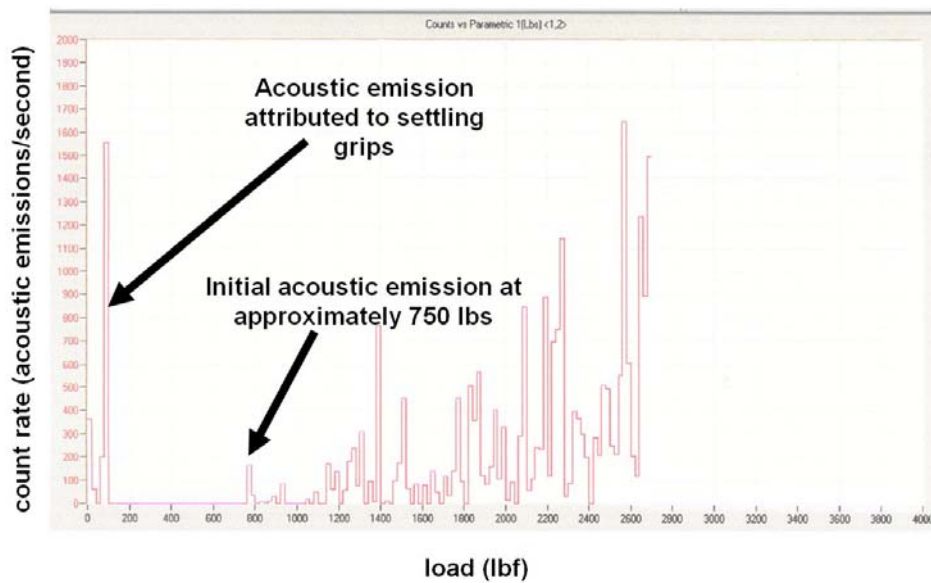


Figure 207. Count rate versus load (lb_f) for stepped-lap specimen #5.

Tests 6-7: Scarf Specimens

Two scarf specimens were tested to failure. Scarf specimen #2 fractured at 3760.38 lb_f, or about 41.5% of the virgin specimen's strength. Scarf specimen #5 fractured at 3451.66 lb_f, or 38.2% of the virgin specimens strength. The load versus displacement behavior of both stepped-lap specimens is shown in Figure 208.

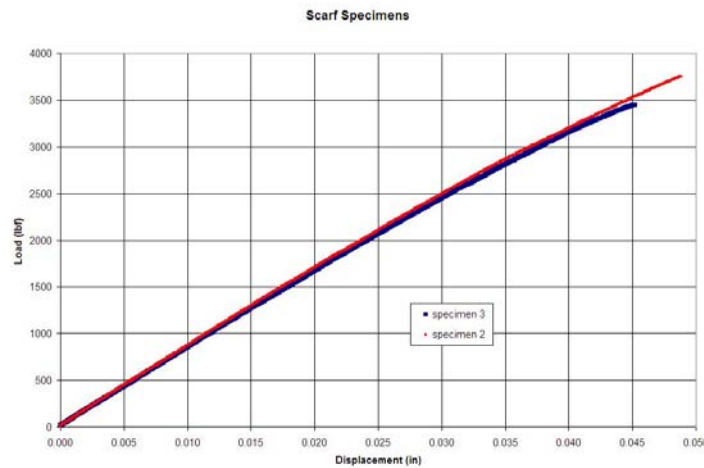


Figure 208. Load versus displacement for scarf specimens.

As evident from photographs fracture surfaces, it could be concluded that the scarf repaired specimens failed along the adhesive bond line. Figure 209 provides a good example of cohesive failure. While the adhesive was stronger than the 90° plies, it is evident that the adhesive was again the limiting factor in the strength of the joint. However, while the adhesive bond line was adjacent to 90° plies in three steps of the stepped-lap repair, the adhesive bond line was only adjacent to the 90° plies through the region of those plies in the scarf repair. This reduced the effective area of loaded adhesive by 25%, from about 1.18 in² to about 0.885 in². Using this effective area as an estimate, the strength of the scarf repaired specimens should have been around 4700 lbs. Therefore, while the stepped-lap specimens only retained 39.9% of their original strength,

the stepped-lap specimens actually demonstrated 76.3% of predicted strength based on this strength of materials approach. Photographs of the fracture surfaces can be seen in Figure 209 and Figure 210.

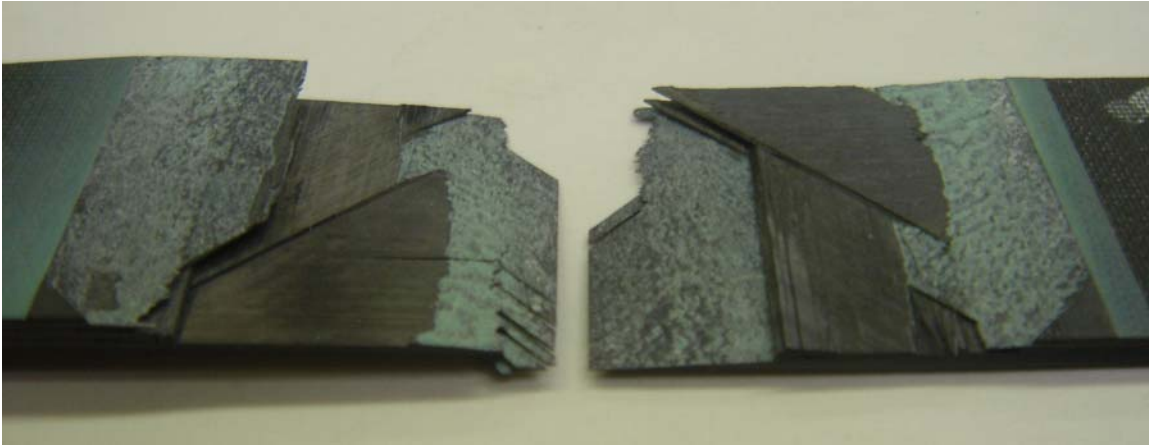


Figure 209. Fracture surface of scarf specimen 2.

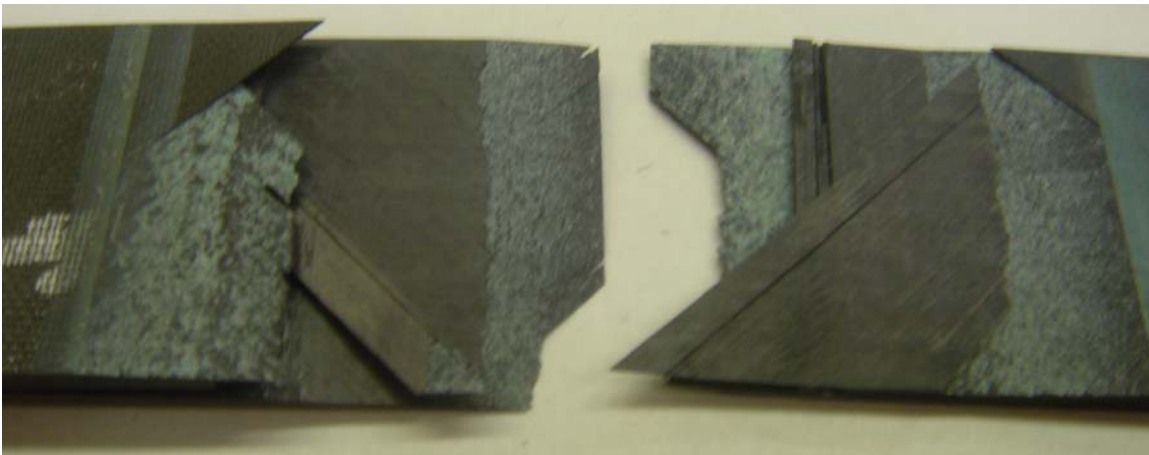


Figure 210. Fracture surface of scarf specimen 3.

Assuming acoustic emission detected below 200 lb_f was a result of tabs or grips settling, initial acoustic emission from the material was detected in scarf specimen #2 at a load of approximately 1900 lb_f, as shown in Figure 211.

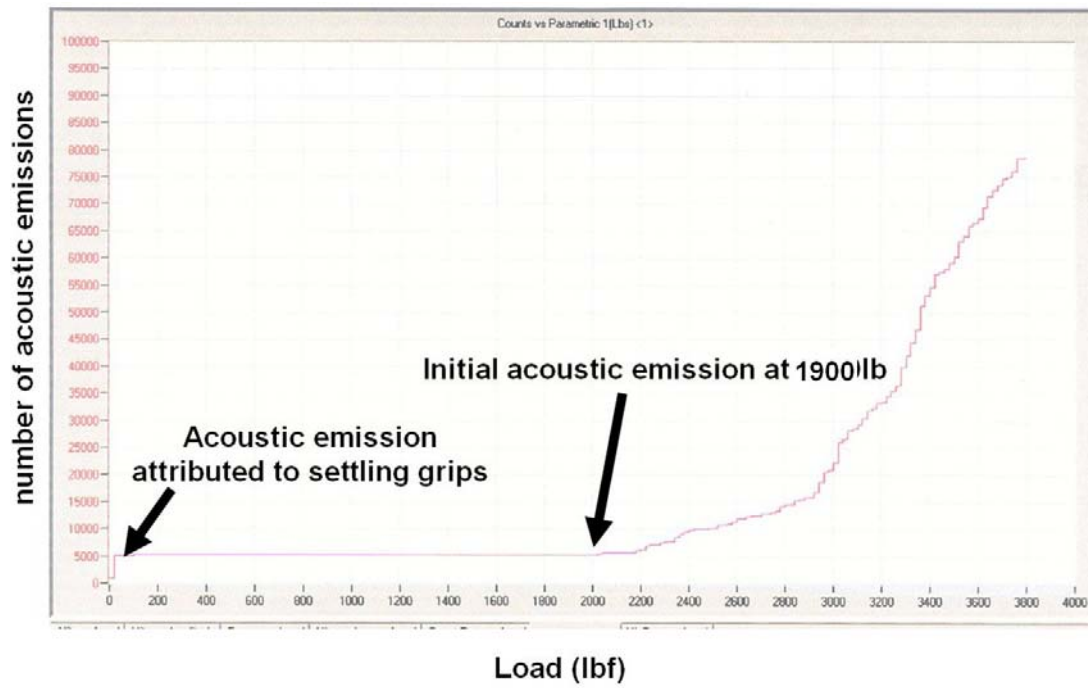


Figure 211. Counts versus load (lb_f) for scarf specimen #2.

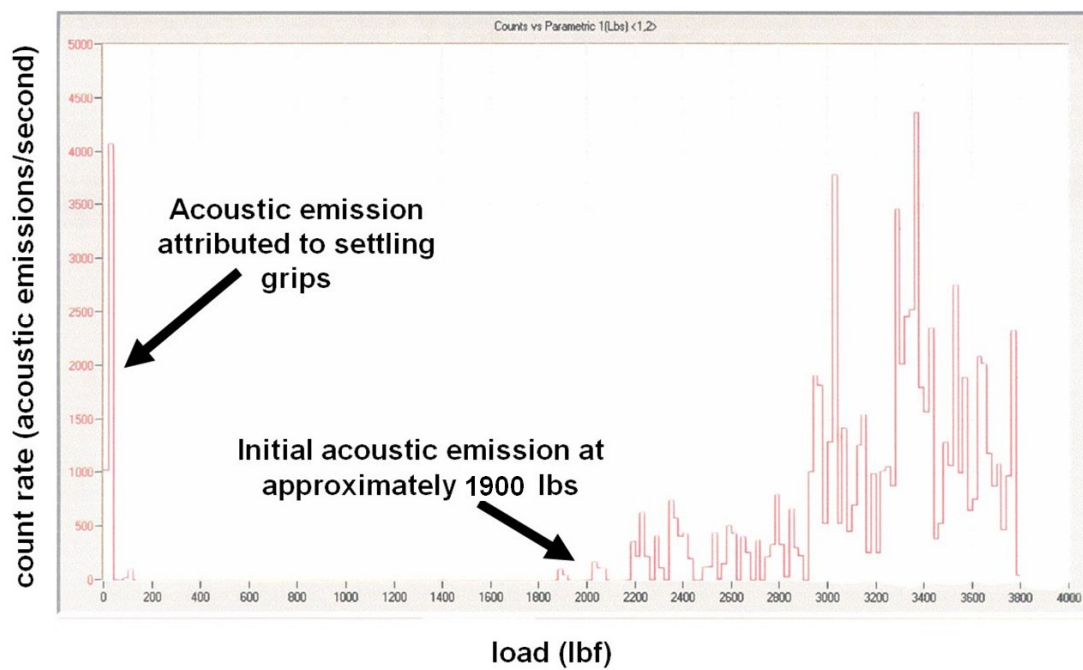


Figure 212. Count rate versus load (lb_f) for scarf specimen #2.

Using the same assumption for scarf specimen #3, initial acoustic emission from the material was detected at a load of approximately 1900 lb_f, as shown in Figure 214.

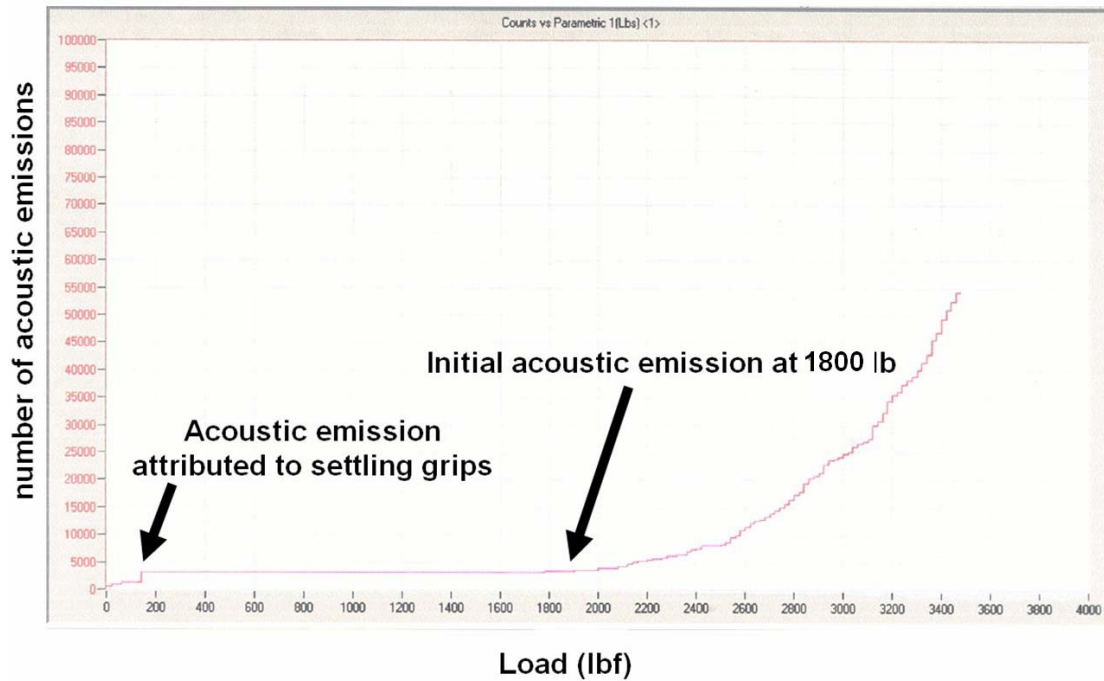


Figure 213. Counts versus load (lb_f) for scarf specimen #3.

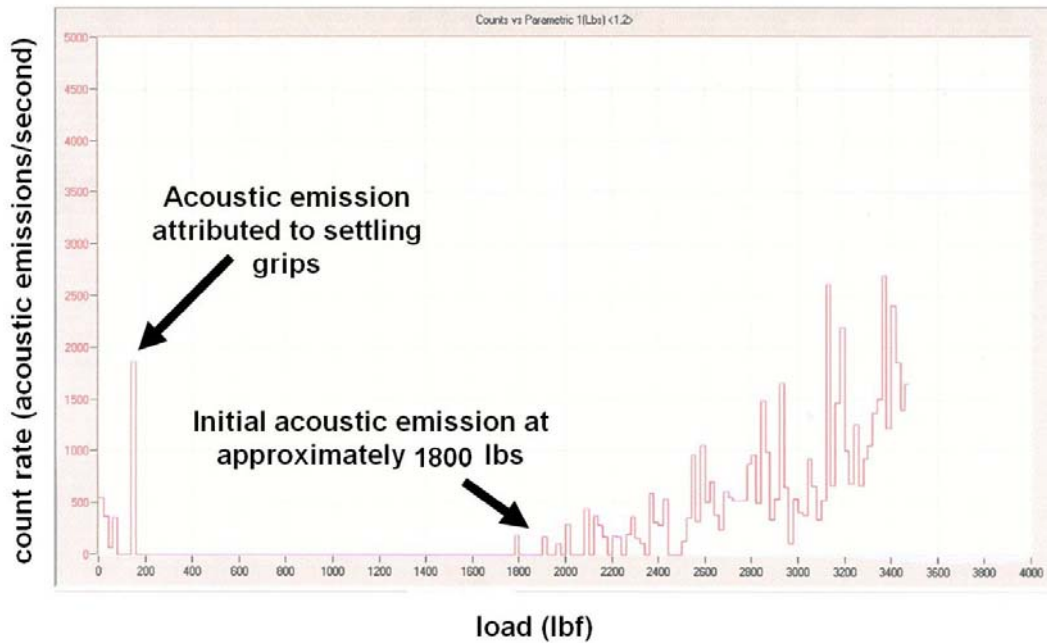


Figure 214. Count rate versus load (lb_f) for scarf specimen #3.

Summary

Results of the tests are summarized in Table 3 and Table 4. It was determined that the scarf repaired specimens exhibited approximately 40% of the parent materials strength while the stepped-lap repaired specimens only exhibited 30% of original strength. Taking the tensile strength of the adhesive and the area of repair into consideration, the scarf repaired specimens demonstrated about 76.3% of their estimated strength, while the stepped-lap repaired specimens held about 80% of their estimated strength. Overall, the tests were deemed successful and the results obtained were used in determining appropriate loading for moiré fringe pattern visualization.

Table 3. Summary of tensile test results.

specimen #	repair type	width (in)	thickness (in)	length (in)	failure load (lbf)
1	virgin	1.00305	0.08915	10	9036.12
2	virgin	1.00335	0.0893	10	9047.12
2	scarf	1.0035	0.0891	10	3760.38
3	scarf	1.00405	0.089	10	3451.66
1	stepped-lap	0.9426	0.08845	10	2466.14
5	stepped-lap	0.98915	0.0896	10	2679.65

Table 4. Strength retained by repaired specimens.

repair type	avg failure load (lbf)	% of strength retained
virgin	9041.62	n/a
scarf	3606.02	39.88%
stepped-lap	2572.895	28.46%

While these tests yielded ultimate strengths of the repaired and virgin specimens and gave some insights into the mechanical behavior of the specimens, the load corresponding to initial acoustic emission was the most pivotal in determining an appropriate load for moiré fringe pattern visualization. Table 5 provides a summary of

the loads corresponding to initial acoustic emissions produced by the specimens under tensile loading.

Table 5. Summary of initial acoustic emissions in specimens.

specimen #	repair type	load at initial acoustic emission (lbf)
1	virgin	1900
2	virgin	1700
2	scarf	1900
3	scarf	1800
1	stepped-lap	900
5	stepped-lap	750

Acoustic emission detected below 200 lb_f was attributed to settling in the grips and tabs. Emissions were picked up in the stepped-lap specimen #5 at around 750 lb_f. This was the lowest load at which acoustic emission was produced. Using 750 lb_f as a conservative estimate for initial damage in all specimens, it was concluded that a load of 450lb_f should provide a good strain field while not cracking or damaging the test specimens.

Appendix D: Initial line plots comparing predicted strain data and experimental results

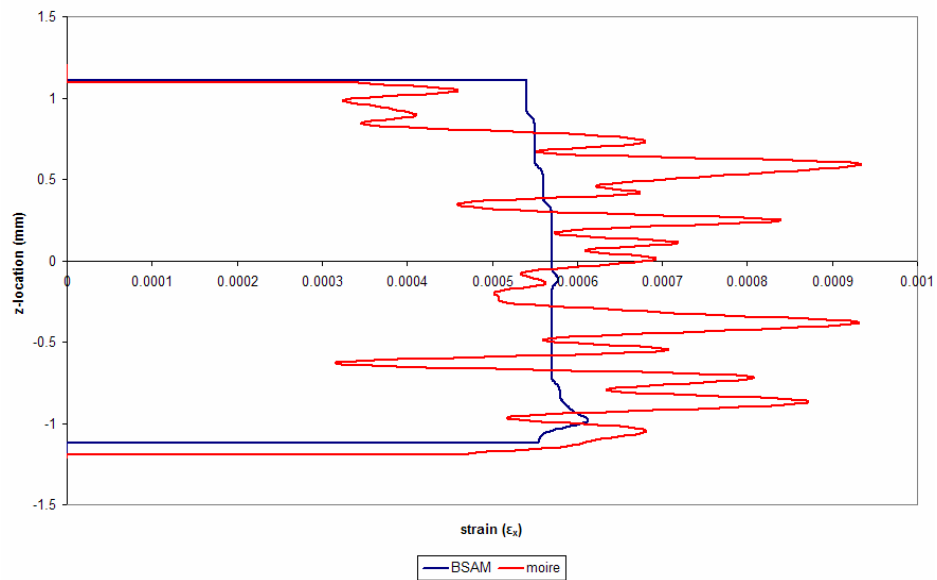


Figure 215. Scarf Joint: strain distribution (ϵ_x) through specimen thickness (z) at

$x = -15\text{mm}$

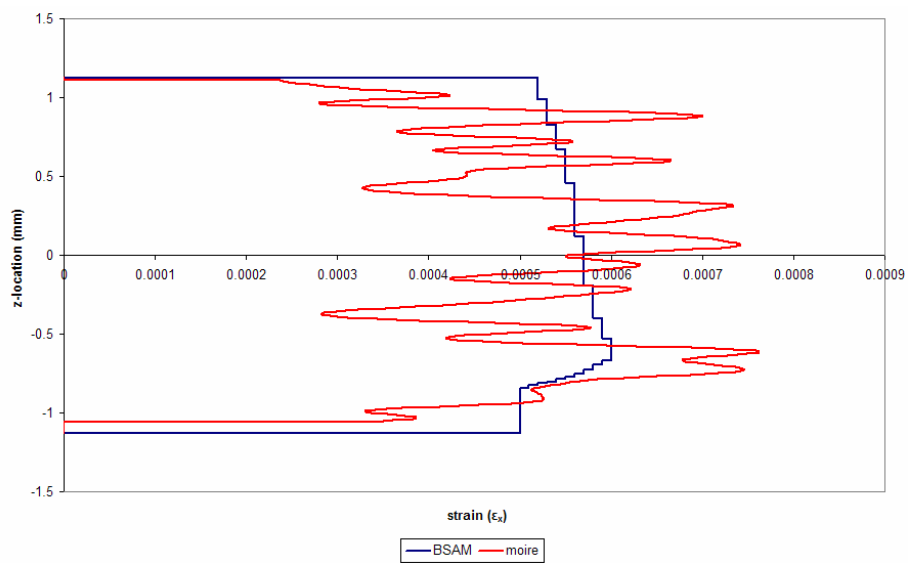


Figure 216. Stepped-Lap Joint: strain distribution (ϵ_x) through specimen thickness (z) at

$x = 15\text{mm}$

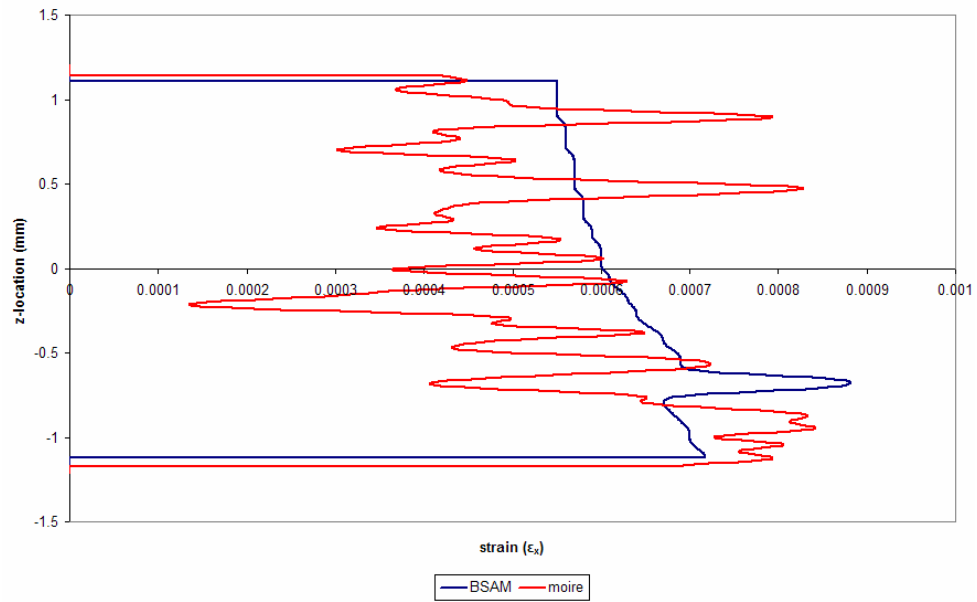


Figure 217. Scarf Joint: strain distribution (ϵ_x) through thickness (z) at x = -10mm

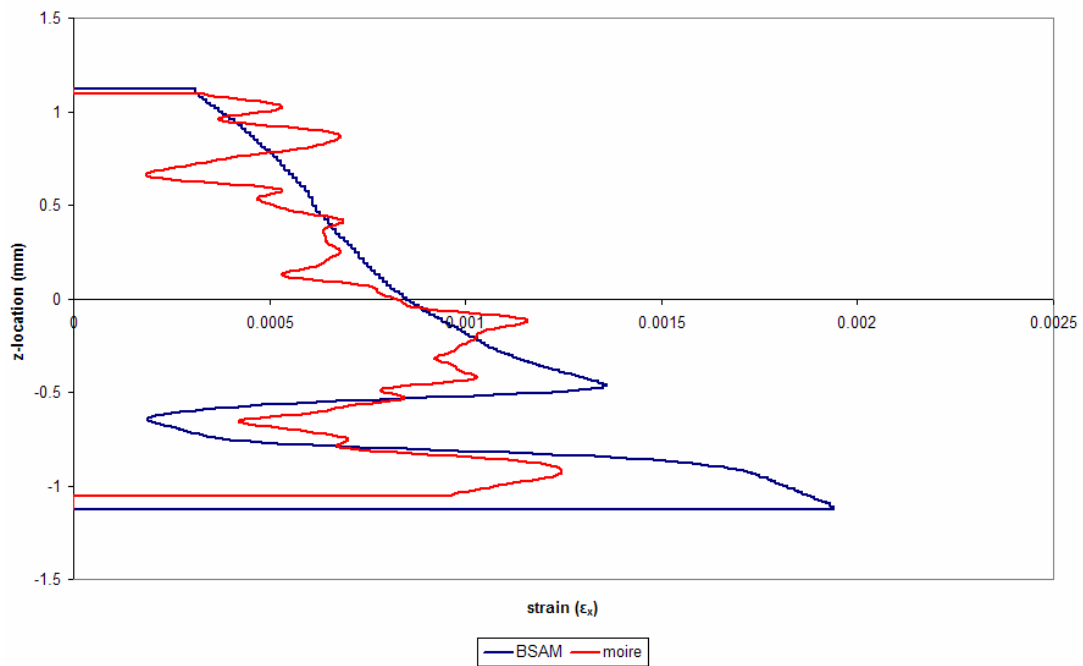


Figure 218. Stepped-Lap Joint: strain distribution (ϵ_x) through specimen thickness (z) at x = 10mm

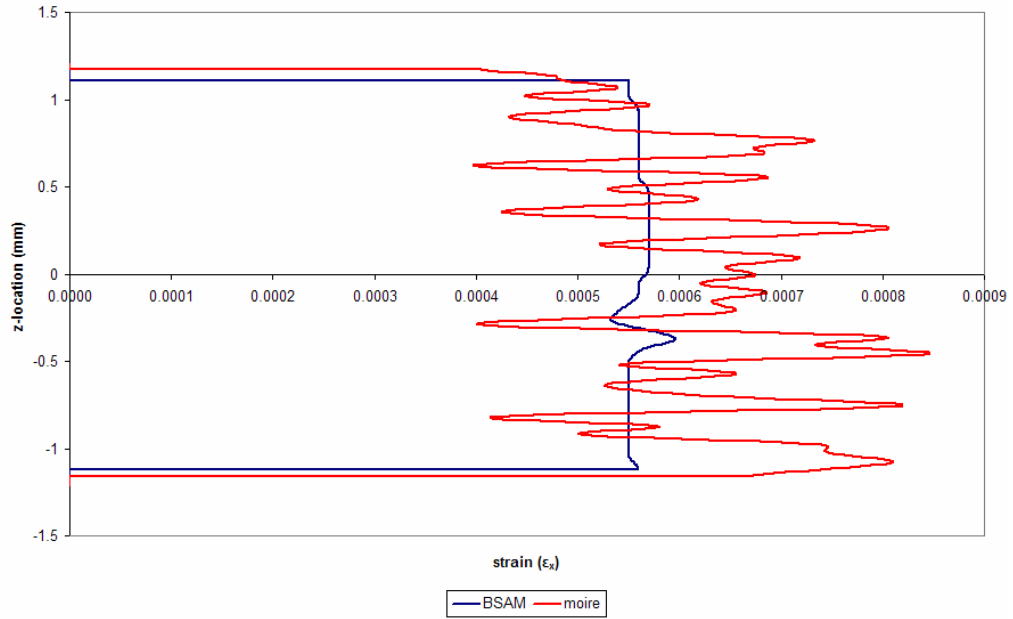


Figure 219. Scarf Joint: strain distribution (ϵ_x) through specimen thickness (z) at $x = -5\text{mm}$

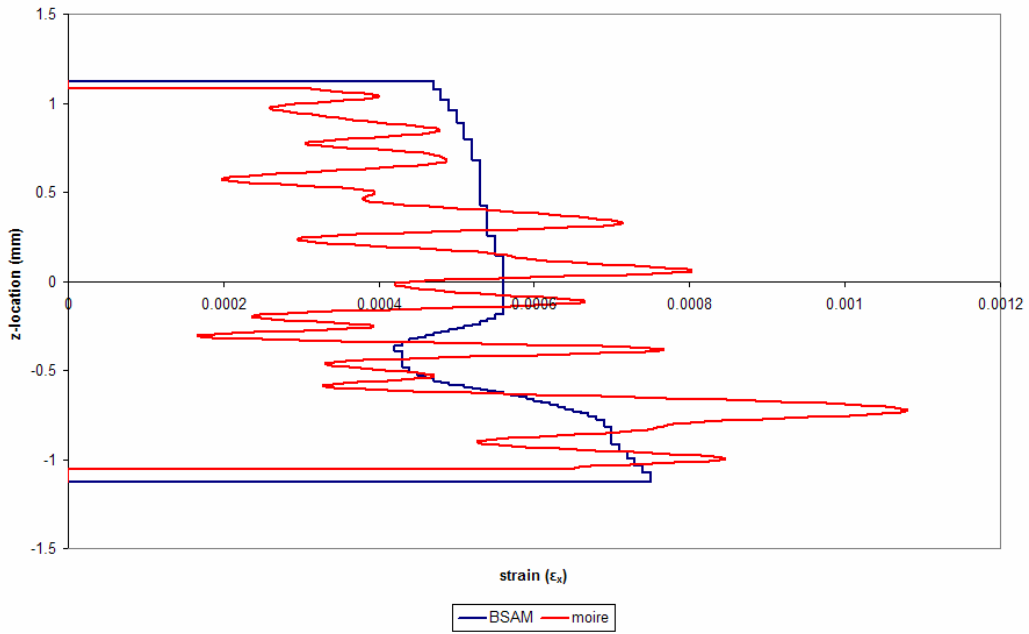


Figure 220. Stepped-Lap Joint: strain distribution (ϵ_x) through specimen thickness (z) at $x = 5\text{mm}$

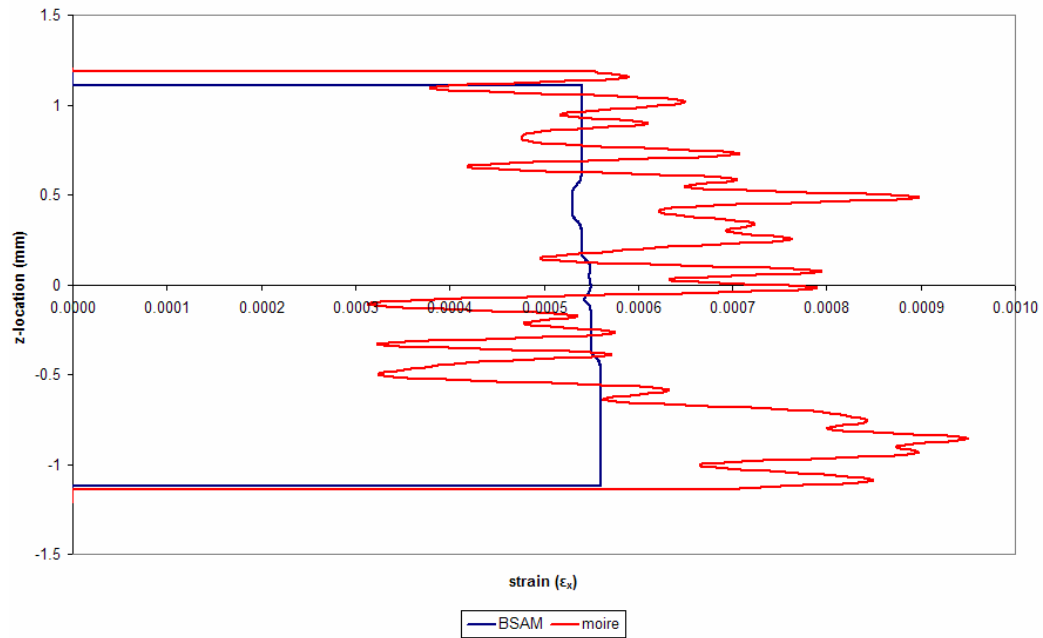


Figure 221. Scarf Joint: strain distribution (ϵ_x) through specimen thickness (z) at $x = 0\text{mm}$

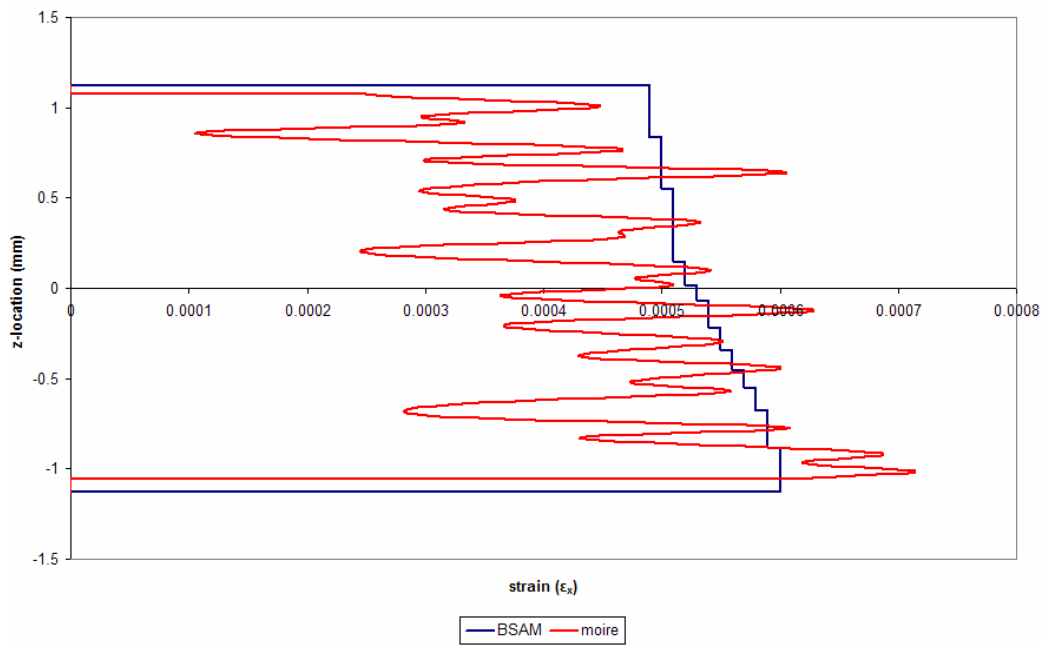


Figure 222. Stepped-Lap Joint: strain distribution (ϵ_x) through specimen thickness (z) at $x = 0\text{mm}$

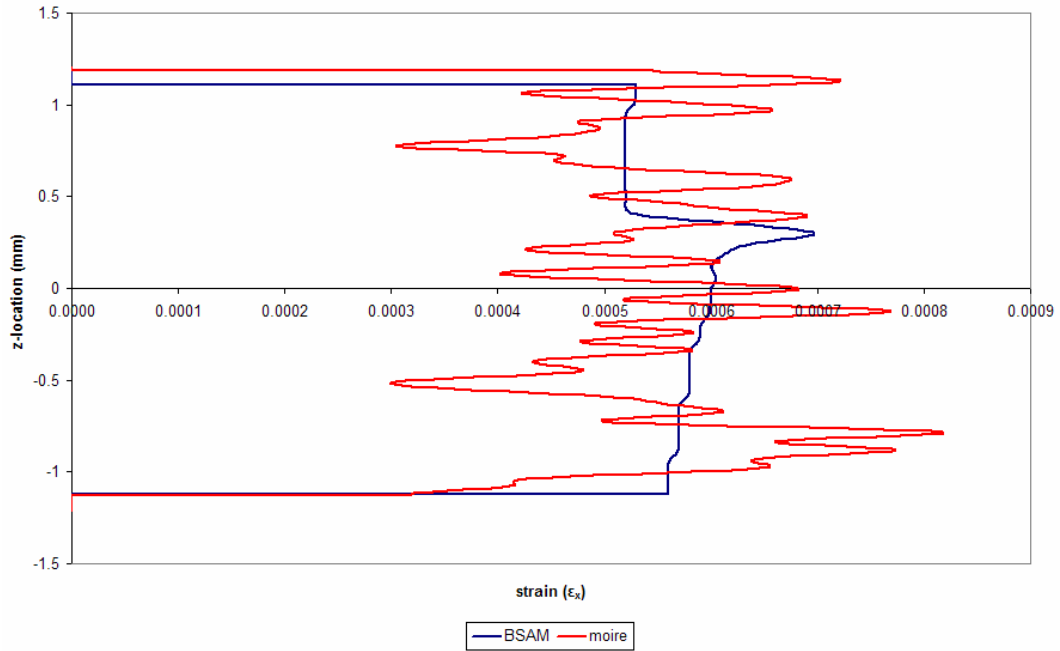


Figure 223. Scarf Joint: strain distribution (ϵ_x) through specimen thickness (z) at $x = 5\text{mm}$

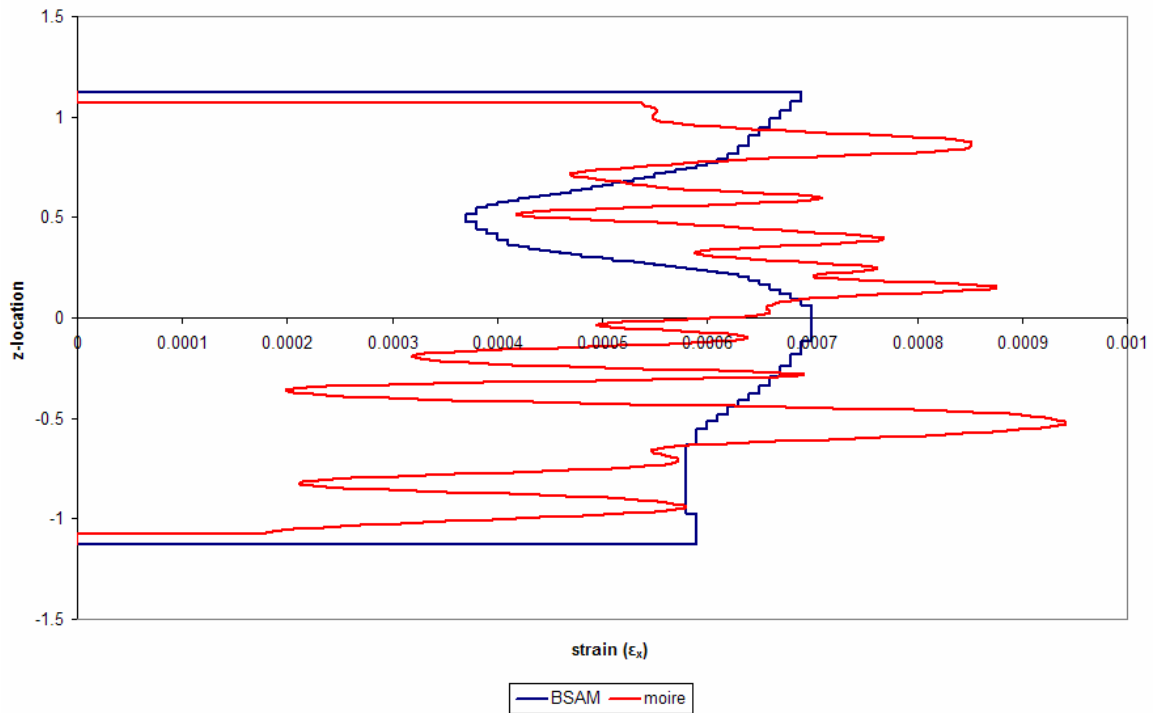


Figure 224. Stepped-Lap Joint: strain distribution (ϵ_x) through specimen thickness (z) at $x = -5\text{mm}$

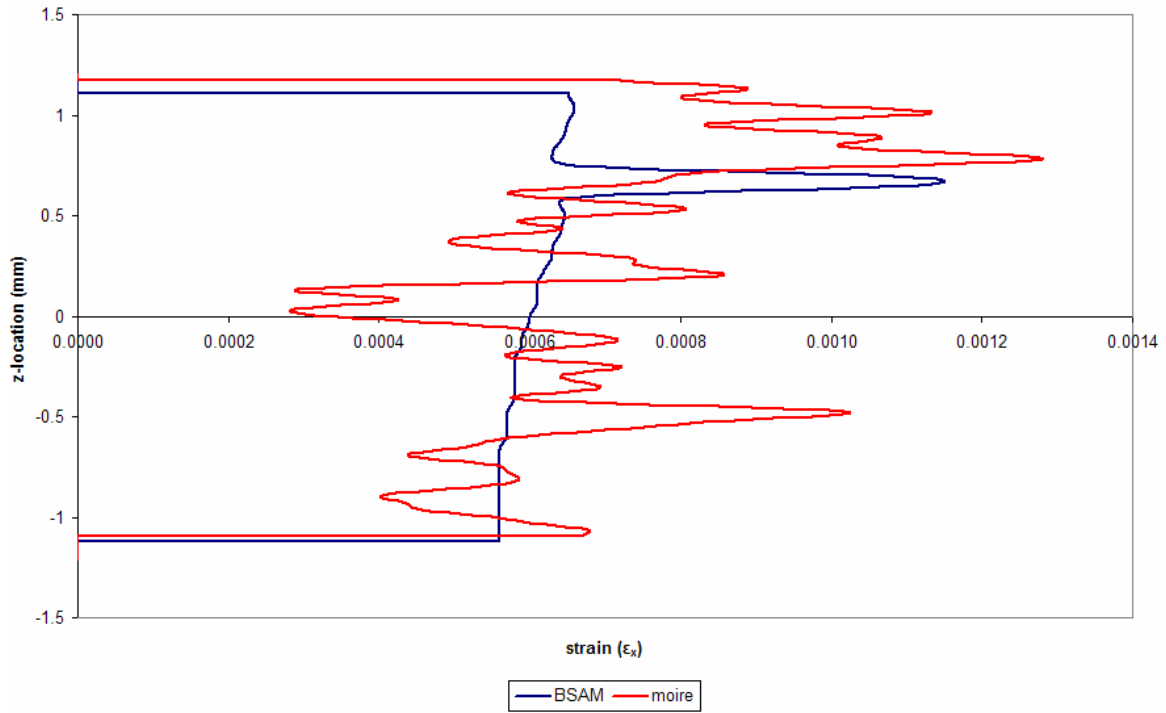


Figure 225. Scarf Joint: strain distribution (ϵ_x) through specimen thickness (z) at $x = 10\text{mm}$

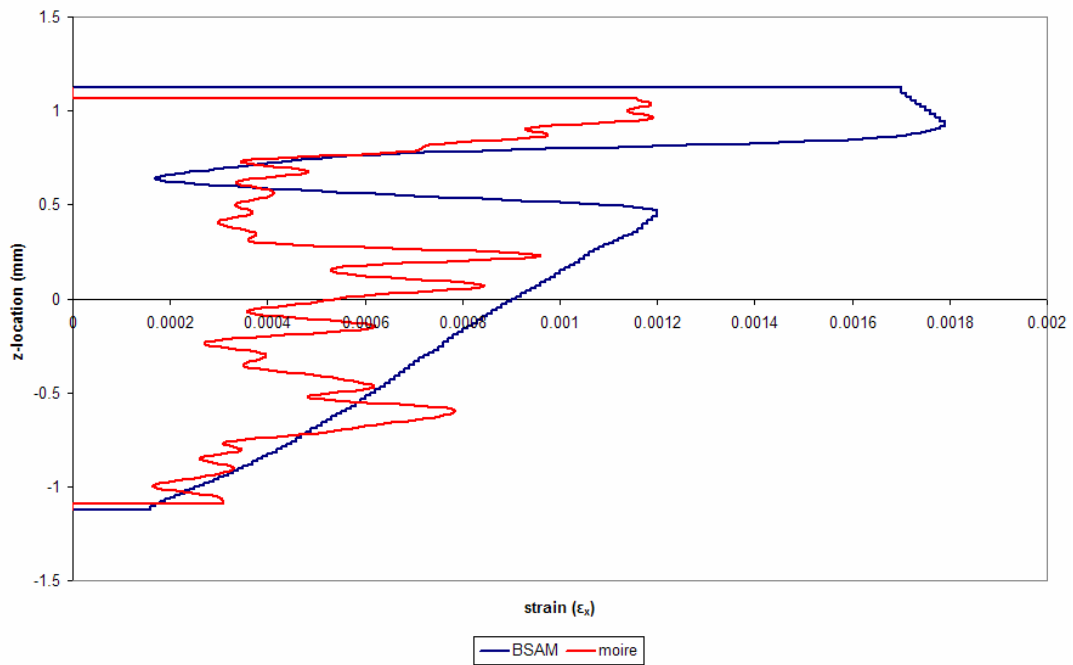


Figure 226. Stepped-Lap Joint: strain distribution (ϵ_x) through specimen thickness (z) at

$x = -10\text{mm}$

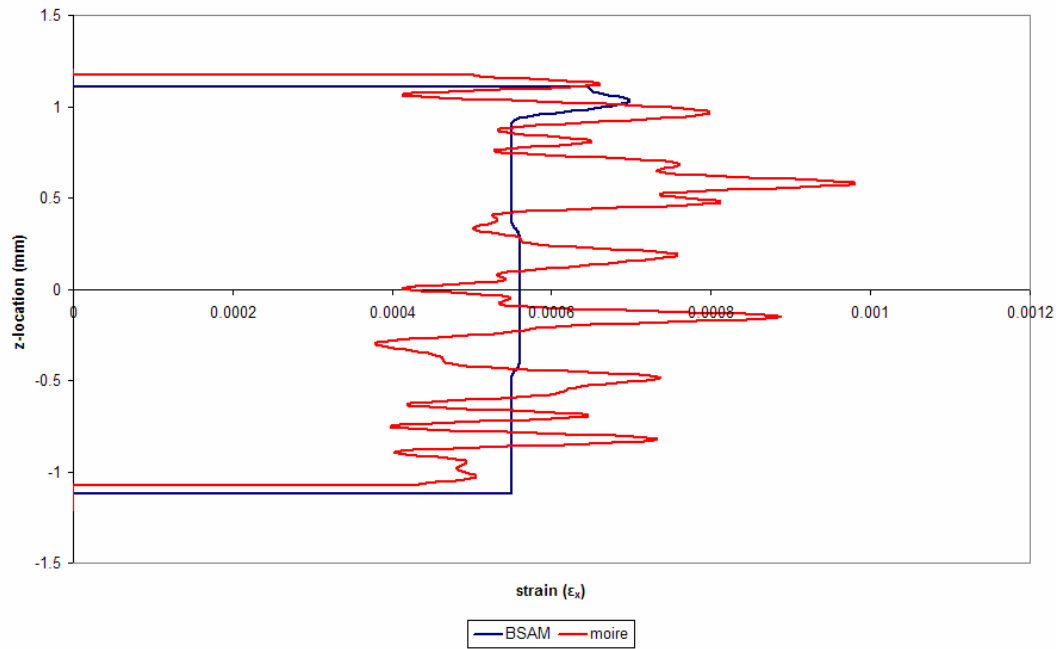


Figure 227. Scarf Joint: strain distribution (ϵ_x) through specimen thickness (z) at $x = 15\text{mm}$

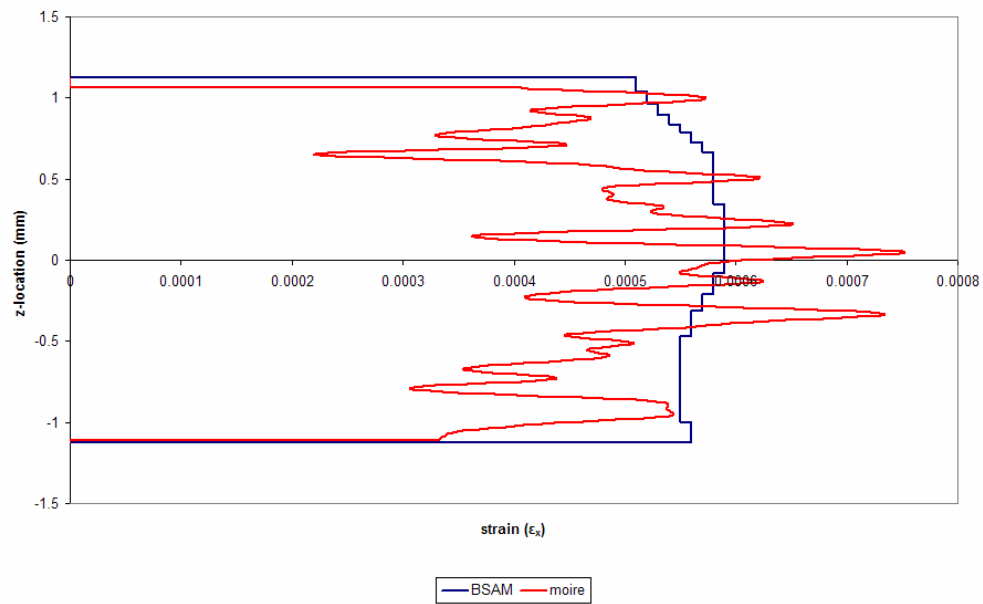
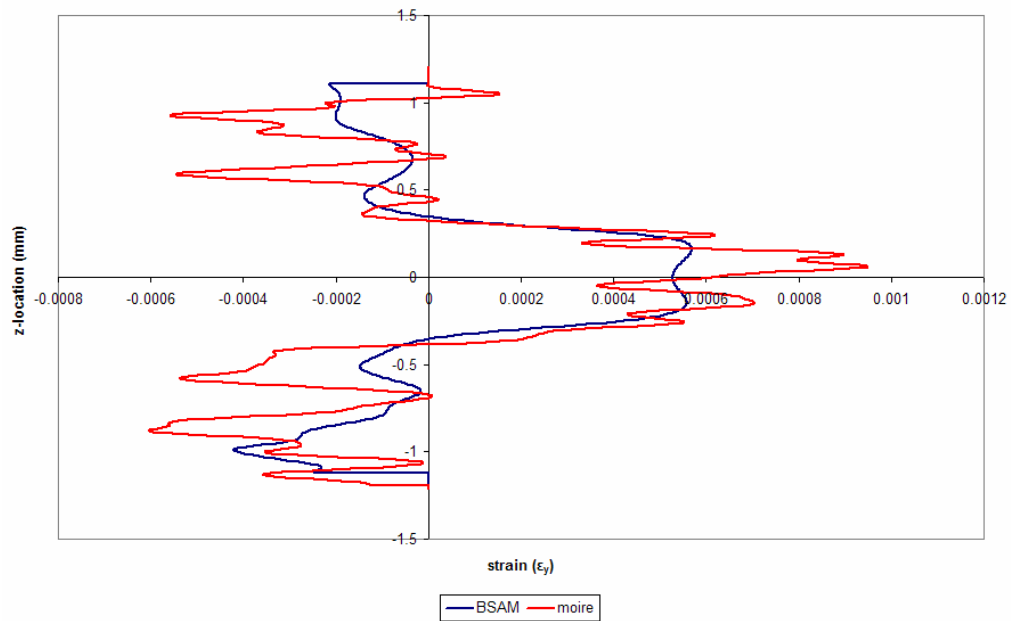
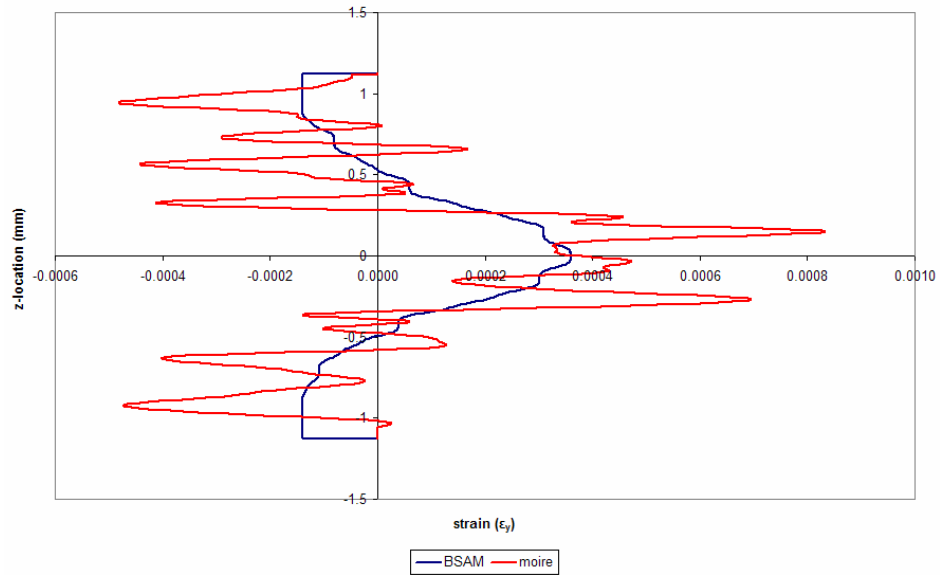


Figure 228. Stepped-Lap Joint: strain distribution (ϵ_x) through specimen thickness (z) at $x = -15\text{mm}$



**Figure 229. Scarf Joint: strain distribution (ϵ_y) through specimen thickness (z) at
 $x = -15\text{mm}$**



**Figure 230. Stepped-Lap Joint: strain distribution (ϵ_y) through specimen thickness (z) at
 $x = 15\text{mm}$**

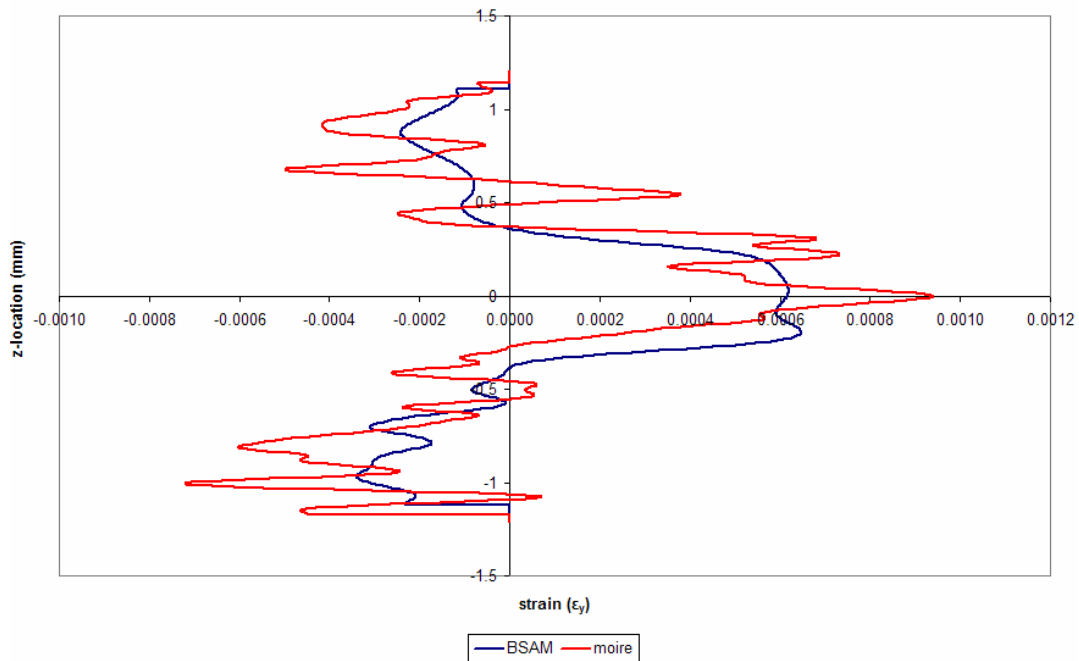


Figure 231. Scarf Joint: strain distribution (ϵ_y) through specimen thickness (z) at $x = -10\text{mm}$

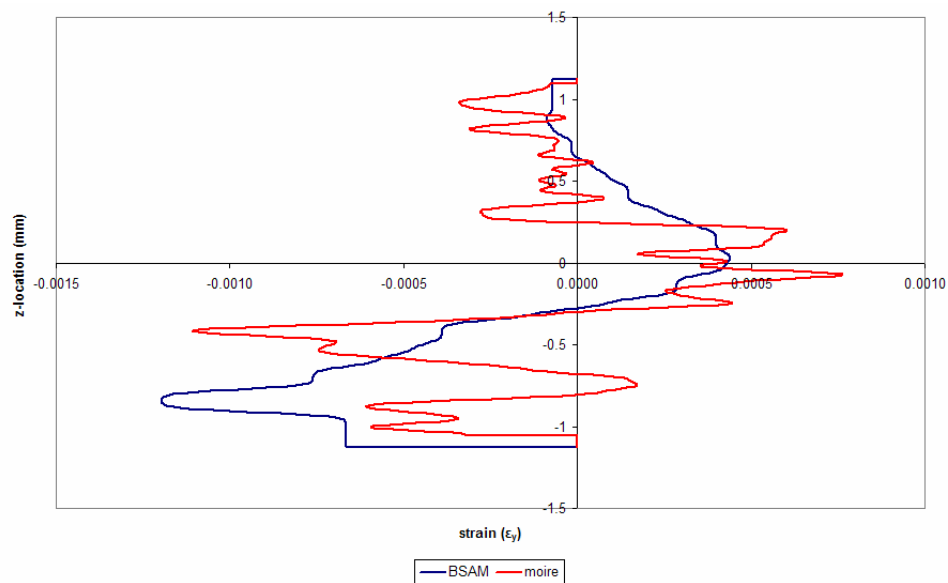


Figure 232. Stepped-Lap Joint: strain distribution (ϵ_y) through specimen thickness (z) at $x = 10\text{mm}$

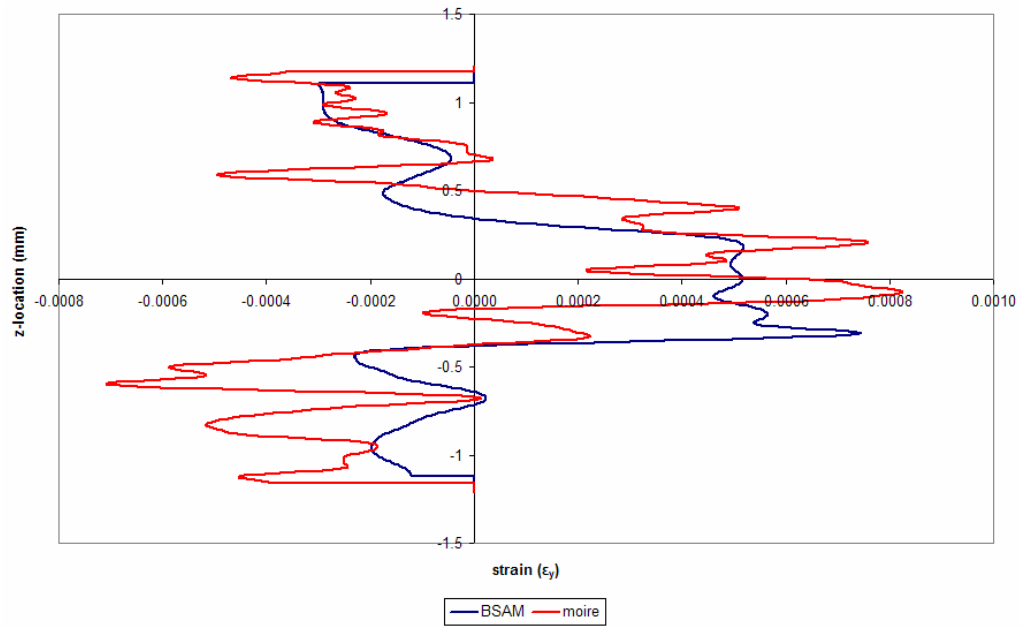


Figure 233. Scarf Joint: strain distribution (ϵ_y) through specimen thickness (z) at $x = -5\text{mm}$

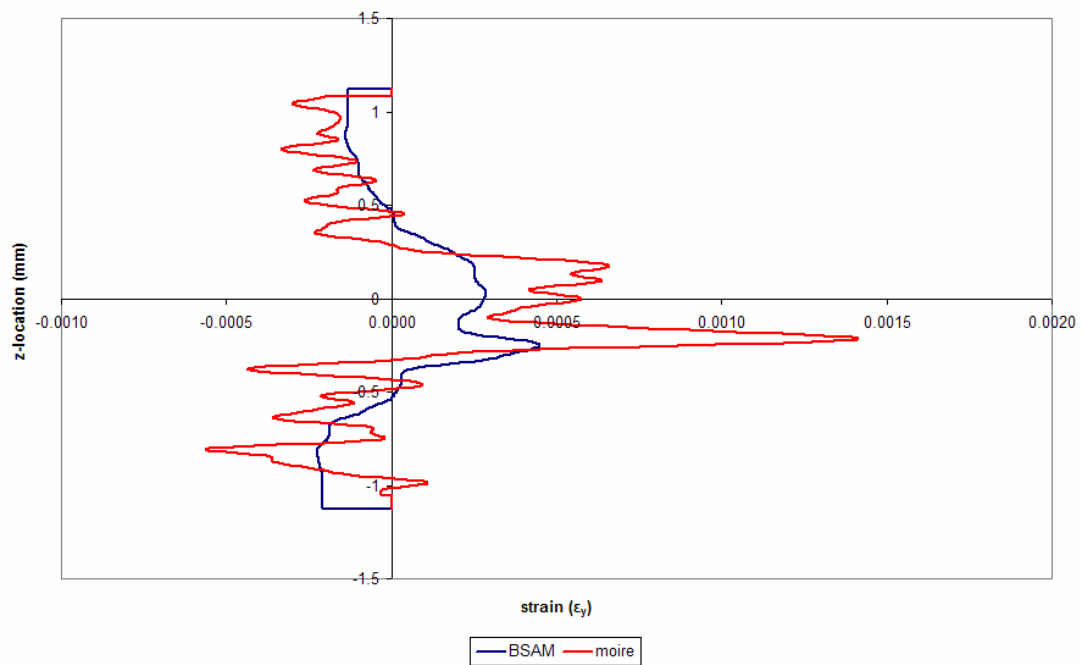


Figure 234. Stepped-Lap Joint: strain distribution (ϵ_y) through specimen thickness (z) at $x = 5\text{mm}$

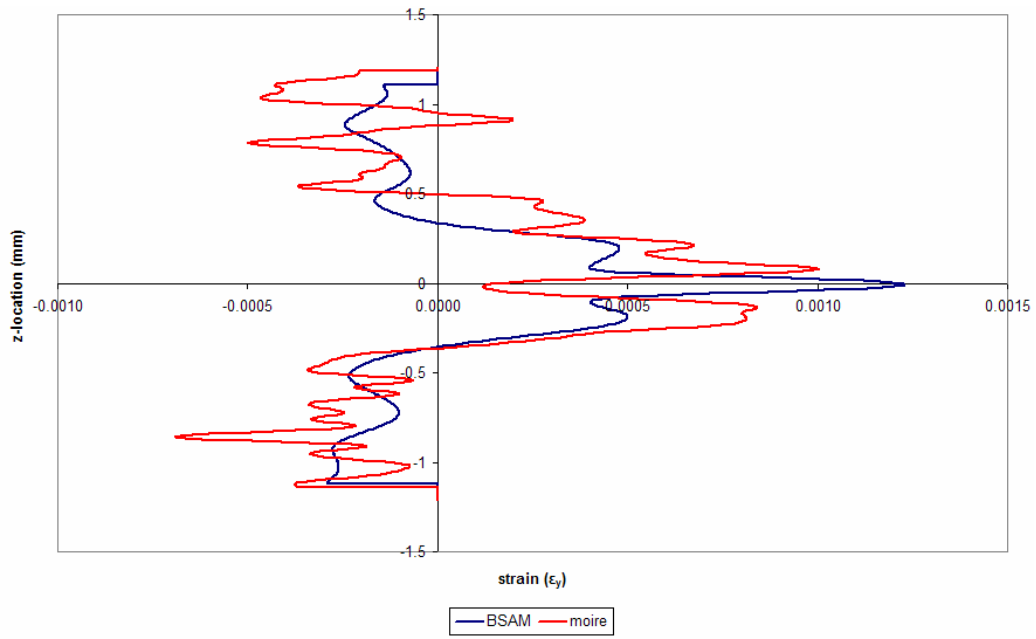


Figure 235. Scarf Joint: strain distribution (ϵ_y) through specimen thickness (z) at $x = 0\text{mm}$

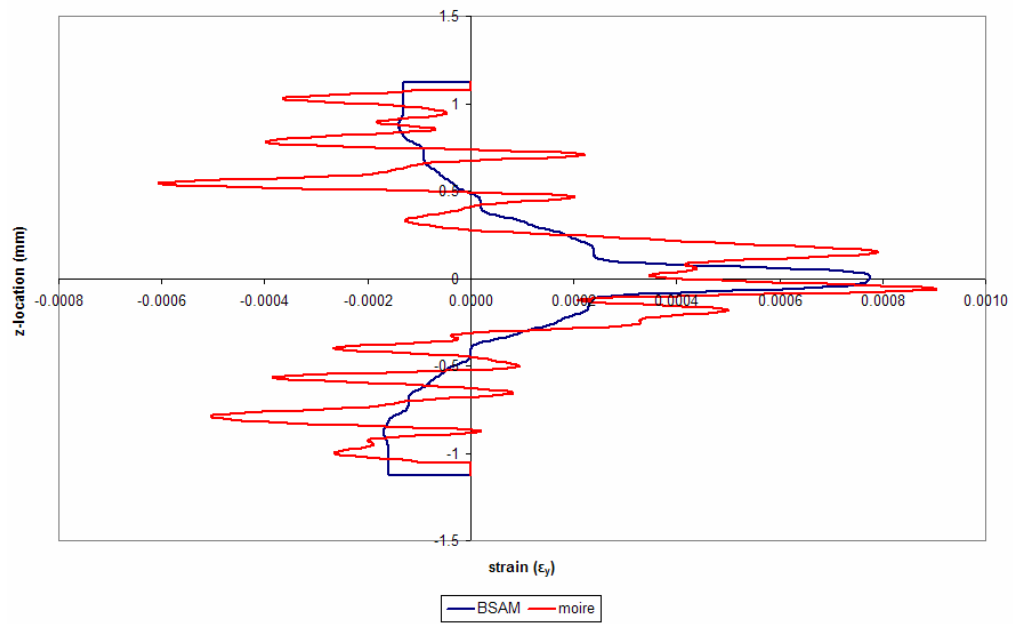


Figure 236. Stepped-Lap Joint: strain distribution (ϵ_y) through specimen thickness (z) at
 $x = 0\text{mm}$

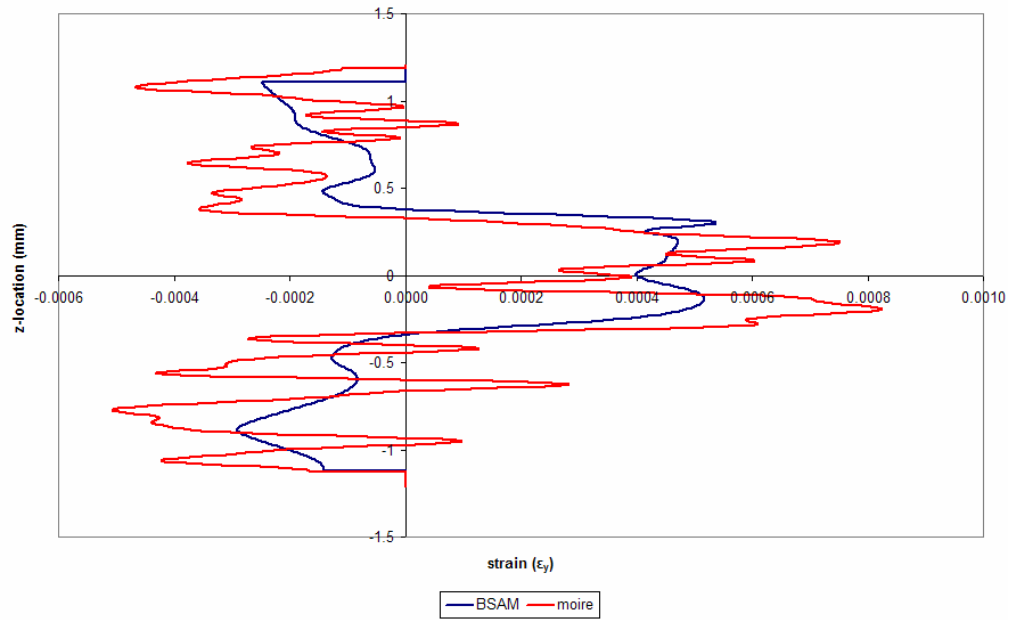


Figure 237. Scarf Joint: strain distribution (ϵ_y) through specimen thickness (z) at x = 5mm

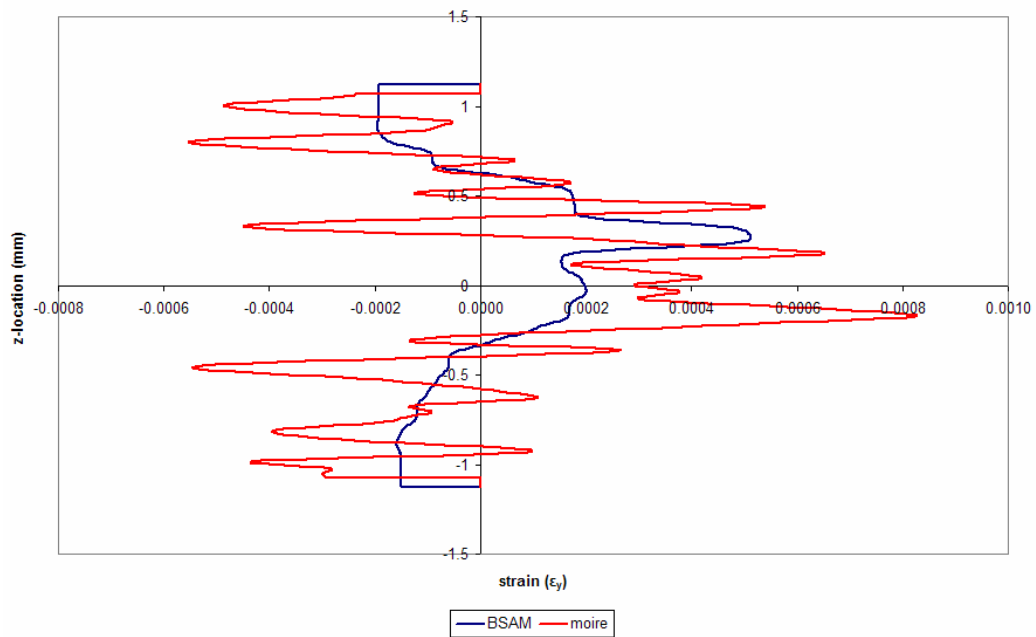


Figure 238. Stepped-Lap Joint: strain distribution (ϵ_y) through specimen thickness (z) at
x = -5mm

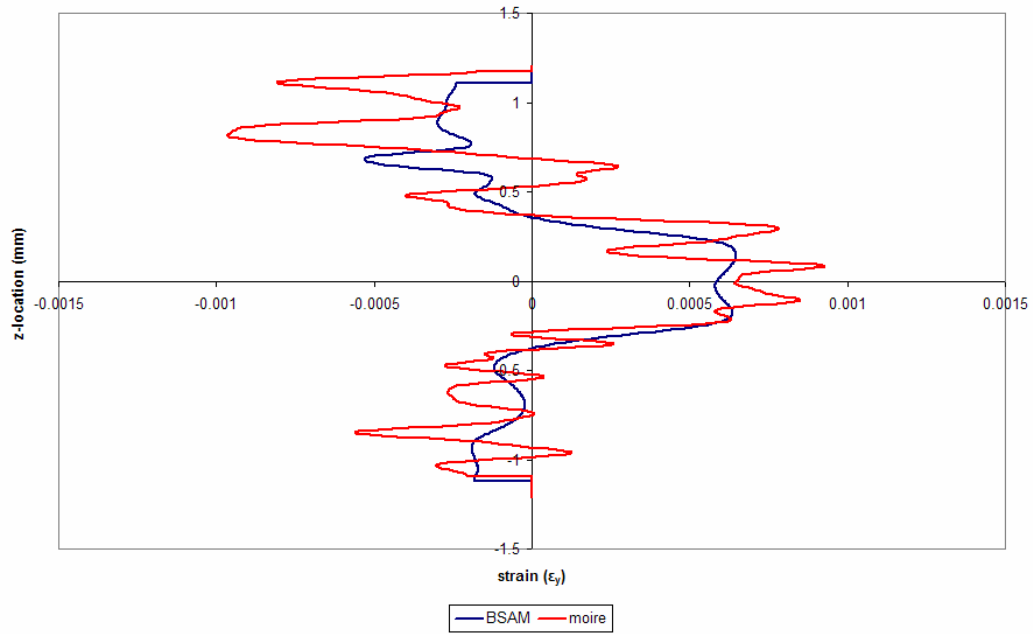


Figure 239. Scarf Joint: strain distribution (ϵ_y) through specimen thickness (z) at $x = 10\text{mm}$

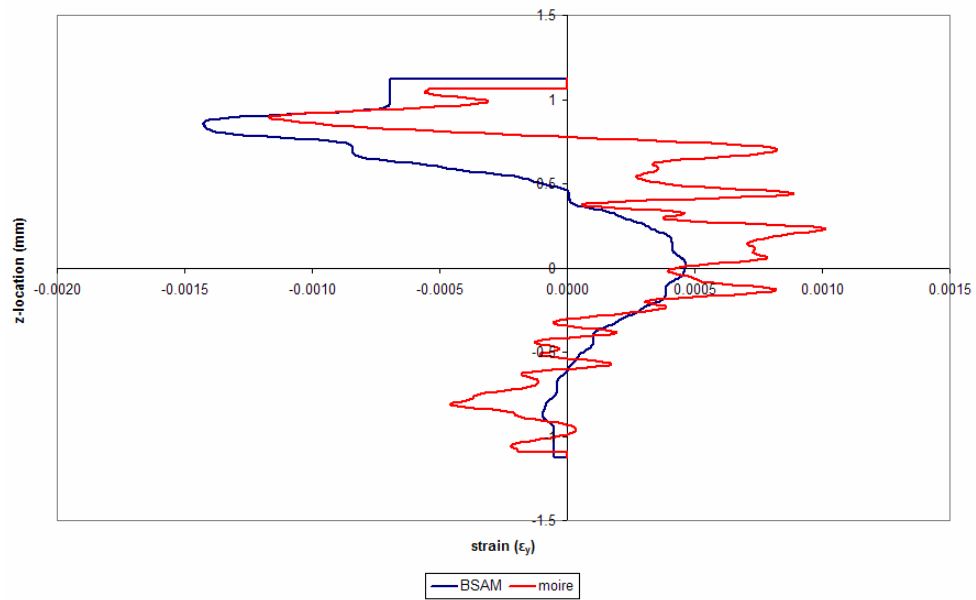


Figure 240. Stepped-Lap Joint: strain distribution (ϵ_y) through specimen thickness (z) at $x = -10\text{mm}$

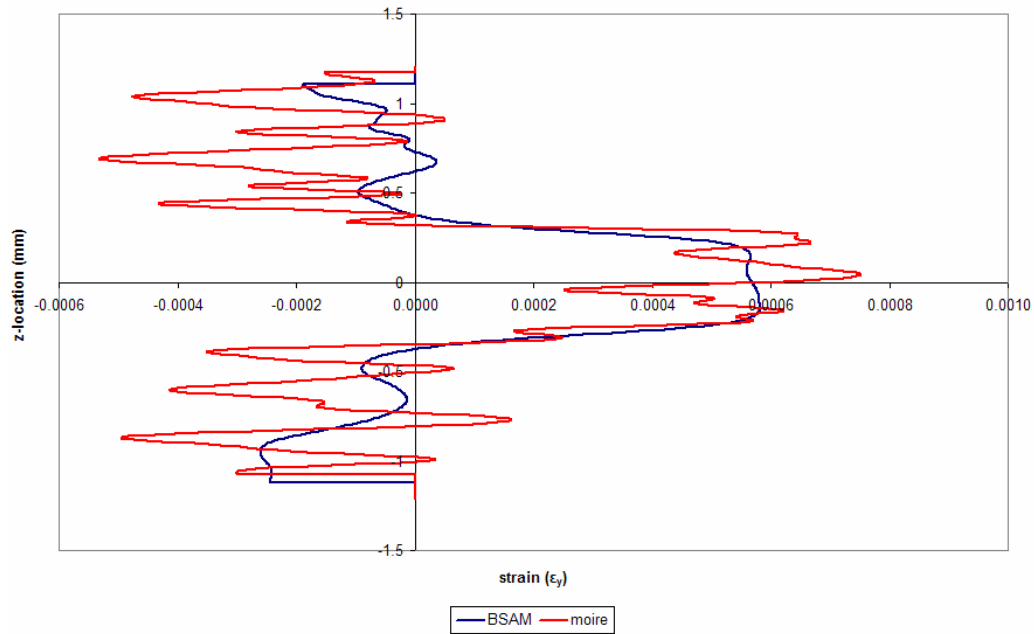


Figure 241. Scarf Joint: strain distribution (ϵ_y) through specimen thickness (z) at $x = 15\text{mm}$

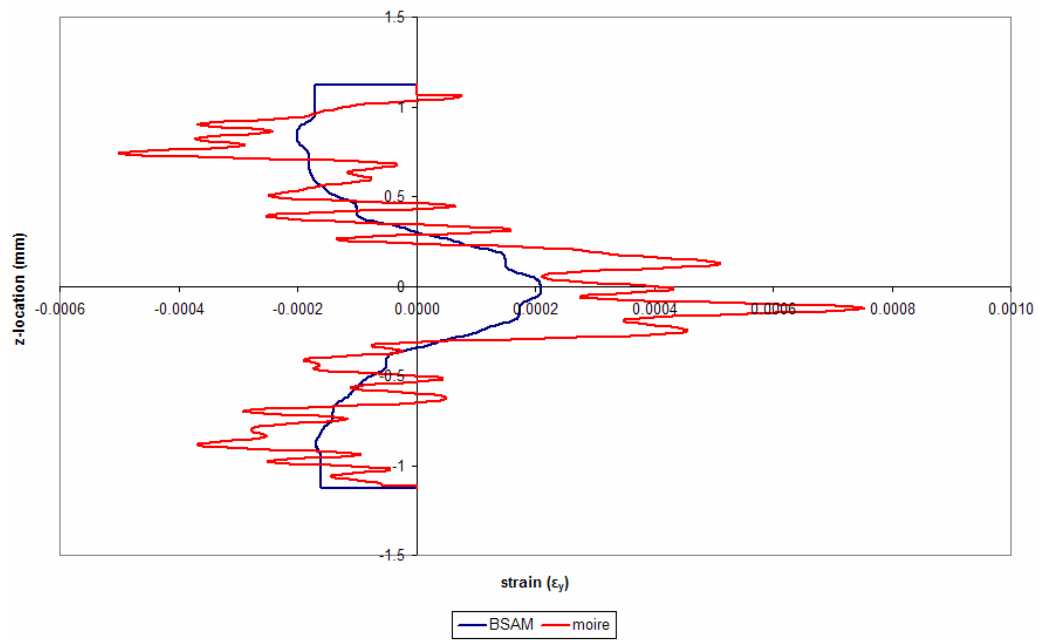


Figure 242. Stepped-Lap Joint: strain distribution (ϵ_y) through specimen thickness (z) at

$x = -15\text{mm}$

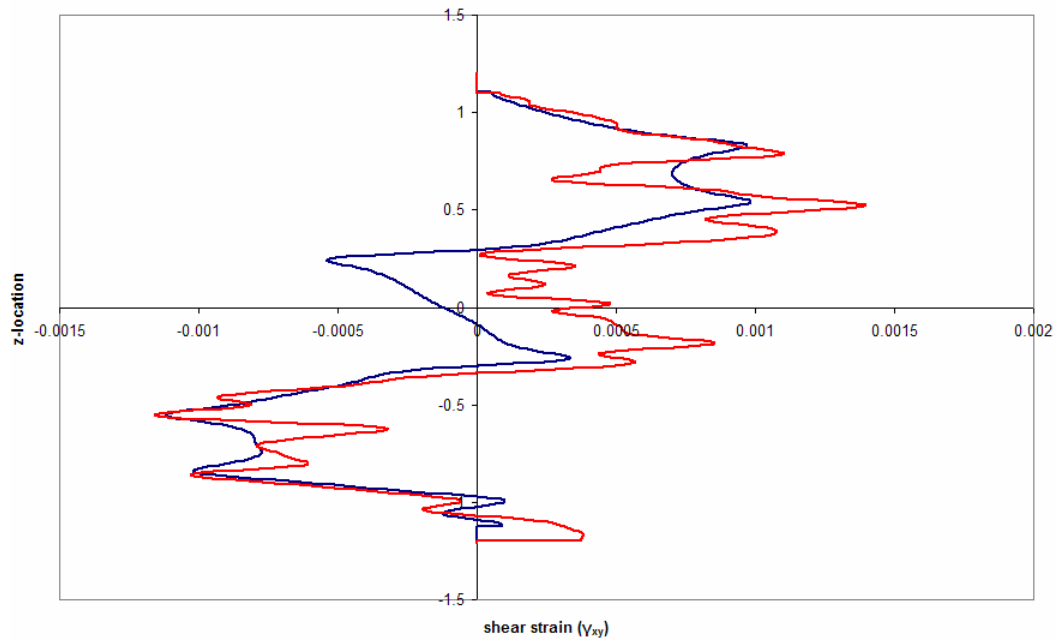


Figure 243. Scarf Joint: shear strain distribution (γ_{xy}) through specimen thickness (z) at $x = -15\text{mm}$

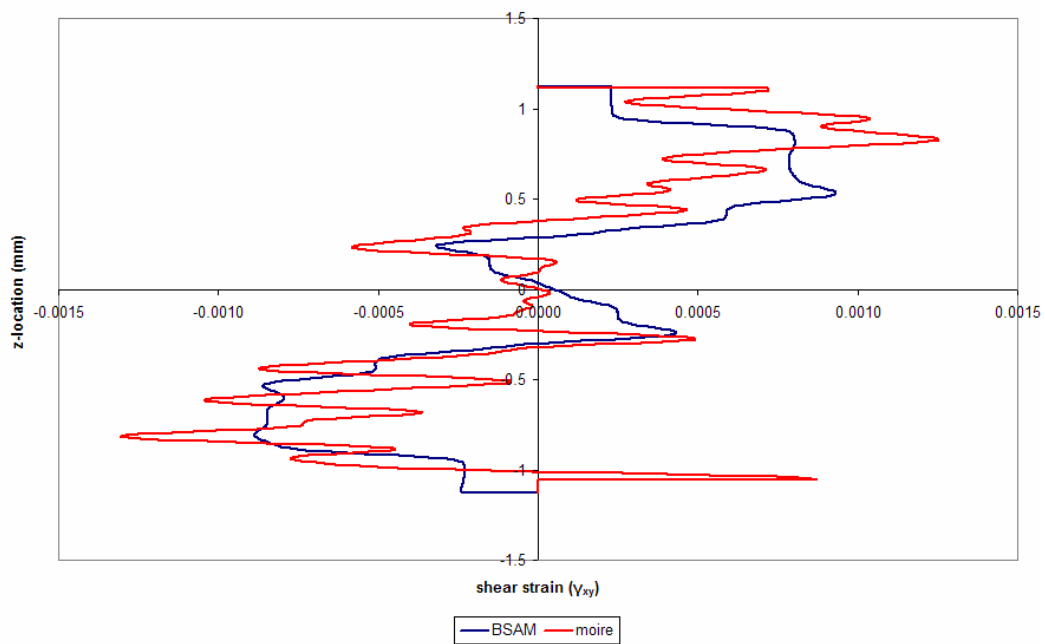


Figure 244. Stepped-Lap Joint: shear strain distribution (γ_{xy}) through specimen thickness (z) at $x = 15\text{mm}$

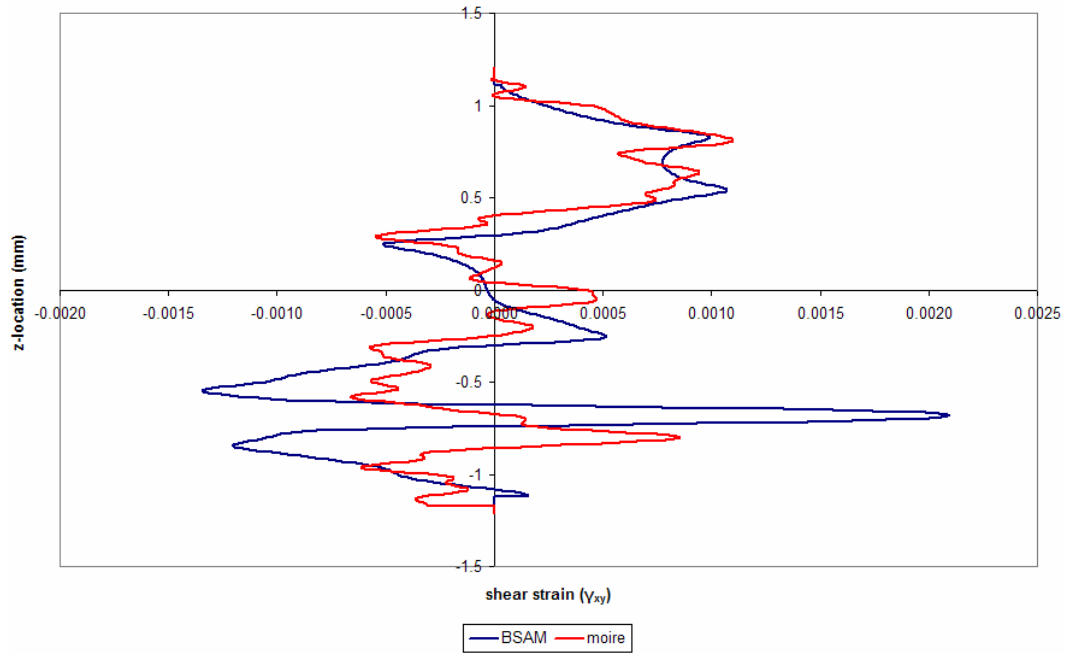


Figure 245. Scarf Joint: shear strain distribution (γ_{xy}) through specimen thickness (z) at $x = -10\text{mm}$

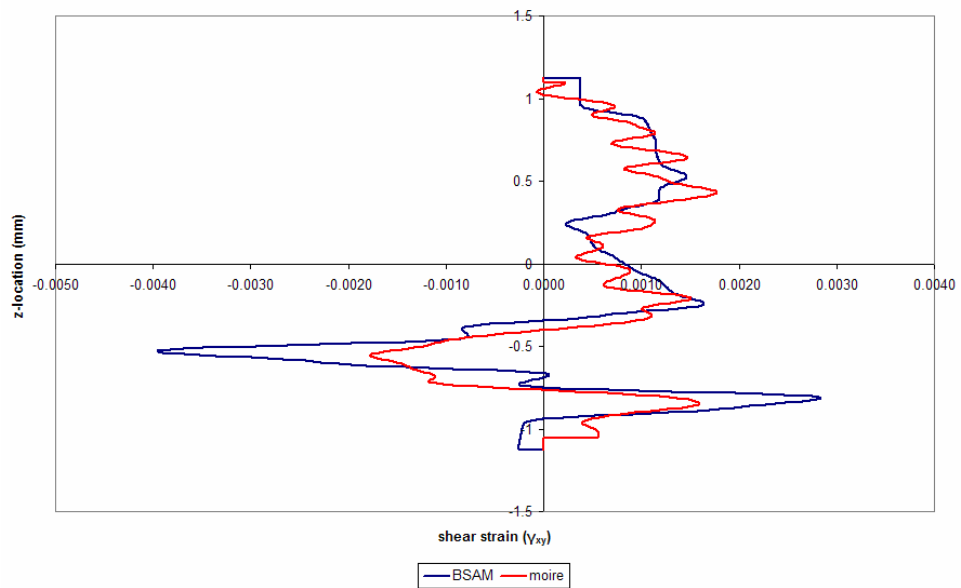


Figure 246. Stepped-Lap Joint: shear strain distribution (γ_{xy}) through specimen thickness (z) at $x = 10\text{mm}$

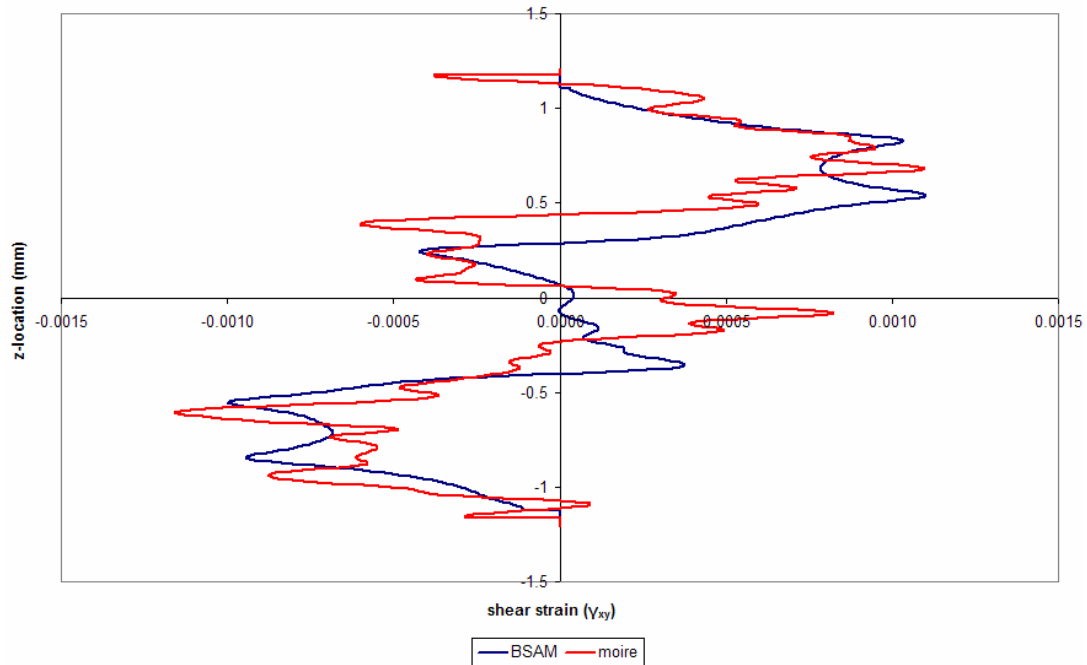


Figure 247. Scarf Joint: shear strain distribution (γ_{xy}) through specimen thickness (z) at

$x = -5\text{mm}$

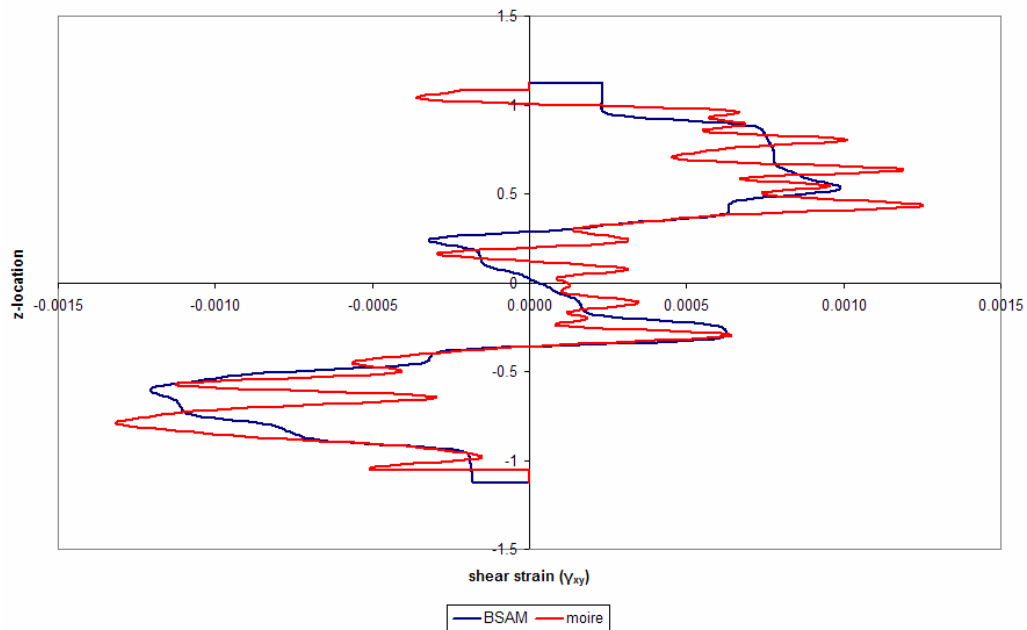


Figure 248. Stepped-Lap Joint: shear strain distribution (γ_{xy}) through specimen thickness

(z) at $x = 5\text{mm}$

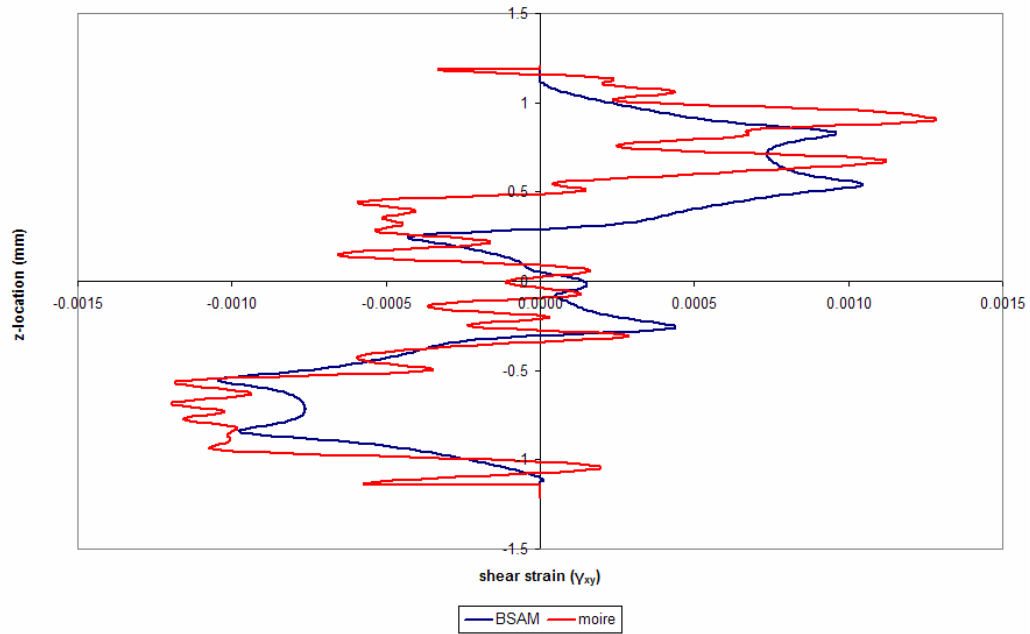


Figure 249. Scarf Joint: shear strain distribution (γ_{xy}) through specimen thickness (z) at $x = 0\text{mm}$

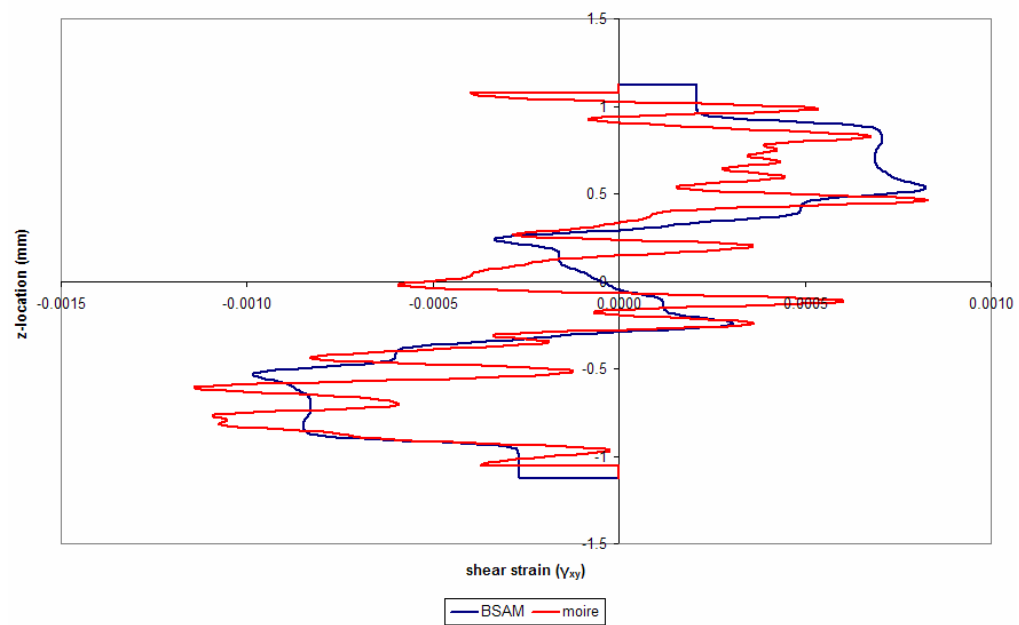


Figure 250. Stepped-Lap Joint: shear strain distribution (γ_{xy}) through specimen thickness (z) at $x = 0\text{mm}$

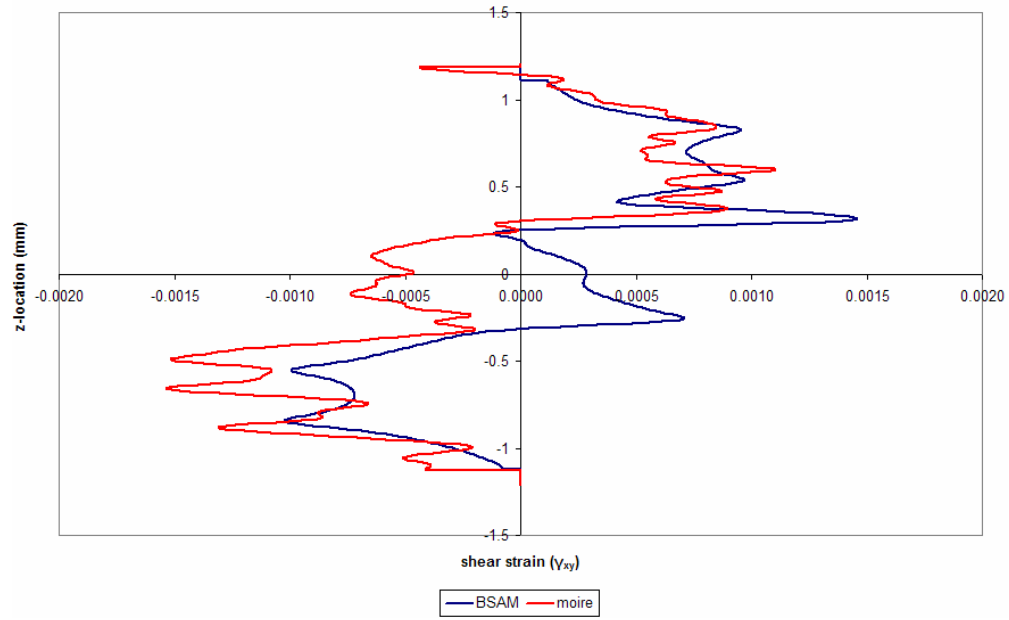


Figure 251. Scarf Joint: shear strain distribution (γ_{xy}) through specimen thickness (z) at

$x = 5\text{mm}$

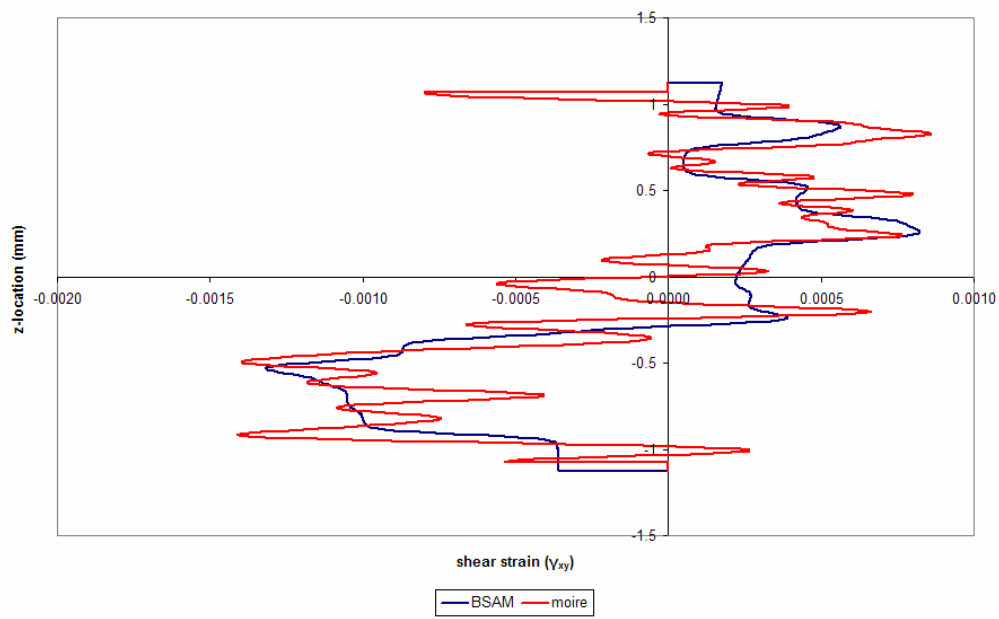


Figure 252. Stepped-Lap Joint: shear strain distribution (γ_{xy}) through specimen thickness

(z) at $x = -5\text{mm}$

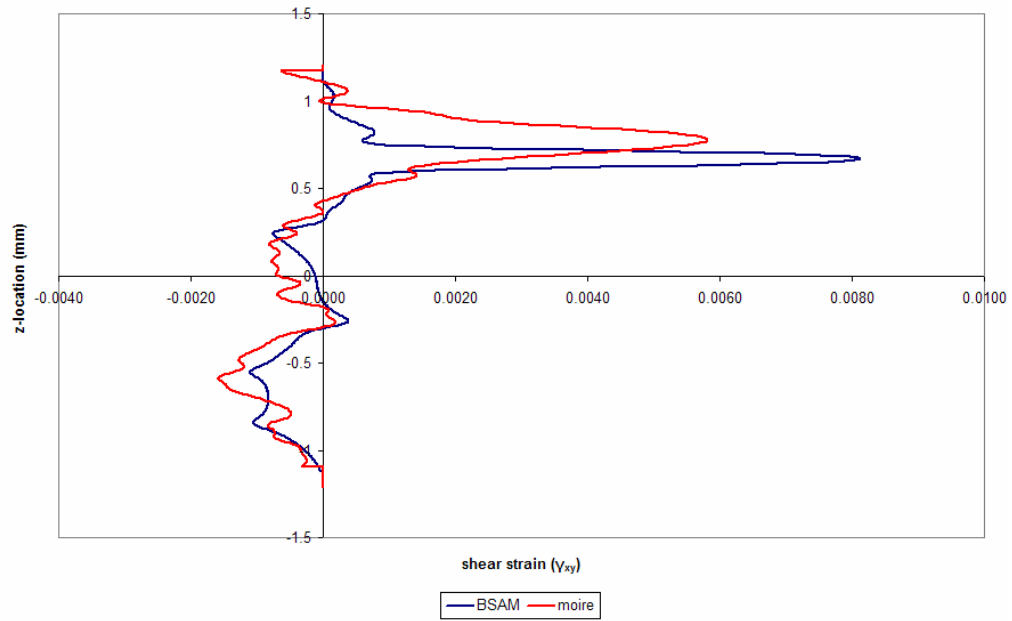


Figure 253. Scarf Joint: shear strain distribution (γ_{xy}) through specimen thickness (z) at $x = 10\text{mm}$

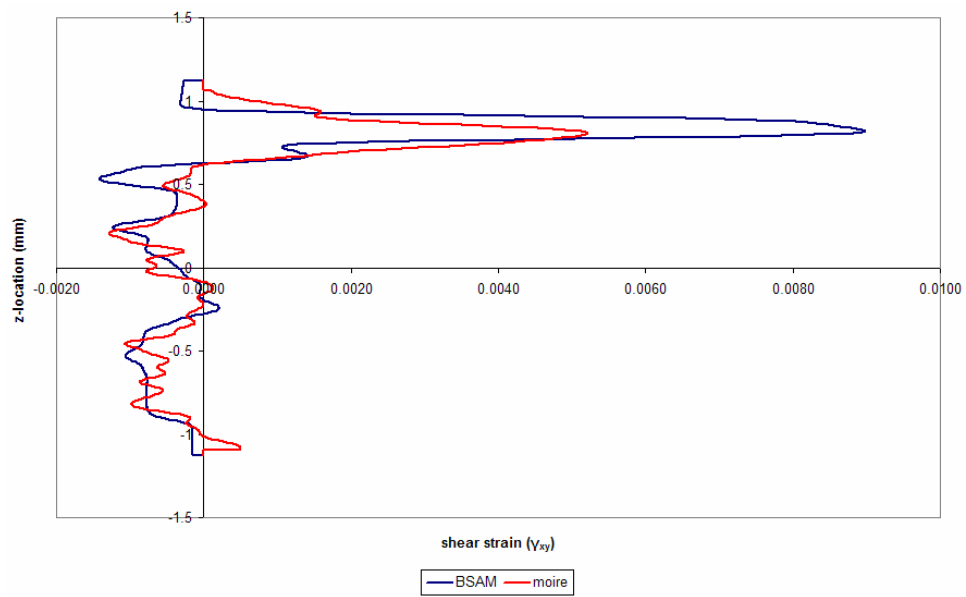


Figure 254. Stepped-Lap Joint: shear strain distribution (γ_{xy}) through specimen thickness (z) at $x = -10\text{mm}$

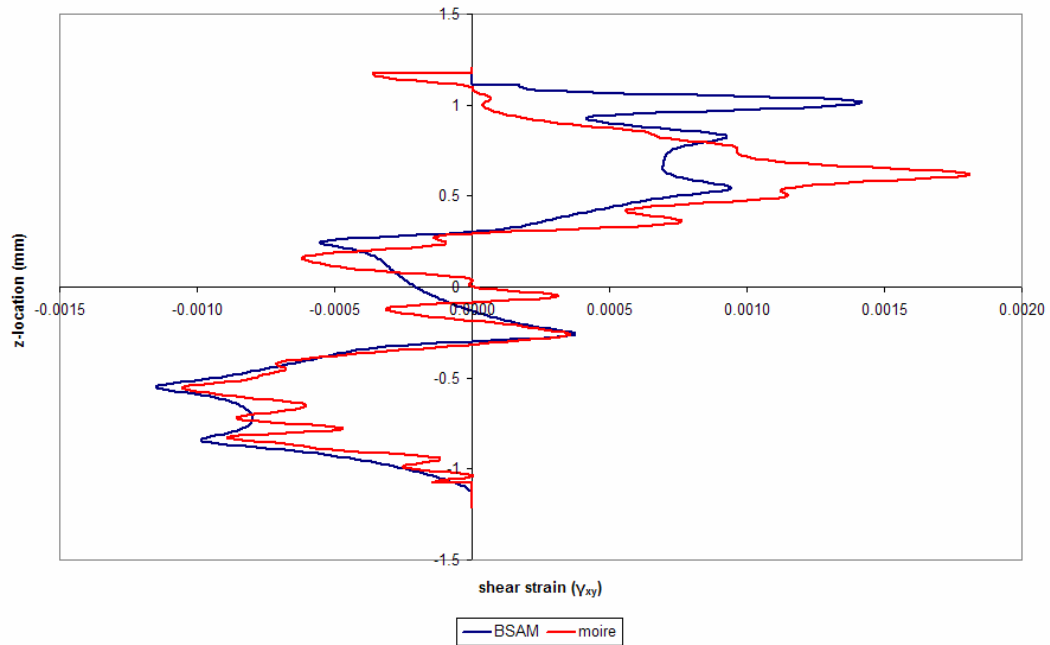


Figure 255. Scarf Joint: shear strain distribution (γ_{xy}) through specimen thickness (z) at

$x = 15\text{mm}$

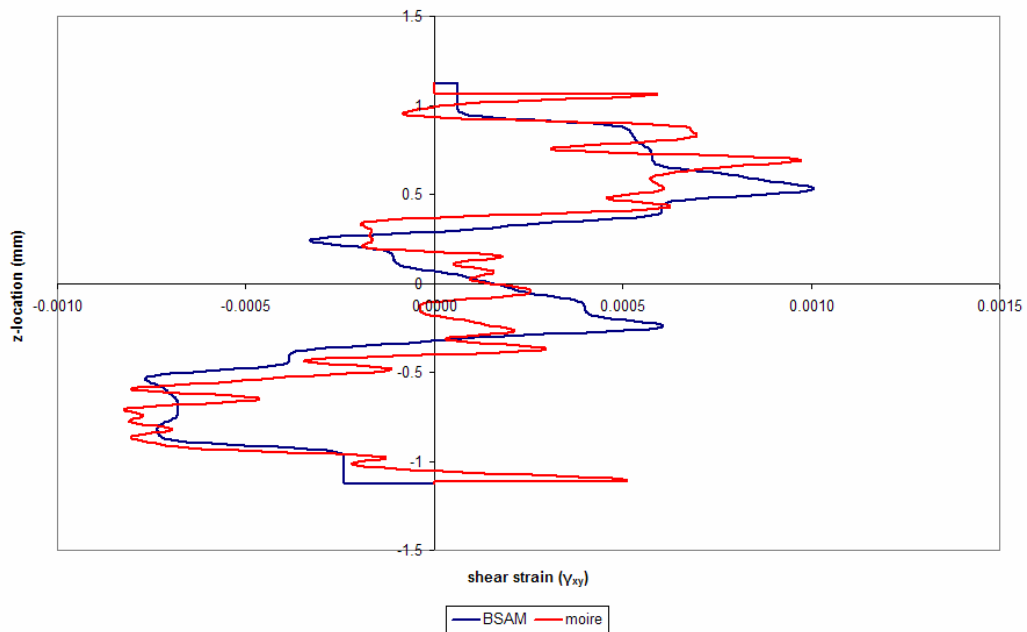
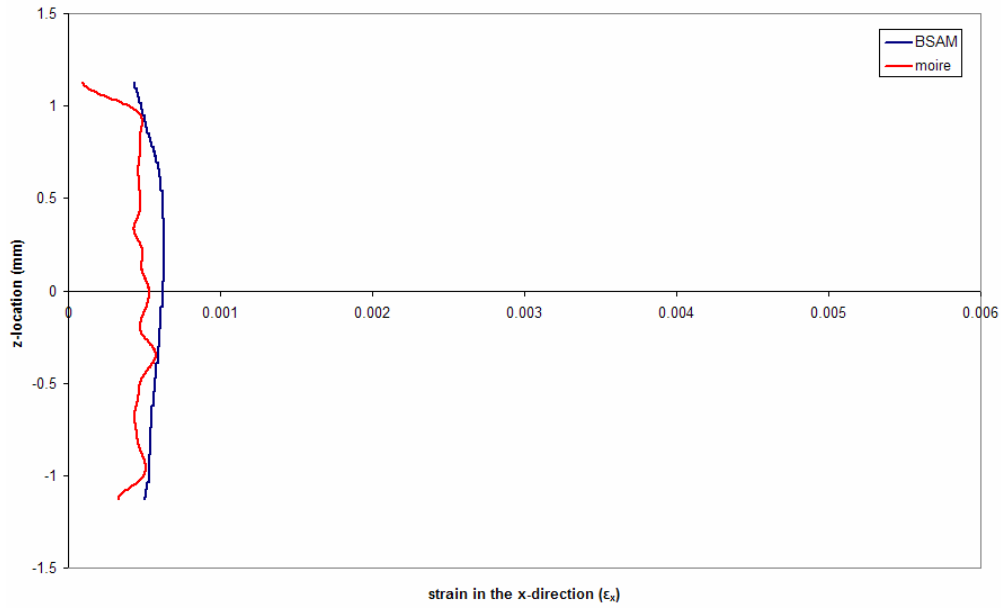


Figure 256. Stepped-Lap Joint: shear strain distribution (γ_{xy}) through specimen thickness

(z) at $x = -15\text{mm}$

Appendix E: Refined line plots comparing predicted strain data and experimental results



**Figure 257. Stepped-lap Joint: strain (ϵ_x) through thickness (z) at $x = -15\text{mm}$
(data smoothed 250 times)**

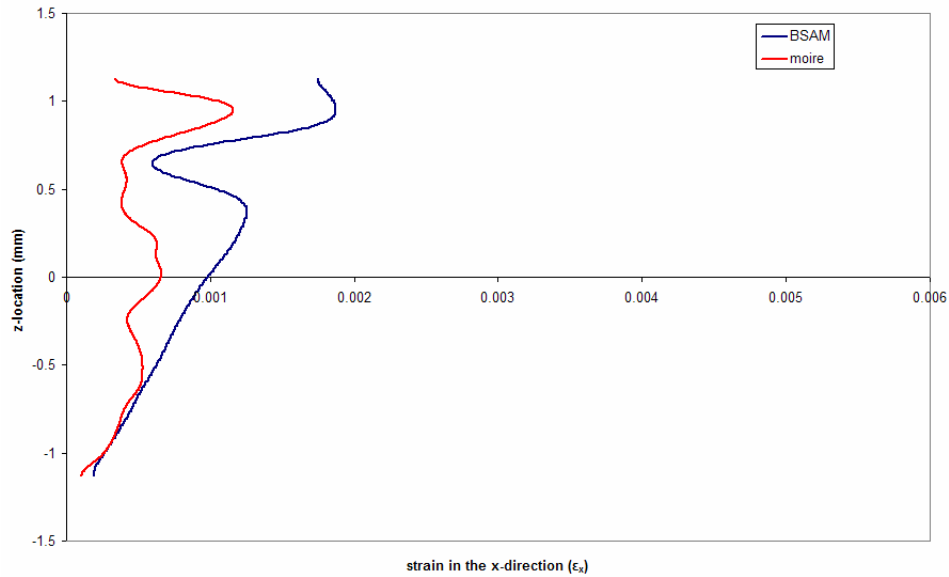


**Figure 258. Stepped-lap Joint: strain (ϵ_x) through thickness (z) at $x = -10\text{mm}$
(data smoothed 250 times)**

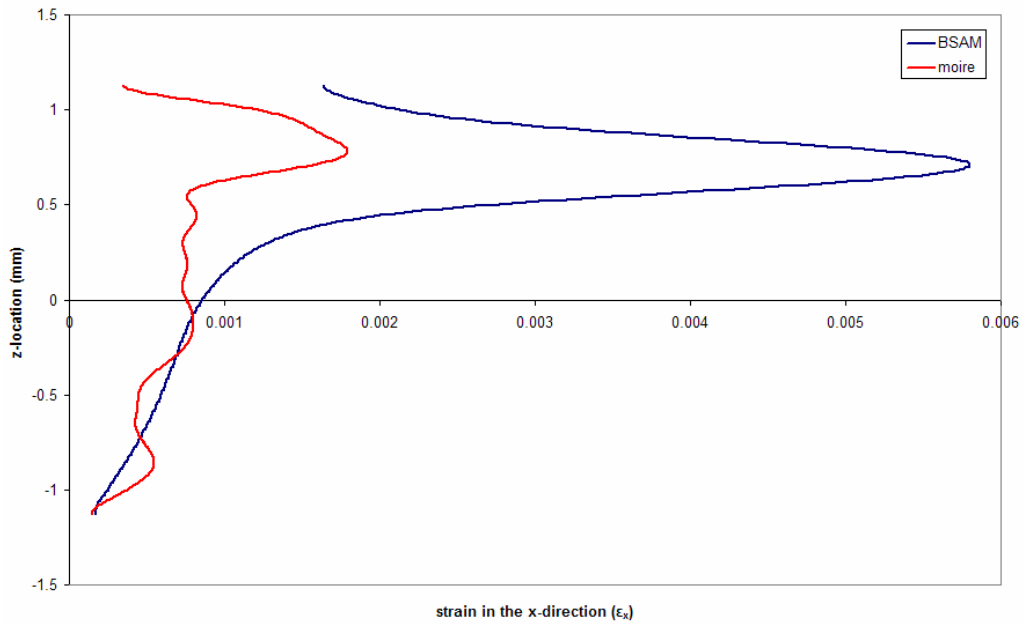


Figure 259. Stepped-lap Joint: strain (ϵ_x) through thickness (z) at $x = -9.6\text{mm}$
(data smoothed 250 times)

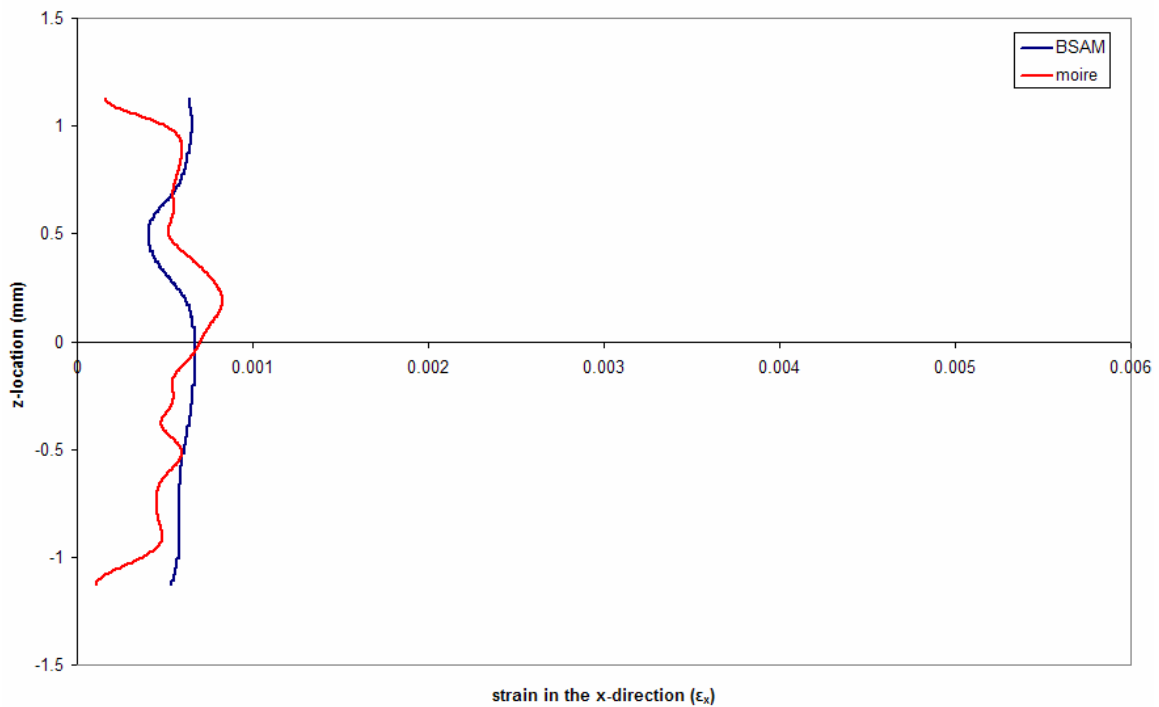


Figure 260. Stepped-lap Joint: strain (ϵ_x) through thickness (z) at $x = -5\text{mm}$
(data smoothed 250 times)

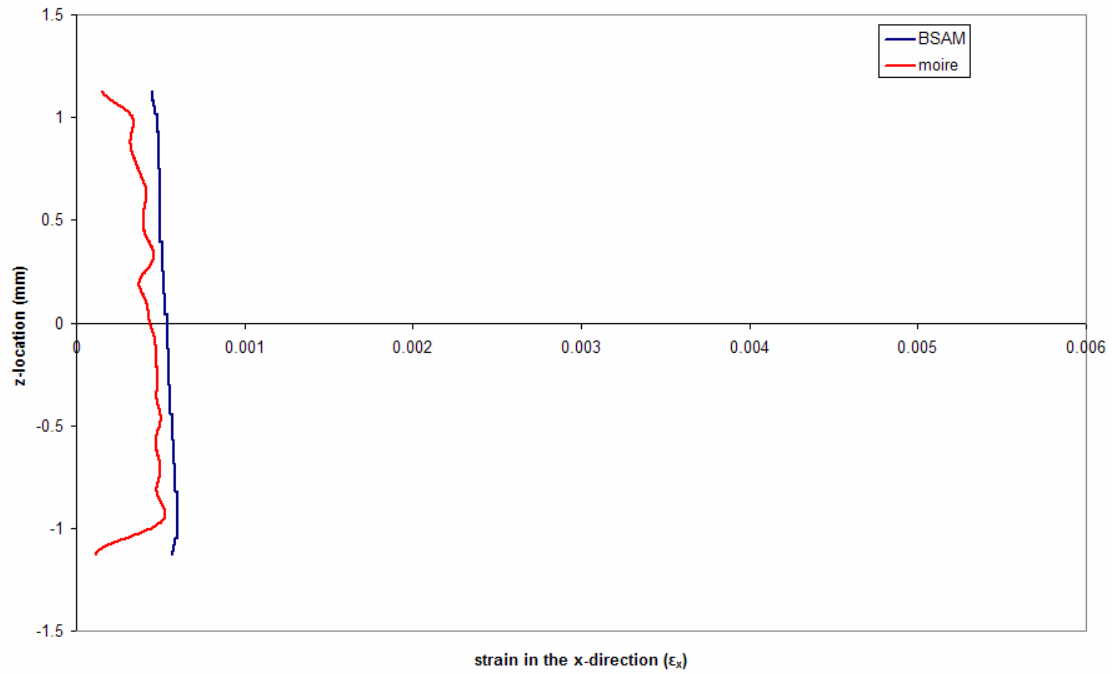


Figure 261. Stepped-lap Joint: strain (ϵ_x) through thickness (z) at $x = 0\text{mm}$
(data smoothed 250 times)

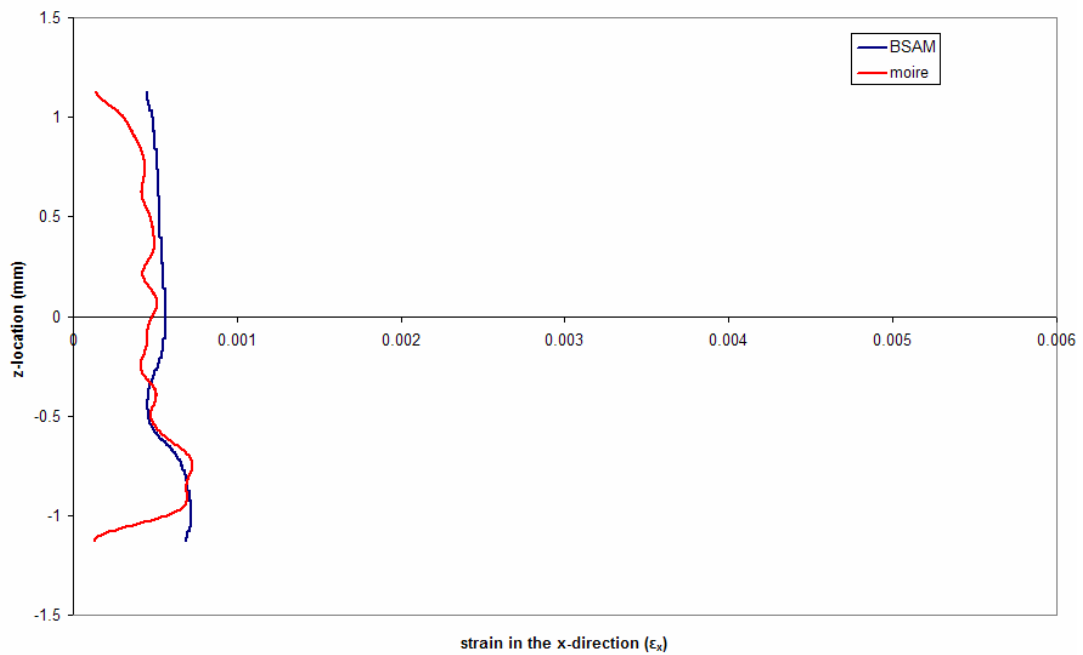


Figure 262. Stepped-lap Joint: strain (ϵ_x) through thickness (z) at $x = 5\text{mm}$
(data smoothed 250 times)

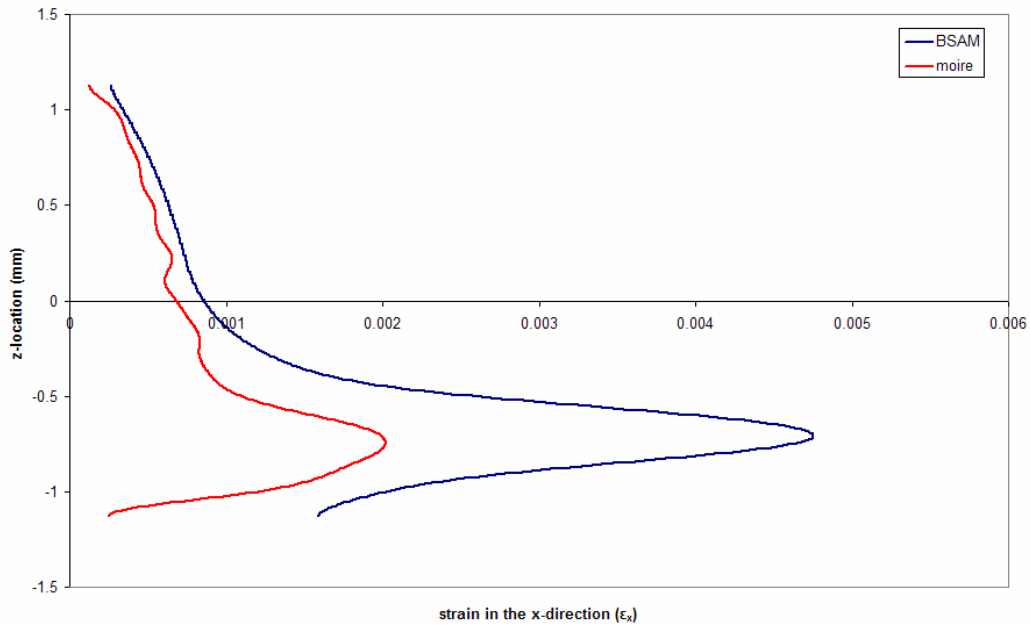


Figure 263. Stepped-lap Joint: strain (ϵ_x) through thickness (z) at $x = 9.6\text{mm}$
(data smoothed 250 times)

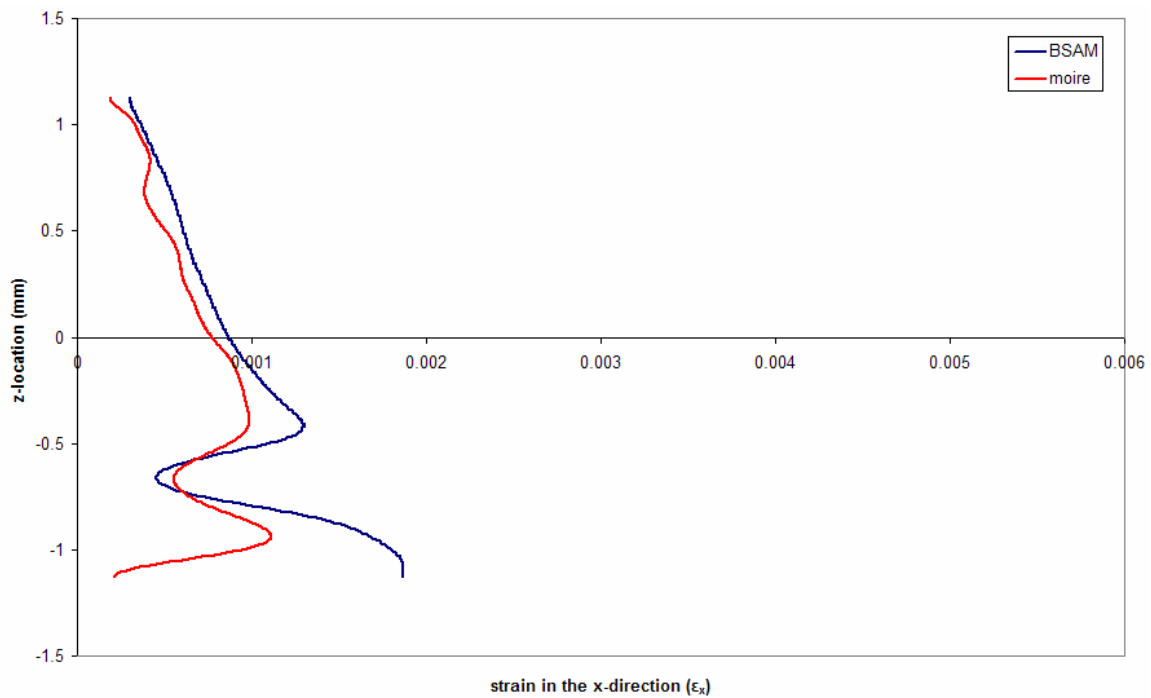


Figure 264. Stepped-lap Joint: strain (ϵ_x) through thickness (z) at $x = 10\text{mm}$
(data smoothed 250 times)

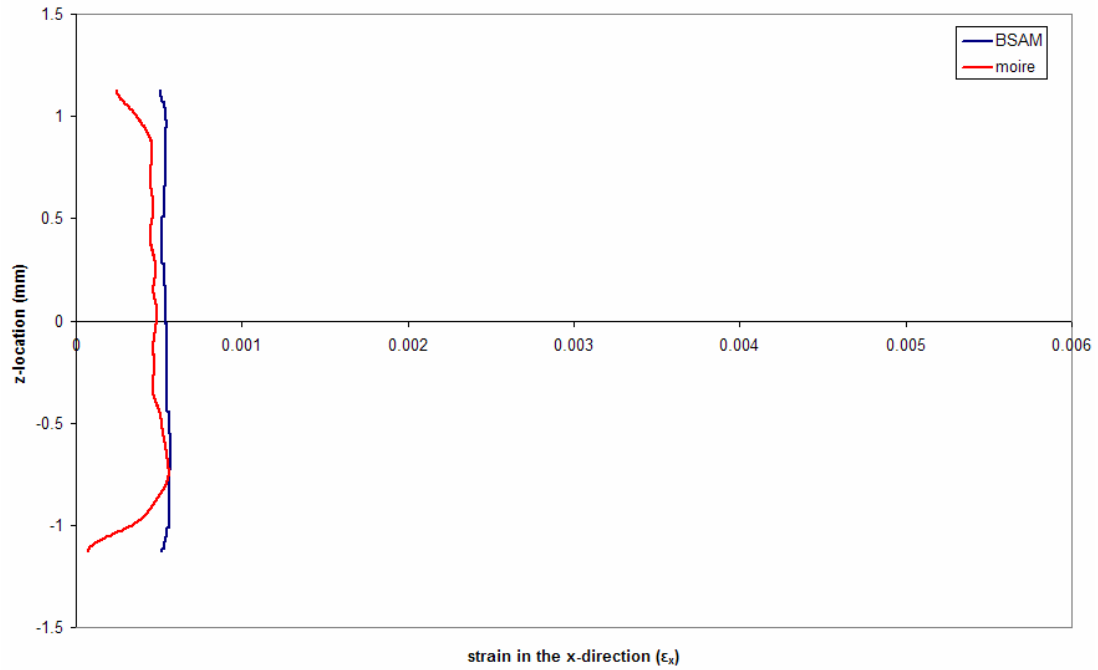


Figure 265. Stepped-lap Joint: strain (ϵ_x) through thickness (z) at x = 15mm
(data smoothed 250 times)

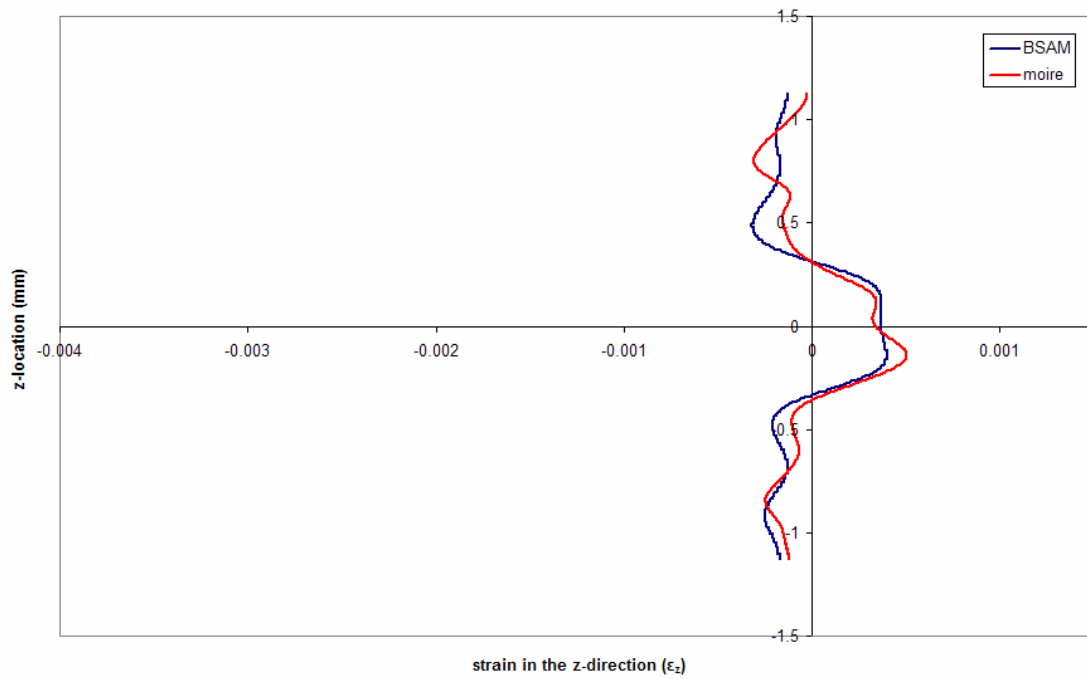


Figure 266. Stepped-lap Joint: strain (ϵ_z) through thickness (z) at x = -15mm
(data smoothed 250 times)

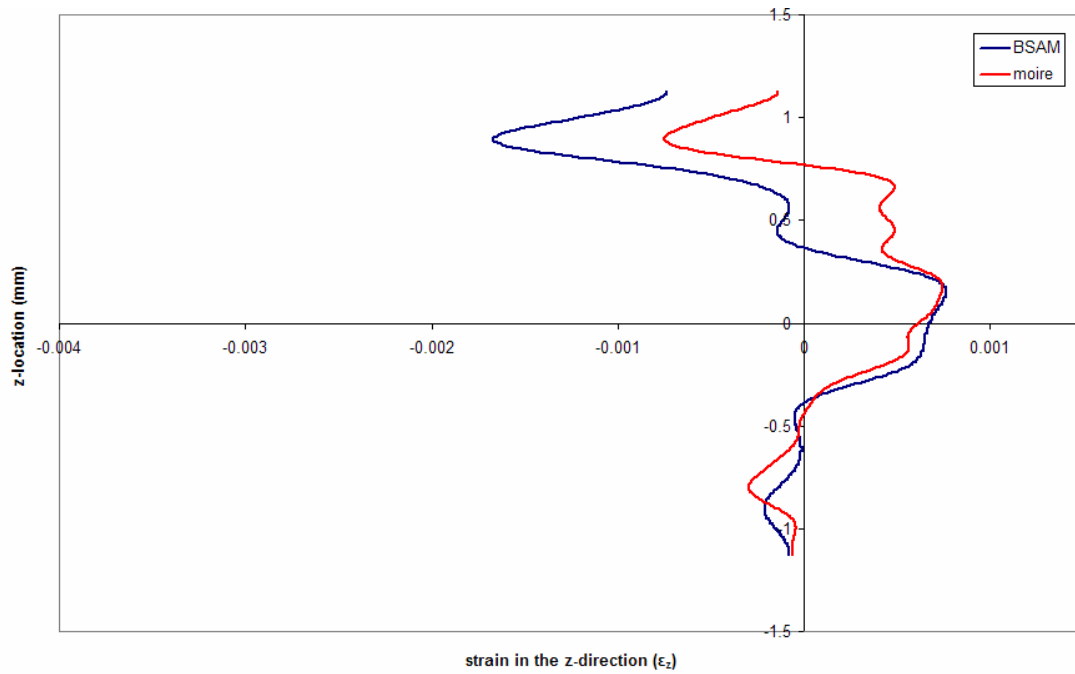


Figure 267. Stepped-lap Joint: strain (ϵ_z) through thickness (z) at x = -10mm
(data smoothed 250 times)

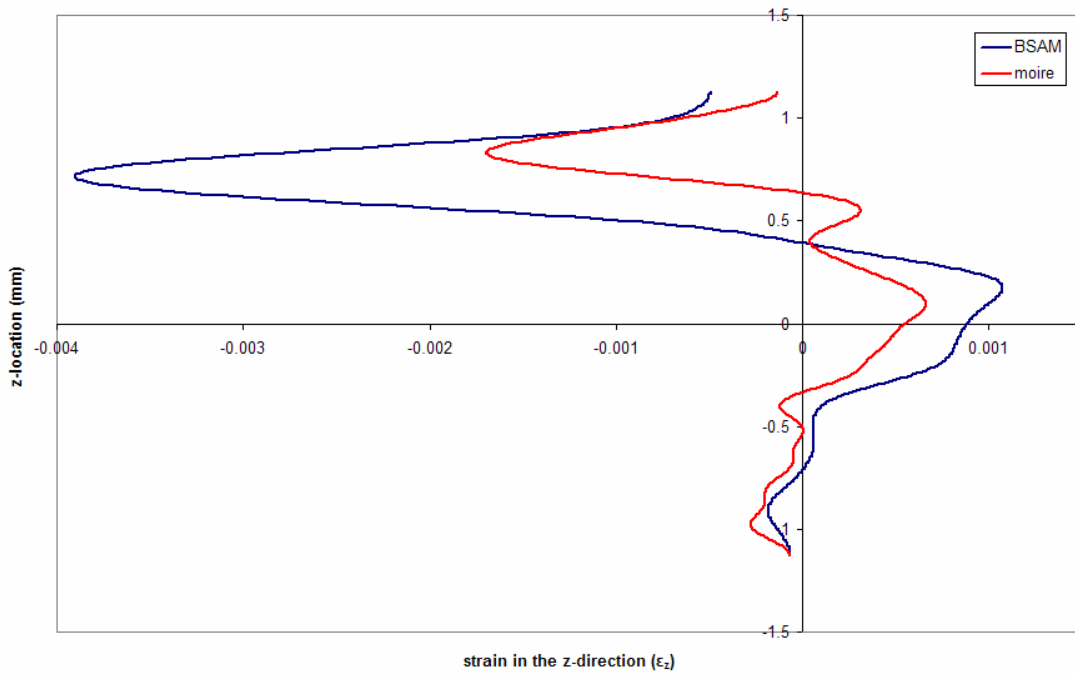


Figure 268. Stepped-lap Joint: strain (ϵ_z) through thickness (z) at x = -9.6mm
(data smoothed 250 times)

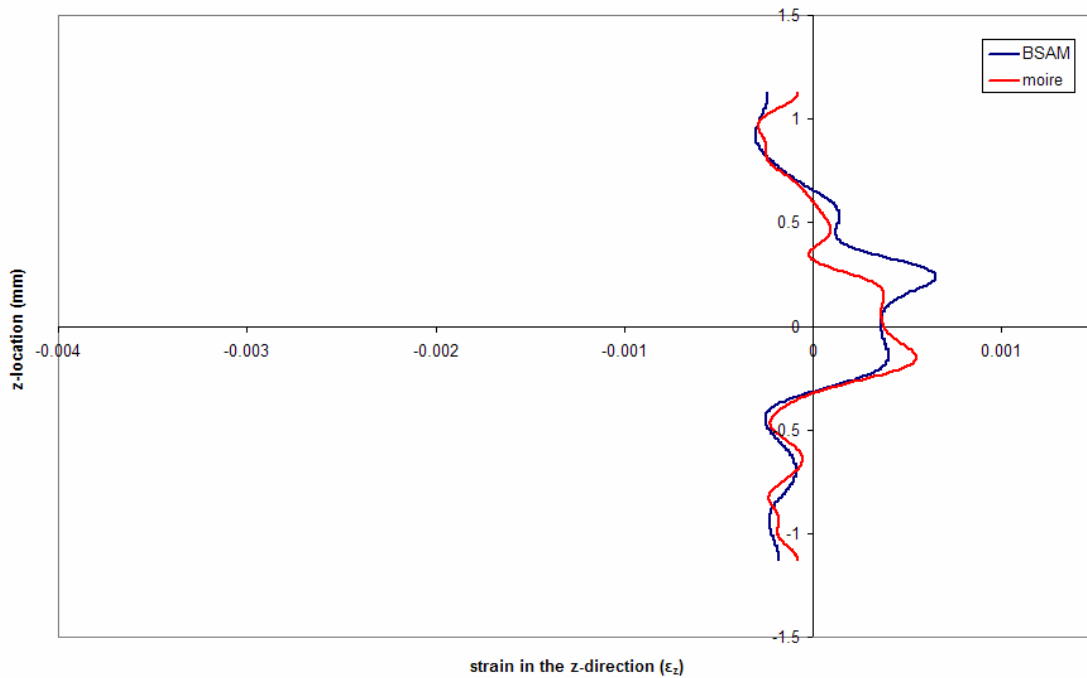


Figure 269. Stepped-lap Joint: strain (ϵ_z) through specimen thickness (z) at x = -5mm
(data smoothed 250 times)

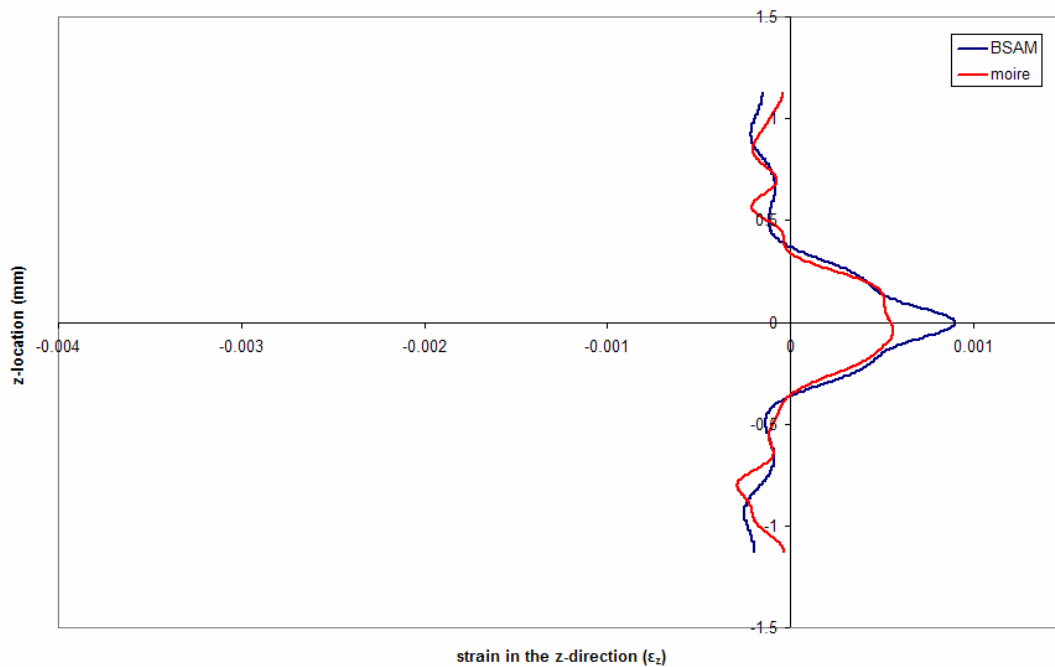


Figure 270. Stepped-lap Joint: strain (ϵ_z) through thickness (z) at x = 0mm
(data smoothed 250 times)

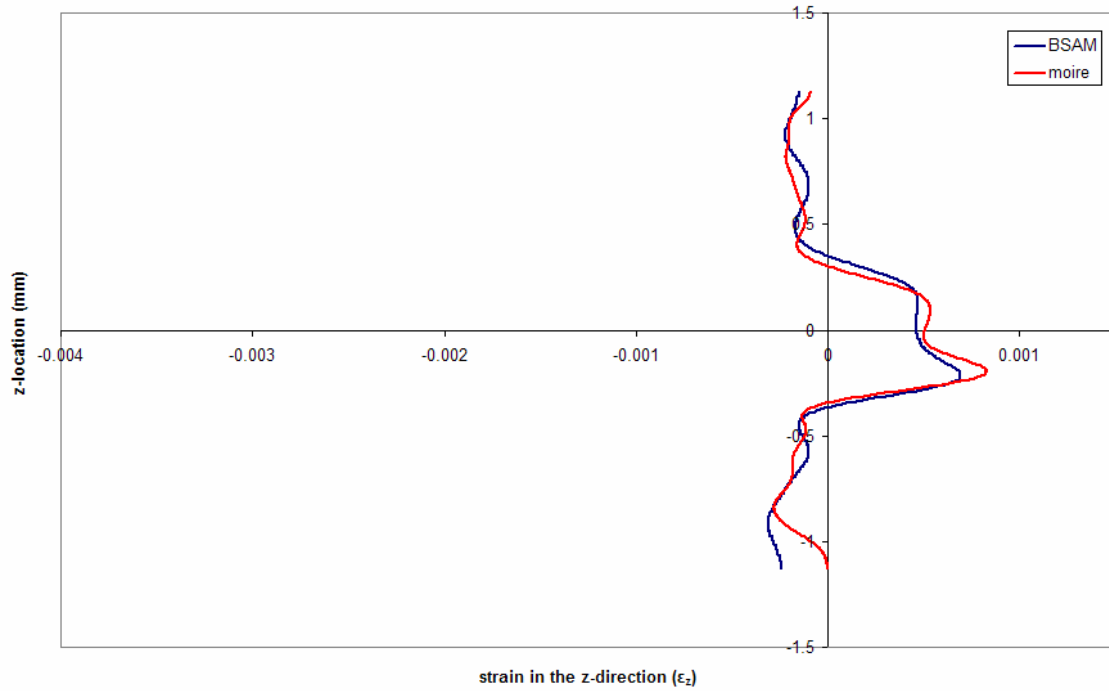


Figure 271. Stepped-lap Joint: strain (ϵ_z) through specimen thickness (z) at $x = 5\text{mm}$

(data smoothed 250 times)

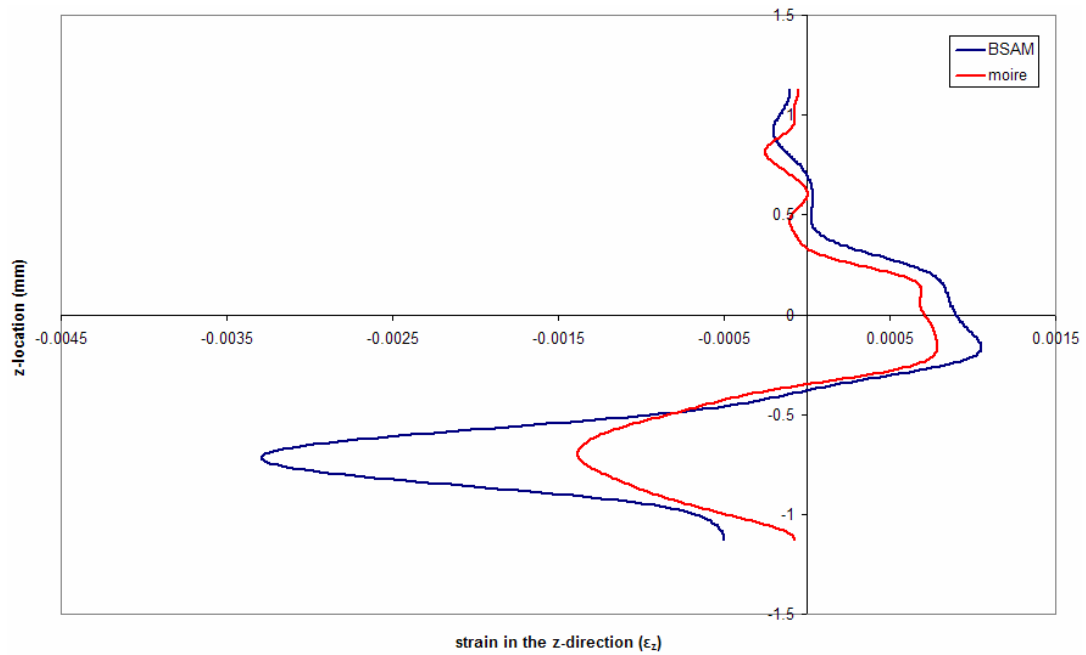


Figure 272. Stepped-lap Joint: strain (ϵ_z) through thickness (z) at $x = 9.6\text{mm}$

(data smoothed 250 times)

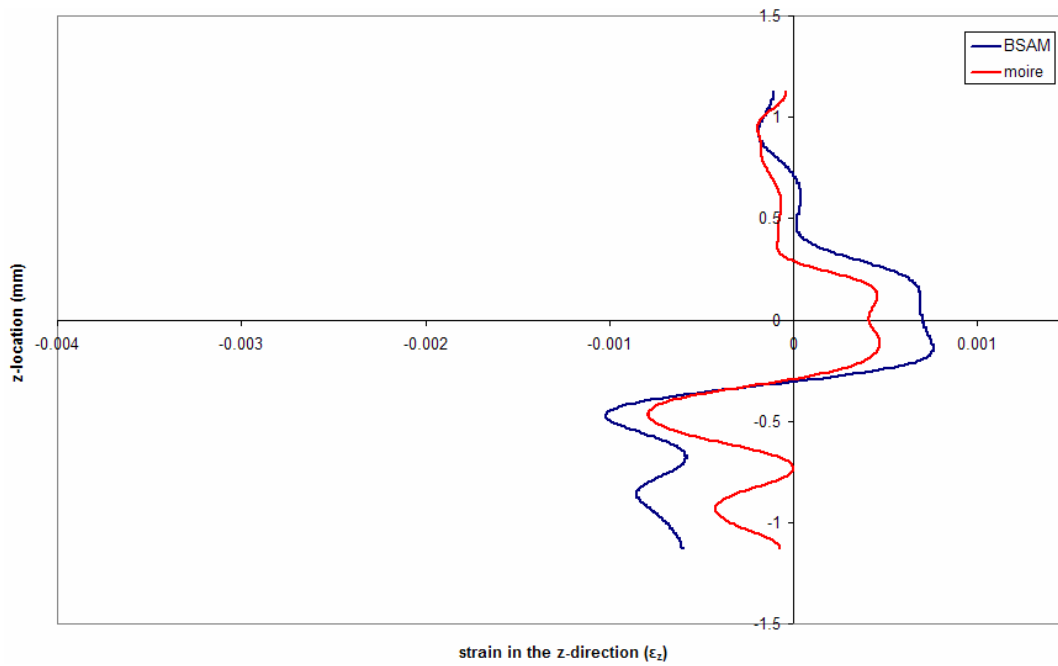


Figure 273. Stepped-lap Joint: strain (ϵ_z) through thickness (z) at $x = 10\text{mm}$
(data smoothed 250 times)

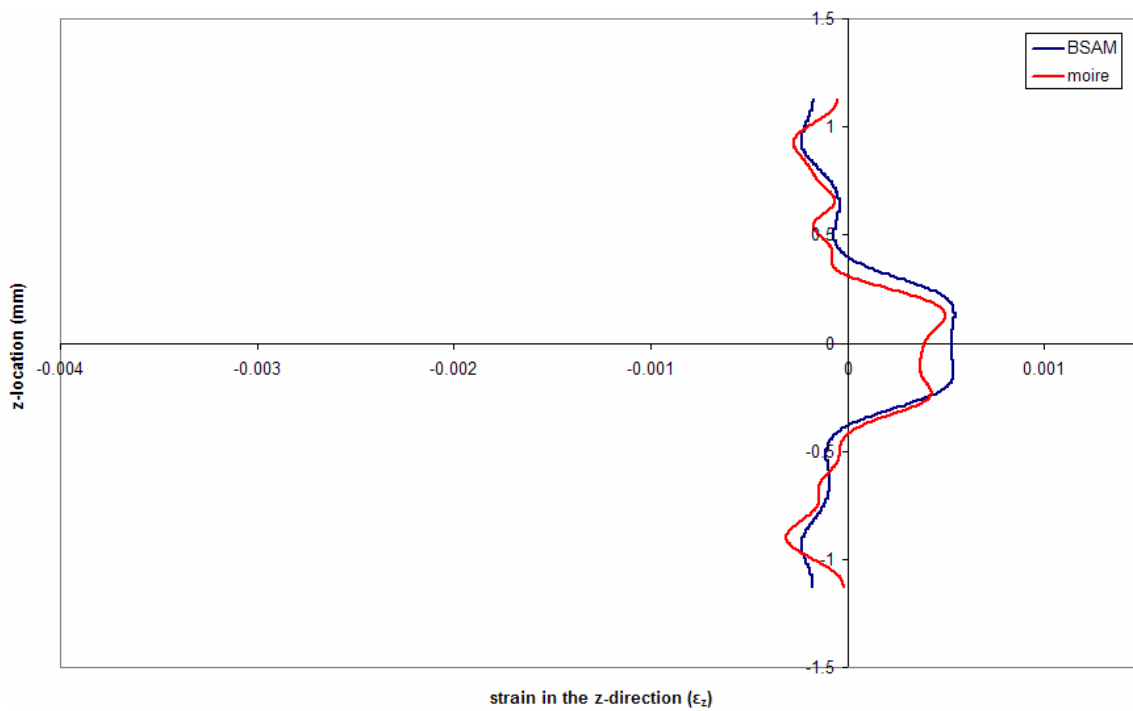
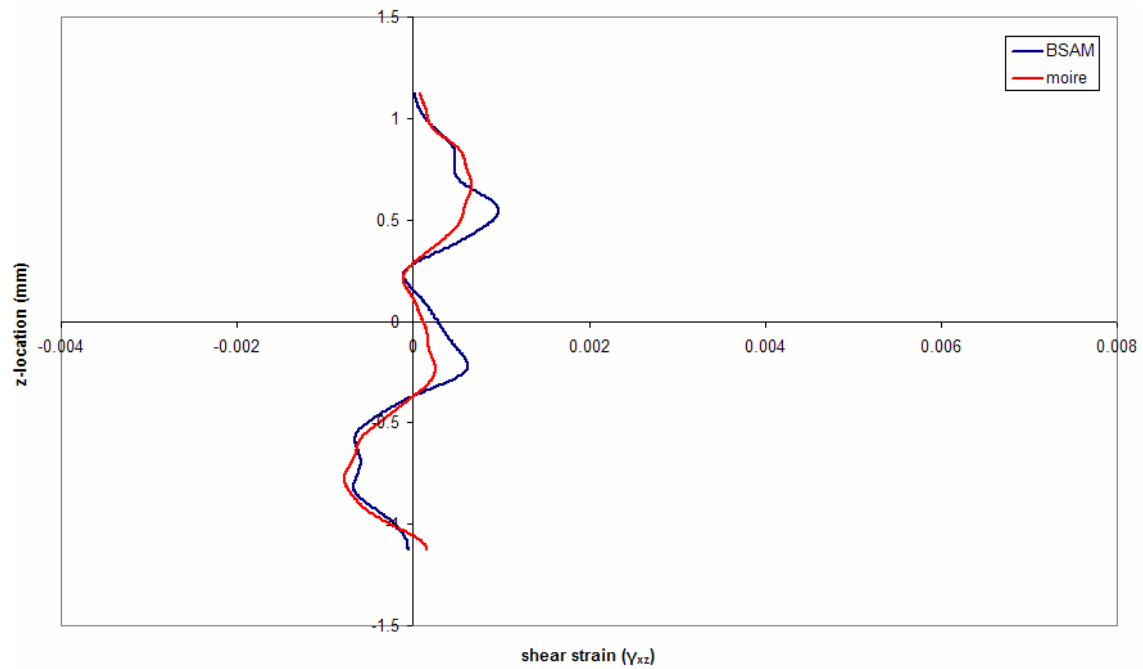
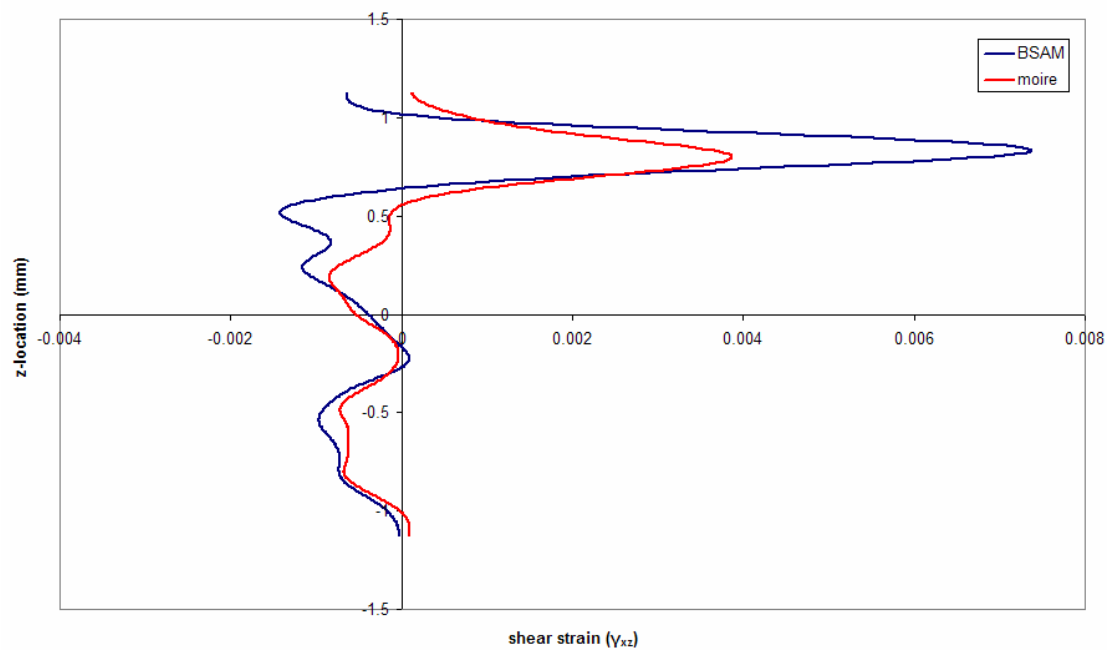


Figure 274. Stepped-lap Joint: strain (ϵ_z) through thickness (z) at $x = 15\text{mm}$
(data smoothed 250 times)



**Figure 275. Stepped-lap Joint: shear strain (γ_{xz}) through thickness (z) at $x = -15\text{mm}$
(data smoothed 250 times)**



**Figure 276. Stepped-lap Joint: shear strain (γ_{xz}) through thickness (z) at $x = -10\text{mm}$
(data smoothed 250 times)**

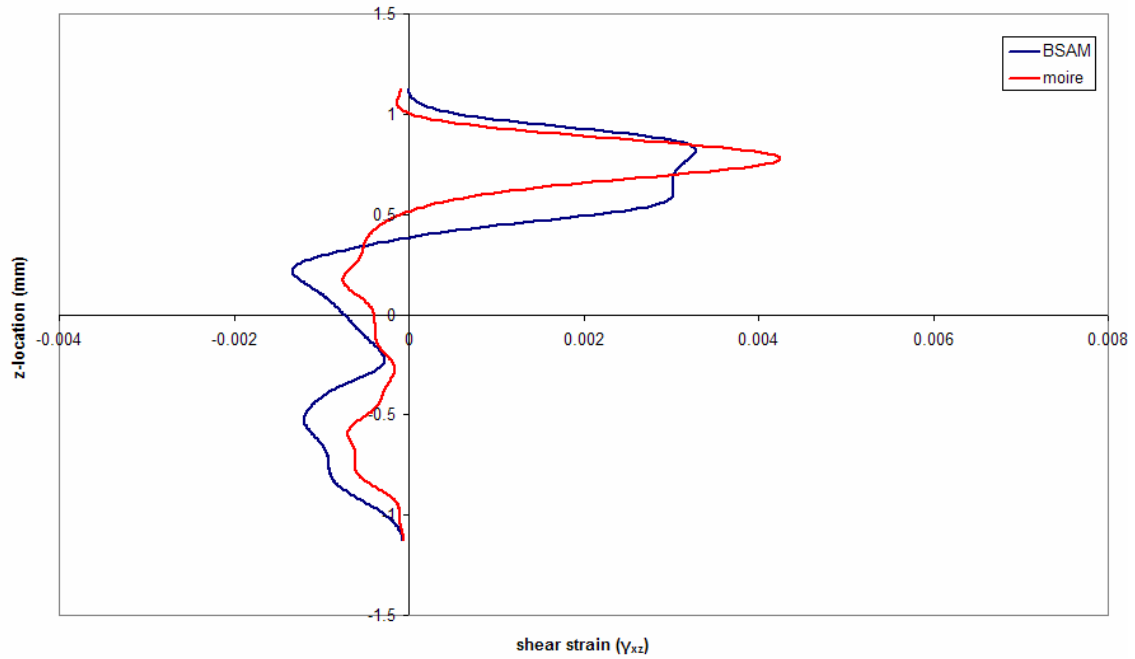


Figure 277. Stepped-lap Joint: shear strain (γ_{xz}) through thickness (z) at $x = -9.6\text{mm}$
(data smoothed 250 times)

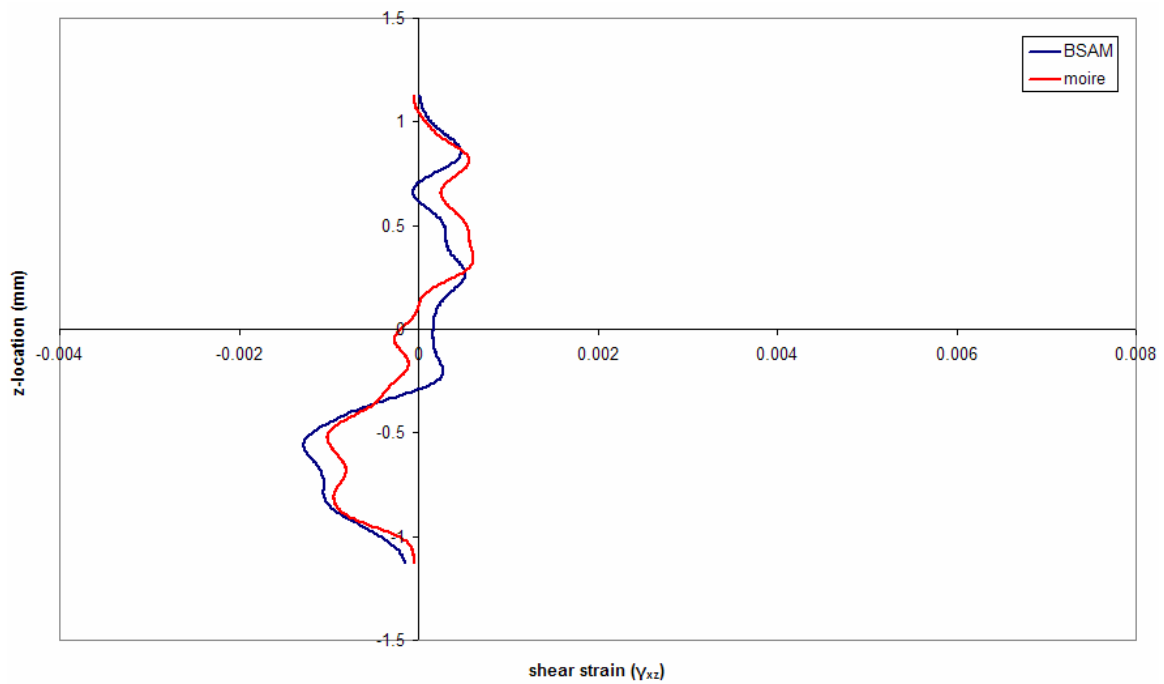


Figure 278. Stepped-lap Joint: shear strain (γ_{xz}) through thickness (z) at $x = -5\text{mm}$
(data smoothed 250 times)

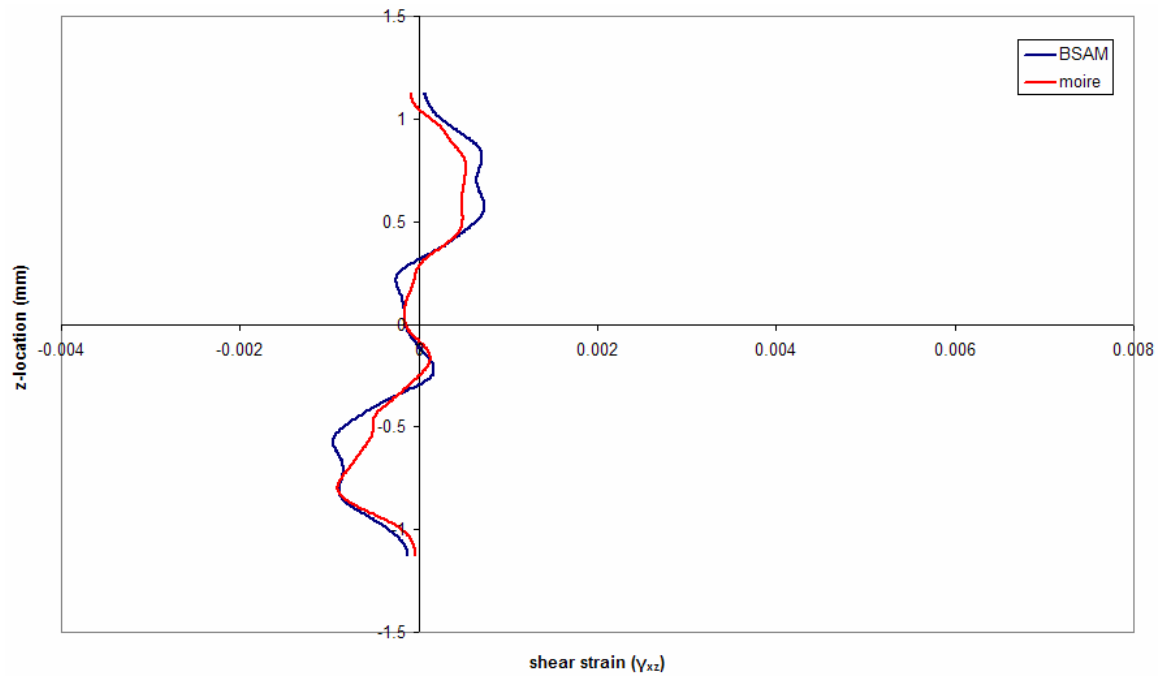


Figure 279. Stepped-lap Joint: shear strain (γ_{xz}) through thickness (z) at $x = 0\text{mm}$
(data smoothed 250 times)

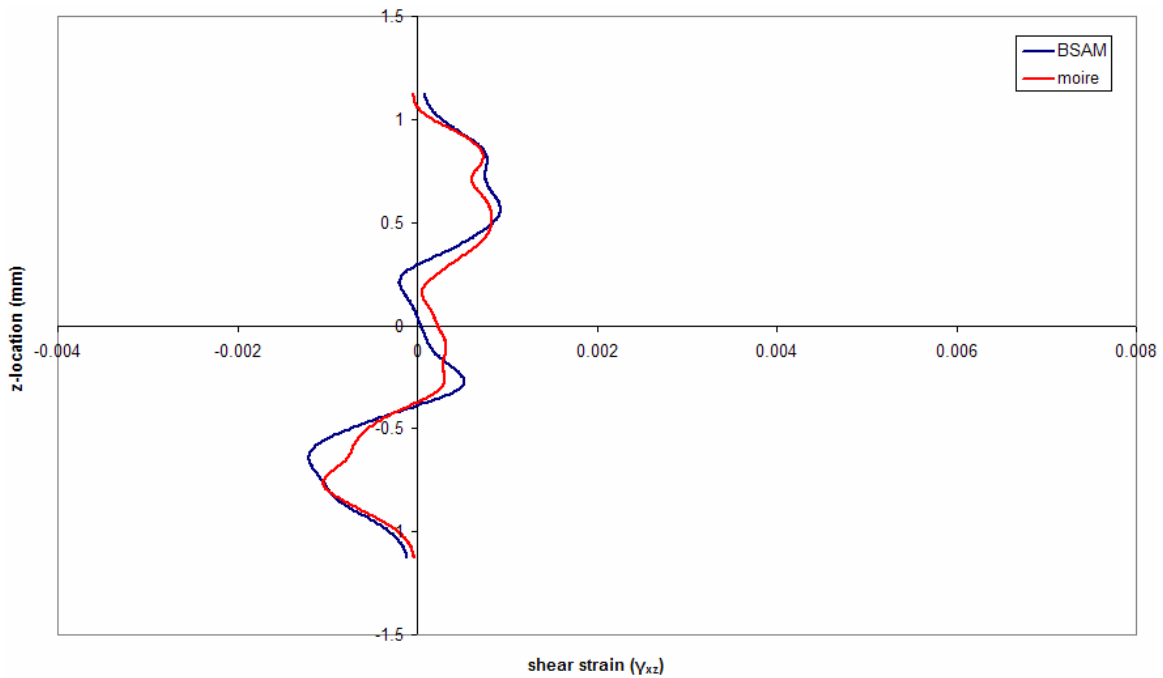


Figure 280. Stepped-lap Joint: shear strain (γ_{xz}) through thickness (z) at $x = 5\text{mm}$
(data smoothed 250 times)

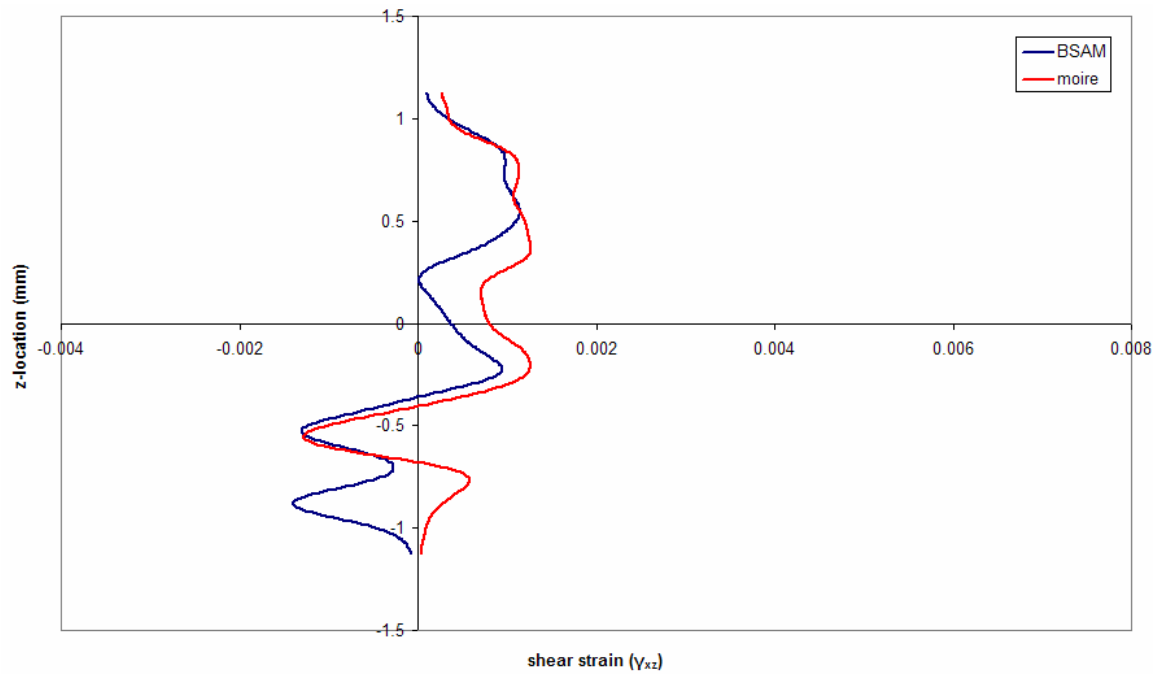


Figure 281. Stepped-lap Joint: shear strain (γ_{xz}) through thickness (z) at $x = 9.6\text{mm}$
(data smoothed 250 times)

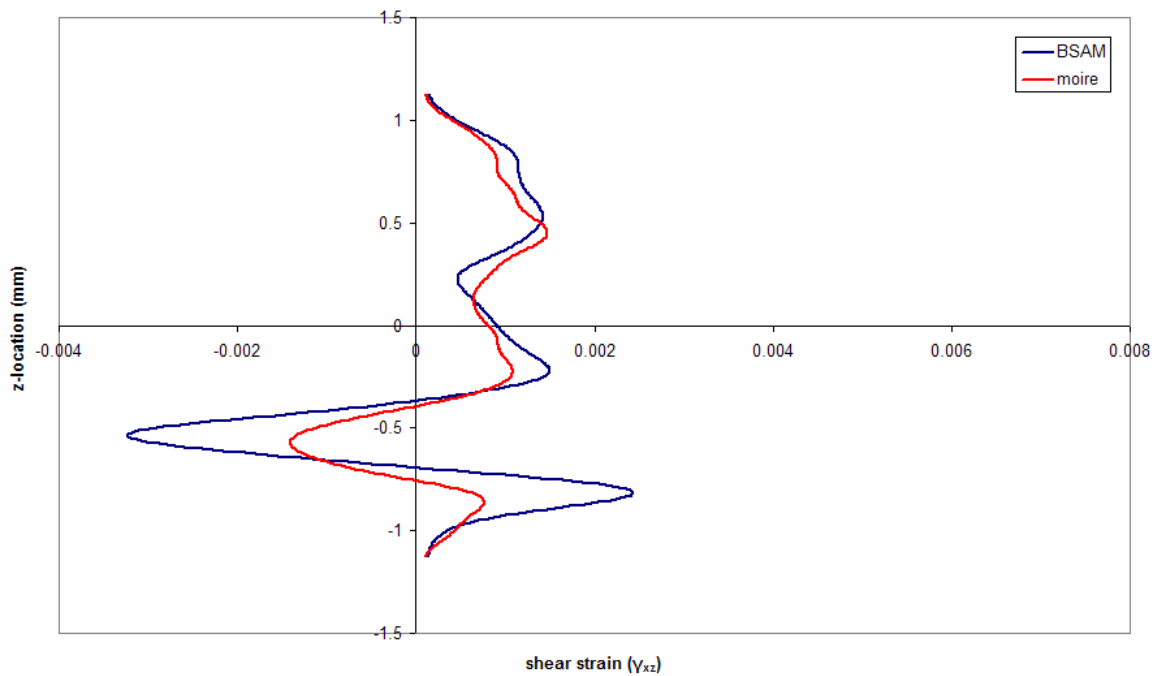


Figure 282. Stepped-lap Joint: shear strain (γ_{xz}) through thickness (z) at $x = 10\text{mm}$
(data smoothed 250 times)

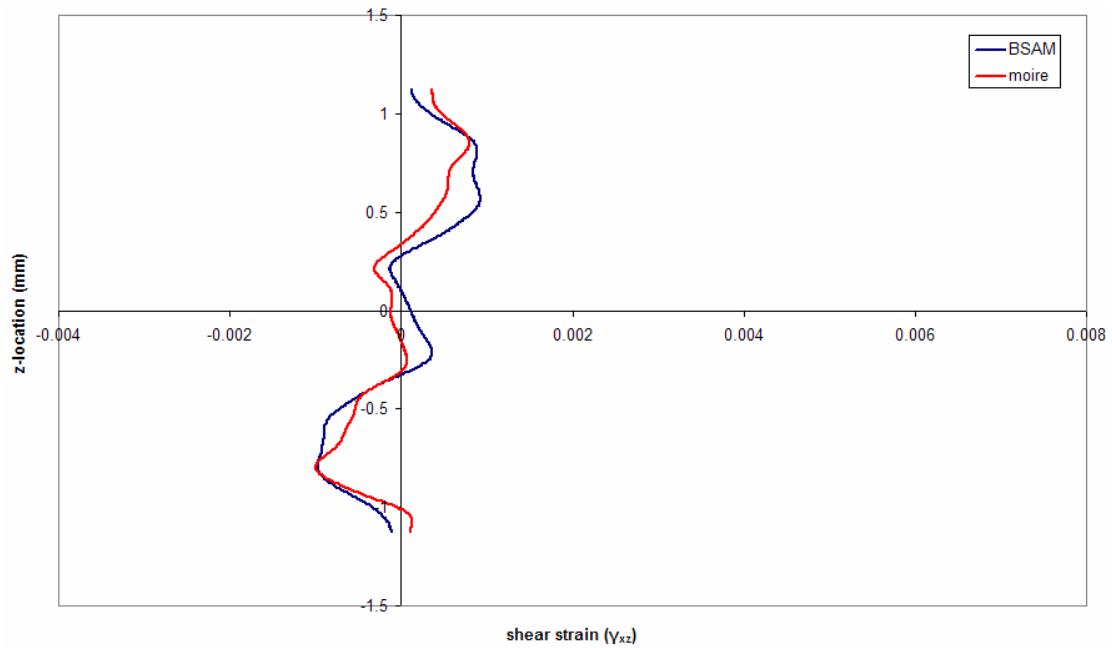


Figure 283. Stepped-lap Joint: shear strain (γ_{xz}) through thickness (z) at x = 15mm
(data smoothed 250 times)

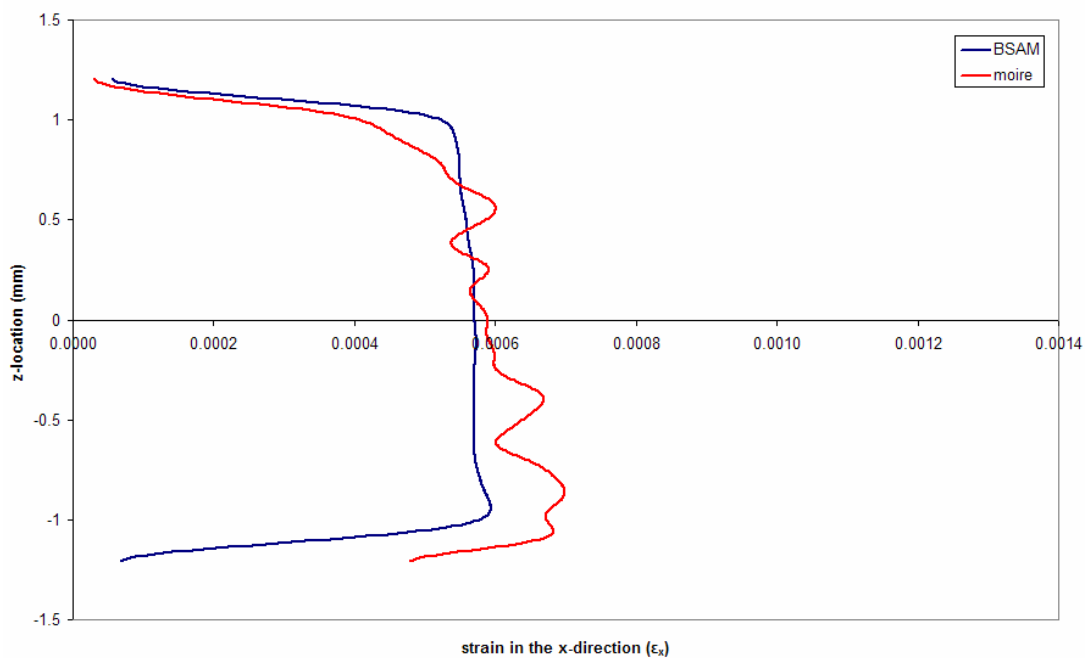


Figure 284. Scarf Joint: strain (ϵ_x) through thickness (z) at x = -15mm
(data smoothed 250 times)

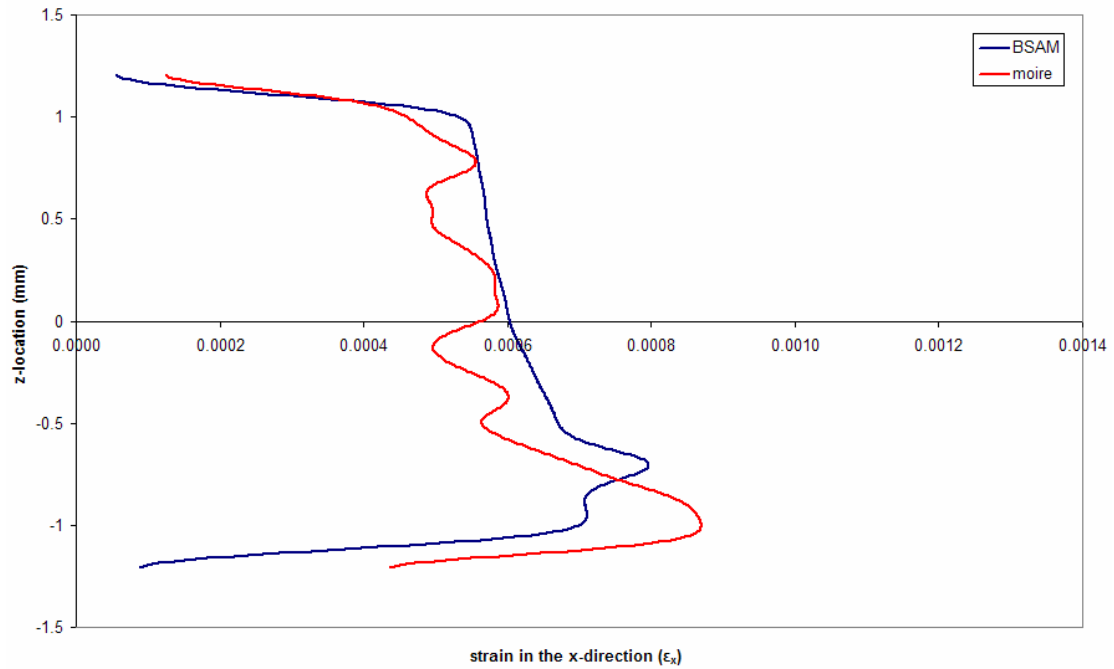


Figure 285. Scarf Joint: strain (ϵ_x) through thickness (z) at $x = -10.3\text{mm}$

(data smoothed 250 times)

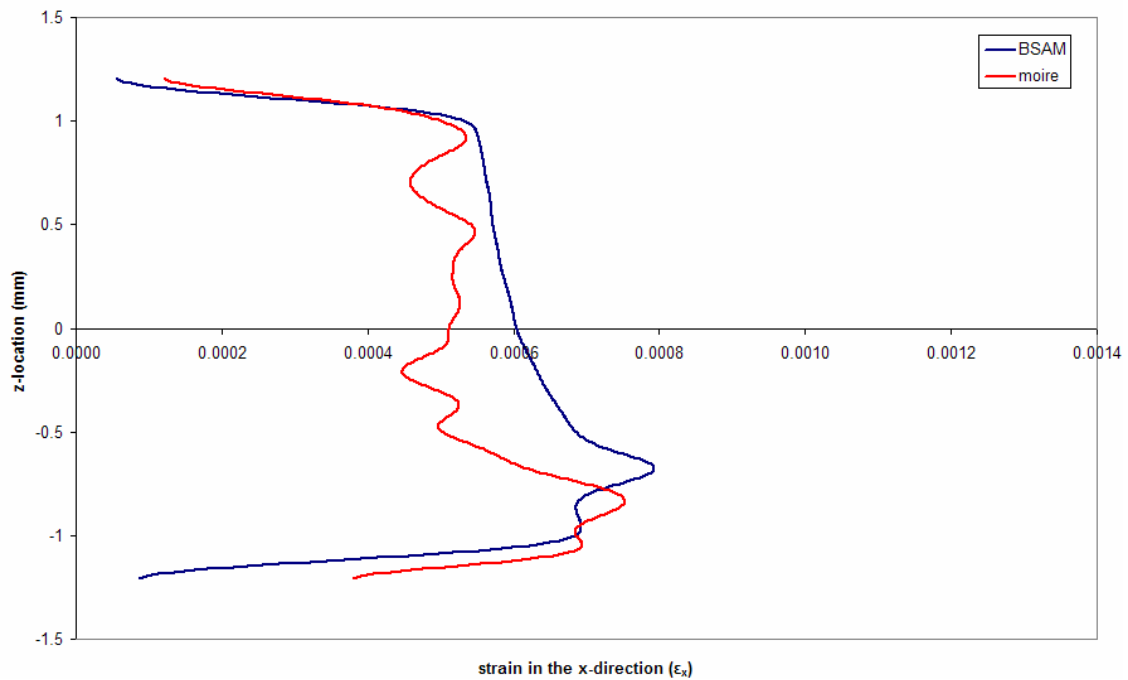


Figure 286. Scarf Joint: strain (ϵ_x) through thickness (z) at $x = -10\text{mm}$

(data smoothed 250 times)

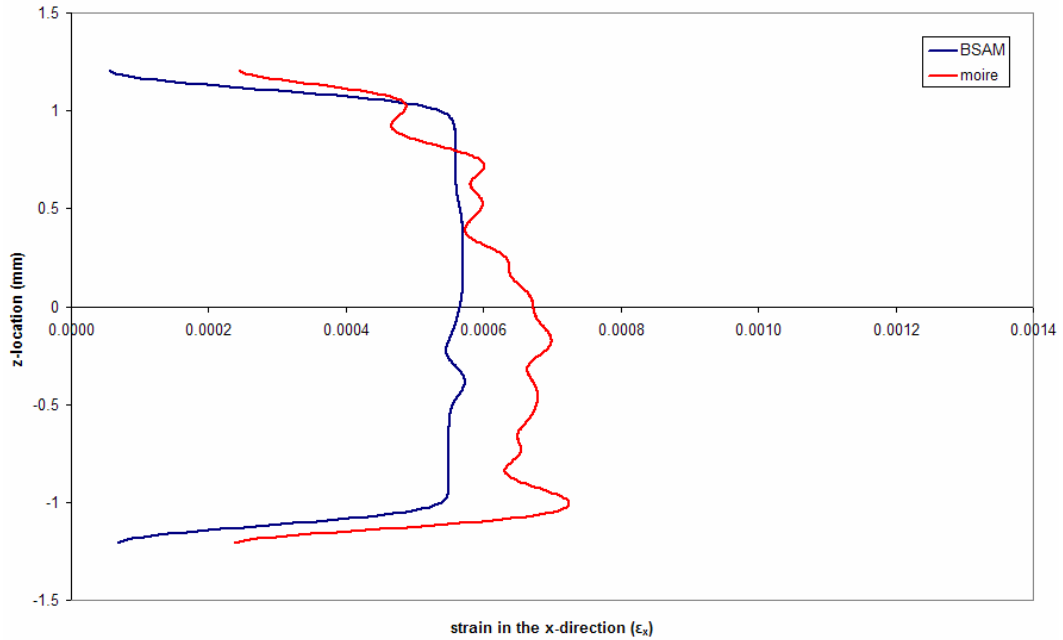


Figure 287. Scarf Joint: strain (ϵ_x) through thickness (z) at $x = -5\text{mm}$
(data smoothed 250 times)

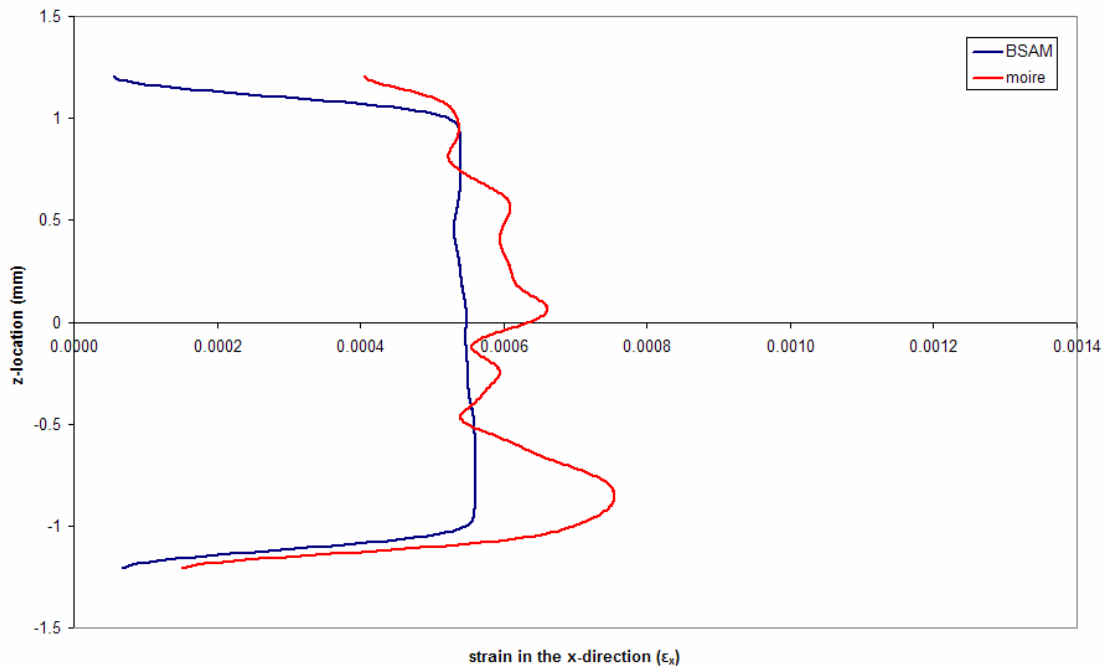


Figure 288. Scarf Joint: strain (ϵ_x) through thickness (z) at $x = 0\text{mm}$
(data smoothed 250 times)

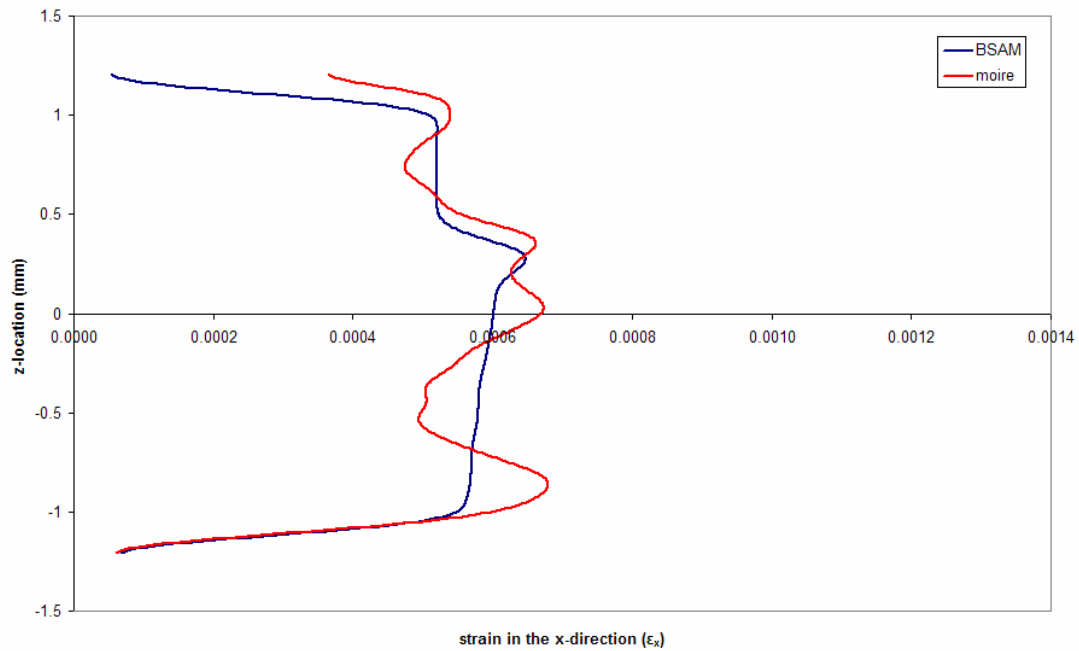


Figure 289. Scarf Joint: strain (ϵ_x) through thickness (z) at $x = 5\text{mm}$

(data smoothed 250 times)

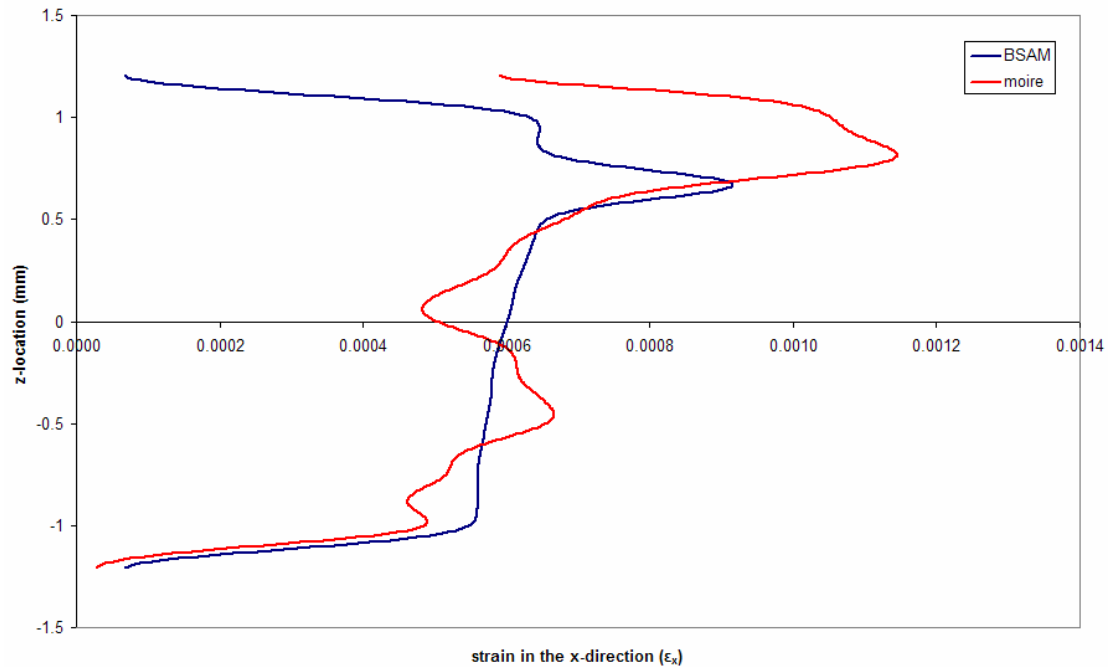


Figure 290. Scarf Joint: strain (ϵ_x) through thickness (z) at $x = 10\text{mm}$

(data smoothed 250 times)

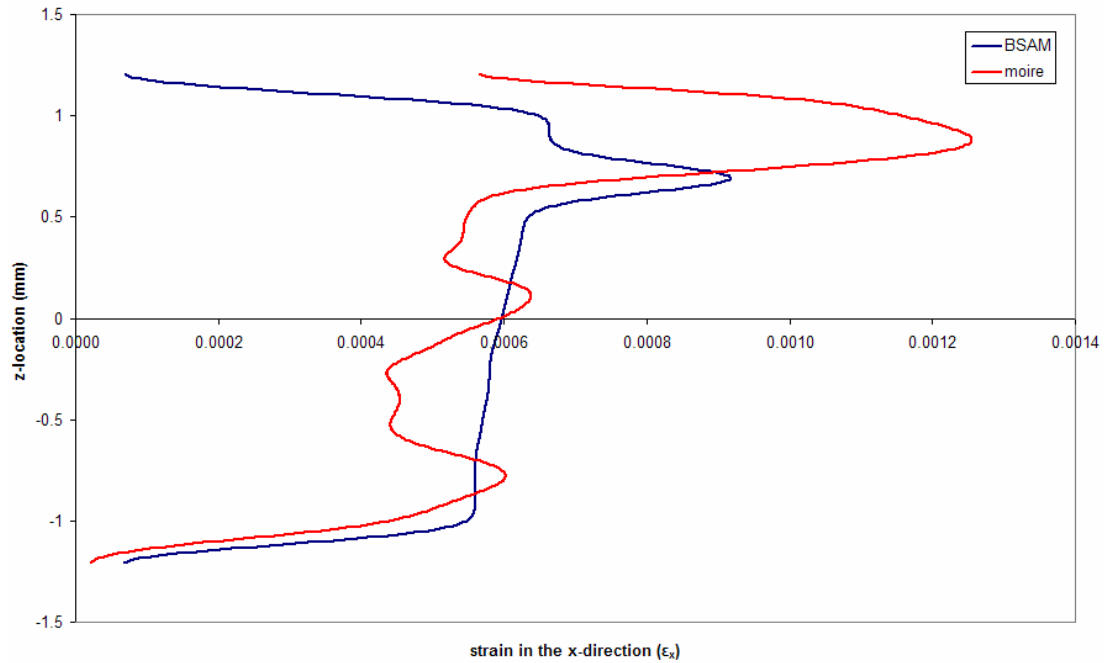


Figure 291. Scarf Joint: strain (ϵ_x) through thickness (z) at $x = 10.3\text{mm}$
(data smoothed 250 times)

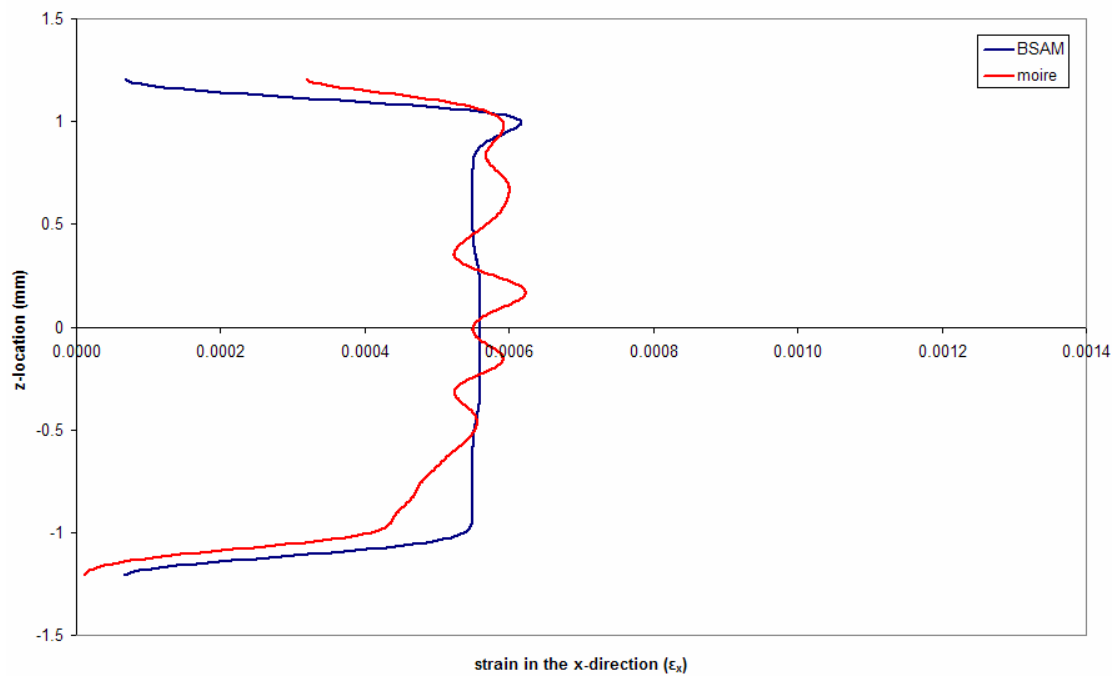


Figure 292. Scarf Joint: strain (ϵ_x) through thickness (z) at $x = 15\text{mm}$
(data smoothed 250 times)

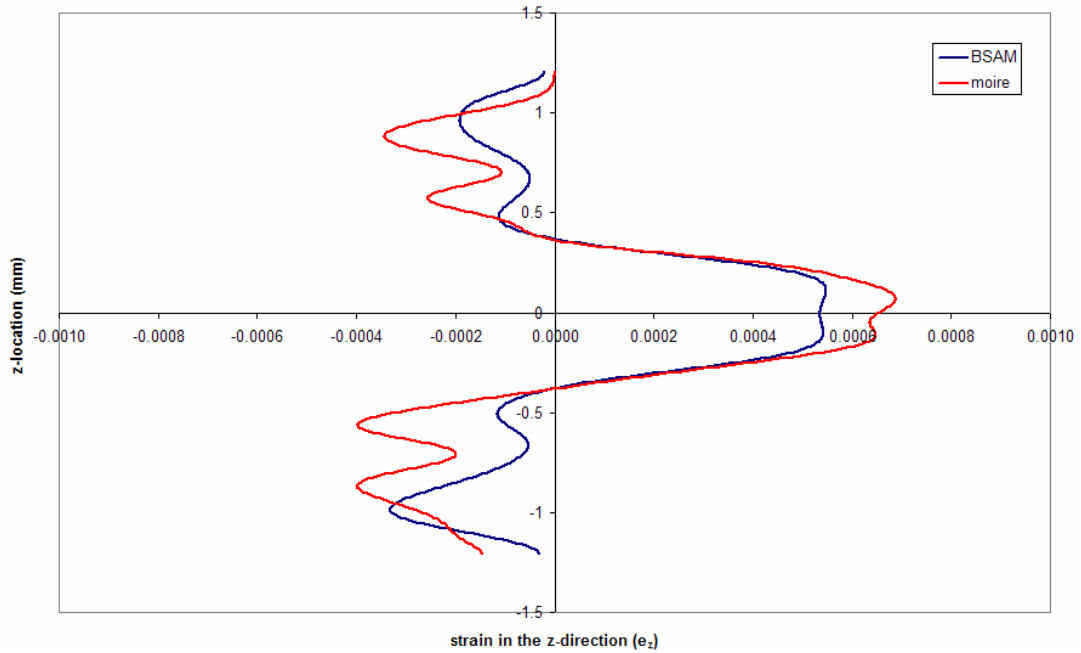


Figure 293. Scarf Joint: strain (ϵ_z) through thickness (z) at $x = -15\text{mm}$
(data smoothed 250 times)

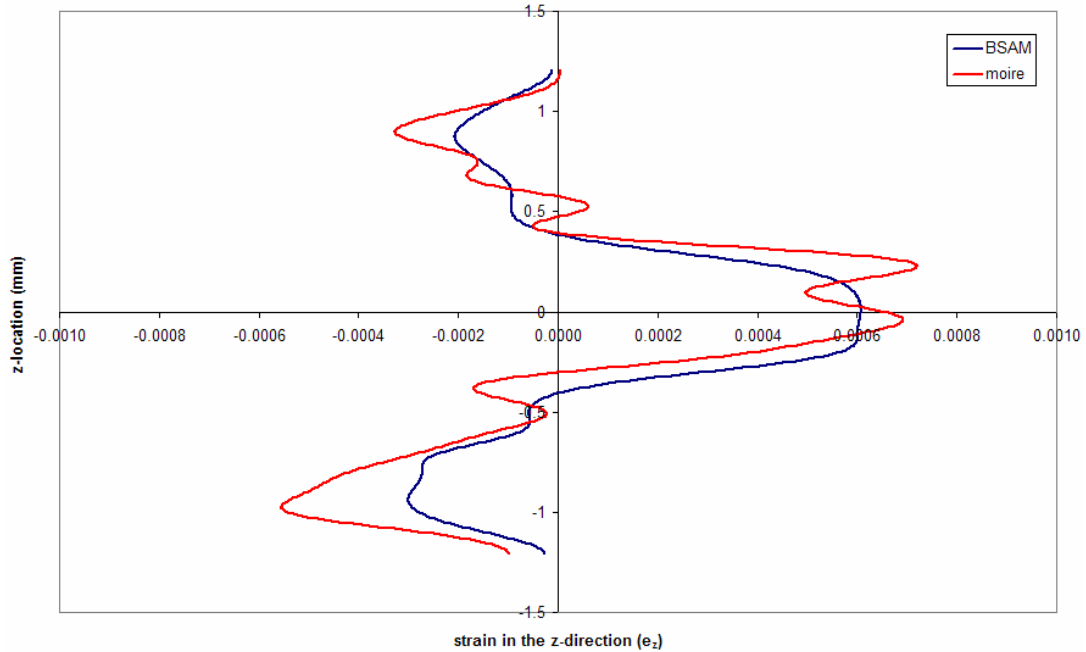


Figure 294. Scarf Joint: strain (ϵ_z) through thickness (z) at $x = -10.3\text{mm}$
(data smoothed 250 times)

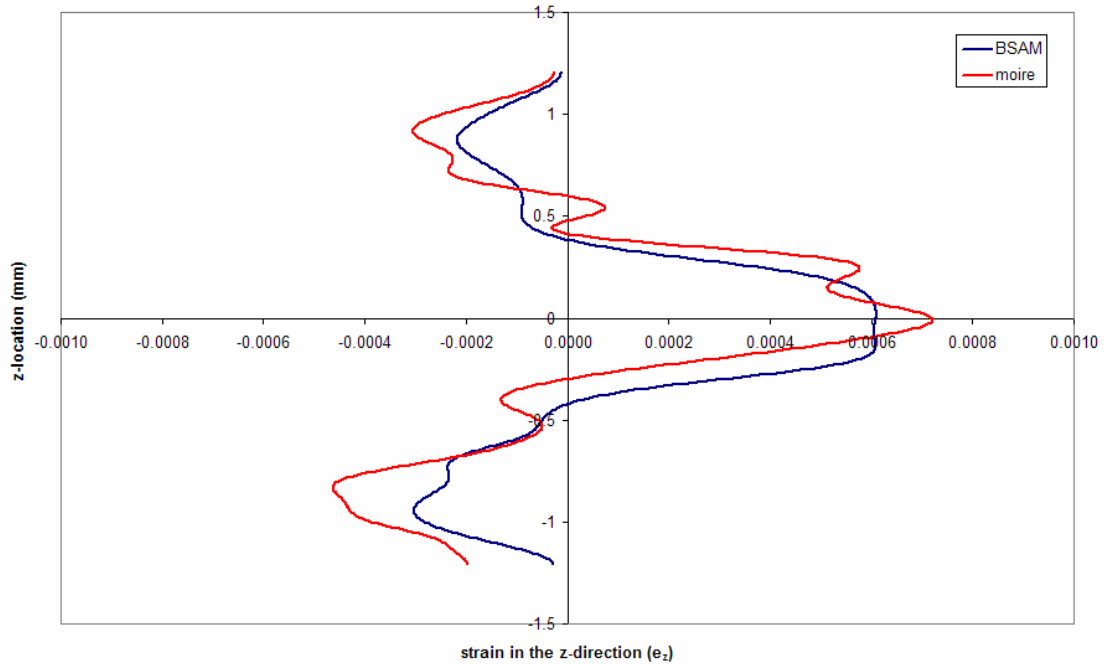


Figure 295. Scarf Joint: strain (ϵ_z) through thickness (z) at $x = -10\text{mm}$
(data smoothed 250 times)

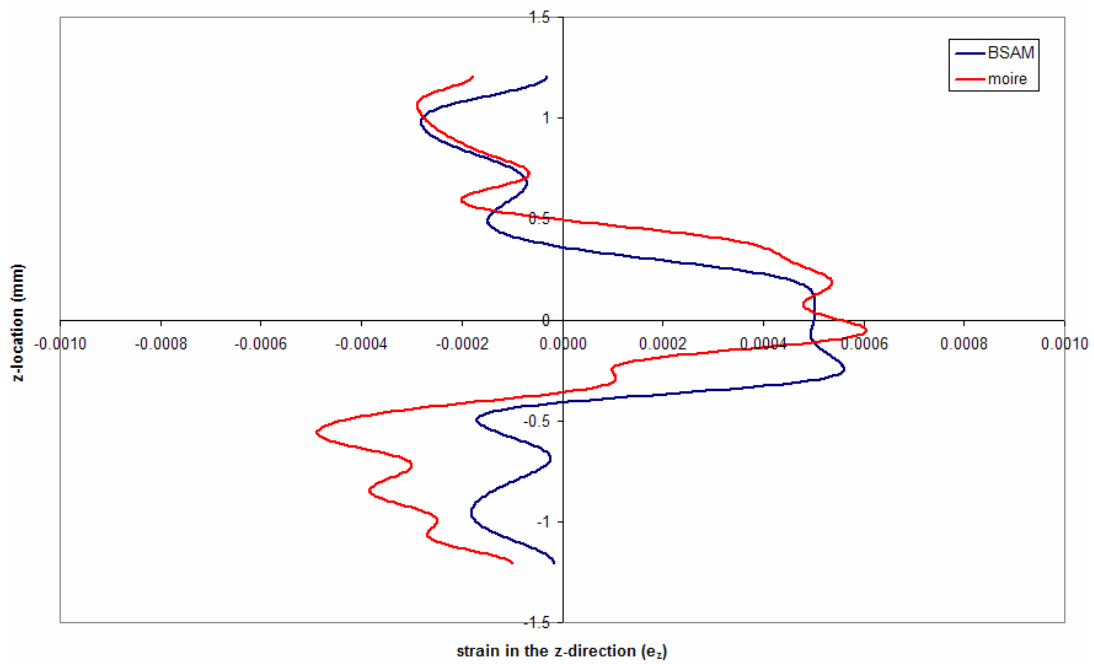


Figure 296. Scarf Joint: strain (ϵ_z) through thickness (z) at $x = -5\text{mm}$
(data smoothed 250 times)

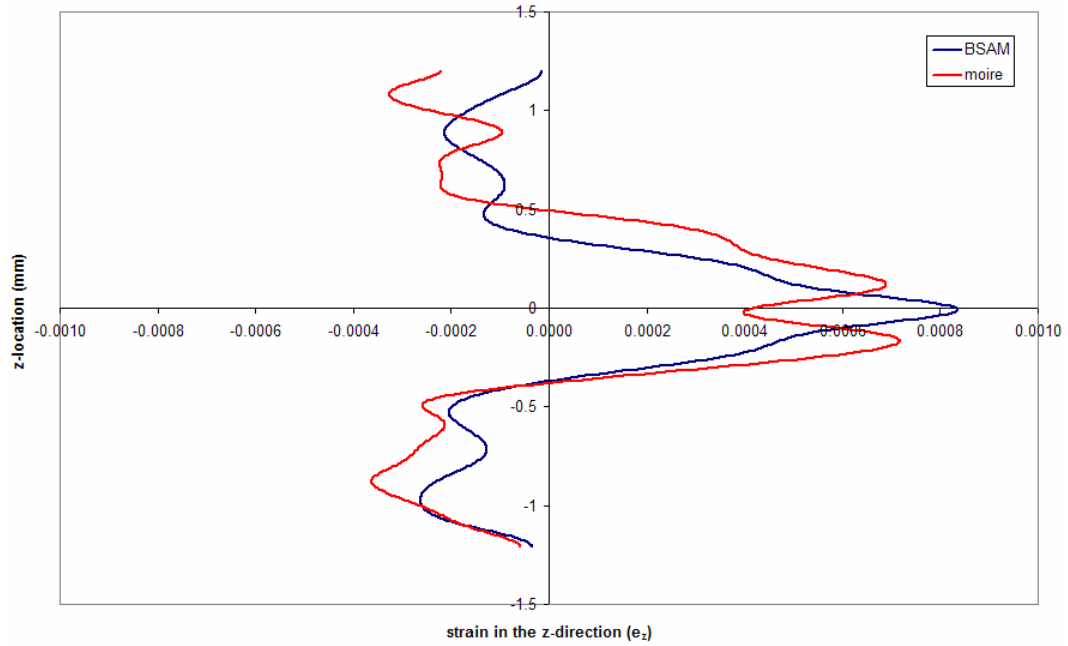


Figure 297. Scarf Joint: strain (ϵ_z) through thickness (z) at x = 0mm
(data smoothed 250 times)

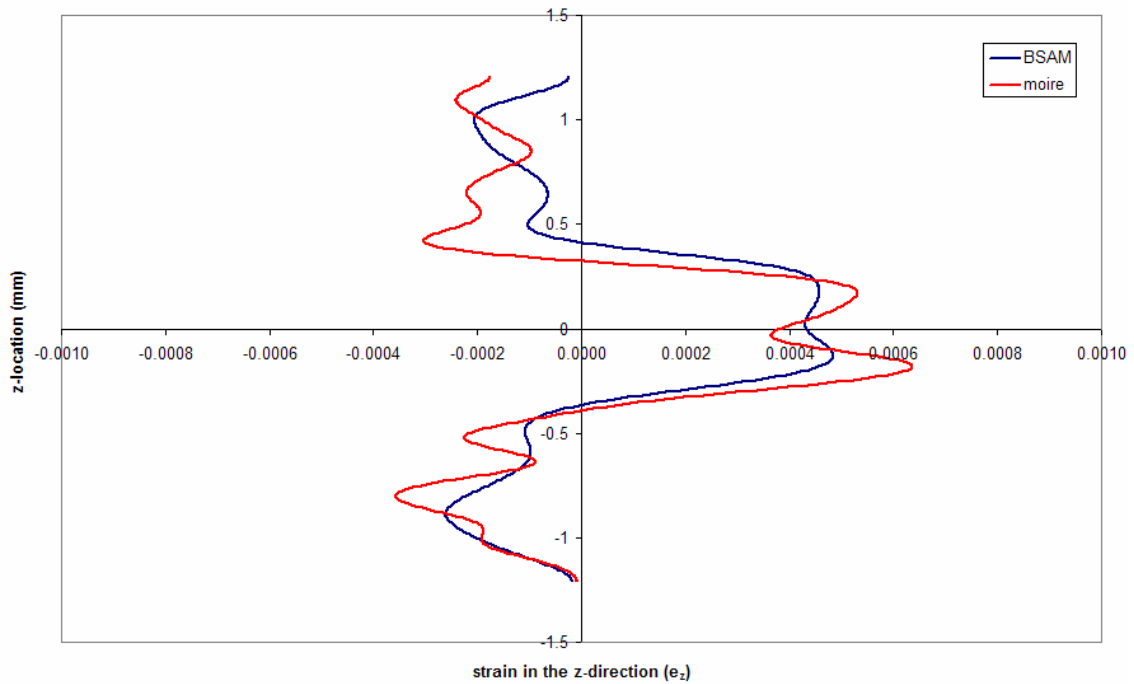


Figure 298. Scarf Joint: strain (ϵ_z) through thickness (z) at x = 5mm
(data smoothed 250 times)

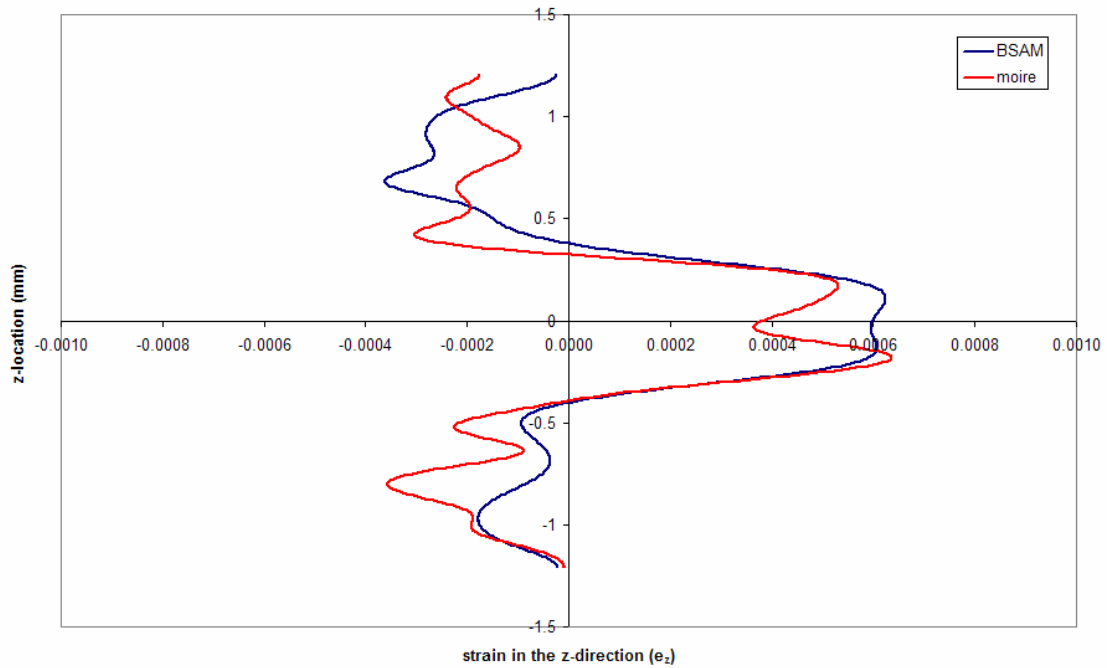


Figure 299. Scarf Joint: strain (ϵ_z) through thickness (z) at $x = 10\text{mm}$

(data smoothed 250 times)

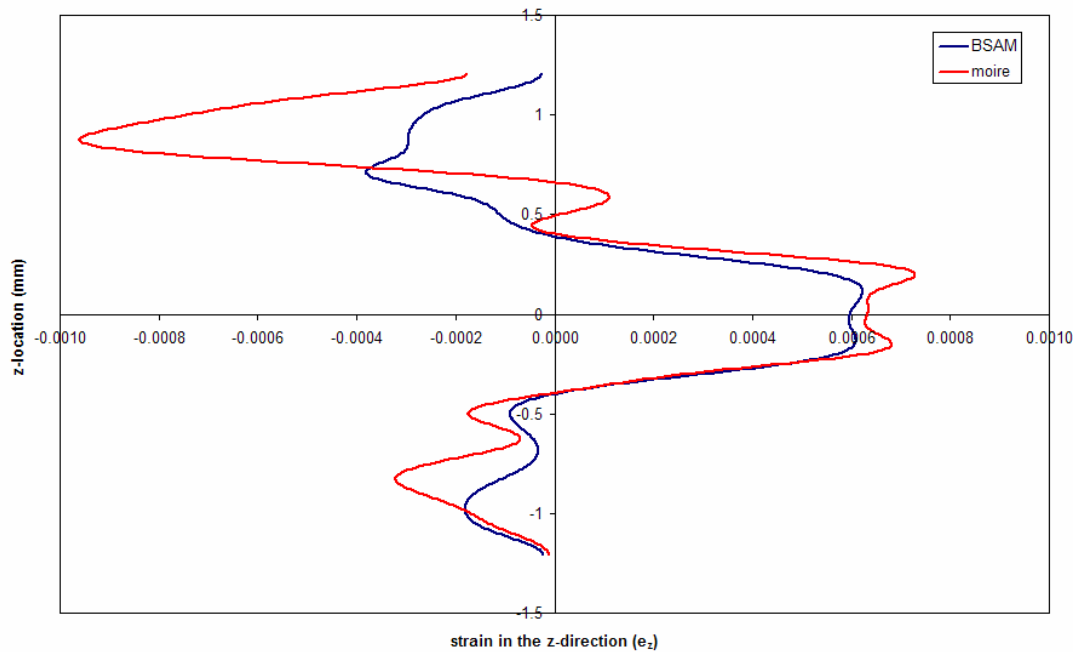


Figure 300. Scarf Joint: strain (ϵ_z) through thickness (z) at $x = 10.3\text{mm}$

(data smoothed 250 times)

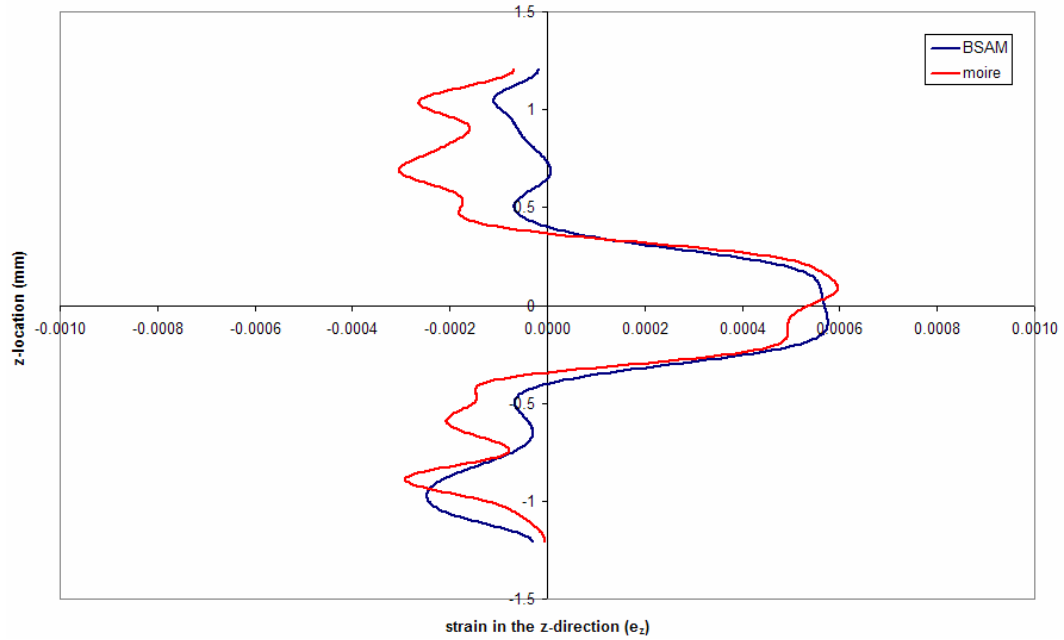


Figure 301. Scarf Joint: strain (ϵ_z) through thickness (z) at $x = 15\text{mm}$
(data smoothed 250 times)

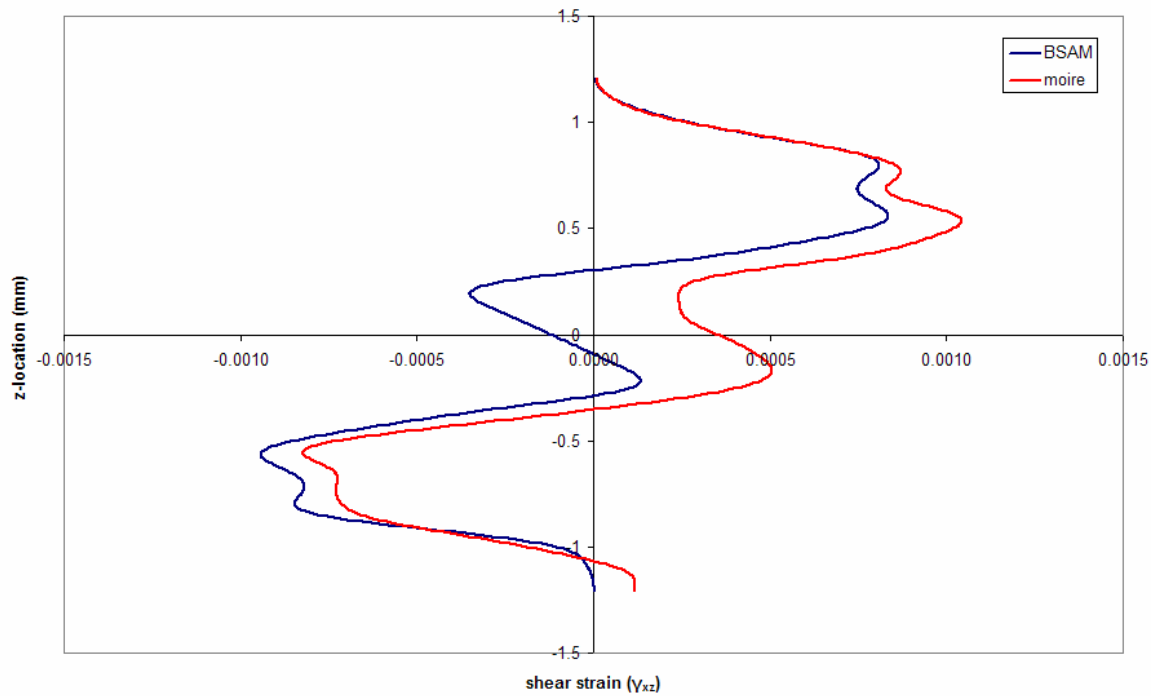


Figure 302. Scarf Joint: shear strain (γ_{xz}) through thickness (z) at $x = -15\text{mm}$
(data smoothed 250 times)

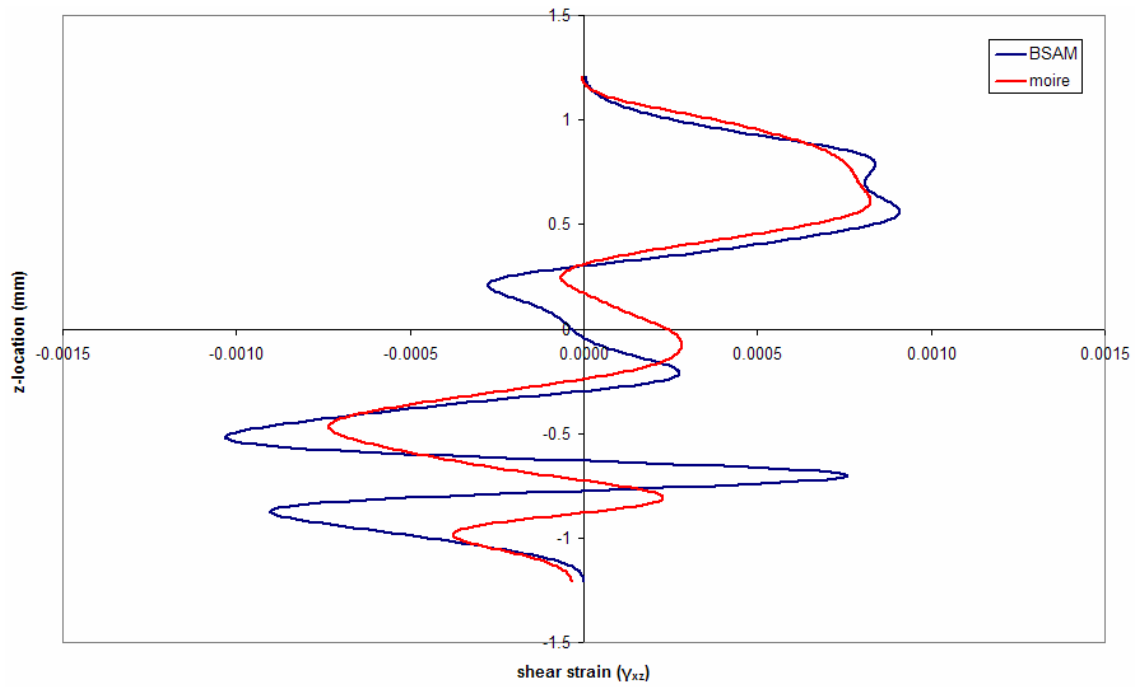


Figure 303. Scarf Joint: shear strain (γ_{xz}) through thickness (z) at $x = -10.3\text{mm}$
(data smoothed 250 times)

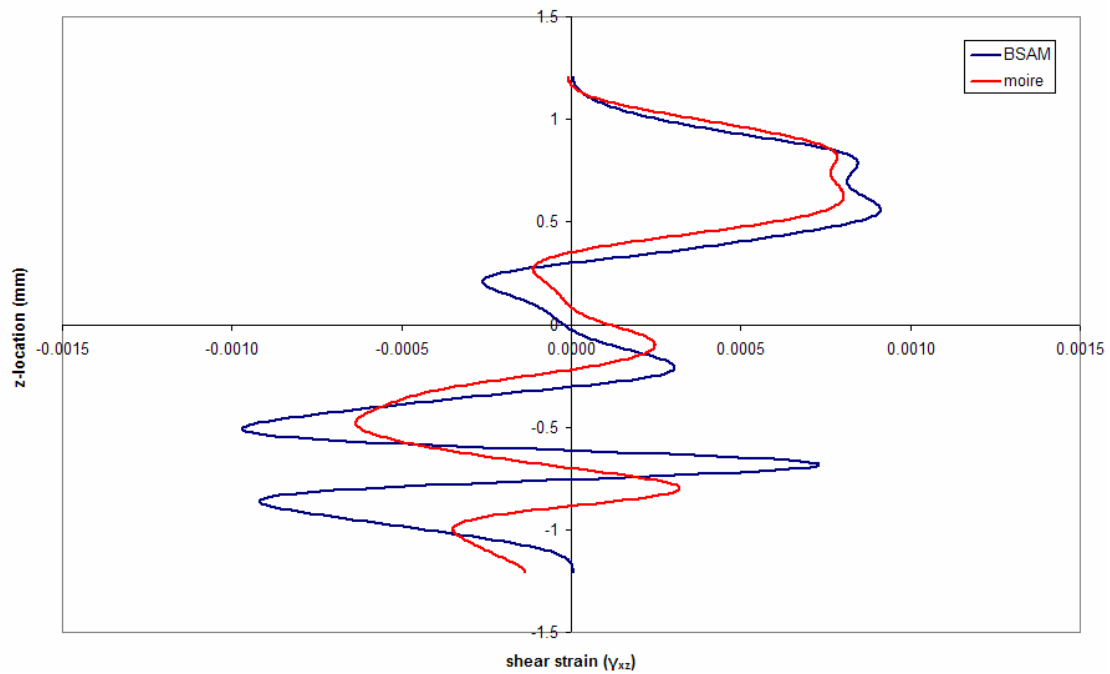


Figure 304. Scarf Joint: shear strain (γ_{xz}) through thickness (z) at $x = -10\text{mm}$
(data smoothed 250 times)

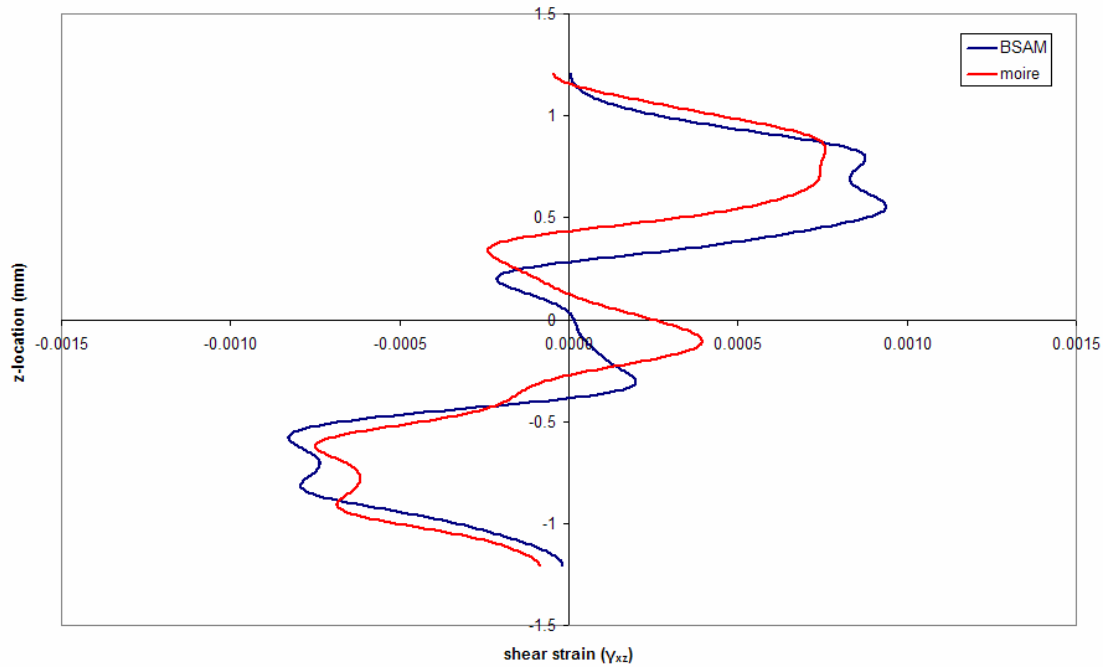


Figure 305. Scarf Joint: shear strain (γ_{xz}) through thickness (z) at $x = -5\text{mm}$
(data smoothed 250 times)

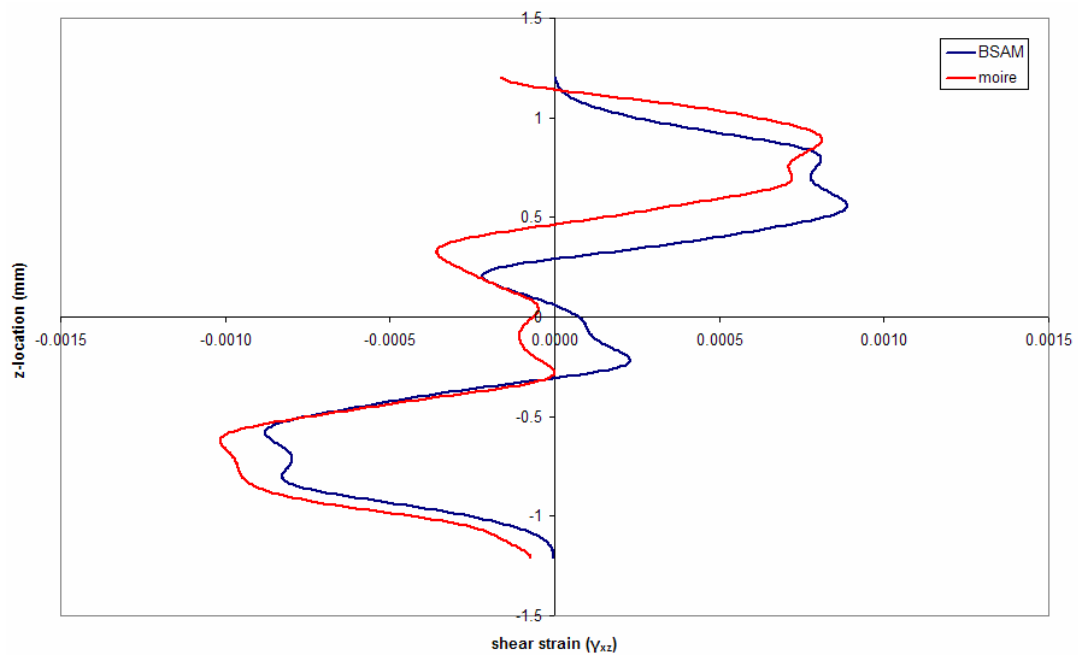


Figure 306. Scarf Joint: shear strain (γ_{xz}) through thickness (z) at $x = 0\text{mm}$
(data smoothed 250 times)

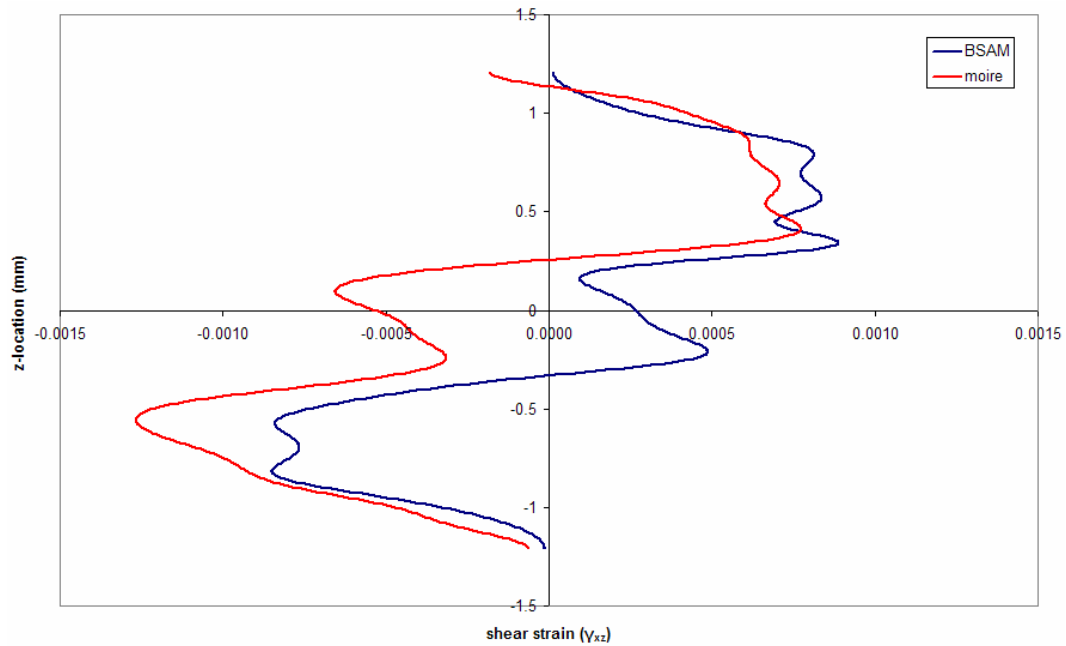


Figure 307. Scarf Joint: shear strain (γ_{xz}) through thickness (z) at $x = 5\text{mm}$
(data smoothed 250 times)

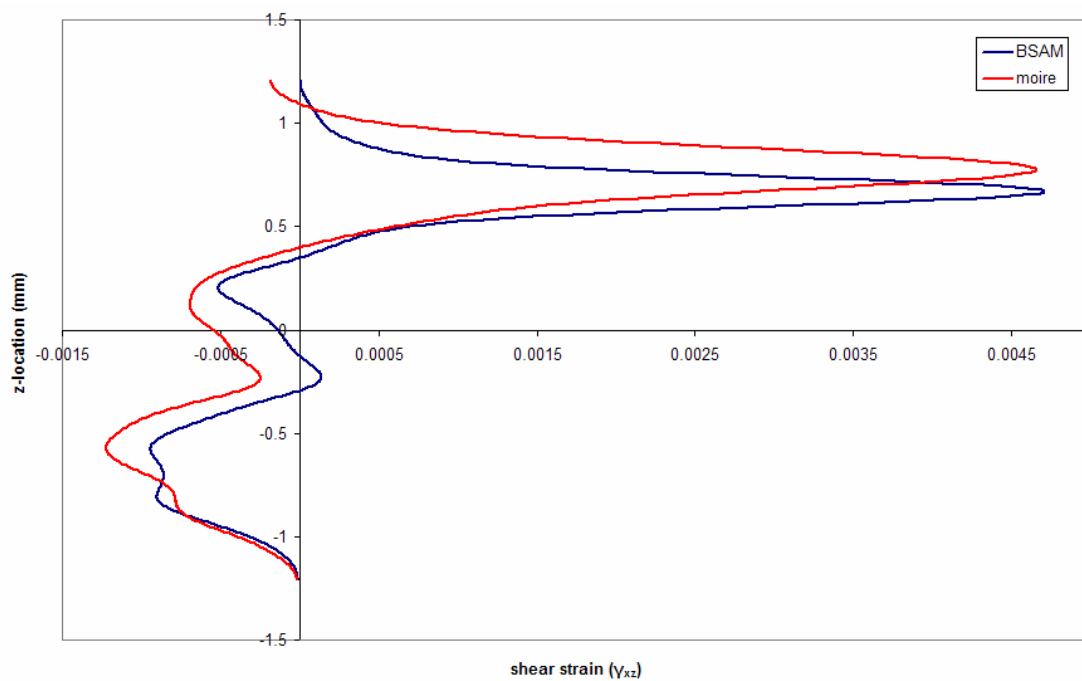


Figure 308. Scarf Joint: shear strain (γ_{xz}) through thickness (z) at $x = 10\text{mm}$
(data smoothed 250 times)

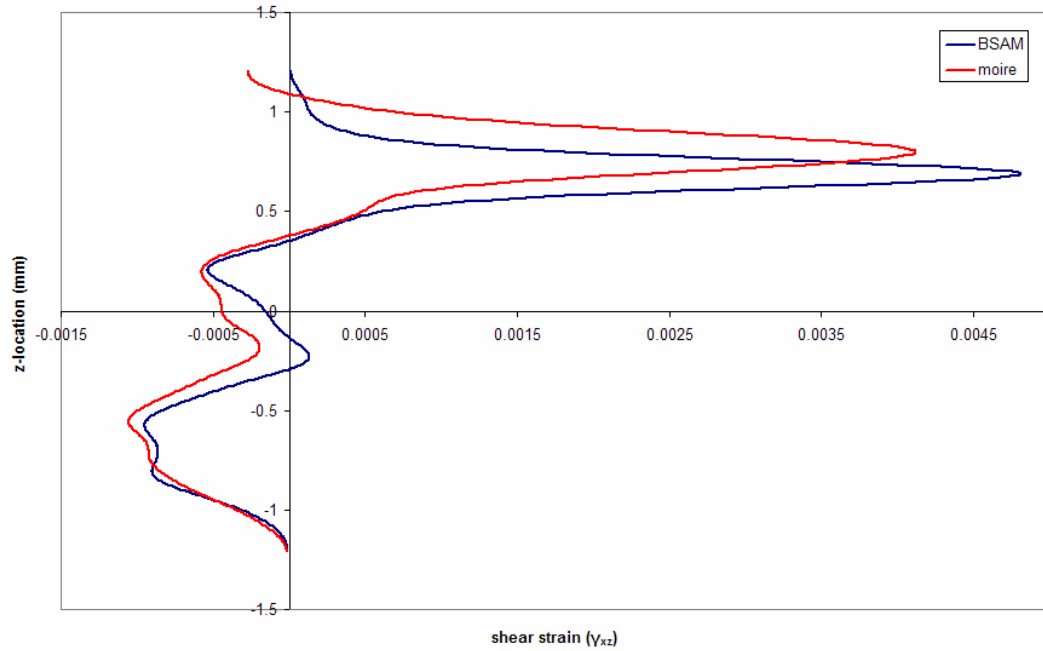


Figure 309. Scarf Joint: shear strain (γ_{xz}) through thickness (z) at $x = 10.3\text{mm}$
(data smoothed 250 times)

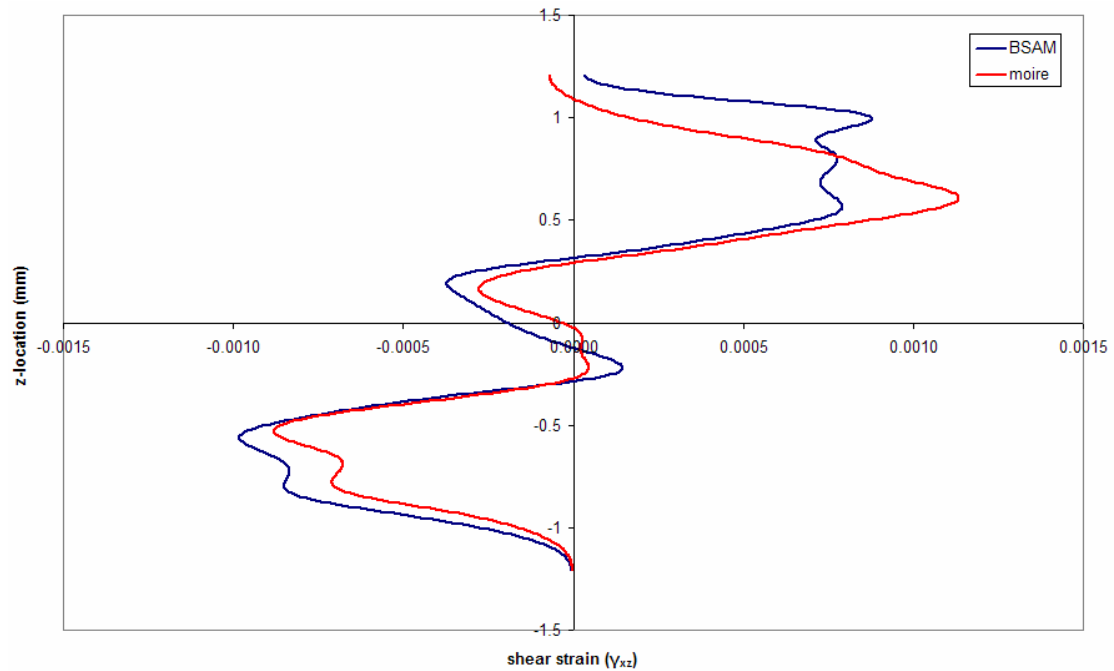
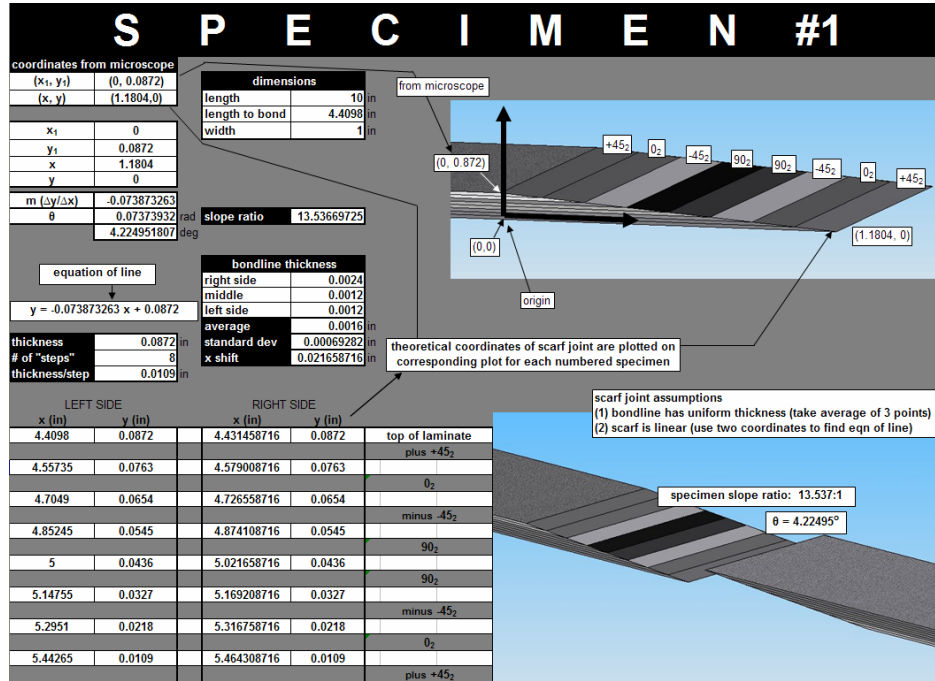


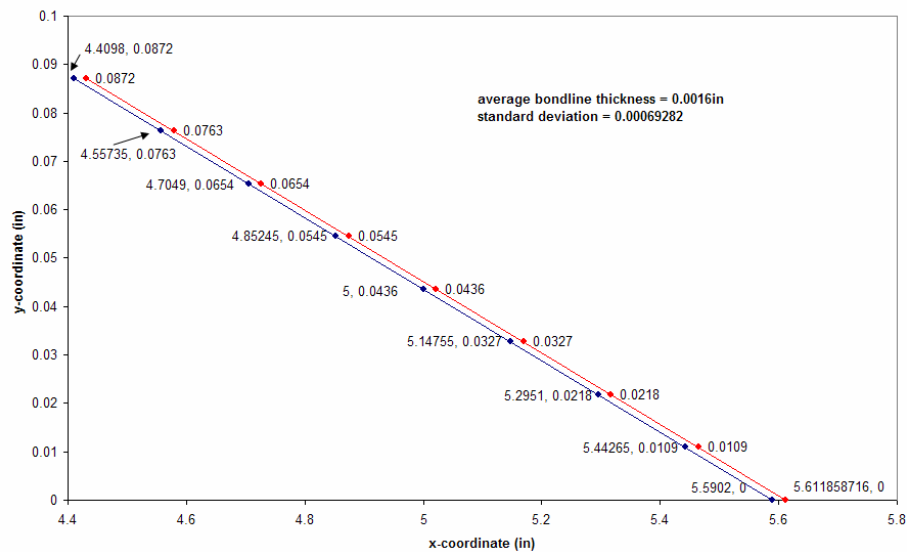
Figure 310. Scarf Joint: shear strain (γ_{xz}) through thickness (z) at $x = 15\text{mm}$
(data smoothed 250 times)

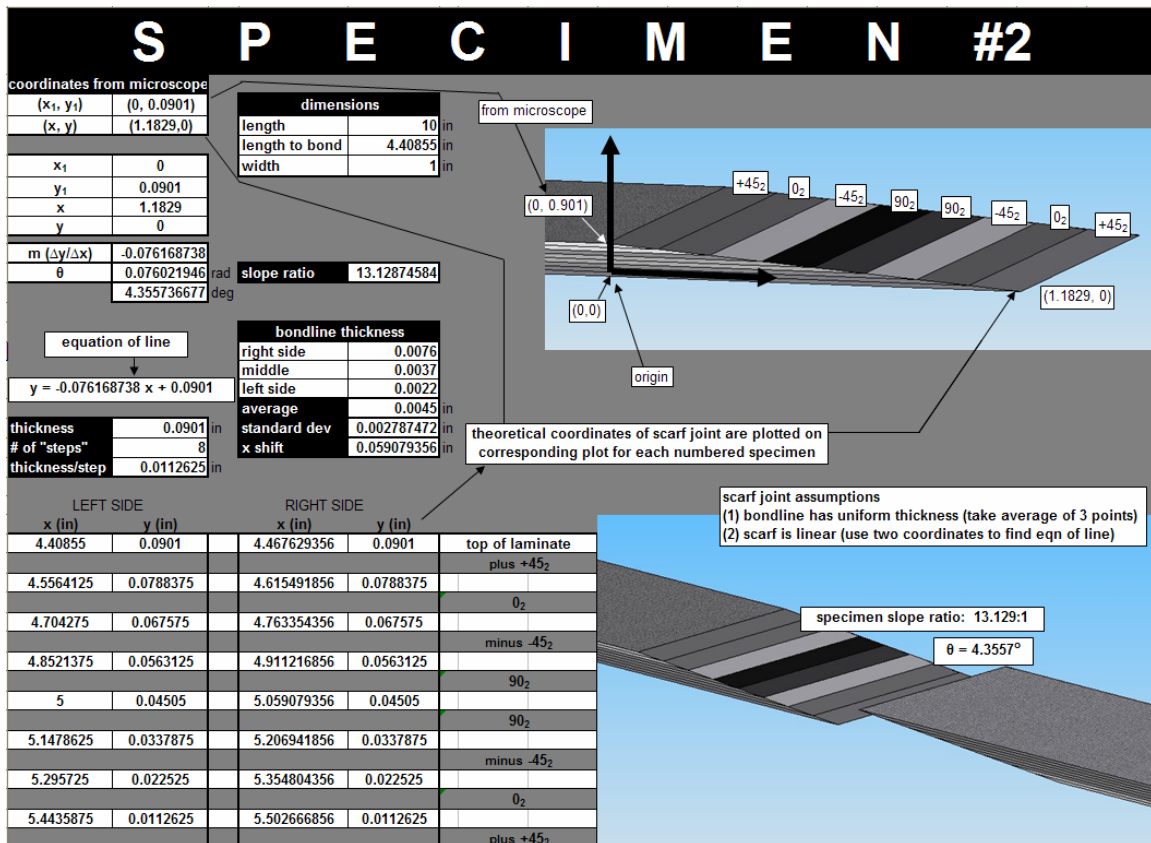
Appendix F: Idealization of scarf specimens

This appendix illustrates the process used in finding the idealized coordinates to model the scarf specimens. All dimensions were found using a microscope with (+/-) 0.0001in accuracy. Experimental scarf joint results were found using the dimensions and coordinates of Specimen #4.

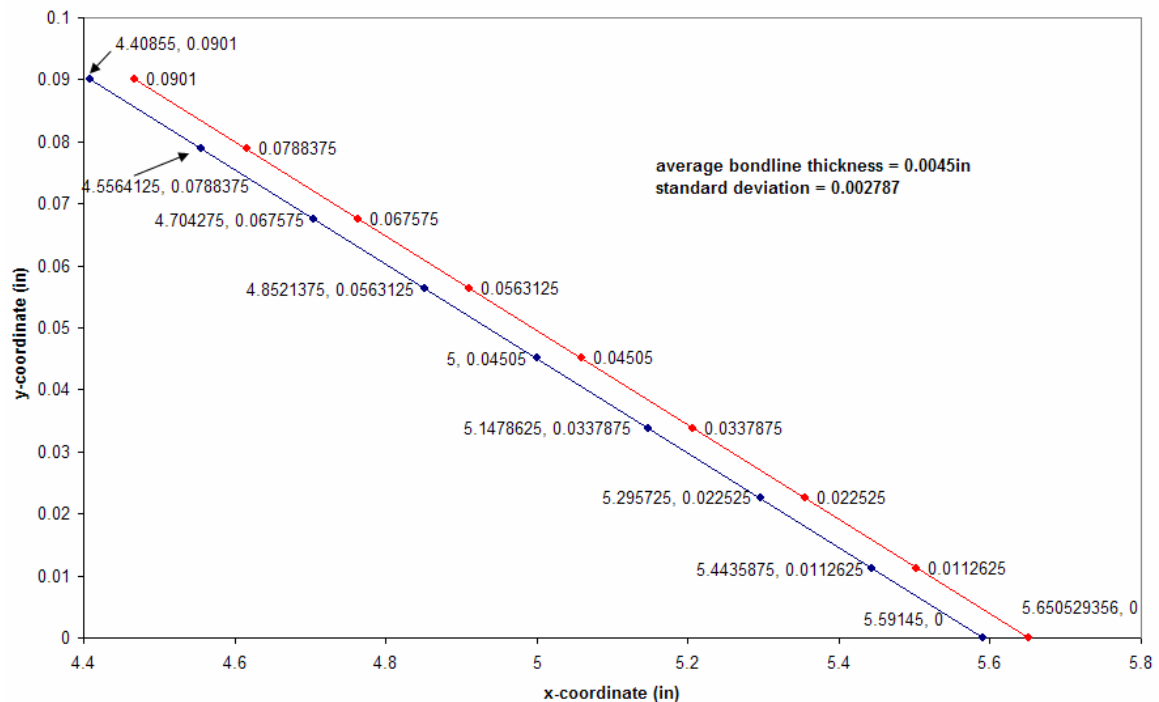


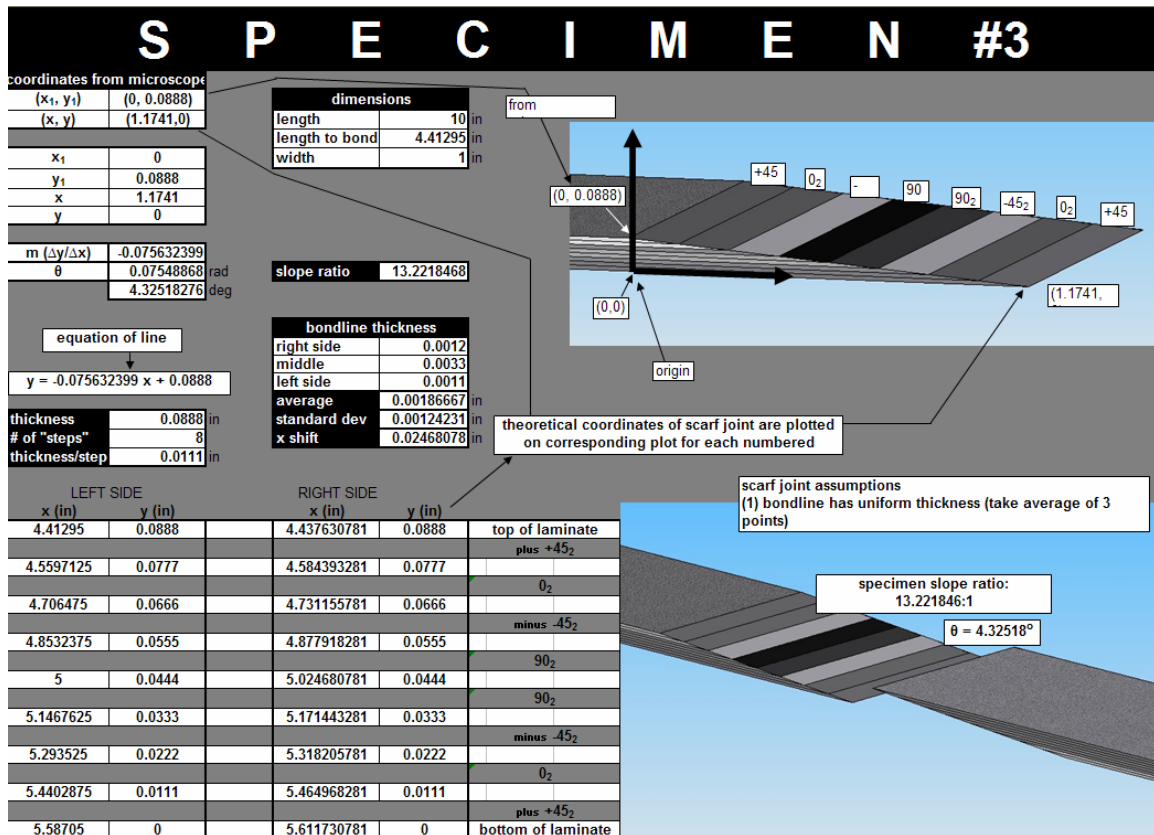
Idealized Scarf Coordinates (Specimen #1)



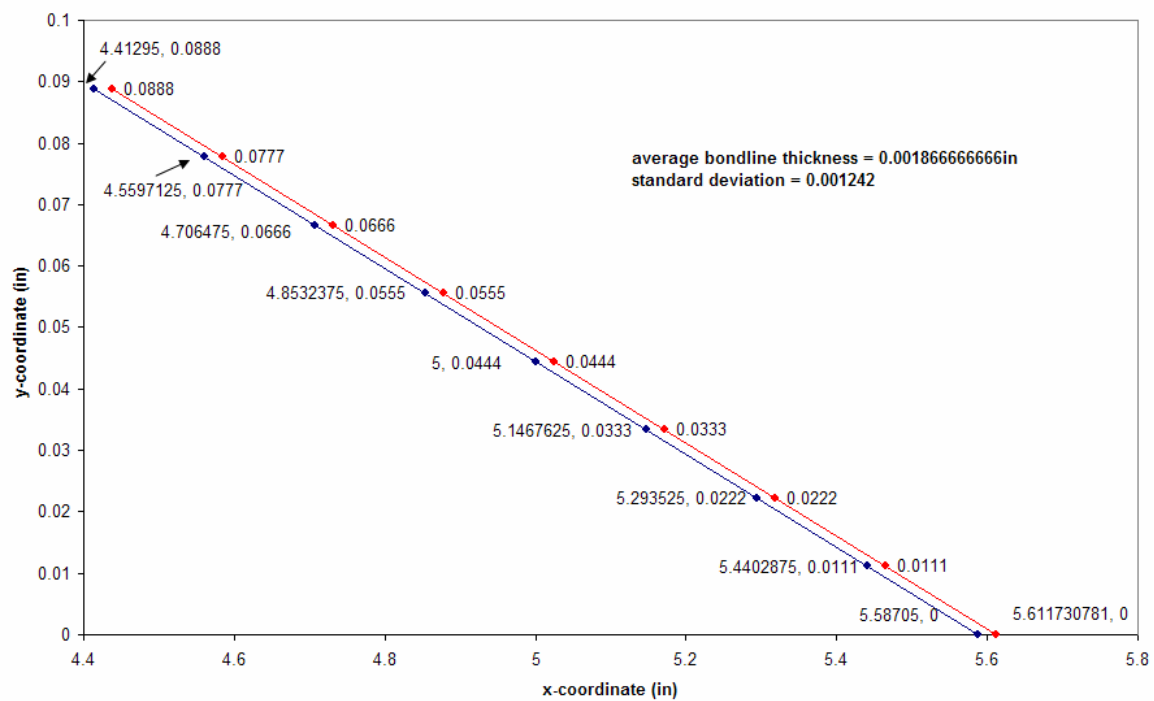


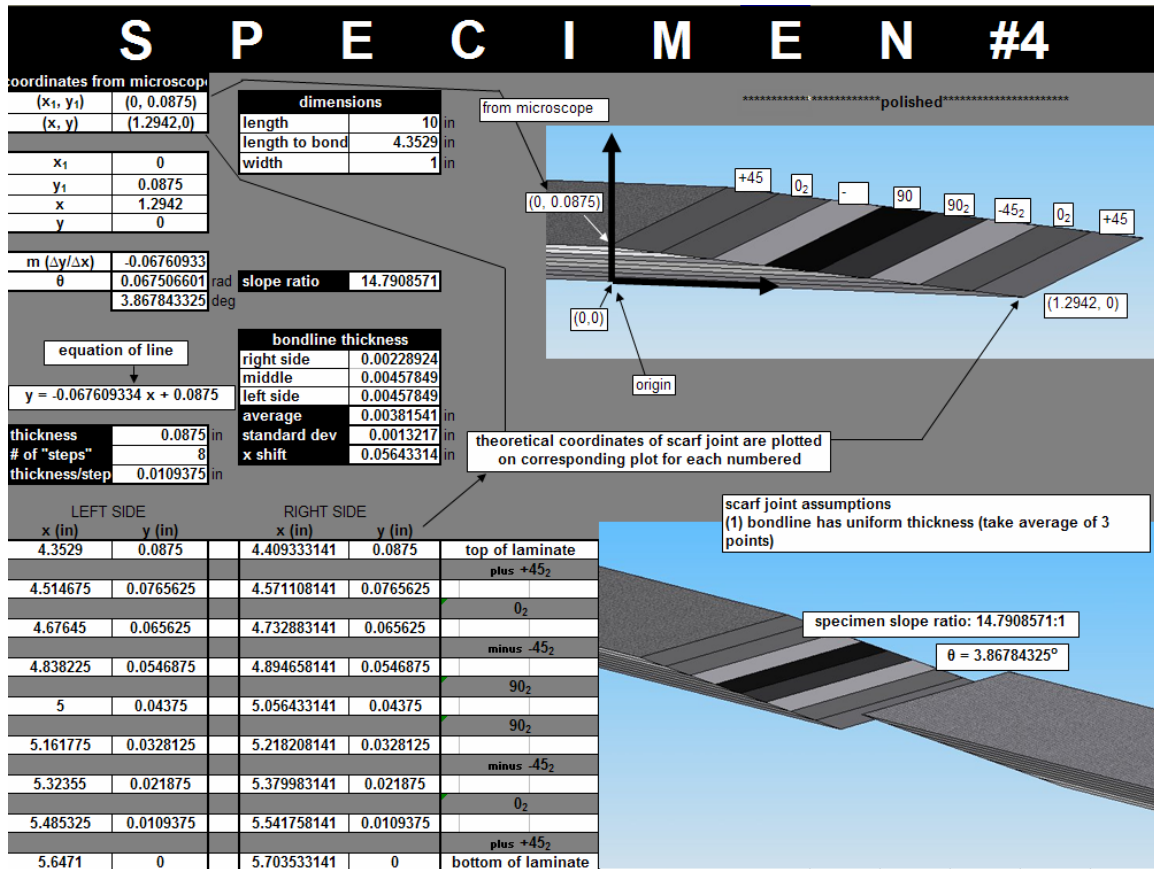
Idealized Scarf Coordinates (Specimen #2)



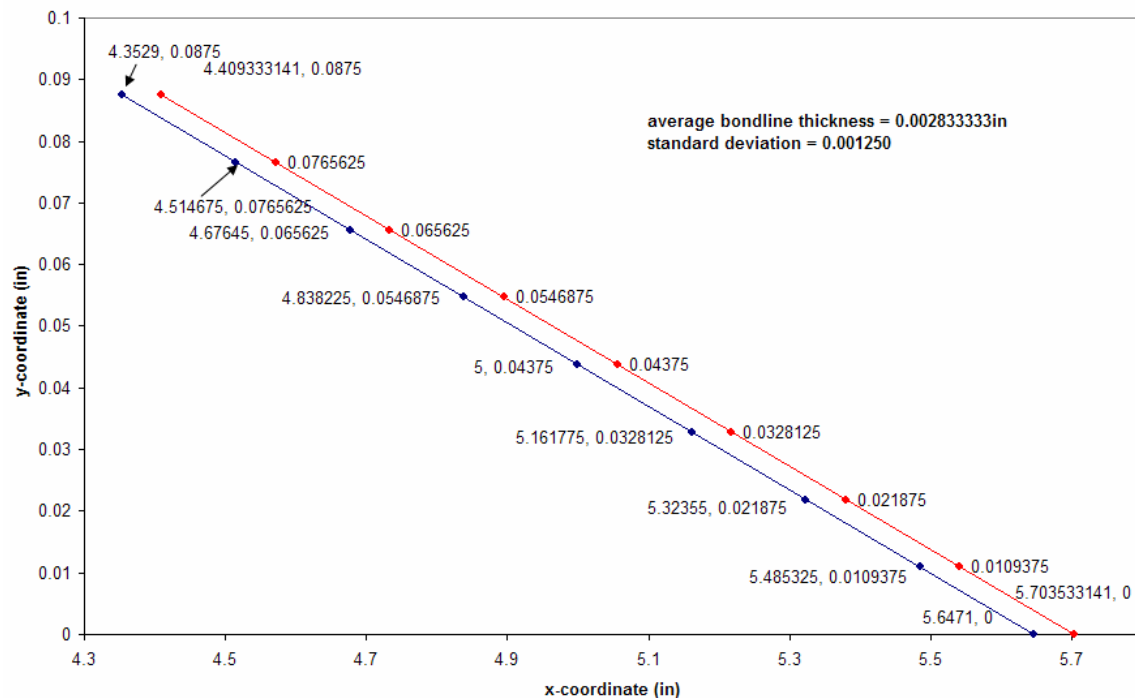


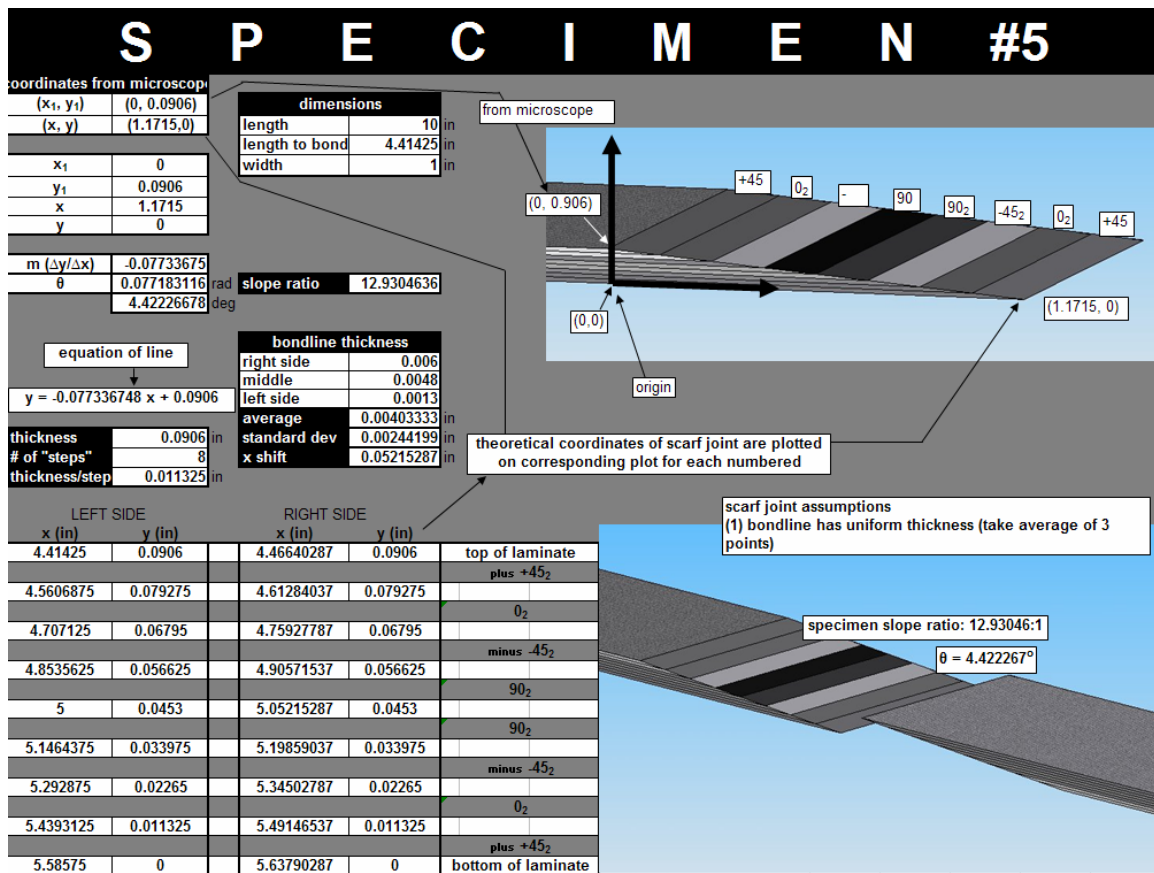
Idealized Scarf Coordinates (Specimen #3)



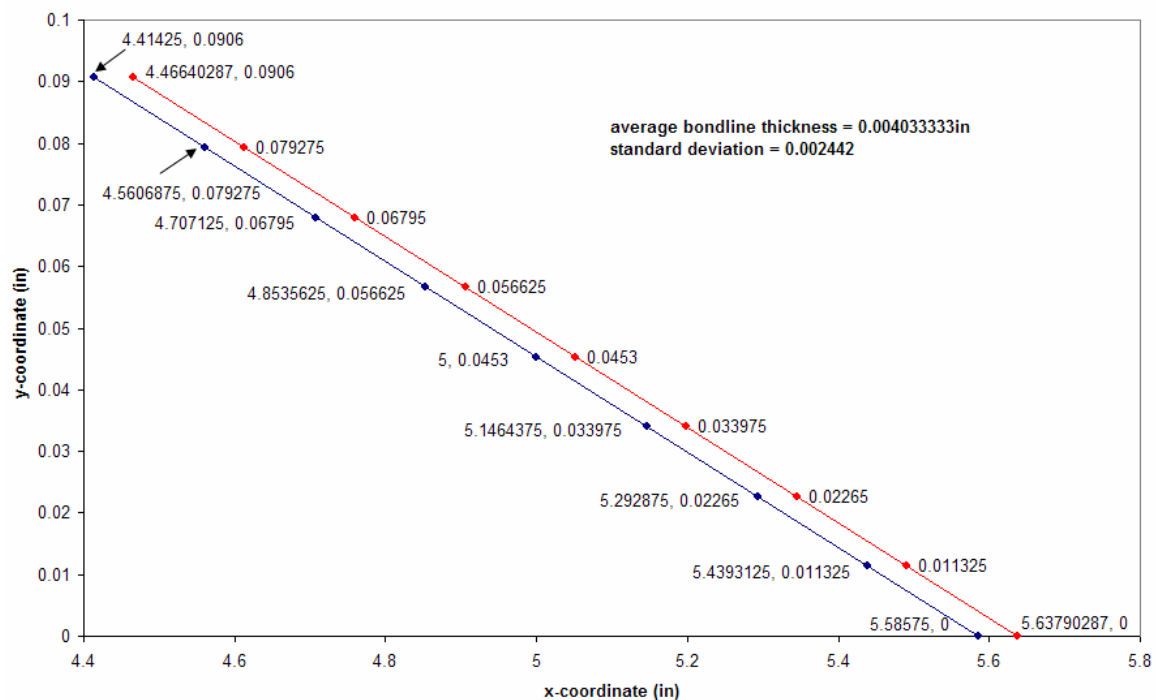


Idealized Scarf Coordinates (Specimen #4)





Idealized Scarf Coordinates (Specimen #5)



Bibliography

- Abdel Wahab, M.M, I.A. Ashcroft, A.D. Crocombe, P.A. Smith. "Finite element prediction of fatigue crack propagation lifetime in composite bonded joints." *Composites: Part A*, 35:213-222 (2004).
- Abdel Wahab, M.M, I.A. Ashcroft, A.D. Crocombe, D.J. Hughes, and S.J Shaw. "The effect of environment on the fatigue of bonded composite joints. Part 2: Fatigue Threshold Prediction", *Composites: Part A*, 32:59-69 (2000).
- Applications of Composites*. Composite Materials: Unit III. Rai University.
<http://rcw.raifoundation.org/mechanical/BTec-Mec/compositematerial/lecture-notes/lecture-17.pdf>.
- Ashcroft, I.A., M.M. Abdel Wahab, A.D. Crocombe, D.J. Hughes and S.J Shaw. "The effect of environment on the fatigue of bonded composite joints. Part 1: Testing and Fractography", *Composites: Part A*, 32:45-58 (2000).
- Baker, Alan, Stuart Dutton, and Donald Kelly. *Composite Materials for Aircraft Structures*. Reston, VA: American Institute of Aeronautics and Astronautics, Inc., 2004.
- Butkus, Lawrence M. Deputy USAF Aircraft Structural Integrity Program Manager, Wright-Patterson AFB, OH. Personal Correspondence. 2 March 2006.
- Post, Daniel, Bongtae Han, and Peter Ifju. *High Sensitivity Moiré: Experimental Analysis for Mechanics and Materials*. New York, NY: Springer-Verlag, 1994.
- Carlos, Mark. "Acoustic Emission: Heeding the Warning Sounds from Materials." ASTM Acoustic Emission Standards. October 2003.
http://www.astm.org/SNEWS/OCTOBER_2003/carlos_oct03.html
- Charalambides, M.N., R. Hardouin, A.J. Kinloch, and F.L Matthews. "Adhesively-bonded Repairs to Fibre-composite Materials I: Experimental", *Composites: Part A*, 29A:1371-1381 (1998).
- Charalambides, M.N., R. Hardouin, A.J. Kinloch, and F.L Matthews. "Adhesively-bonded Repairs to Fibre-composite Materials I: Finite Element Modeling", *Composites: Part A*, 29A:1383-1396 (1998).
- Chotard, T.J, J. Pasquier and M.L. Benzeggagh. "Residual Performance of Scarf Patch-Repaired Pultruded Shapes Initially Impact Damaged", *Composite Structures*, 53: 317-331 (2001).

- Cook, Benjamin. *Modeling and Experimental Measurement of Tensile Loaded Straight Scarf Joint*. MS thesis, AFIT/GA/ENY/05-M03. School of Engineering and Management, Air Force Institute of Technology (AU), Wright-Patterson AFB OH, March 2005.
- Cycom 5215 Modified Epoxy Resin Out-of-Autoclave processing*. Technical Datasheet. Anaheim, CA: Cytec Engineered Materials. 11 June 2002.
<http://www.cytec.com/business/EngineeredMaterials/Datasheets/CYCOM%205215.pdf>
- Department of the Air Force. *Technical Manual: General Advanced Composite Repair Processes Manual*. Technical Order 1-1-690. Hill AFB, Utah. 1990.
- FM 300 Film Adhesive*. Product Catalog. Harve de Grace, MD: American Cyanamid Company, 1990.
- Found, M.S., and M.J. Friend. "Evaluation of CFRP panels with scarf repair patches", *Composite Structures*, 32: 115-122 (1995).
- Hart-Smith, L.J. Adhesive-Bonded Scarf and Stepped-Lap Joints. Contract NAS1-11234. Hampton VA: Langley Research Center, January 1973 (NASA CR 112237)
- Iarve, E.V. "Spline Variational Three Dimensional Stress Analysis of Laminated Composite Plates with Open Holes", *International Journal of Solids and Structures*, 33: 2095-2118 (1996).
- Iarve, E.V. and N.J. Pagano. "Singular Full-Field Stresses in Composite Laminates with Open Holes", *International Journal of Solids and Structures*, 38:1-28 (2001).
- Kim, Hyun Surk, Su Jeong Lee, and Dai Gil Lee. "Development of a strength model for the cocured stepped lap joints under tensile loading", *Composite Structures*, 32: 593-600 (1995).
- Kim, J.H. B.J Park and Y.W. Han. "Evaluation of fatigue characteristics for adhesively-bonded composite stepped lap joint", *Composite Structures*, 66: 69-75 (2004).
- Knox, E.M., S. Lafferty, M.J. Cowling and S.A. Hashim. "Design Guidance and Structural Integrity of Bonded Connections in GRE Pipes", *Composites: Part A: Applied Science and Manufacturing*, 32: 231-241 (2001).
- Mehrkam, P.A., E. Armstrong-Carroll and R. Cochran. "Fire Damage Assessment of A-6 Composite Wing BUNO 152951." Naval Air Warfare Center Aircraft Division: Warminster, PA, 29 September 1993.

- Middleton, Donald H. *Composite Materials in Aircraft Structures*. New York, NY: Longman Scientific and Technical, 1990.
- Mollenhauer, David. Handout. *Moiré Interferometry*. Air Force Research Laboratories, Wright-Patterson AFB OH, no date.
- Mortensen, Flemming and Ole Thybo Thomsen. "Simplified Linear and Non-Linear Analysis of Stepped and Scarfed Adhesive-Bonded Lap-Joints between Composite Laminates", *Composite Structures*, 38:281-294 (1997).
- Mortensen, F. and O.T. Thomsen. "Analysis of Adhesive Bonded Joints: A Unified Approach," *Composites Science and Technology*, 62:1011-1031 (2002).
- Odi, Randolph A. and Clifford M. Friend. "An Improved 2D Model for Bonded Composite Joints", *International Journal of Adhesion and Adhesives*, 24:389-405 (2004)
- Schoeppner, G.A., D.H. Mollenhauer, and E.V. Iarve. "Prediction and Measurement of Residual Strains for a Composite Bonded Joint", *Mechanics of Composite Materials*, 40: 119-134 (2004).
- SolidWorks*. Education Edition SP3.1. Computer software. SolidWorks Corporation, Concord MA, 2004.
- Soutis, C. and F.Z. Hu. "A 3D Failure Analysis of Scarf Patch Repaired CFRP Plates", *American Institute of Aeronautics and Astronautics, Inc.*, 1943: 1971-1977 (1998).
- Tong, Liyong and Costas Soutis. *Recent Advances in Structural Joints and Repairs for Composite Materials*. Dordrecht: Kluwer Academic Publishers, 2003.
- Transform User's Guide and Reference Manual*. Transform Version 3.4. Fortner Software. Sterling VA, May 1999.
- Tsai, M.Y., D.W. Oplinger, and J. Morton. "Improved Theoretical Solutions for Adhesive Lap Joints", *International Journal of Solids and Structures*, 35:1163-1185 (1998).
- Ultrasonic C-scan (high frequency)*. Department of Metallurgy and Materials Engineering. K.U. Leuven. 5 June 2000.
http://www.mtm.kuleuven.ac.be/Research/Equipment/Mechanical/C-scan_high.html.
- Wang, B.S., F.P. Chiang, and S.Y. Wu. "Whole-field Residual Stress Measurements in Rail Using Moire Interferometry and Twyman/Green Interferometry via Thermal Annealing", *Experimental Mechanics*, 39:71-76 (1999).

Zou, G.P., K. Shahin, and F. Taheri. "An Analytical Solution for the Analysis of Symmetric Composite Adhesively Bonded Joints", *Composite Structures*, 65:499-510 (2004).

Vita

Second lieutenant Brian M. Fredrickson graduated from Thomas Jefferson Senior High School in Auburn, Washington in 2000. He entered undergraduate studies at the United States Air Force Academy in Colorado Springs, Colorado where he graduated with a Bachelor of Science degree in Mechanical Engineering and was recognized as a Distinguished Graduate. He was commissioned in June 2004.

In September 2004, he entered the Graduate School of Engineering and Management, Air Force Institute of Technology, to pursue a Masters of Science in Aeronautical Engineering. Upon graduation, he will to be assigned to the Materials Directorate of the Air Force Research Laboratory at Wright-Patterson AFB.

REPORT DOCUMENTATION PAGE				Form Approved OMB No. 074-0188	
<p>The public reporting burden for this collection of information is estimated to average 1 hour per response, including the time for reviewing instructions, searching existing data sources, gathering and maintaining the data needed, and completing and reviewing the collection of information. Send comments regarding this burden estimate or any other aspect of the collection of information, including suggestions for reducing this burden to Department of Defense, Washington Headquarters Services, Directorate for Information Operations and Reports (0704-0188), 1215 Jefferson Davis Highway, Suite 1204, Arlington, VA 22202-4302. Respondents should be aware that notwithstanding any other provision of law, no person shall be subject to a penalty for failing to comply with a collection of information if it does not display a currently valid OMB control number.</p> <p>PLEASE DO NOT RETURN YOUR FORM TO THE ABOVE ADDRESS.</p>					
1. REPORT DATE (DD-MM-YYYY) 23 Mar 06		2. REPORT TYPE Master's Thesis		3. DATES COVERED (From – To) Aug 04 – Mar 06	
4. TITLE AND SUBTITLE Application of Spline Variational Analysis Method in the Modeling of Composite Repairs				5a. CONTRACT NUMBER	
				5b. GRANT NUMBER	
				5c. PROGRAM ELEMENT NUMBER	
6. AUTHOR(S) Fredrickson, Brian M., Second Lieutenant, USAF				5d. PROJECT NUMBER	
				5e. TASK NUMBER	
				5f. WORK UNIT NUMBER	
7. PERFORMING ORGANIZATION NAMES(S) AND ADDRESS(S) Air Force Institute of Technology Graduate School of Engineering and Management (AFIT/EN) 2950 Hobson Way WPAFB OH 45433-7765				8. PERFORMING ORGANIZATION REPORT NUMBER AFIT/GAE/ENY/06-M09	
9. SPONSORING/MONITORING AGENCY NAME(S) AND ADDRESS(ES) AFRL/MLBCM Attn: Dr. Greg Schoeppner 2941 Hobson Way WPAFB OH 45433-7750 DSN: 785-9072 PHONE: (937) 255-0972				10. SPONSOR/MONITOR'S ACRONYM(S)	
				11. SPONSOR/MONITOR'S REPORT NUMBER(S)	
12. DISTRIBUTION/AVAILABILITY STATEMENT APPROVED FOR PUBLIC RELEASE; DISTRIBUTION UNLIMITED.					
13. SUPPLEMENTARY NOTES					
14. ABSTRACT The purpose of this thesis is to apply a non-commercialized spline-based (B-Spline Analysis Method or BSAM) computer program to model and predict strain fields in two composite repairs, a scarf joint and a stepped-lap joint, subjected to static tensile loading. Test specimens with straight scarf and stepped-lap joints are fabricated using quasi-isotropic sixteen ply panels made from IM6/3501-6 prepreg. The panels were bonded together with FM-300M (0.05psf), a 176°C cure film adhesive. A total of five coupons of each joint type are made. Two of the stepped-lap and scarf coupons are instrumented with acoustic emission sensors and loaded in tension to determine loading for experimentation. Moire interferometry, a high resolution full-field optical technique used to measure displacements on a surface, is used to acquire experimental strain data. Diffraction grating is applied to the polished edge of two stepped-lap and two scarf coupons, while one coupon of each was selected for experimentation under a static tensile load of 450lb _f . Using measurements from the actual coupon specimens, idealized models of the stepped-lap and scarf joints are developed for the BSAM computer program. Overall, both the full-field strain images and line plots show a good agreement between the BSAM analysis and the experiment.					
15. SUBJECT TERMS Composites, Adhesive Bonding, Acoustic Emissions, Static Load, B-Spline Analysis Method					
16. SECURITY CLASSIFICATION OF:			17. LIMITATION OF ABSTRACT	18. NUMBER OF PAGES	19a. NAME OF RESPONSIBLE PERSON
REPORT	ABSTRACT	c. THIS PAGE			Dr. Anthony Palazotto
U	U	U	UU	300	19b. TELEPHONE NUMBER (Include area code) (937)255-6565; e-mail: @afit.edu

Standard Form 298 (Rev. 8-98)
Prescribed by ANSI Std. Z39-18